BIFUNCTIONALITY: NEW INSIGHTS IN THE CLASS OF (6-4) PHOTOLYASES AND ANIMAL-LIKE CRYPTOCHROMES

Kumulative Dissertation

Zur Erlangung des Doktorgrades der Naturwissenschaften

(Dr. rer. nat.)

dem

Fachbereich Chemie

der Philipps-Universität Marburg

Hochschulkennziffer 1180

vorgelegt von

Sophie Elisabeth Franz-Badur

geb. Franz, M.Sc. Chemie

aus Hüttenberg

(geb. in Gießen)

Marburg an der Lahn, Dezember 2018

Erstgutachter: Prof. Dr. Lars-Oliver Essen (Fachbereich Chemie)

Zweitgutachter: Prof. Dr. Alfred Batschauer (Fachbereich Biologie)

Einreichungstermin: 15.12.2018

Prüfungstermin: 22.02.2019

Marburg 2019

“It is still magic even if you know how it is done”

-Terry Pratchett

Sophie Elisabeth Franz-Badur geb. Franz
Hauptstraße 42
35625 Hüttenberg

Erklärung

Ich erkläre, dass eine Promotion noch an keiner anderen Hochschule als der Philipps-Universität Marburg, Fachbereich Chemie, versucht wurde.

Ich versichere, dass ich meine vorgelegte Dissertation

„Bifunctionality: New Insights in the Class of (6-4) Photolyases and animal-like Cryptochromes“

selbst und ohne fremde Hilfe verfasst, nicht andere als die in ihr angegebenen Quellen oder Hilfsmittel benutzt, alle vollständig oder sinngemäß übernommenen Zitate als solche gekennzeichnet, sowie die Dissertation in der vorliegenden oder einer ähnlichen Form noch bei keiner anderen in- oder ausländischen Hochschule anlässlich eines Promotionsgesuchs oder zu anderen Prüfungszwecken eingereicht habe.

Ort/Datum Unterschrift

(Sophie Elisabeth Franz-Badur)

List of publications

Franz-Badur S, Penner A, Straß S, von Horsten S, Linne U and Essen LO*. *Structural changes within the bifunctional cryptochrome/photolyase CraCRY upon blue light excitation* (submitted to Nature Scientific Reports, **2018**),

Maestre-Reyna M, Yang CH, Huang WC, Putu EPGN, **Franz-Badur S**, Wu WJ, Wu HY, Wang PH, Liao JH, Lee CC, Huang KF, Chang YK, Weng JH, Sugahara M, Owada S, Joti Y, Tanaka R, Tono K, Nango E, Kiontke S, Yamamoto J., Iwata S, Essen LO*, Bessho Y*, Tsai MD*. *An arginine-aspartate electrostatic gate tunes the photolyase flavin chromophore* (submitted to Science, **2018**).

Franz S, Ignatz E, Wenzel S, Zielosko H, Putu EPGN., Maestre-Reyna M, Tsai MD, Yamamoto J, Mittag M and Essen LO* (**2018**), *Structure of the bifunctional cryptochrome aCRY from Chlamydomonas reinhardtii,* Nucleic Acids Res. 46(15):8010-8022.

Essen LO*, **Franz S**, Banerjee A. (**2017**), *Structural and evolutionary aspects of algal blue light receptors of the cryptochrome and aureochrome typ.,* J Plant Physiol.217:27-37.

Nohr D, **Franz S**, Rodriguez R, Paulus B, Essen LO*, Weber S, Schleicher E.* (**2016**), *Extended Electron-Transfer in Animal Cryptochromes Mediated by a Tetrad of Aromatic Amino Acids*., Biophys J. 111(2):301-311.

Oldemeyer S, **Franz S**, Wenzel S, Essen LO, Mittag M, Kottke T.* (**2016**), *Essential Role of an Unusually Long-lived Tyrosyl Radical in the Response to Red Light of the Animal-like Cryptochrome aCRY.*, J Biol Chem. 291(27):14062-71.

*=corresponding author

CV – Wissenschaftlicher Werdegang

09/2014 –12/2018 PhD thesis in the research group of Professor Dr. Lars-Oliver Essen, Department of Chemistry, Philipps-University Marburg
PhD project: Bifunctionality: "Bifunctionality: New Insights in the Class of (6-4) Photolyases and animal-like Cryptochromes"
Major: Biochemistry

Promotion in der Arbeitsgruppe von Prof. Dr. Lars-Oliver Essen, Fachbereich Chemie, Strukturbiologie, Philipps-Universität Marburg
Schwerpunkt: Biochemie und Bioanalytik

09/2014 – 09/2016 IMPRS fellow of the Max Planck Institute for Environmental, Cellular and Molecular Biology, Marburg

IMPRS Stipendiatin des Max-Planck-Instituts für terrestrische Mikrobiologie, Marburg

Master studies

10/2011 – 07/2014 Department of Chemistry, Philipps-University Marburg
Awarded: Master of Science (Chemistry)
Thesis: "Structural and functional characterization of the animal-like Cryptochrome of *Chlamydomonas reinhardtii*"; Supervisor: Prof. Dr. Lars-Oliver Essen

Fachbereich Chemie, Philipps-Universität Marburg
Master of Science (Chemie)
Schwerpunkt: Biochemie

Bachelor studies

10/2008 – 09/2011 Department of Chemistry, Philipps-University Marburg
Awarded: Bachelor of Science (Chemistry)
Thesis: "Study of the synthesis of the amino acid 3,4-dihydroxy-L-homotyrosine"; Supervisor: Dr. Markus Oberthür

Fachbereich Chemie, Philipps-Universität Marburg
Bachelor of Science (Chemie)

Table of Content

Zusammenfassung

Die Familie der Cryptochrome und Photolyasen (CPF) ist eine große Proteinfamilie von Blaulicht Photorezeptoren, welche in allen Bereichen des Lebens vertreten sind. Alle Vertreter dieser Familie verwenden einen Flavinchromophor als katalytischen Kofaktor und zeigen hohe Sequenz- und Strukturähnlichkeiten, obwohl sich ihre Funktionen in lebenden Organismen stark unterscheiden. Einerseits verwenden Photolyasen die Energie des Sonnenlichts zur Reparatur von UV-induzierten DNA Schäden wie dem Cyclobutan-Pyrimidin-Dimer (CPD) Schaden oder dem Pyrimidin-(6-4)-Pyrimidon Photoprodukt ((6-4)PP). Cryptochrome sind andererseits involviert in verschiedenen Blaulicht-regulierten Mechanismen, wie zum Beispiel die photoperiodischen Blühzeiten in Pflanzen oder die Regulierung des circadianen Rhythmus in Tieren.

Diese Arbeit befasst sich mit der Charakterisierung der Photoreduktion sowie des (6-4)-Reparaturmechanismus einer Untergruppe von tierischen Cryptochromen und (6-4)-Photolyasen anhand des *animal-like* Cryptochromes aus der Grünalge *Chlamydomonas reinhardtii* (*Cr*aCRY). Durch multiple Sequenzvergleiche mit anderen CPFs und Mutationsstudien konnten die spezifischen und für die Photoreduktion relevanten Aminosäure-Reste identifiziert werden. Dies führte zur Entdeckung eines Tyrosins als vierten Elektronendonor am Ende der konservierten Tryptophantriade. Die Photoreduktion wurde weiterhin mit verschiedenen spektroskopischen Methoden untersucht mit besonderem Augenmerk auf der Entstehung und den Abbau des Tyrosylradikals.

Wie gezeigte wurde, handelt es sich bei *Cr*aCRY nicht nur um ein Cryptochrom, sondern es zeigt darüber hinaus (6-4)-Photolyase Aktivität, was es zu einem bifunktionellen Mitglied der CPF macht. Um die Beziehung zwischen Struktur und Funktion zu untersuchen, habe ich die 3D-Struktur von *Cr*aCRY im Komplex mit seinen Chromophoren sowie einem (6-4)PP per Röntgenstrukturanalyse entschlüsselt. Dabei zeigte sich ein neuer Modus für die DNA Bindung sowie ein detaillierter Einblick in die aktive Tasche. Ein essentieller Rest für die DNA Reparatur (His_1) wies eine veränderte Konformation im Vergleich zu dem bisher

veröffentlichen Model auf. Dies könnte auf einen alternativen Reparaturprozess für (6-4)PP hindeuten.

Die wissenschaftlichen Erkenntnisse über die Struktur von Cryptochromen basieren vor allem auf dem Vergleich zu Photolyasen, jedoch besitzen Cryptochrome einen elongierten C-Terminus (CTE), welcher den Photolyasen fehlt. Dieser CTE ist in *Cr*aCRY ca. 100 Aminosäuren lang und nicht in der Kristallstruktur enthalten. Um den CTE weiter zu analysieren wurde Wasserstoff-Deuterium-Austausch gekoppelt mit Massenspektrometrie durchgeführt und die unterschiedlichen Reduktionszustände miteinander verglichen. Die erhaltenen Ergebnisse decken zwar den CTE nicht vollständig ab, jedoch konnten klare Unterschiede zwischen den Reduktionszuständen festgestellt werden. Daraus können wir schließen, dass es durch die Bildung des Tyrosylradikals bei der Photoreduktion zur Umstrukturierung im Bereich der Tyr-Schleife sowie der C-terminalen α22-Helix kommt.

Um die intramolekularen strukturellen Veränderungen durch die Photoreduktion und DNA-Reparatur weiter zu untersuchen, wurde zeitaufgelöste Röntgenstrukturanalyse am freien Elektronenlaser SACLA mit einer Klasse II CPD Photolyase (*Mm*CPDII) und *Cr*aCRY durchgeführt. Dadurch war es möglich geworden die verschiedenen Konformationen des *Mm*CPDII Flavinchromophors in seinen unterschiedlichen Oxidationszuständen zu zeigen. Diese Arbeiten legen den Grundstein dafür, dass der komplette Reparaturmechanismus der CPD sowie (6-4) Schäden durch zeitaufgelöste SFX aufgelöst werden kann.

Summary

The cryptochrome/photolyase family (CPF) is a huge protein family of blue-light photoreceptors, which occur in all kingdoms of life. All members of this family utilize a flavin chromophore as catalytic cofactor and show high sequence and structural similarity, although they have different functions inside the living organism. Photolyases use the energy of light to repair UV-light induced DNA lesions like the cyclobutane pyrimidine dimer (CPD) or the pyrimidine-(6-4)-pyrimidone photoproduct ((6-4)PP). Cryptochromes, on the other hand, are involved in many different blue-light regulated mechanisms, like the photoperiodic flowering in plants and the entrainment of the circadian rhythm in animals.

This study focuses on the characterization of the photoreduction and (6-4) repair mechanism of the subclass of animal cryptochromes and (6-4) photolyases on the basis of the animal-like cryptochrome from the green algae *Chlamydomonas reinhardtii* (*Cr*aCRY). Through multiple sequence alignment with other CPFs and mutational studies, the specific residues involved in the photoreduction mechanism were successfully identified, leading to the discovery of a tyrosine as distal electron donor at the end of the conserved tryptophan triad. The photoreduction, with regard to the formation and decay of a tyrosyl radical, was extensively studied with several spectroscopic methods. All analyses resulted in the observation of an unusually long-lived tyrosyl radical upon photoreduction.

As it turned out, *Cr*aCRY is not only a cryptochrome, but also has (6-4) photolyase function, which makes it a bifunctional member of this group. To study structure-function relationships, the 3D structure of *Cr*aCRY in complex with its chromophores as well as a (6-4)PP was solved by X-ray crystallography. The structure reveals a new binding mode of the DNA lesion and provides insight into the active site. One of the essential residues for DNA repair (His_1) exhibits a different conformation as in the common model, which may indicate an alternative mechanism for (6-4)PP repair.

The main knowledge about cryptochrome structures derived from the comparison with photolyases, but cryptochromes contain a highly variable C-terminal extension (CTE), which is missing in photolyases. In *Cr*aCRY this CTE is about 100 amino acids long and not shown in

the solved crystal structure. For analysis of the CTE, hydrogen-deuterium-exchange coupled with mass spectrometry was used including a comparison of different reduction. Although, the coverage of the CTE was incomplete, there were significant changes between the oxidized and fully reduced state $FADH^-$ detectable. It was concluded, that the photoreduction process and the formation of the tyrosyl radical is triggering a structural change in the region between the loop carrying the tyrosyl radical and the C-terminal α22-helix.

For further investigation of the intramolecular changes upon photoreduction and DNA repair, time-resolved crystal measurements of a class II CPD photolyase (*Mm*CPDII) and *Cr*aCRY were performed within a joint project at the free electron laser SACLA. So far, the different conformations of the flavin cofactor of *Mm*CPDII in its different oxidation states have been successfully derived. In future, it is expected to show the whole repair mechanism for the CPD lesion as well as for the (6-4)PP by time-resolved SFX.

1 Introduction

1.1 Importance of sunlight and photoreceptors for biological processes

Sunlight is one of the most important driving forces on earth and the basis of life as we know it. The total amount of sun energy that hits the surface of the earth is around 1.36 kW m^{-2} (1) and organisms developed several mechanisms to use this energy to perform specific metabolic processes. To absorb the energy, organisms use special photoactive enzymes called photoreceptors. For sensing the different characteristics of light like intensity, direction, quality and spectra composition and triggering cellular signaling processes (2). Except the more recently discovered UV-light resistant locus 8 (UVR8) (3), which absorbs UV-B light intrinsically with a set of tryptophan residues as chromophore, all photoreceptors utilize one or more chromophores to absorb specific wavelengths of the whole light spectrum. The six most studied photosensory modules (Figure 1), which form the different photoreceptors are rhodopsins, phytochromes, photoactive yellow proteins (PYP), blue-light using flavin (BLUF) proteins, light-oxygen-voltage (LOV) proteins and cryptochromes (4–9). Even though these six well-studied and highly common types of photosensory proteins only use four different kinds of chromophores, they are able to show a high variety in their structural, spectral and biophysical properties (7).

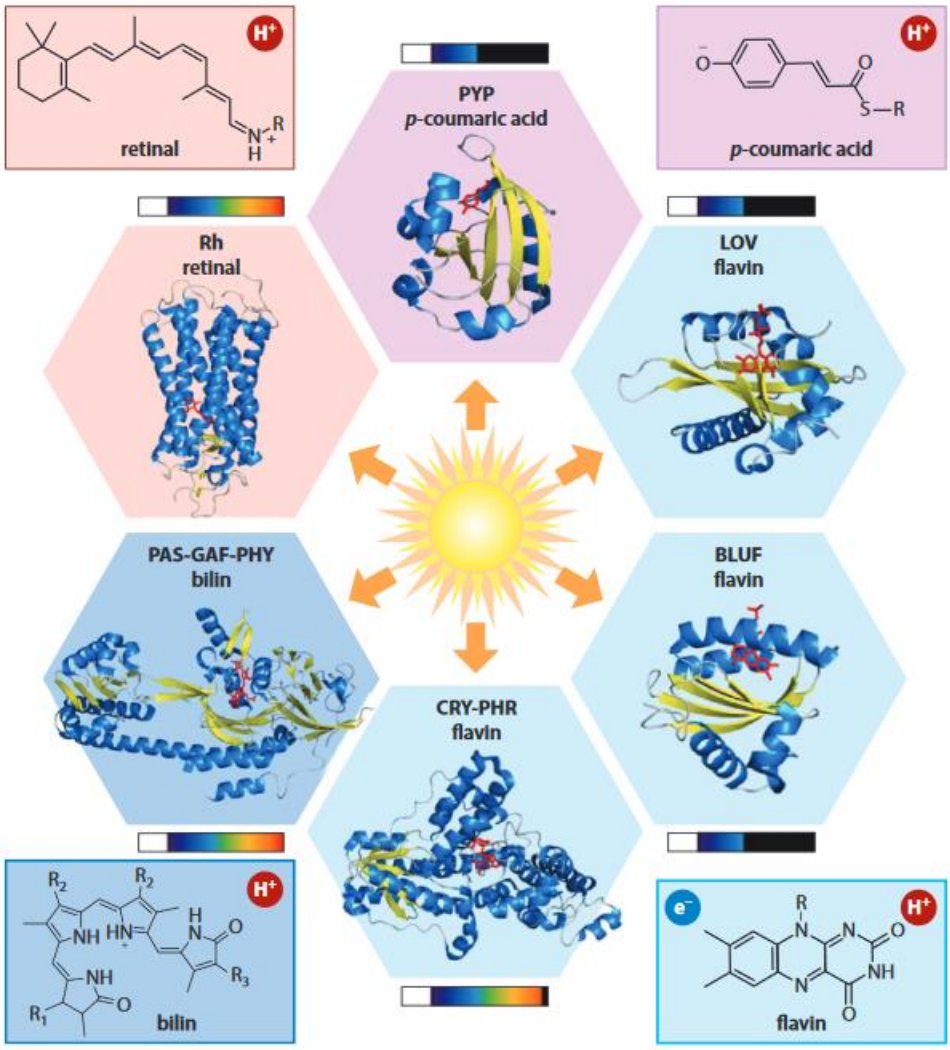

Figure 1 Overview of the six well-studied photosensory modules and their chromophores (figure adapted from (7)). Starting from the upper left: Rh, rhodopsin (PDB: 1F88) with retinal; PYP, photoactive yellow protein (1NWZ) with *p*-coumaric acid; LOV, light-oxygen voltage domain (2V0U) with flavin, BLUF, blue-light using flavin (2BYC); CRY-PHR, cryptochrome photolyase-homology region (1U3D) with flavin; PAS-GAF-PHY, Per-ARNT-Sim-cGMP phosphodiesterase/adenylyl cyclase/FhlA-phytochrome-specific domain (2VEA) with bilin. The spectral range absorbed by each receptor is indicated with colored bars and the intrinsic, light-dependent transfer mechanisms the different chromophores utilize is marked with either a proton (H^+) or an electron (e^-).

However, sunlight can not only help organisms to entrain signaling processes as its high energetic UV radiation below 300 nm can cause severe damages to DNA as well (10). The damages that appear are commonly cyclobutane pyrimidine dimer (CPD) lesions (ca. 80-90% of all UV-damages (11)) as well as pyrimidine-(6-4)-pyrimidone photoproducts ((6-4)PP) (Figure 2). To repair DNA damages, higher eukaryotes utilize a complex repair system called

nucleic excision repair (NER), which removes a whole stretch of DNA to cut out UV-damaged nucleic acid stretches (12). In most other organisms, the repair of UV-lesions is conducted by a more specific enzyme, the blue-light activated photolyase.

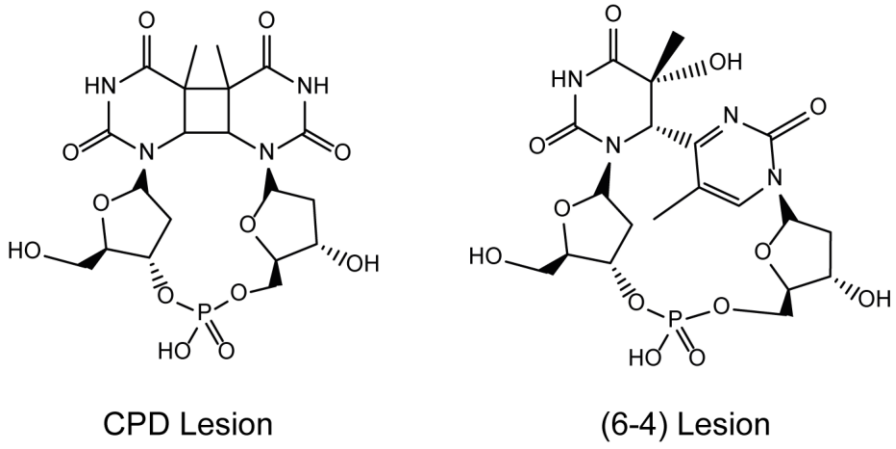

Figure 2 The most common UV-light induced DNA lesions. The cyclobutane pyrimidine dimer (CPD) lesion is the product of a [2+2] cyclo-addition, whereas the pyrimidine-(6-4)-pyrimidone photoproduct ((6-4)PP) is formed via an oxetane intermediate and a PATERNO-BÜCHI rearrangement (13).

1.2 The Cryptochrome/Photolyase Family

The cryptochrome/photolyase family (CPF) is a large family of flavoproteins, which occurs in all three kingdoms of life. They are roughly classified by their function either as photolyases (PHL) or cryptochromes (CRY).

Historic overview

Photolyases were first described 60 years ago by Rupert *et al.*, who called them photoreactive enzymes (14). They are involved in the process for reversing the lethal effect of UV radiation by exposure to visible light called photoreactivation as discovered by KELNER in the 40ies (15). RUPERT and SANCAR were then able to clone the *phr* gene in *E. coli* (16) and purify the expressed photolyase (17). Since then, a lot more photolyases from different organisms were described and isolated (18–23). Photolyases are categorized into two subgroups according to their damaged DNA substrate, namely the cyclobutane-pyrimidine dimers (CPD) or pyrimidine-(6-4)-pyrimidone photoadducts, (6-4)PP. In contrast to the well-known and highly characterized CPD-photolyases, (6-4) photolyases have been discovered

over two decades later in *Drosophila* (24). Even though PHLs can be found in all kingdoms of life, they are not ubiquitously found in all orders and families (19). For example, there are no CPD-PHLs nor (6-4)PHLs present in humans and other placental mammals (25, 26). Surprisingly, in some animal viruses with large genomes like the Fowlpox or Entomopoxvirus PHL genes were identified (27, 28).

Blue-light (BL)-photoreceptors like cryptochromes and phototropins were discovered more recently, even though CHARLES DARWIN already described the influence of blue-light on plants (29). The name "cryptochrome" originates from a publication from GRESSEL in 1979, who was referring to their "cryptic" nature as a "pigment system responsible for many photo processes" (30). At that time he was talking about all BL-dependent receptors in plants. In 1993, AHMAD and CASHMORE were able to isolate the HY4 gene from *Arabidobsis thaliana*, which was later renamed to CRY1 (*At*CRY1) (31). Its gene product was identified to be responsible for the inhibition of hypocotyl elongation under BL-illumination. *At*CRY1 was found to utilize FAD as primary cofactor (32). Despite its selectively high sequence identity to bacterial PHL and utilization of the same cofactors, *At*CRY1 was not able to repair UV-damaged DNA *in vitro* (32). Later on, a lot of *At*CRY1-like sequences were identified in animals (flies, mouse, human) as well as bacteria (6, 33). Since 1993 it is known that humans lack photolyases (25) and also the human CRY1 and CRY2 do not display any DNA repair activity, even though they show 73 % sequence identity to the *Drosophila melanogaster* (6-4)PHL (26). Their role as a key factor in circadian photoreception in mammals was identified in 1998 in mice (34).

Phylogenetic classification

Despite belonging to one family, CRYs are having different ancestors as plant CRYs are more similar to CPD Photolyases and animal CRYs are related to (6-4)PHL (33). As this is a huge and diverse protein family, a classification into different subclasses is non-trivial. One phylogenetic analysis by OZTURK (35) is shown in Figure 3a. Here, 10 major classes of PHLs and CRYs were identified. Class I CPD-PHL is found manly in unicellular organisms as class II is present also in multicellular organisms (36). Class III CPD photolyases were identified in

several eubacteria (37). Also belonging to the CPD PHL-related class, the single strand repairing PHLs were firstly annotated as cry-DASH (*DASH: Drosophila, Arabidopsis, Synechocystis, Human*) (38). This class was initially thought to belong to the cryptochrome family, but is better termed ssDNA PHL or class 0 PHL according to OZTURK (35). This term might be not completely suitable as *At*CRY3, which also belongs to the DASH subclass, is able to repair double stranded DNA as well as single stranded DNA substrates, if the lesion is present on a loop structure (39). More recently the dsDNA repair activity of *Phycomyces* CryA was shown, which resulted in the hypothesis that canonical CPD-PHLs were lost in fungi, but DASH CRYs were able to maintain DNA repair (40). However, plant CRYs or type 3 CRYs are likewise included into the branch of CPD PHL-related proteins, but lack any photolyase function. They are mediating photomorphogenetic responses (inhibition of stem elongation, stimulation of leaf expansion, control of photoperiodic flowering, entrainment of the circadian clock) (35) as well as functioning as photosensors for resetting the plant circadian clock. Evidently, phylogenetic classification does not automatically correlate with the function of an enzyme.

(6-4)PHLs are additionally branching in a completely different direction and show high relationship to type 1, type 2 and type 4 cryptochromes. Animal CRYs were first classified as insect-type/ type 1 and mammal-type/ type 2 cryptochromes. Later on, type 2 CRYs (41) were also found in some insects, honeybees and ants even harbor only type 2 CRYs (42, 43). In case of type 1 CRYs, the *Dm*CRY from *Drosophila melanogaster* is the most studied family member (44). Type 1 and type 2 CRYs are mainly differing by their functionality. Type 1 CRYs represent the main photoreceptor for resetting the circadian clock. In contrast, type 2 CRYs are involved in the core clock, but lack any photosensory function (35). The CRY genes in mice and humans are both coding for type 2 CRYs (35). Type 4 CRYa are mainly found in frogs, fishes and birds (45), but the *in vivo* function of this class is not yet identified. Between CPD PHL-related and (6-4)PHL-related CRYs is another class of sponge cryptochromes, also called I-CRY or type 0, as they are located at one pole, the “eye” of the sponge (46), which mediates phototactic swimming. I-CRYs function as a cryptochrome-based photoreception system inside the glass fiber network of the siliceous skeleton of

sponges (47, 48), where they convert photons into radicals (49). It is worth to be noted, that CRYs and PHRs can coexist in the same organism.

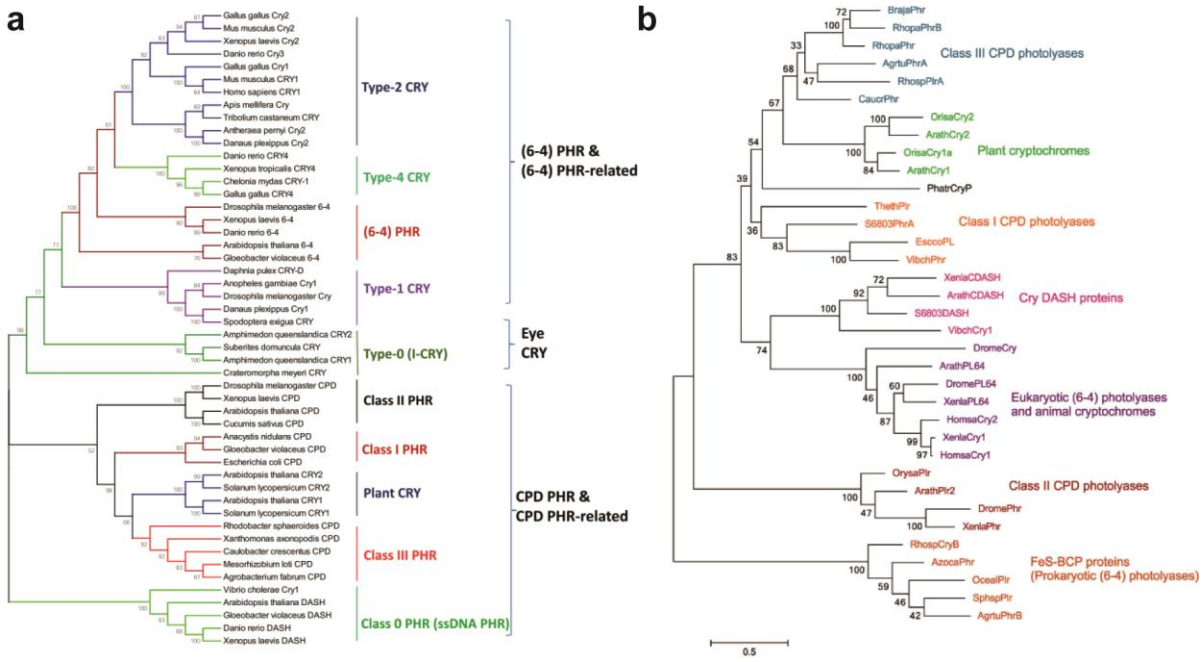

Figure 3 a) Phylogenetic classification of the cryptochrome/photolyase family from OZTURK (35). Over 200 sequences of PHLs and CRYs were aligned using *ClustalW* and after further analysis, ten major classes were identified. These can be summarized further into 3 categories, the (6-4)PHLs (PHR) or (6-4)PHL-related ones, the CPD PHLs (PHR) or CPD PHL-related ones, and the Eye CRYs (I-CRYs), which is a newly identified group from sponges. **b)** Phylogenetic tree of the CPF by Scheerer *et al.* (50). Here, seven distinct classes are identified and indicated in different colors. PhatrCryP (from *Phaeodactylum tricornutum*) is shown in black, as it cannot be assigned to one of the classes. This tree is also taking the iron-sulfur cluster containing bacterial cryptochromes and photolyases (FeS-BCP or CryPro) into account.

Figure 3b displays a phylogenetic tree published by Scheerer *et al.* (50), which reveals some differences to the classification done by OZTURK (35). In this tree, the subclass of iron-sulfur cluster containing bacterial cryptochromes and photolyases (51), FeS-BCP or also known as CryPro (52), is represented. These enzymes were identified in proteobacteria and cyanobacteria. They were shown to miss the catalytic triad (52, 53), which is also the case in class II CPD photolyases (54, 55). However, in this classification animal CRYs and (6-4)PHLs are already put together in one big subgroup as they exhibit such a high relationship. Another analysis, focusing more on aquatic organisms, done by Oliveri *et al.* (56) is shown in Figure 4. Hitherto, four major classes are presented with a novel plant CRY superclass

(Figure 4C), which comprises of the classical plant CRYs as well as a new group of plant-like CRYs and class I and class III CPDs. This new subgroup of plant-like CRYs also includes the CryP from *Phaeodactylum tricornutum*, which could not be allocated in the analysis of Scheerer *et al.* (50).

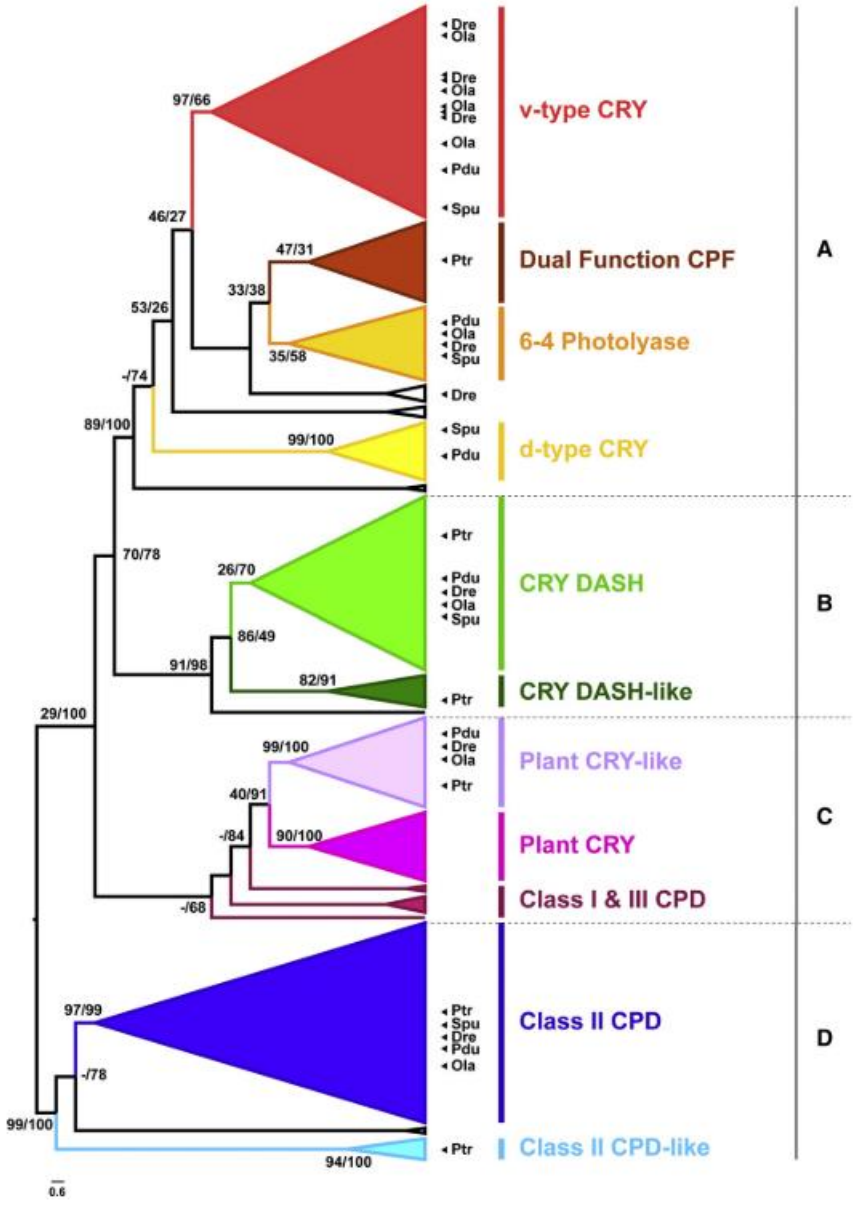

Figure 4 Phylogenetic analysis of the CPF with a focus on aquatic organisms done by Oliveri *et al.* (56). Here, 215 sequences from 56 different species were used including 26 aquatic species. Four major groups are highlighted with letters: the animal CRYs/(6-4)PHLs (A), CRY-DASH (B), plant CRYs (C) and class II CPD PHLs (D).

In this analysis, the group of animal CRYs/(6-4)PHLs (A) is the most divers superclass, which consists of four major subgroups: type 2 or v-type CRYs, type 1 or d-type CRYs, (6-4) photolyases and a group of proteins with a putative double function (56–58).

Comparison of these different phylogenetic analysis shows that a classification of this huge protein family considering evolutionary constrains is not an easy task and that functions might differ from the predicted subclass.

1.3 Structure of the CPF

The first structure to be deposited in the RCSB protein data bank (PDB) was the crystal structure of the CPD photolyase of *E. coli* (59), *Ec*CPDI, in 1995. The resulting crystal structure (1DNP) is resolved up to 2.3 Å and includes two cofactors, the catalytic FAD and the ancillary antenna MTHF. Up to now (November 2018), there are 54 entries in the PDB for “photolyase”, which includes several structures of mutants and substrate complexes as well as cryptochromes.

Comparing the structures, they are all presenting the same bilobal domain architecture. The N-terminal domain consists of alternating alpha-helices and beta-sheets, which can be assigned as a ROSSMANN-fold. Typical ROSSMANN domains are able to bind a nucleotide cofactor like flavin, $NADP^+$ or ATP (60, 61). In photolyases, this domain is harboring the binding site for the antenna pigment. N- and C-terminal domains are connected over a linker, which is a flexible loop region and includes in some cases also alpha-helices of variable length (Figure 5a). The C-terminal domain or FAD binding domain consists only of alpha-helices. The catalytic flavin cofactor is non-covalently bound near to a highly conserved asparagine residue (N378 in *Ec*CPDI). There are a few structural variations around the FAD and DNA binding sites in the different repair classes, which correlates with a divergence in reaction rates and quantum yields (62). For example, an asparagine residue forming an H-bond with the N5-nitrogen of flavin chromophore is preserved in class II CPD PHLs, but located on a different α-helix than in class I PHLs (54, 55). Likewise, in cry-DASH /ssDNA-PHLs two conserved residues in the DNA binding site are different, which normally support the flipping of the CPD lesion inside the pocket in CPD-PHLs (63). DNA binding in

CPD- and (6-4) photolyases is highly affected of the electrostatic potential of the surface of the enzyme. Therefore, the DNA binding site features a positively charged cleft on top of the FAD binding domain (Figure 5c) to match the negatively charged phosphate backbone of the DNA.

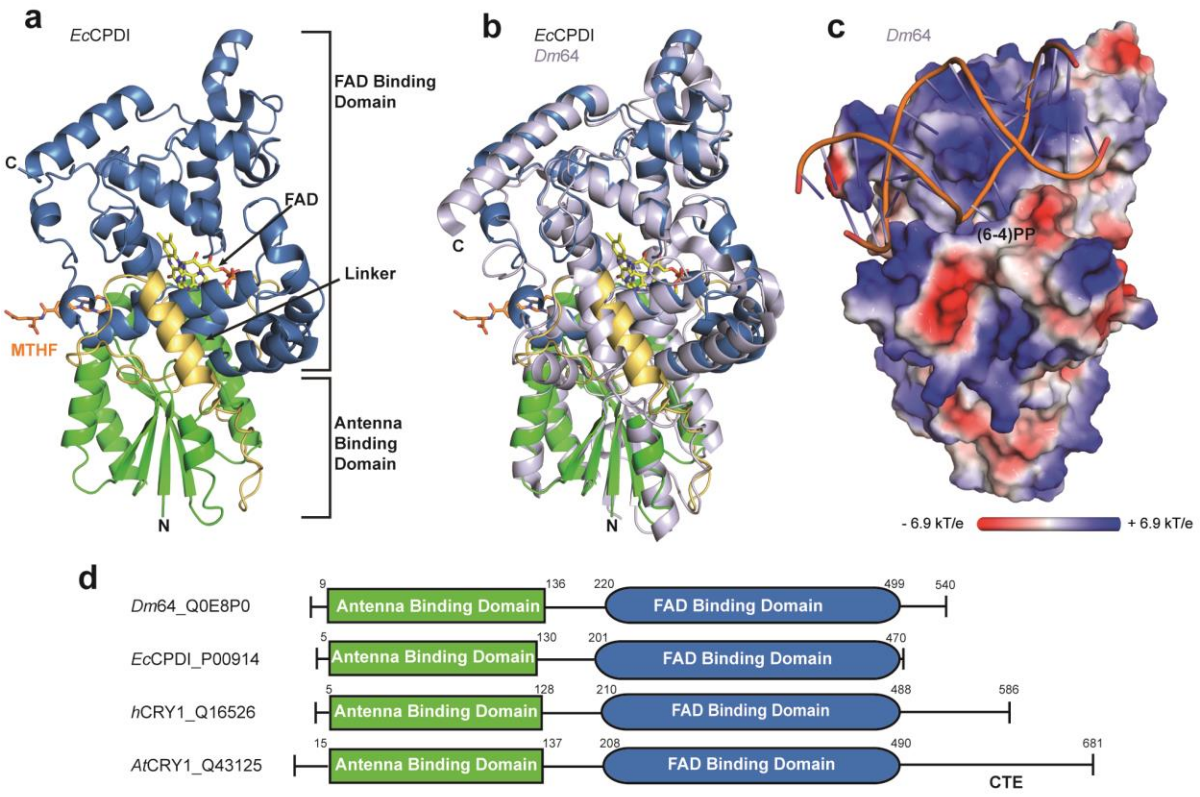

Figure 5 Structural overview of the cryptochrome/photolyase family. **a)** 3D structure of the *E. coli* CPD class I PHL (1DPN). The photolyase is build of two chromophor binding domains, which is connected via a linker (yellow). FAD is bound in a U-shaped conformation. **b)** Structural alignment of *Ec*CPDI and *Dm*64 (3CVU). The high structural similarity is shown and only small differences can be seen. **c)** Electrostatic surface view of *Dm*64 in complex with UV-damaged DNA. The positively charged cleft of the DNA binding site is presented. **d)** Schematic scheme of the structural domains of *Dm*64 (Uniprot: Q0E8P0), *Ec*CPDI (P00914), *human* CRY1 (Q16526) and *Arabidobsis thaliana* CRY1 (Q43125). Cryptochromes possess a much longer, variable C-terminal extension (CTE).

In cryptochromes, the FAD binding domain and the antenna binding domain together are called the photolyase homology region (PHR), which is highly conserved throughout the whole CPF. In addition to the PHR, CRYs have an elongated C-terminus, which is sometimes called the C-terminal tail (CTT) (64) or the C-terminal extension (CTE or CCE) (6). This CTE varies in length between only a few amino acids (*e.g.* 23 aa in *Dm*CRY) to over a 100 aa, *e.g.*

191 aa in *At*CRY1. The CTE is predicted to be disordered in most cryptochromes (37). One exception is the CTE of *Dm*CRY (3TVS), which is the only crystal structure of a full-length cryptochrome so far. Here, the CTE is bound to the DNA binding site over a hydrophobic "FFW" motif located on the tail helix (64, 65). In *Dm*CRY, the CTE undergoes a light activated structural change, that enables the circadian regulator TIMELESS (TIM) to bind to the cryptochrome (66, 67). In type 2 CRYs, the role of the CTE is much more elusive. It has been demonstrated, that the CTE is not essential for circadian clock function in type 2, but the deletion leads to changes in the period and amplitude of cycling (68–70). Furthermore, phosphorylation of the CTE is regulating the stability of type 2 CRYs, which is also affecting the circadian rhythm (71, 72). The fact that mouse CRY2 displays a much smaller FAD binding pocket results in decreased affinity for FAD (73) and presents a unique feature of this class.

Another highly discussed topic is the identification of the interaction sites between animal type I and type II cryptochromes with their core components of the circadian clock. In a new study from Rosensweig *et al.* (74), they analyzed conserved features across the whole CPF with statistical coupling analysis (SCA). With this method they are able to correlate specific sequence motifs in a protein section with phylogenetic and/or functional alterations within the CPF. For mouse CRY2 they were able to show that PER2 and FBXL3 interacts with the FAD-binding site and around the last helix, called CC helix, before the CTE. In contrast, the CLOCK:BMAL1 interaction site was identified in the antenna cofactor pocket of mCRY1 (74). A separate study shows that especially CLOCK is binding to the secondary pocket (75).

1.4 The antenna chromophore in the CPF

The function of the N-terminal domain appears often to bind a second chromophore as light-harvesting antenna for broadening absorption in the visible spectral region (6). However, this domain has been recently found to provide also specific interaction sites for signaling partners in type II cryptochromes (74). Antenna chromophores identified so far include 5,10-methenyltetrahydrofolate (MTHF) (76, 77), 8-hydroxydeazaflavin (8-HDF) (78), flavin mononucleotide (FMN) (79), 6,7-dimethyl-8-ribityllumazine (DLZ) (53) and FAD in its

fully oxidized state (80) (Figure 6). These aromatic cofactors all absorb in a spectral range between 380 and 420 nm. The energy gets transferred *via* a intermolecular Coulombic decay (ICD) process (81), in contrast to a classical FÖRSTER transfer mechanism (78), to the catalytic active $FADH^-$. Therefore, the energy has to overcome a distance between 16 to 18 Å.

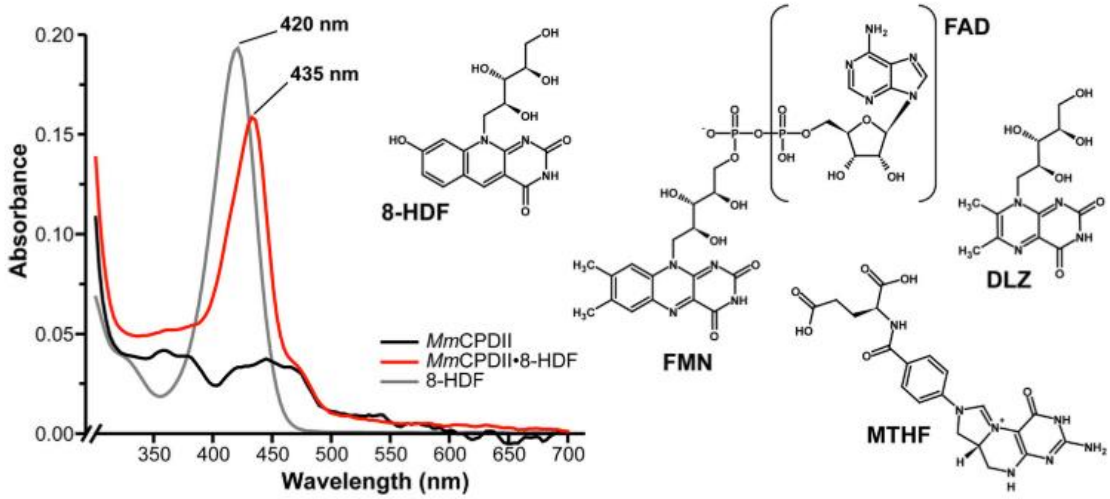

Figure 6 Spectral properties of class II CPD-photolyase from *Methanosarcina mazei* (*Mm*CPDII) with and without the 8-hydroxydeazaflavin (8-HDF) antenna chromophore bound. On the right site is an overview of the different antenna chromophores that have been identified within the CPF (figure adapted from (78)).

1.5 Photoactivation of Cryptochromes and Photolyases

In general, the non-covalently bound FAD cofactor of flavoproteins adapt three different redox states in five different kinds: the fully oxidized FAD_{Ox}, the semiquinone state as anionic radical $FAD°^-$ or neutral radical FADH° and the fully reduced hydroquinone state as $FADH^-$ or $FADH_2$ (82, 83). In photolyases, the fully reduced $FADH^-$ is the only form which is able to repair UV-damaged DNA (84, 85), a process called photo**re**activation. *At*CRY1 and *At*CRY2 demonstrate a photocycle between FAD_{Ox} and $FADH^-$, they harbor FAD_{Ox} in the dark, can be reduced to semiquinone state with blue light (BL) and further reduced to $FADH^-$ with green light (86–88), this process is called photoactivation. It was demonstrated, that the semiquinone FADH° is the active state of *At*CRY1 and *At*CRY2 *in vivo*, as the hypocotyl elongation and photoperiodic flowering is defected upon illumination with green

light, *e.g.* formation of the hydroquinone (88). For type 1 CRYs from animals, the reduction of FAD_{Ox} to the semiquinone $FAD°^{-}$ was demonstrated to be essential, as mutations that destabilize $FAD°^{-}$ abolished the function of the photoreceptor *in vivo* (89). Additionally, type 1 and sponge CRYs can only be reduced to anionic radicals (35) whereas type 4 CRYs can also be further reduced to the hydroquinone state $FADH^{-}$ (45).

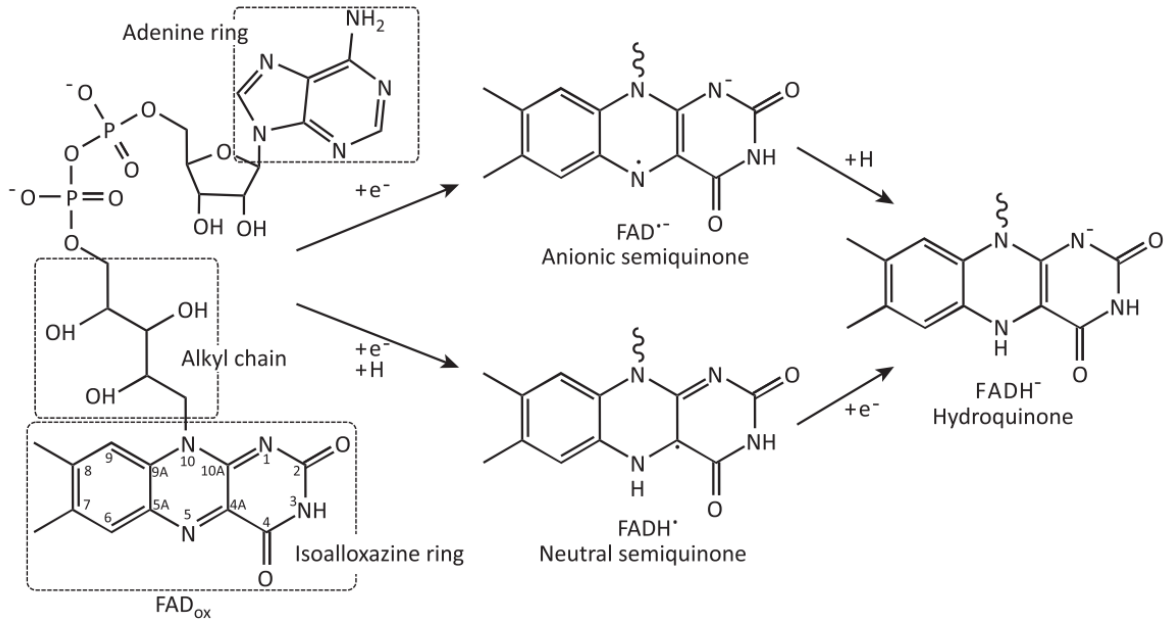

Figure 7 Photocycle of the flavin adenine dinucleotide (FAD) (90). After absorption of a photon, the excited FAD_{Ox} abstracts an electron to form the semiquinone state as anionic radical $FAD°^{-}$ or neutral radical FADH°. Through another electron transfer, the hydroquinone $FADH^{-}$ can be formed.

Given their photochemistry, how is the common reduction from FAD_{Ox} to $FADH^{-}$ in CRYs and PHLs realized? Upon illumination with BL of a wavelength of about 450 nm, the FAD chromophore absorbs a photon to achieve the excited state FAD_{Ox}*. This highly energetic state is now able to abstract an electron from a nearby residue. Several studies (36, 85, 91–95) showed that a highly conserved Trp triad is involved in an electron transfer to the photoexcited FAD (Figure 8). This triad can be found in almost all members of the CPF. When the electron is abstracted from the first Trp (W382 in *Ec*CPDI) nearest to the FAD, the semiquinonical $FAD°^{-}$ forms an initial radical pair with $Trp°^{+}$. This tryptophanyl radical abstracts an electron from the next medial Trp (W359 in *Ec*CPDI) which takes an electron from the distal Trp (W306) by itself (82). The resulting electron hole gets filled by an

extrinsic reductant (96). This all happens on a picosecond time scale as BRETTEL and BYRDIN (96) could show for the photoreduction of the semiquinone FADH° to the hydroquinone $FADH^-$ in *Ec*CPDI (Figure 8).

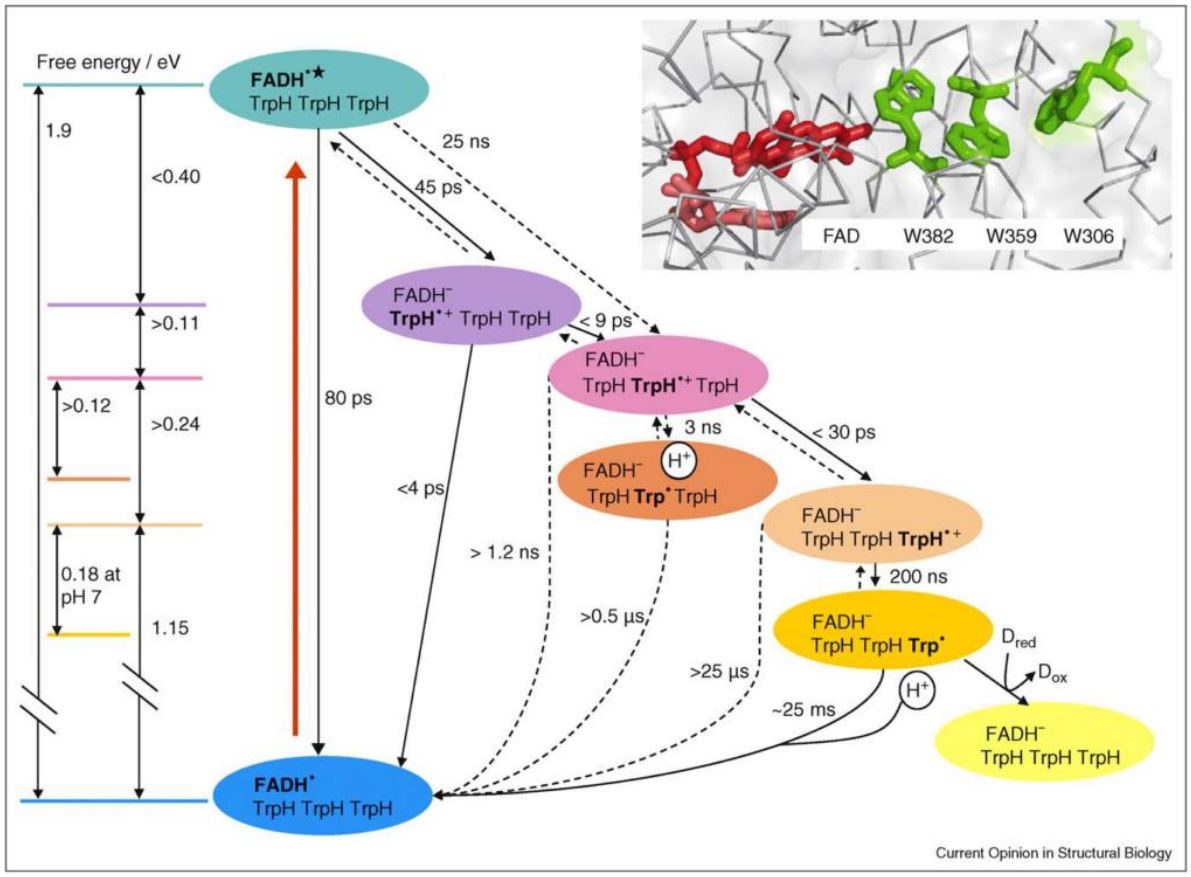

Figure 8 Scheme of the photoactivation process of *Ec*CPDI (figure adapted from (96)). Solid arrows represent the major electron and proton transfer reactions, whereas minor reactions are described by the broken arrows. Here, the photoactivation starts with the absorption of blue light by the semiquinone FADH°, which gets in its high energy state FADH°*. This state triggers the electron transfer cascade, described by the figure. D_{red}/D_{ox} is an extrinsic reductant, which is able to re-reduce the terminal electron donor Trp° in competition with the back electron transfer to FADH°. TrpH TrpH TrpH represents the Trp triad W382-W359-W306, which is shown on the upper right (PDB: 1DNP). The proton in TrpH indicates the proton on the N1 position of the indole moiety of the Trp.

In some members of the CPF, mutations in the Trp-triad can revoke photoreduction *in vitro* but still show activity *in vivo* (85, 91, 97, 98). In other representatives of the family, *e.g.* the bacterial CRY from *Rhodobacter sphaeroides* (CryB) (99) or *Mm*CPDII (54), even some alternative pathways or a different structural orientation of the Trp-triad were revealed.

These findings question the necessity of the triad, as other residues or the reductive cytosolic environment may be sufficient for keeping the FAD chromophore in its reduced state.

Recently, the role of the lumiflavin and adenine moiety of the FAD chromophore itself were investigated (100, 101). The study revealed the possibility of a two-step hopping mechanism from the lumiflavin to the lesion *via* the FAD's adenine (100). $FADH^-$ is more feasible to represent the active state, as ET from $FAD^{\bullet-}$ is intrinsically slower (2 ns) compared to 12ps for the hydroquinone (101).

1.6 Repair of UV-induced DNA damages by photolyases

As written above, UV-induced DNA damages can be repaired by photolyases in different organisms up to higher vertebrates. The sun light produces either cyclobutane pyrimidine dimers (CPDs) or pyrimidine (6-4) pyrimidone photoproducts ((6-4)PPs), which are repaired by distinct photolyase families with specific repair mechanisms. These mechanisms will be described in the following. Both, CPD and (6-4) photolyases require the fully reduced state of the flavin $FADH^-$, for DNA repair (84, 85).

CPD Photolyases

CPD photolyases and their mechanism have been extensively studied since their discovery (18, 96, 102–107). Especially the *E. coli* photolyase has become a model enzyme to study the complete photocycle of CPD repair in class I PHLs. However, not all CPD PHLs show the same behavior, as there are differences between the classes in terms of their $FADH^-$ and DNA interaction, different DNA binding modes or different elementary reaction rates, which result in different quantum yields for repair (62). Class I PHLs have the highest quantum yield (0.83 for *Ec*CPDI, 0.84 *An*CPDI), whereas class II, class III PHLs and cryDASH exhibit relatively low QYs (62). Furthermore, many cryDASHs lost their ability to flip the CPD lesion out of the duplex DNA, as shown for AtCRY3 by Pokorny *et al.* (39), because they are missing two residues that are conserved in CPD class I&II PHLs. In 6-4 PHLs one of these crucial residues is exchanged to a highly conserved histidine.

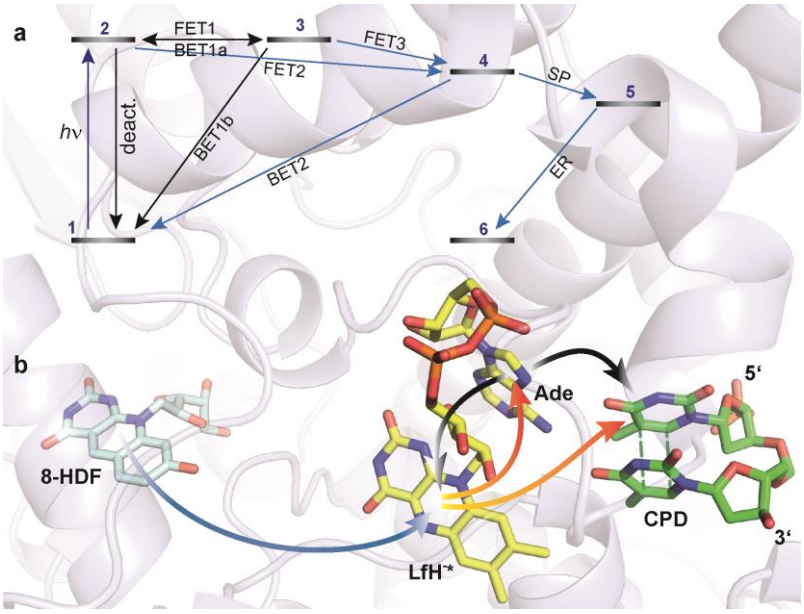

Figure 9: a) Scheme of seven elementary electron transfer steps with their relative energy levels identified from Zhang *et al.* (62). 1: LfH^{-}-Ade + T<>T(CPD); 2: LfH^{-}*-Ade + T<>T; 3: LfH°-Ade^{-} + T<>T; 4: LfH°-Ade + T<>T^{-}, 5: LfH°-Ade + T + T^{-}; 6: LfH^{-}-Ade + T + T; FET: forward electron transfer; BET: back electron transfer; SP: bond splitting; ER: electron return. **b)** Structural view of the class I *An*CPDI (1TEZ). Excited 8-HDF transfers energy (blue arrow) onto the reduced lumiflavin (1, LfH^{-}) moiety, to produce the active state (2, LfH^{-}*). The electron either hops (red arrows) to the adenine moiety (FET1, 3, Ade^{-}) or directly to the CPD lesion (FET2, 4). From Ade^{-}, the electron can move to the CPD (4, FET3) or back to the lumiflavin (2, BET1a) (62).

In Figure 9 the elementary steps of the electron transfer are shown. After excitation of flavin ($FADH^{-}$*), the first forward electron transfer (FET1) and also back electron transfer (BET1a) happens intramolecular between the lumiflavin (LfH^{-}*) moiety and the adenine residue (Ade^{-}). By studying the intramolecular ET dynamics, $FADH^{-}$ is the only redox state capable of an initial electron transfer to the CPD lesion (101). This finding is conclusive with the increase of reduction potential upon substrate binding (+65 mV) by the hydroquinone state, which points to a higher stability of the catalytic state of the photolyase (108). Electron transfer (FET2) happens from the LfH^{-}* to the damaged DNA happens within 250 ps in class I PHLs as the BET1a process from Ade^{-} is ultrafast (<100 ps) (106). Through direct tunneling of the electron a high quantum yield can be achieved by class I PHLs (0.84 for *An*CPDI, 0.83 for *Ec*CPDI) (62). In class II PHLs, FET2 is much slower, so the direct tunneling process is not dominant and a two-step hopping mechanism involving electron

transfer (FET3) from Ade^- to the CPD lesion becomes prominent. This ensures efficient DNA repair with lower quantum yields ranging from 0.32 to 0.62. The electron is always bifurcating into both electron transfer routes (tunneling vs. hopping), but two-step hopping is less important in class I.

Electron transfer to the CPD lesion (*via* FET2 or FET3) leads to the splitting of the C5-C5', which results either in successful repair of DNA by subsequent splitting the C6-C6' bond or futile back ET (BET2) and ring closure (109). If the DNA is repaired, the electron will be transferred back to the LfH° moiety to form the hydroquinone ground state (Figure 10).

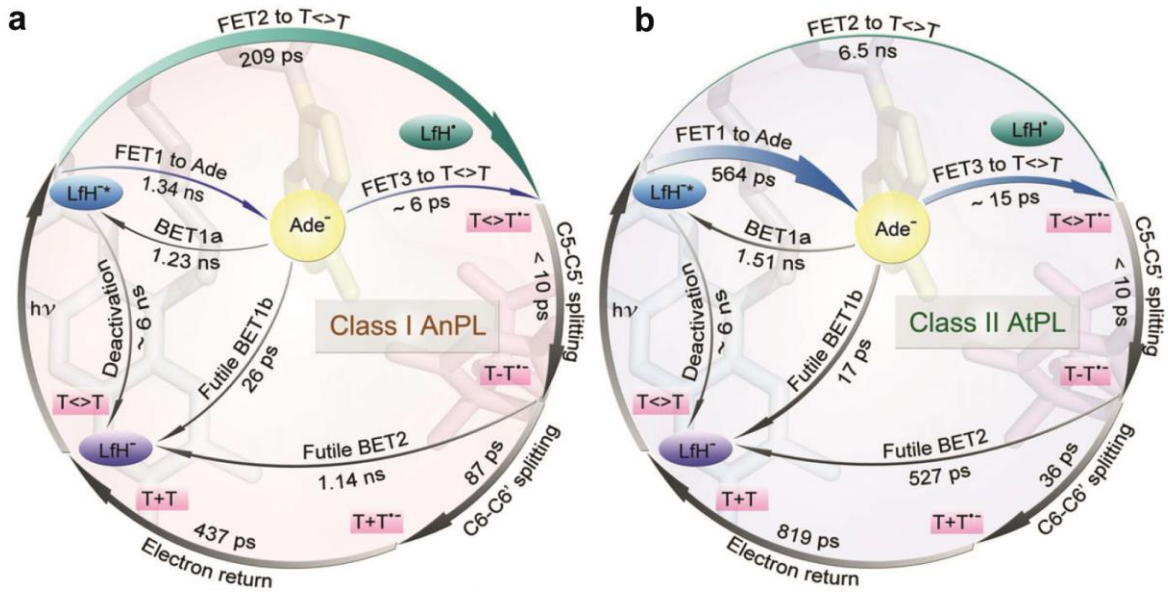

Figure 10: Repair cycle of the class I *An*CPDI (**a**, *An*PL) and class II *At*CPDII (**b**, *At*PL). FET: forward electron transfer; BET: back electron transfer. In class I, the direct electron transfer to the CPD lesion (FET2) is much faster than the FET1 to adenine moiety (Ade), so FET2 is dominant (green arrow). In class II, the opposite is occurs, so the two-step hopping pathway (blue arrows) is more prominent. Schemes copied from (62).

From a structural point of view, the CPD repair reaction gets mainly stabilized by two highly conserved residues in the substrate binding site (18, 39, 50, 54, 110, 111) (Figure 11). A glutamic acid (E283 in *An*CPDI, E275 in *Ec*CPDI) forms two hydrogen bridges with the 5'-residue whereas the 3'-residue of the lesion interacts with an asparagine (N349 in *An*CPDI, N341 in *Ec*CPDI). This is applicable either if the pyrimidine is a thymine or a cysteine, as this only demands another rotamer of the corresponding amino acid (18). It was shown by BERG

and SANCAR that the binding affinity of CPD-DNA and the quantum yield of *Ec*CPDI decreases up to 60 % if the glutamate is mutated (112). The hydrogen bonding network is needed for transfer of a proton to a C4-carbonyl group to stabilize the formation of the radical at an sp^2 hybridized carbon (110). The proton gets back transferred after the C6-C6' bond splitting and during the electron return to the $FADH^-$.

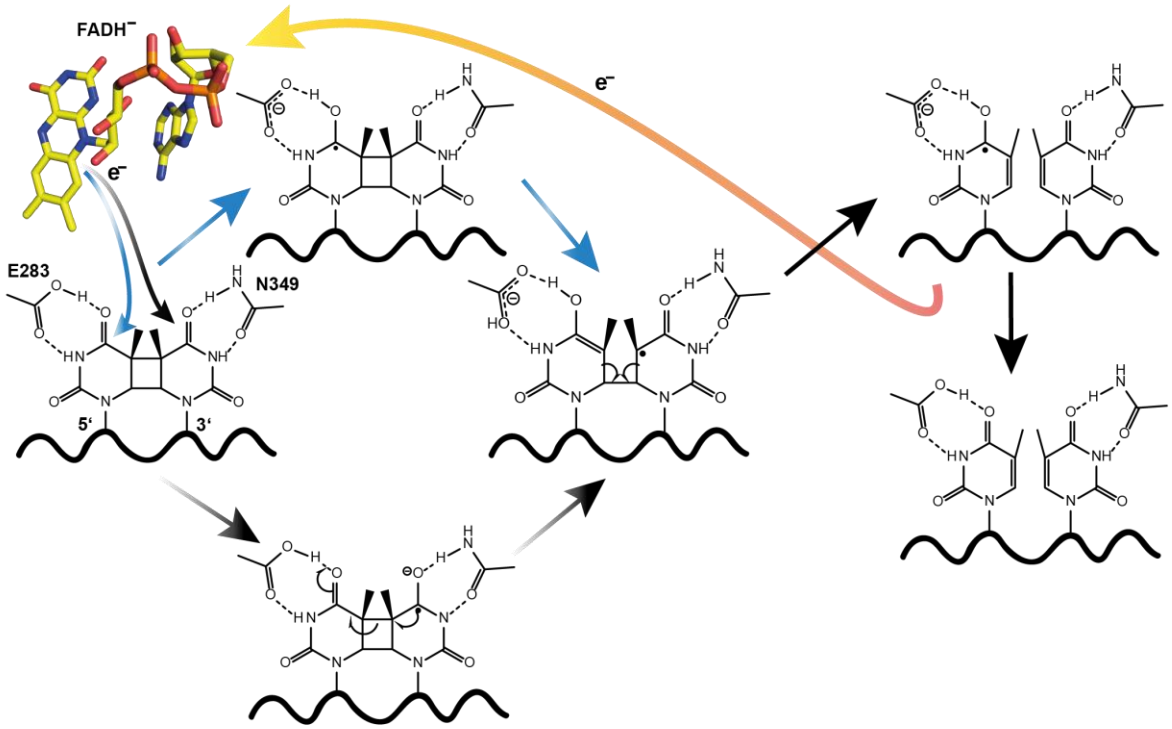

Figure 11: Scheme of the CPD repair as shown in (18). The CPD lesion is fixed in the active site by a glutamic acid (E283 in *An*CPDI) and an asparagine (N349 in *An*CPDI). The electron can either move to the 5'-thymine (red arrow) or the 3'-thymine (black arrow) to perform the first splitting of the C5-C5' bond. Afterwards the breakage of the C6-C6'-bond follows and the electron transfers back to the flavin (blue arrow).

In most class II photolyases the asparagine is exchanged to glycine residue (54). In the crystal structure of *Mm*CPDII the resulting hole is filled by a cluster of six water molecules (Figure 12). These water molecules form interactions between the 3'-thymine and the C2'-hydroxyl of the ribityl group as well as the diphosphate moiety of the FAD cofactor. This H-bond network changes the polarity of the DNA-binding site and therefore favors the two-step hopping mechanism (Figure 10b).

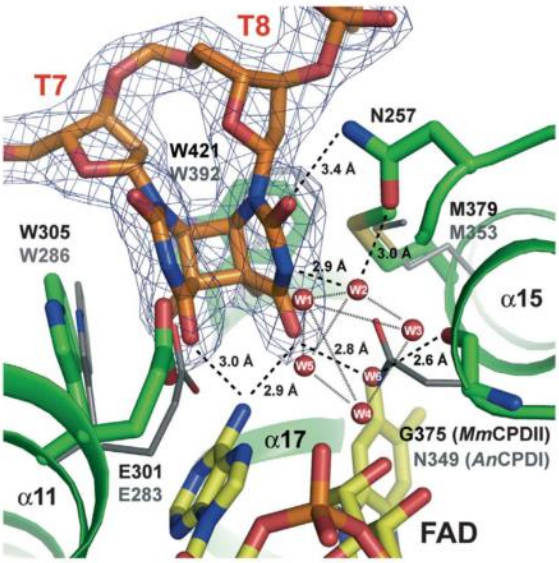

Figure 12: Detailed view of the CPD-binding site of a class II photolyase *Mm*CPDII (green, 2XRZ) in comparison with a class I PHL *An*CPDI (grey, 1TEZ) in complex with a CPD lesion (orange). N329 in *An*CPDI is replaced by G375 in *Mm*CPDII. The resulting space is filled by a network of six water molecules (red), which are interacting with the lesion (figure adapted from (54)).

The CPD lesion is also fixed by two conserved tryptophan residues, W305 and W421 in *Mm*CPDII, which form an L-shaped wall around the thymine dimer. W305 is performing π-stacking with the 5'-thymine and is assumed to keep the base in place after splitting of the C5-C5' bond (54).

(6-4) DNA repair

(6-4) DNA lesions make 20 to 30 % of the total sun-induced DNA damage (21), which can be repaired by either nuclear excision repair or (6-4) photolyases. This type of lesion gets formed by a PATERNÒ-BÜCHI reaction over an oxetane-bridged intermediate and transfer of an hydroxy-group (113). The binding of (6-4)PPs to its corresponding (6-4)PHL is highly specific with a K_D in the order of 10^{-9} M (114, 115). However, compared to the repair of CPD lesions the quantum yield of the photo repair process is up to 100 times lower (114). Additionally, the repair mechanism of the (6-4) photoproduct is still under discussion and there are several hypothetical models existing (13, 114, 116–124). Recently, a review by Yamamoto *et al.* sums up the different mechanisms, which have been proposed during the last 20 years (125). The currently discussed mechanisms can be summarized under three different scenarios: Simple OH transfer, proton-transfer-steered OH transfer and two-photon mechanism.

The earliest hypothesis states, that (6-4)PP repair happens like the formation over an oxetane intermediate. This idea was supported by several studies of oxetane ring splitting with model compounds, which consisted of an isoalloxazine linked to an oxetane ring and thymine derivatives (126–128). By mutational studies in 2001, Hitomi *et al*. could proof that two highly conserved histidines, His_1 and His_2, play an essential role in (6-4)PP repair (119). One of the histidines was supposed to be protonated, which was proven for *Xl*64 at pH 9.5 (129). In the suggested mechanism, the proton was supposed to be transferred to the N3', which results in the formation of the oxetane before electron transfer through $FADH^{-}$*(119). This mechanism was disproven by the first co-crystal structure (1TEZ) of a (6-4)PHL of *Drosophila melanogaster* (*Dm*64) in complex with (6-4)PP (13) as there was no oxetane intermediate formed in the dark. His_1 and His_2 (H365 and H369 in *Dm*64) are in close proximity to the DNA lesion and form a hydrogen bond network together with a tyrosine (Y423). His_1 forms a direct interaction with the hydroxyl group of the C5, which has to be transferred during the repair reaction. Based on the structural information of *Dm*64, plenty of theoretical studies (121–123, 130–138) have been performed, which led to the three currently discussed mechanisms. In the "simple OH-transfer" mechanism (Figure 13a), His_1 remains in the neutral protonation state (133, 136). It stabilizes the hydroxy group (O4'H) *via* a hydrogen bound and after FET, the 5' base forms a radical anion. This leads to spontaneous transfer of the hydroxy group to the 3' base, which results in the cleavage of the C6-C4' bond and electron back transfer (122, 136).

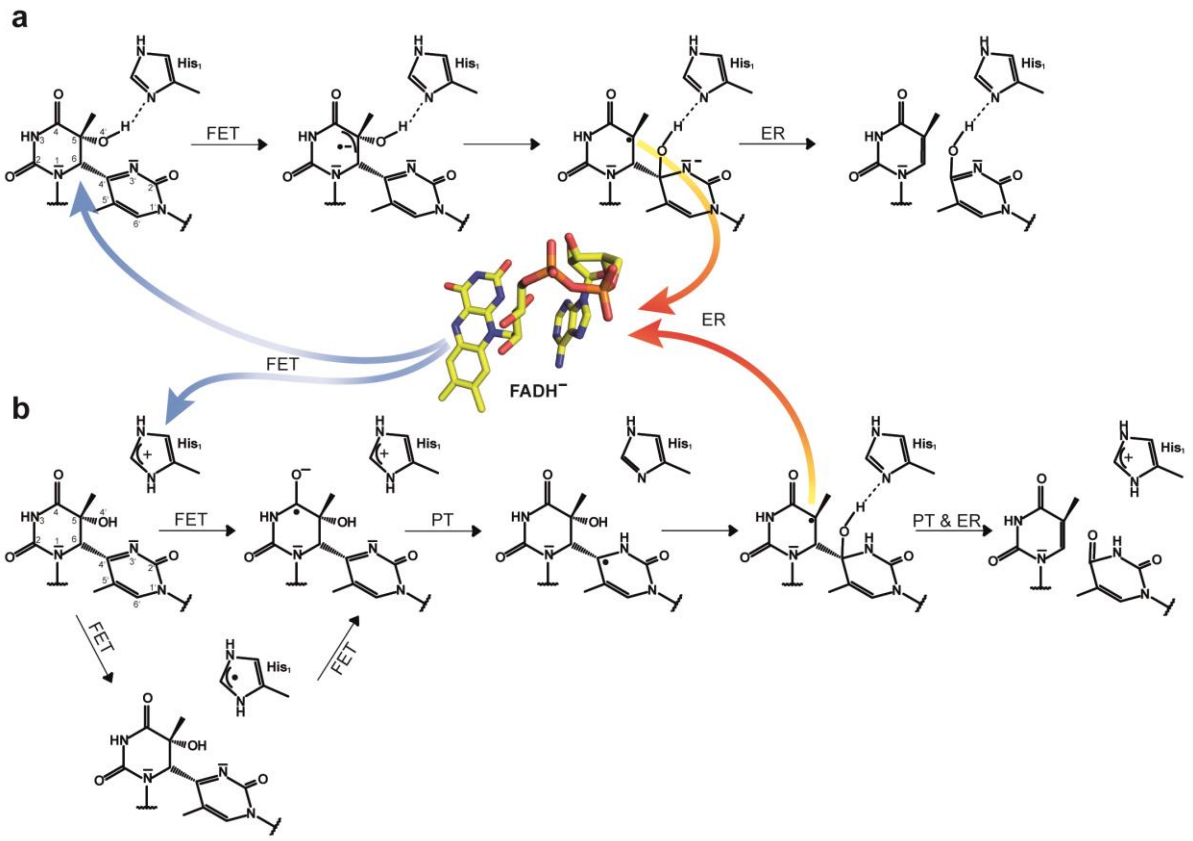

Figure 13: a) Reaction scheme of the "simple OH-transfer" mechanism as proposed by Domratcheva *et al.* (139). After forward electron transfer (FET), the hydroxy-group is moving under support of VAN DER WAALS interaction to His_1. In this mechanism, His_1 remains in the neutral protonation state. **b)** Representation of the "proton-transfer-steered OH-transfer" as designed by Faraji *et al.* (121, 131, 138, 140, 141). Here, His_1 is protonated from the start and FET can also happen first to His_1 and afterwards to the lesion. The anionic radical is formed at the 5' base, following protonation (PT) of N3'. The proton gets abstracted back to His_1 after OH-transfer and electron return (ER). Figure is based on Yamamoto *et al.* (125).

The second mechanism named "proton-transfer-steered OH-transfer" (Figure 13b) was developed over several years by Faraji *et al.* (121, 131, 138, 140, 141). The important difference is that His_1 is protonated and transfers a proton to the 3' base after FET. In the proposed mechanism, the electron from the photoexcited $FADH^{-}$* is either directly transferred to the 5' base or it could also be transferred first to the His_1 (121, 130, 137) and afterwards to the lesion. After proton transfer, the hydroxy group is moving to C4' of the 3' base, which induces the splitting of the C6-C4' bond and the release of the electron back to the flavin. In case of this mechanism, the highest activation barrier derives from the OH transfer with about 20 kcal mol^{-1} or even lower (137).

The third proposed mechanism based on theoretical studies is the "two–photon mechanism" (Figure 14), which claims that $FADH^-$ has to absorb a photon and transfer an electron twice (123). Here, the protonated His_1 also transfers one hydrogen to the 3' base, but instead of leading to direct OH-transfer, the electron is released and an oxetane intermediate is formed. Because of the second photoexcitation, an oxetane radical anion is created, following spontaneous splitting of the C5-O4' bond and finally the breakage of the lesion. In this mechanism, the cleavage of the C6-C4' bond has the highest activation barrier with 9 kcal mol^{-1}.

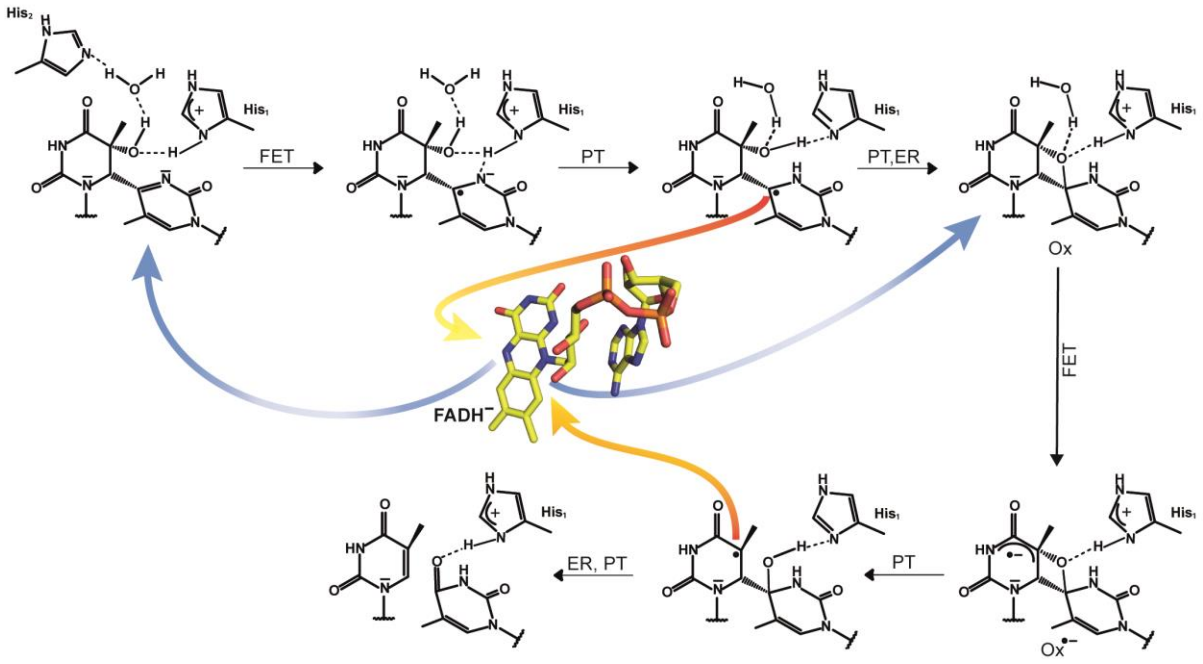

Figure 14: Reaction scheme of the (6-4) repair by the "two-photon mechanism" as proposed by Sadeghian *et al.* (123). In the initial steps, His_1, His_2 and a water molecule are involved to stabilize the anionic radical forming after FET. His_1 is supposed to be protonated from the beginning. After proton transfer and electron return the oxetane intermediate (Ox) gets formed. By a second FET, the oxetane radical anion $Ox^{\bullet -}$ is produced, which abstracts a proton from His_1. Finally, ER and PT produce the repaired thymines.

To clear up the controversy between these different mechanisms, experimental studies have been performed. Li *et al.* investigated *At*6-4 PHL and several mutants with ultrafast fluorescence and transient absorption spectroscopy (120). This was also reviewed and amended by Zhang *et al.* (62). Here, FET2 from excited $FADH^{-}$* or more precisely LfH^{-}* to the (6-4)PP takes place in 280 ps. When His_1 is mutated to a charged (Lys, Asp), polar (Asn,

Tyr) or hydrophobic (Ala, Met) residue, the electron transfer dynamics from $FADH^{-}$* to the lesion is quite similar, but DNA repair is not happening anymore. After formation of the (6-4)PP° radical, either repair of the lesion or BET2 can happen. Upon proton transfer the radical anionic $(6\text{-}4)PP^{\circ -}$ is produced in around 481 ps, which is supposed to form an oxetane-like intermediate. On the other hand, BET2 is happening in about 51 ps, which explains the low quantum yield of the (6-4)PP repair (0.1) compared to CPD repair reaction (0.8). For lesion repair, bond rearrangement, splitting of the C6-C4' and ER takes place in over 10 ns. In this reaction scheme, only one photon is necessary to trigger the reaction. Yamamoto *et al.* (124, 125) analyzed the possibility of a two-photon mechanism by studying the repair activity of *Xl*6-4 PHL and revisiting old experimental data. They developed an experiment with controlled excitation conditions and spectroscopic monitoring of the repair using the recovery of the 265 nm absorption for the repaired DNA and decay of absorption at 325 nm for the lesion. Applying one 100-ps laser flash which equals one photon per photolyase complex, they could observe a decrease of the 325 nm absorption but no increase at 265 nm. Only after the treatment with more flashes, depletion of the 6-4PP and intact DNA could be detected. These results (124) support the "two-photon mechanism" proposed from Sadeghian *et al.* (123).

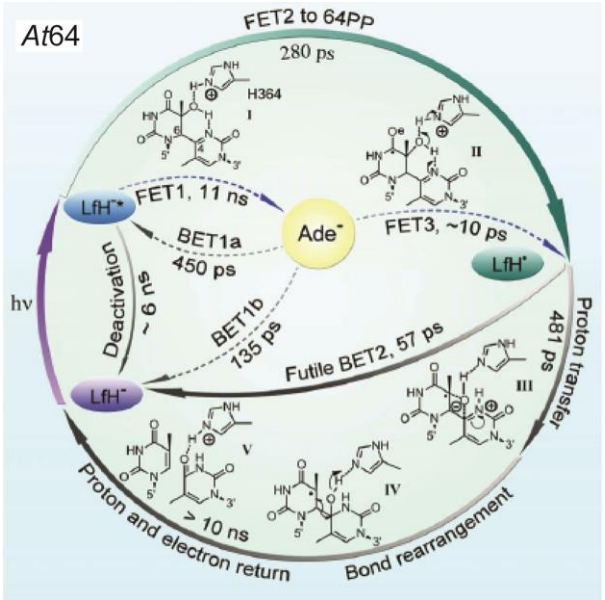

Figure 15: Schematic reaction cycle for the dynamics of (6-4)PP repair by the At64 photolyase. The cycle is based on the works of Li *et al.* (120) and Zhang *et al.* (62). In (6-4)PP repair, direct electron transfer (FET2) is preferred in comparison to a two-step hopping pathway (FET1, FET3). In the here proposed mechanism, His_1 (H364 in At64) is protonated and the O4'H group gets transferred by forming a hydroxyl-anion (III) which gets stabilized by a hydrogen-bonding-network.

As mentioned before, the first 3D-structure of a (6-4)PHL in complex with DNA, is of *Dm*64 (3CVU) published by Maul *et al.* (13) (Figure 16). Besides the *Dm*64 in complex with the (6-4)PP, they also achieved a crystal structure of the photolyase containing the repaired DNA inside the active pocket (3CVY). In the active site a network of charged residues is present, which forms hydrogen bonds with the adenine moiety of the flavin as well as the (6-4)PP. His_1 and His_2 (H365 and H369) as well as a nearby tyrosine (Y423) are slightly shifted in the repaired structure, but still show the same conformation. The complete triad was shown to be essential for the efficient repair of the photolyase (13). The critical hydroxy group which has to be transferred upon repair is interacting with a 2.9 Å distant water molecule and His_1 (2.8 Å).

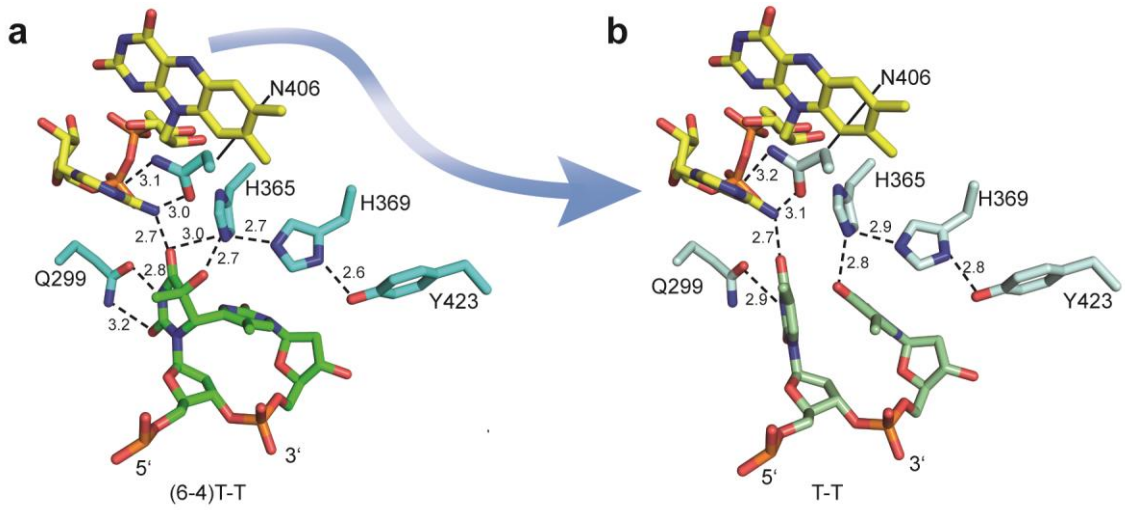

Figure 16: Structural comparison of the (6-4)PHL of *Drosophila melanogaster* (*Dm*64) in complex with the (6-4)PP (**a**, 3CVU) and the repaired DNA (**b**, 3CVY). Distances are represented in Å. The blue arrow represents the repair reaction. By comparing the distances in both structures, a small shift of 0.2 Å in the catalytic triad H365-H369-Y423 can be detected.

So far all computational studies (121–123, 130–138) are based on this structure, which shows not necessarily the only conformation possible for the catalytically active residues, His_1 and His_2 (142).

1.7 Biological functions of cryptochromes

Plant cryptochromes

In plants, CRY1 and CRY2 from *Arabidopsis thaliana* are the best described and studied CRYs till now. They were first described in 1993 (31) and 1996 (143) and both of them play a central role in various BL-regulated mechanisms in plants like de-etiolation and photoperiodic flowering (144). The structure of the PHR domain of *At*CRY1 was solved by Brautigam *et al.* in 2004 (145). They gained a crystal structure of native *At*CRY1 (1U3C) and one with a non-hydrolysable ATP analog (AMP-PNP) (1U3D). AMP-PNP together with a magnesium ion was present in the binding pocket next to the FAD (145). The binding of ATP is not essential for CRY function, but it has a boosting effect on the formation of the active FADH° state of the cofactor (146, 147). In several publications, it was shown that *At*CRY1 and *At*CRY2 form dimers over the PHR domain in plant cells, which is essential for their functionality (148–150). Also it was demonstrated, that the CTE is crucial for downstream signaling for *At*CRY1 (151) and gets digested by proteases in a blue-light dependent manner (37). It was shown before, that the first step in photoactivation of *At*CRY1 and *At*CRY2 is phosphorylation (152–154). Both CRYs have a large number of phosphorylation sites compared to mammalian CRYs (155). ÖZGÜR and SANCAR (156) examined autophosphorylation activity for *At*CRY1, which is not necessarily blue-light dependent. *At*CRY2 on the other hand gets phosphorylated at Ser587 and Thr603 by the casein kinase 1 *in vitro* (157), which might also be the case *in vivo*. Light-dependent phosphorylation of *At*CRY1 and *At*CRY2 is proposed to lead to electrostatic repulsion of the negatively charged surface and the phosphorylation sites (148, 152, 153). This theory was supported by transient grating spectroscopy on full-length *At*CRY1 that revealed a conformational change of the CTE upon illumination (158). This might lead to the exposure of a previously hidden interface, which could bind reaction partners. From all this information, several hypothetical models of the BL-dependent structural change of *Arabidopsis* CRYs and their signal transduction have been proposed. They are summarized in Figure 17 (144).

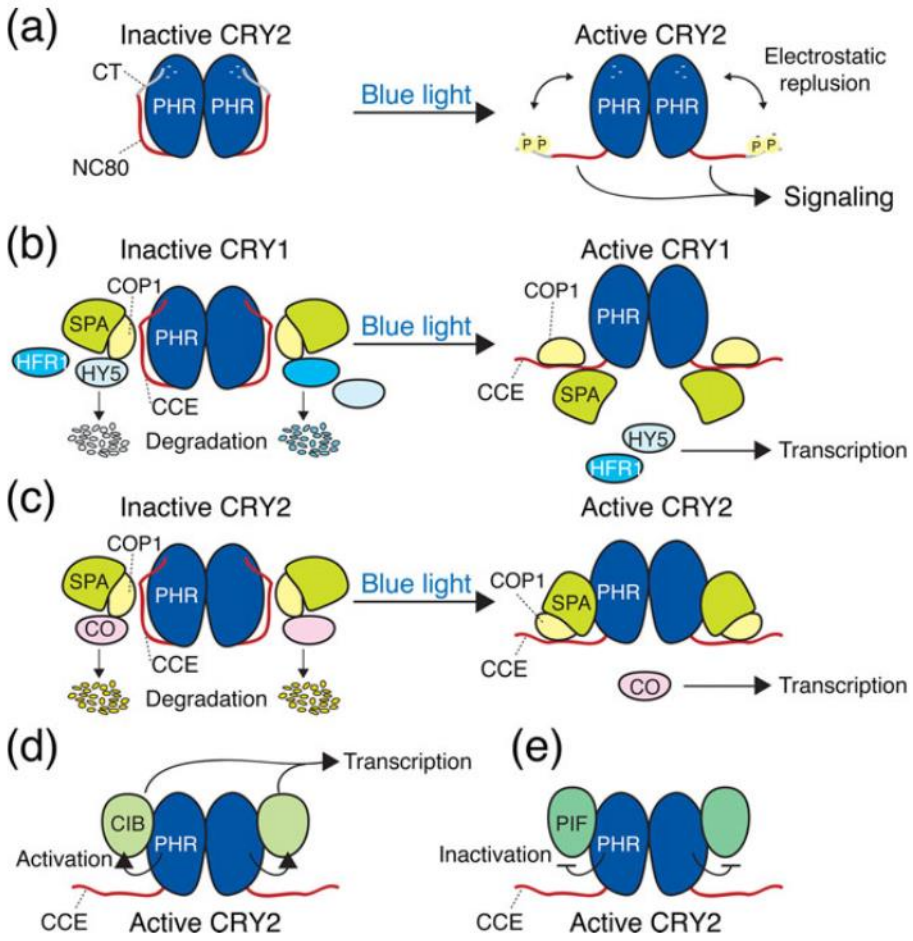

Figure 17 Schematic overview of the proposed BL-induced structural changes and mechanisms in *Arabidopsis* CRY1 and CRY2 (144). In all models, *At*CRY1 and *At*CRY2 form a dimer over the PHR domain in the dark. **a)** Upon BL-activation, the C-terminal tail (CT) gets phosphorylated and by electrostatic repulsion, the C-terminal extension (CTE or CCE) is rearranging and opening a binding site for potential signaling partners. **b, c)** COP1 and SPA form the E3 ubiquitin ligase complex (159), which is responsible of the degradation of the transcription factor hypocotyl 5 (HY5) (160, 161). *At*CRY1 just binds to COP1 in the dark, so the COP1:SPA complex is still active. After BL-activation SPA also binds to the CTE of *At*CRY1 (162), which leads to disassembly of the complex. Therefore HY5 can be accumulated in the nucleus, which promotes photomorphogenesis. In *At*CRY2, the COP1:SPA complex exists in BL, but is not active anymore (163). This leads to the accumulation of the transcriptional factor CONSTANS (CO) which eventually leads to accelerated flowering (164). **d)** Active *At*CRY2 is also able to bind CIB which causes promotion of photoperiodic flowering (165), but the exact mechanism is still elusive. **e)** *At*CRY1 and *At*CRY2 are able to bind PIF4 and PIF5 in the light (166, 167), which results in low BL-induced shade avoidance response (SAR) and warm temperature-induced cell growth.

*At*CRY1 is equally localized in the nucleus and the cytoplasm of a plant cell (168, 169), but *At*CRY1 in the nucleus regulates most CRY1-dependent processes. *At*CRY2 is mainly present in the nucleus (170), where it is also able to form so called photobodies upon BL

illumination (171), which correlates with *At*CRY2 function and degradation (170). The formation of these photobodies is proposed to be involved in signal transduction, but till now there is no plausible model to undermine this hypothesis. *At*CRY1 and *At*CRY2 are able to mediate a variety of BL-induced responses by transcriptional regulation of specific genes (172–174), which gets realized by specific interactions with the COP1:SPA complex, CIB, PIF (as described in Figure 17), phytochromes and also BIC1 (175). This leads to a variety of cryptochrome-mediated responses in *Arabidopsis*, like BL-induced de-etiolation, control of photoperiodic flowering, BL-regulated stomatal opening and development, low blue light (LBL)-induced shade avoidance response (SAR) and BL inhibition of warm temperature-induced hypocotyl elongation (144). These different responses and the involved transcription factors are summarized in Figure 18.

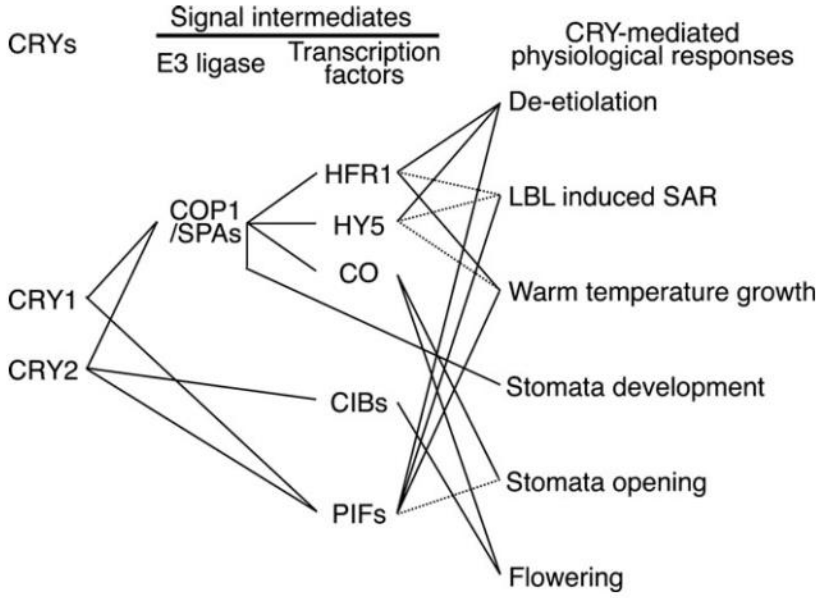

Figure 18 Schematic view of the direct and indirect influence on transcription factors by plant cryptochromes (144). Solid lines indicate examined and dashed lines possible pathways downstream of CRY signaling**.** Here, the negative regulation of CRYs through BIC1 is missing.

Circadian Rhythm in Animals

The name “circadian” is composed of the Latin words *circum* for “in a circle” and *diem* for day, therefore the name already describes the process it stands for. Circadian rhythms are

self-preserving in the absence of external time indications and maintain an intrinsic period of approximately 24 h under constant conditions. The rhythm is entrained or synchronized to the solar light/dark cycle. If the light/dark cycle is exactly 12 h dark and 12 h of light, the circadian rhythms are almost exactly 24 h (176, 177). Light is the major time cue called *Zeitgeber,* which is able to entrain the circadian clock, by synchronizing the free-running rhythms with the light/dark cycles of the environment (177). This process of synchronizing is favorable for organisms to ensure their maximum fitness (178). It was demonstrated that light in the blue range is able to phase-shift the clocks in diverse organisms (177, 179, 180). *Drosophila* is used as a model system for insect organisms and its circadian clock is well studied. Several clock genes, namely *period, timeless, clock, cycle*, have been identified in *Drosophila* (181, 182), which control circadian expression of a number of genes by a time-delayed transcription-translation feedback loop (TTFL). In 1998, a mutant lacking the *Drosophila* type 1 cryptochrome *Dm*CRY, cry^{b}, was created by Stanewsky *et al.* (183). The cry^{b}-mutant flies no longer demonstrated the light-dependent drop of TIMELESS (TIM) protein levels. Also flies, which overexpressed *Dm*CRY, demonstrated a much higher sensitivity to phase shifting through BL illumination. However, neither the cry^{b}-mutant nor the $cry^{b}norp^{A}$ combined mutant displayed a dramatic impact on the ability to adapt to changes in the light/dark cycle (184). In the end, the coupled mutant of cry^{b} and *glass*, which eliminates all known photoreceptors from the *Drosophila* eye, completely abolished the entrainment of the circadian clock (184).

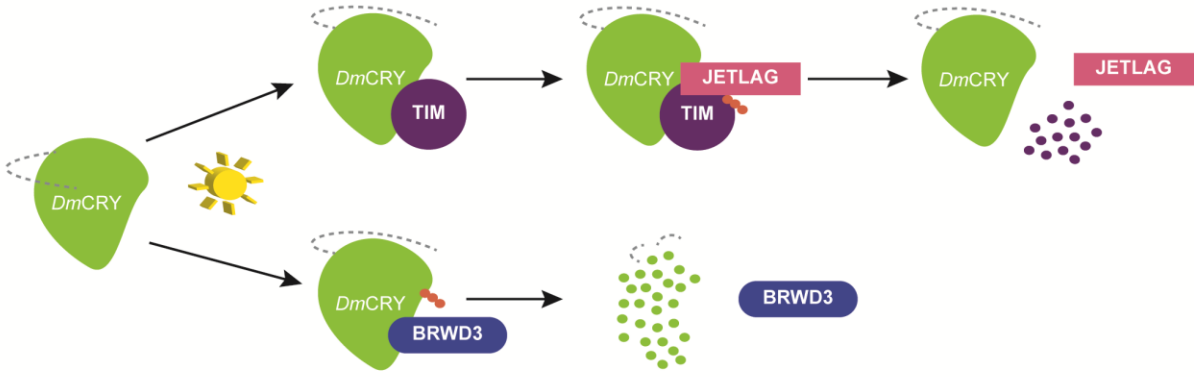

Figure 19 Schematic representation of the light-responsive degradation of *Dm*CRY and TIM adapted form Micheal *et al.* (177). After light exposure, the C-terminal extension (CTE, grey) rearranges and

exposes the binding site for TIM and JETLAG. This leads to ubiquitination (orange circles), following proteasomal degradation of TIM. Another light-activated pathway leads to polyubiquitination by BRWD3 and degradation of *Dm*CRY.

The model presented in Figure 19 derived from *in vitro* studies with a cry^{m}-mutant, consisting only of the PHR domain without the C-terminal extension (CTE) (185). Busza *et al*. showed that CRY^{M} is still a fully functional circadian photoreceptor and able to bind TIM as strongly as wild-type CRY can. In contrast to wild-type CRY, which only binds TIM after light exposure (66, 67), CRY^{M} is also competent of binding TIM in the dark, which suggests a light- dependent structural change of the CTE. After binding of TIM to CRY, the E3 ubiquitin ligase *Jetlag* can recognize TIM and mark it for degradation (186–188). This light-dependent regulation of TIM degradation leads to a phase shift in the circadian clock. As further research showed, not only TIM gets degraded in a light-dependent manner, but also CRY degradation happens after illumination with light at approximately 380 nm (189). Ozturk *et al*. could prove, that BRWD3 is able to ubiquitinate purified CRY after a light-dependent conformational change (190).

The function of cryptochromes in vertebrates differs to the situation in insects (177) and a lot of research was invested over the past two decades to fully understand how the “inner clock ticks” (191–199). Noteworthy, over 40 % of the transcription of the mammalian genome underlies circadian rhythms (194). Since 1999 it is accepted that two cryptochromes (CRY1 and CRY2) act as a negative regulators (191), whereas a complex of the circadian components CLOCK and BMAL1 start the circadian day by driving the transcription of *Per* and *Cry* genes through E-box enhancers (192). The two resulting cryptochromes are forming a multimeric complex with two PERIOD (PER) proteins inside the cytosol, followed by a slow entering of the nucleus, where the huge complex is able to repress CLOCK:BMAL1 activity (198). In this model, *m*CRY underlies light-independent regulation, but its function as a photopigment cannot be precluded as triple mutant mice lacking both cryptochromes, rod and most cone opsins (*mCry1*$^{-/-}$*, mCry2*$^{-/-}$*,rd1/rd1)* exhibit nearly arrhythmic behavior (193). Recent findings show that not only the PER:CRY complex inhibits CLOCK:BMAL1-driven transcription in the early stage of the circadian day, but also CRY1 alone can act as repressor in later stages (195–198). Inevitably, PER and CRY get

degraded, recruitment of the transcriptional activators CBP/p300 to CLOCK:BMAL1 happens and the cycle can start again (195, 198).

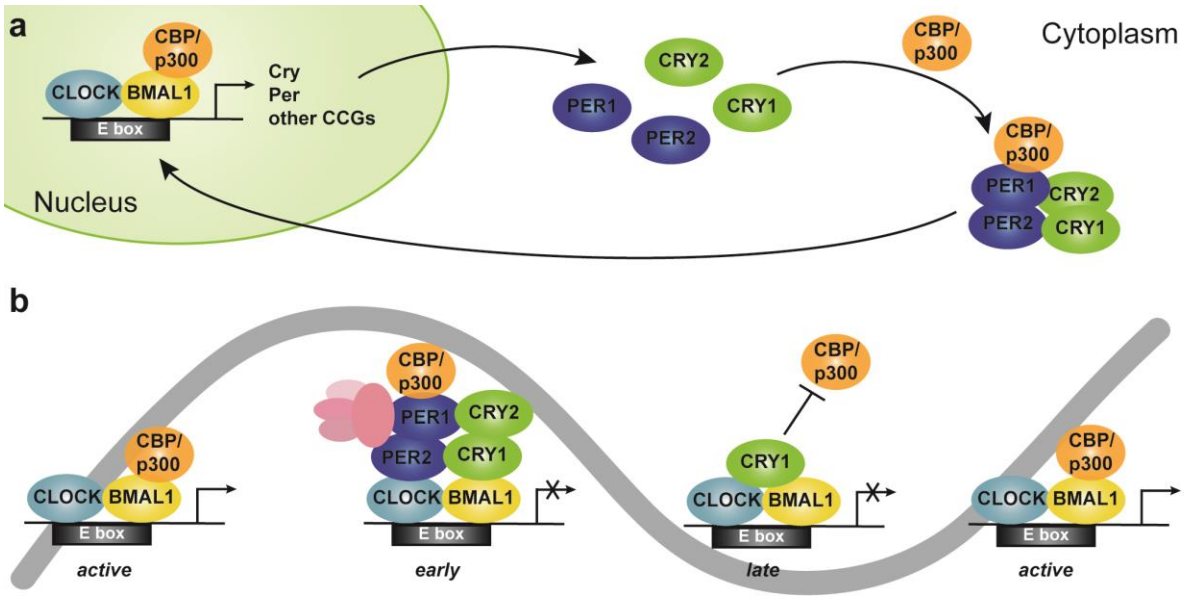

Figure 20 Sketch of the different complexes formed during circadian regulation involving mammalian CRY1 and CRY2. Figure derived from (198). **a)** The CLOCK:BMAL1 complex is active and leads to the expression of several clock regulative genes inside the nucleus. The resulting proteins shuttle inside the cytoplasm, where CRYs and PERs are forming a multimeric complex involving the coactivator CBP/p300. The complex is travelling back inside the nucleus, to inhibit CLOCK:BMAL1 driven transcription. In **(b)** the regulation of the CLOCK:BMAL1 over a whole circadian day is shown. In the early stage, the CLOCK:BMAL1 is deactivated through a huge multimeric complex which might evolve some additional proteins (light pink) besides CRY and PER. Later, only CRY1 acts as an inhibitor to hold off activation by the coactivator CBP/p300.

To activate CLOCK:BMAL1 again, the protein level of CRY1 and CRY2 has to be highly controlled. This is getting realized by the F-box protein FBXL3 (200–202), in the nucleus, and FBXL21 (203), in the cytoplasm, which leads in both cases to ubiquitination and proteasomal degradation of the cryptochromes. A small molecule, KL001, was identified to prevent ubiquitin-dependent degradation by blocking the FBXL3 binding site (204, 205). This leads to stabilization of CRY protein concentration and a longer circadian period. This interference into the circadian rhythm by a small molecule is definitely of relevance for pharmaceutical research looking for manipulation of clock function.

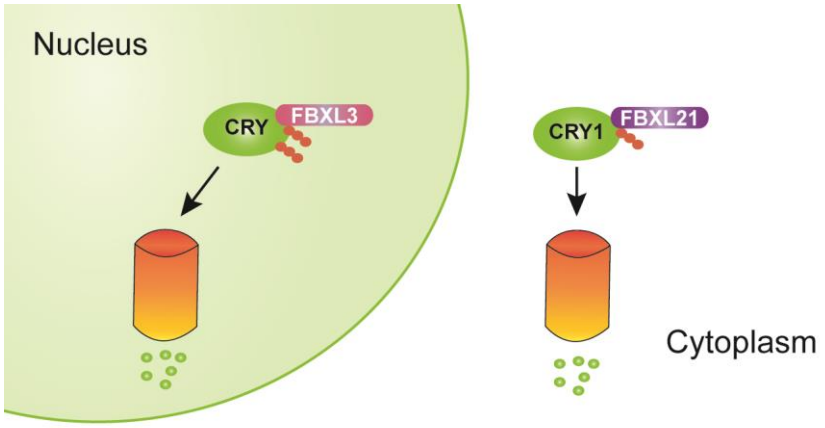

Figure 21 Mammalian CRY degradation as described by Yoo *et al.* (203). In the nucleus, CRY gets ubiquitinated through FBXL3 which leads to proteasomal degradation (proteasome: orange). In the cytosol, CRY degradation is mediated by FBXL21. FBXL21 can also be present in the nucleus, where it antagonizes FBXL3 and stabilizes the nuclear CRY concentration.

Other roles of cryptochromes

Animal cryptochromes not only regulate CLOCK:BMAL1 expression, but also play different roles in metabolism, inflammation and DNA damage response as shown in Figure 22 (177). Both, CRY1 and CRY2, interact with the glucocorticoid receptor and change the transcriptional control through glucocorticoids (206). As a consequence of this regulating patterns, CRY1 and/or CRY2 deficient mice demonstrate glucose intolerance and high levels of corticosterone. CRY1 is also able to modulate G protein-coupled receptor (GPCR) activity by binding to $G_S\alpha$, which leads to changes in cAMP production (207). There is also a relation between disruptions of the circadian rhythm due to shift work or light exposure at night and cancer (208–210) as identified by epidemiological and animal studies. Controversially, Sancar *et al.* could not find increased cancer rates in $Cry1^{-/-}$, $Cry2^{-/-}$ mice, not even after exposure to ionizing radiation (211). More *in vivo* studies with $p53^{-/-}$, $Cry1^{-/-}$, $Cry2^{-/-}$ mice suggest an involvement of CRYs in p53-independent apoptosis in response to DNA damage (212). Furthermore, KANG and SANCAR discovered a link between the control of DNA repair through nucleic excision repair (NER) process and the circadian clock (213, 214).

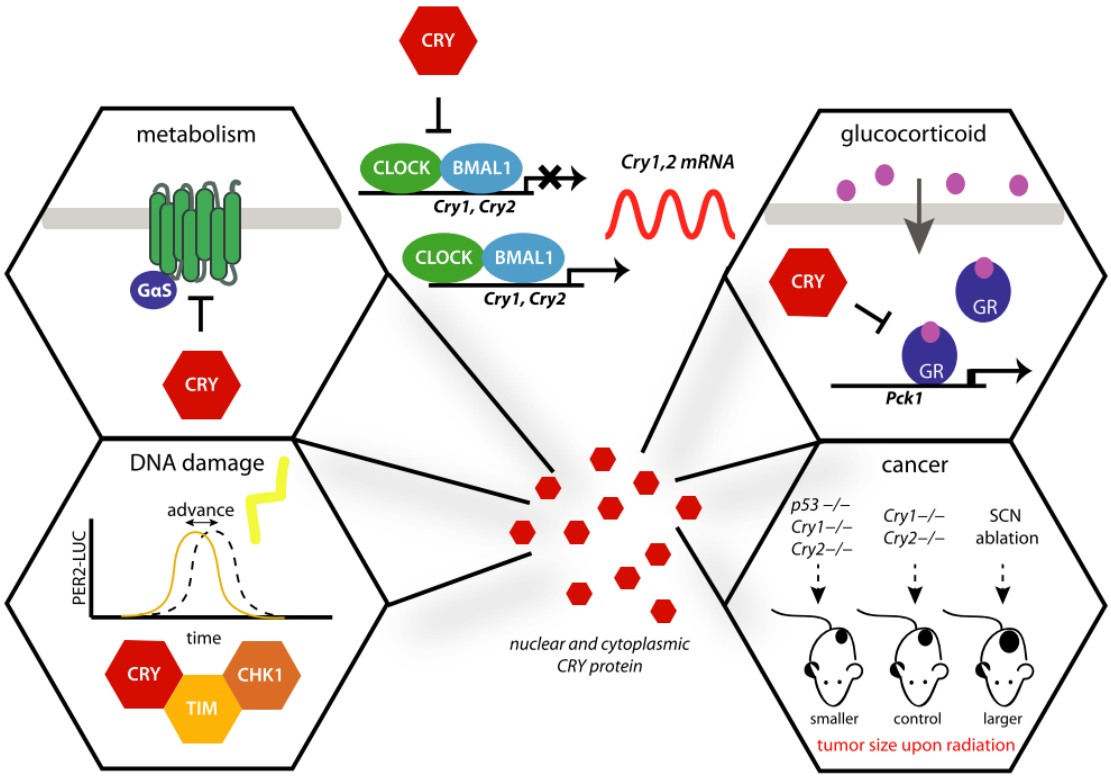

Figure 22 Roles of mammalian CRY besides CLOCK:BMAL1 regulation (copied from (177)). CRY is involved in GPCR signaling and downstream metabolism by blocking glucagon-stimulated production of intracellular cAMP (top left). CRY also negatively regulates the glucocorticoid receptor (top right). It is also able to shift the phases of the clock by interaction with the ATR-mediated DNA damage checkpoint (bottom left). Deletion of CRYs seems to extend the lifespan of mouse models exposed to ionizing radiation (bottom right).

Magnetoreception

Magnetoreception describes the mechanism, which is supposed to unravel the compass of birds and other species along the magnetic field of the earth. Currently there are two models available to explain magnetoreception: (i) magnetically sensitive radical pairs or (ii) magnetic iron containing nanoparticles (215, 216). As CRYs are producing a radical pair during photoreduction, they are discussed to play a role in magnetoreception in different organisms from mammals to *Arabidopsis* (215). Gegear *et al.* showed some evidence that the light-dependent magnetic sense is linked to CRY in *Drosophila* (217) and that flies illuminated with light of just long-wavelengths lack magnetosensitivity. Additionally, Fedele *et al.* showed in 2014 that neither *Dm*CRY deficient flies nor flies that just lack the CTE display magnetosensitivity (218). In another study, they were able to restore

magnetoreception in transgenic flies by adding type 2 CRYs from mammals or insects (219). In a highly controversial electron microscopy (EM) study, Qin *et al.* suggest the interaction of *Dm*CRY and a presumed magnetic receptor MagR (220). MagR and *Dm*CRY are supposed to form round or rod-shaped protein complexes, which exhibit light-dependent feedback *in vitro*, when a magnetic field is applied. Type 2 CRYs in birds (annotated as *gw*CRY1a in the garden warbler) are also associated with magnetoreception (221) and might be the key player in the avian compass. This hypothesis was supported by behavioral studies done with different bird types by Wiltschko *et al.* (222), which proved the light-dependency of the magnetic compass. Type 4 CRYs have not been tested on magnetosensitivity yet (35). Additionally, a magnetic field effect was also observed on CPD photolyase repair, as the splitting of the C6-C6' bond gets disrupted inside a magnetic field (216). All these studies point into the involvement of CRY in the magnetoreception of different organisms, but the process of the resulting signaling has not yet been understood.

1.8 Photoreceptors in *Chlamydomonas reinhardtii*

The green alga *Chlamydomonas reinhardtii* is a well-established model organism for alga and vascular plants for investigating biological processes such as photosynthesis, structure and function of the flagella, phototaxis and circadian rhythmicity (223–226). Multiple biological processes in *C. reinhardtii* are light-controlled and also the sexual life-cycle is highly dependent on external light conditions (227–229). Its complete genome was sequenced in 2007 and several photoreceptors could be identified (223). Among these photoreceptors, different members of the CPF were found: two cryDASH, one CPD class II PHL, one plant CRY (*Cr*pCRY) and one animal-like CRY (*Cr*aCRY). Interestingly, it lacks a further (6-4) photolyase as well as red light-dependent phytochromes (223, 230, 231). *In vivo* studies with *pcry* knock-down mutants demonstrated that *Cr*pCRY is entraining the circadian clock by BL, is associated with the circadian oscillator and is involved in the control of the sexual cycle of *Chlamydomonas* (227, 228). For *Cr*aCRY, a knock-down mutant with a reduced level of protein to approximately 20 % displayed a response to blue and red light. The transcript levels of several genes of light harvesting complexes, nitrogen metabolism, chlorophyll and carotenoid biosynthesis, the cell cycle and the circadian clock revealed

significant changes (232, 233). Also yellow light exerted an effect on the transcript levels of various genes. *In vitro* studies showed, that the flavin in *Cr*aCRY can be easily reduced to its neutral radical $FADH^{\circ -}$, which absorbs almost the entire visible spectrum below 680 nm (233). By further illumination with red-light, *Cr*aCRY can also be reduced to the hydroquinone $FADH^-$ (233). This evidence and the fact, that *Chlamydomonas* is lacking a (6-4) photolyase as well as a classical red-light receptor, makes *Cr*aCRY to an highly interesting candidate for either photolyase activity, or a blue/red light-dependent transcriptional regulator or even both.

2 Overview of advanced Protein Analysis and Structure Solution

A considerable amount of the work presented in this thesis focused on revealing the mysteries of light-dependent structural changes upon electron transfer in cryptochromes and photolyases. To achieve this goal several techniques were used for which a short introduction is given in the following.

2.1 Protein X-Ray Crystallography

X-ray crystallography is the most important method to gain structural information of proteins on an atomic level. Almost 90 % of the structures deposited in the RCSB-PDB (*Research Collaboratory for Structural Bioinformatics (RCSB) Protein Data Bank (PDB)*) (234) in September 2018 derived from X-ray crystallography and the number of protein structures available is still exponentially growing since the release of the first protein structure of myoglobin in 1958 (235).

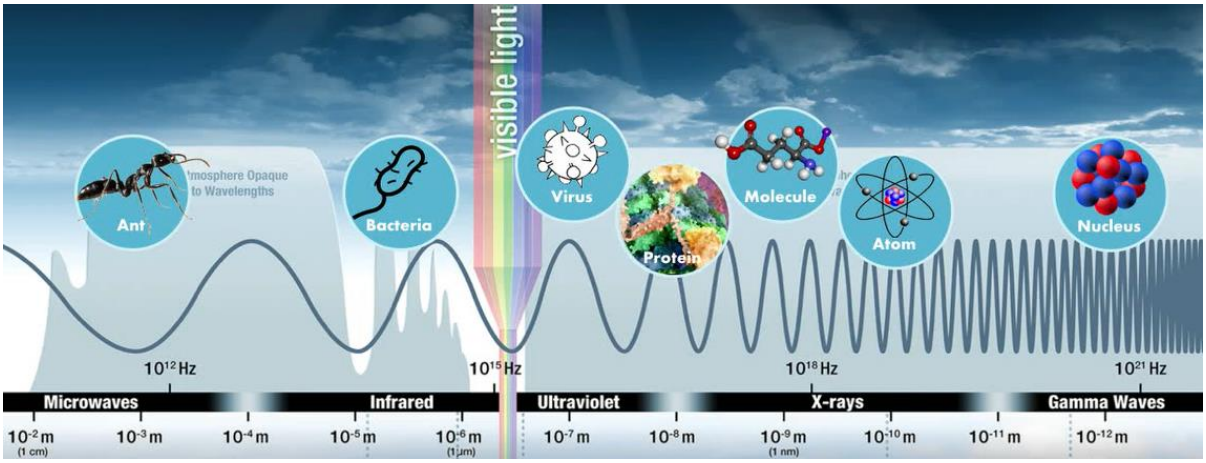

Figure 23 An overview of a part of the electromagnetic spectrum and its resolution limits (236). X-ray radiation can have a wavelength between 0.01 nm and 10 nm with energy in the range of 100 eV to 100 keV.

Principles of X-Ray Crystallography

The growth and quality of a protein crystal depend on different factors like pH, concentration, temperature and the chosen crystallization method. One of the most important points to consider before starting of a crystallization screening is the homogeneity of the protein solution. Inhomogeneous solutions tend to precipitate and crystals are not able to form.

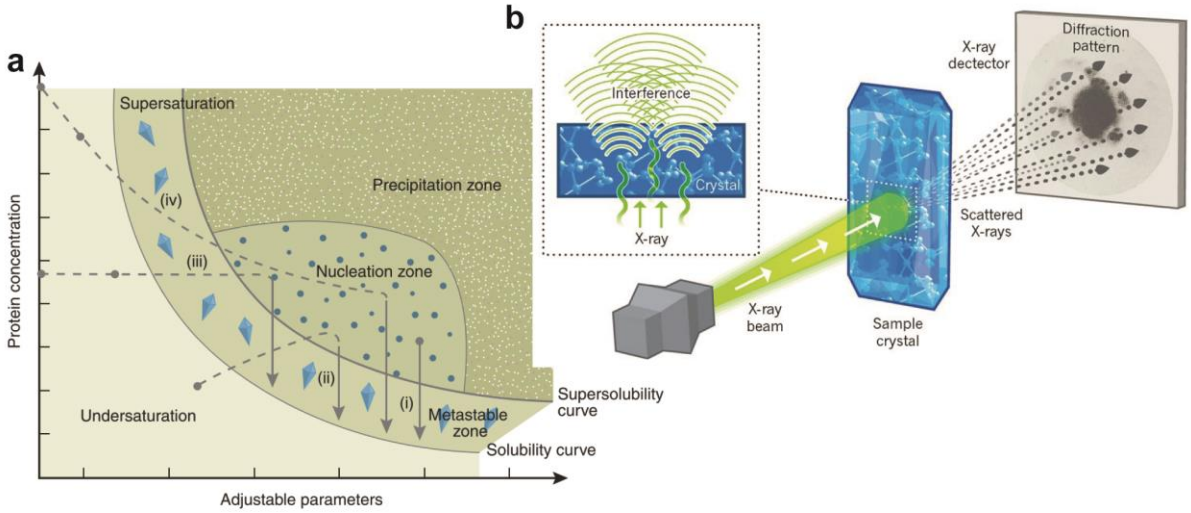

Figure 24 a) Sketch of the protein crystallization phase diagram (figure adapted from (237)). The arrows represent the four major crystallization methods: (i) microbatch, (ii) vapor diffusion, (iii) dialysis, (iv) free interface diffusion. In all cases, the crystallization solution has to be in the nucleation zone to be able to produce stable protein crystals. b) Simplified representation of an X-

ray diffraction experiment (figure adapted from (238)). The X-ray beam is focused on the protein crystal, which scatters the waves. Through positive and negative interference a diffraction pattern is forming on the X-ray detector.

There are different methods for protein crystallization. The most prominent ones are microbatch experiments as well as vapor diffusion (239, 240). In the latter, the protein solution is present in either a sitting or a hanging drop, which equilibrates against a crystallization solution with either higher or lower concentration of crystallization agents as in the drop. Throughout the equilibration process the protein solution should go from the undersaturated (Figure 24, ii) or oversaturated phase (Figure 24, iv) to the nucleation zone followed by formation of stable protein crystals (237). In the microbatch method, the crystallization conditions are prepared and incubated under a layer of paraffin oil. There is almost no diffusion happening so the precipitant concentrations remain constant during the incubation. Therefore the initial concentration should already be starting in the nucleation zone (Figure 24, i). Two other methods, which are shown in the phase diagram but not used in this study, are dialysis (Figure 24, iii) and free interface diffusion (FID, Figure 24, iv).

To obtain structural information of a protein crystal, the crystal is flash frozen in liquid nitrogen with a cryo-protectant (*e.g.* 20% glycerol) and measured at a synchrotron X-ray source, like the *European Synchrotron Radiation Facility* (ESRF, Grenoble, France). Highly ordered protein crystals are able to diffract X-ray radiation and give rise to a diffraction pattern, according to BRAGG'S law (241). From the diffraction patterns, taking the intensities and relative phases into account, the position of each atom inside the crystal can be ideally determined (242). The electron density at every position in the unit cell can be calculated through the following equation:

$$\boldsymbol{\rho(x\ y\ z)} = \frac{\mathbf{1}}{\boldsymbol{V}} \sum_{\boldsymbol{h}} \sum_{\boldsymbol{k}} \sum_{\boldsymbol{l}} |\boldsymbol{F_{hkl}}| \times \boldsymbol{e}^{-\mathbf{2}\boldsymbol{\pi i}(\boldsymbol{hx}+\boldsymbol{ky}+\boldsymbol{lz})+\boldsymbol{i\alpha}(\boldsymbol{hkl})}$$

Equation 1 The electron density ρ(x y z) at every position (x y z) can be calculated with the volume of the unit cell (V), the MILLER indices (h k l), the structure amplitude (F_{hkl}) and the phase angles α(h k l).

The phase angles α(h k l) cannot be derived straightforward from the diffraction pattern, but there are several methods available to solve this so called phase problem (242). One method uses the PATTERSON function, which is a simplification of Equation 1.

$$\boldsymbol{P(u\,v\,w) = \frac{1}{V}\sum_{\substack{hkl \\ -\infty}}^{+\infty} |F_{hkl}|^2 \times cos\,2\pi[hu + kv + lw]}$$

Equation 2 The PATTERSON function calculated at the point (u v w). The summation is done on F_{hkl}^2 and all phases are assumed to be zero.

This method is called multiple isomorphous replacement (MIR) and helped PERUTZ and KENDREW to be awarded a Nobel prize in 1962 for solving the structure of hemoglobin and myoglobin, respectively (243). The second technique to solve the phase problem is named multi-wavelength anomalous diffraction (MAD), which utilizes heavy atoms that scatter X-rays anomalously (244, 245). This method involves measurement of diffraction patterns using X-rays with different energies and analyzing the differences between them. From these differences it is possible to calculate the phases generated by the anomalous scatters and with that information, the electron density map for the whole protein. The last prominent method, which was used in the presented study, is molecular replacement (MR). For that, the phases are approximated by taking a protein with a homologous amino acid sequence known structure (246). The minimum of sequence identity should be around 30 % to achieve a straight-forward solution for the phase problem by MR (247).

If one of the described methods gives a successful solution for the phases, the electron density can be calculated. In this density, the amino acid sequence will be fitted and the resulting structure refined using the *maximum-likelihood* method (248), which tries to minimize the differences between the calculated and the observed structure factors. To compare the calculated structure factors (F_{cal}) after refinement with the observed ones (F_{obs}), the reliability-factor R can be determined. This factor defines the disagreement between the experimental dataset and the structural model and can be hence used to compare the quality of different structures. This R-factor can be calculated for all reflexes, which have been considered in the refinement (R_{work}) as well as for a test data set (R_{free}),

which only holds about 5 % of the whole data and is used for validation of the refinement process.

$$R = \sum \frac{\big||F_{obs}| - |F_{cal}|\big|}{|F_{cal}|}$$

Equation 3 Characterization of the reliability-factor R, which includes the calculated (F_{cal}) and the observed (F_{obs}) diffraction pattern.

2.2 Time resolved serial X-ray crystallography using X-ray free electron lasers

Classical X-ray crystallography can give us a 3D structure of a protein, but to learn more about the structural dynamics of a biomolecule, different methods have to be used. In the last decade, X-ray free electron lasers (XFELs) have been developed and are in operation in a few locations over the world. This technology is a breakthrough for crystallography, because it is allowing atomic resolution on a timescale from femtoseconds to seconds and time-resolved diffraction at room temperature without the usual effects of radiation damage (249). To answer a lot of questions concerning the structural dynamics of photolyases and cryptochromes upon photoreduction a cooperation between the ESSEN laboratory, the *Academia Sinica* (Taipei, Taiwan) and the *RIKEN Harima Institute* (Hyogo Prefecture, Japan) was initiated. All members of the cooperation provided their assets for measuring photolyase and cryptochrome crystals at the *SPring-8 Angstrom Compact Free Electron Laser* (SACLA, Japan).

Principles of an X-ray free electron Laser (XFEL)

The SACLA XFEL facility was completed in March 2011 and produces an X-ray free electron laser beam which is generated as shown in Figure 25. Free-electron lasers are known to combine the technology of particle accelerators and lasers to generate electromagnetic radiation with very high intensity and brightness (250, 251). The electrons are produced by an electron source, followed by a linear electron accelerator (*linac*) with energies from 1 to 15 GeV. At the SACLA facility, there are 128 linacs installed to amplify the energy of the

electron beam before it gets injected into the undulator (252). The undulator block itself is made out of a maximum of 18 undulators, each consisting of 560 powerful dipole magnets. Inside the undulator, the "SASE" (*self-amplified spontaneous emission*) process starts (253), which causes the intensity of the radiation to grow exponentially to the point of saturation. Because of the periodic magnetic field, the electron beam can be converted into an X-ray pulse with a short wavelength. At SACLA, the wavelength ranges from 0.275 to 0.063 nm and the pulse duration can be tuned between 1.68 and 107 fs (251, 254). Because the pulses are so short and have very high energies (up to 10^{12} photons per fs), the diffraction of a nanocrystal can be monitored before the crystal is destroyed. Therefore the XFEL pulse is taking a "snapshot" of a crystal in a random orientation without any radiation damage (255). The feasibility of crystals ranging from a few micrometers to a few hundred nanometers is another advantage of this method, because it can be difficult to grow large well-ordered crystals of some macromolecules, especially membrane proteins (256, 257).

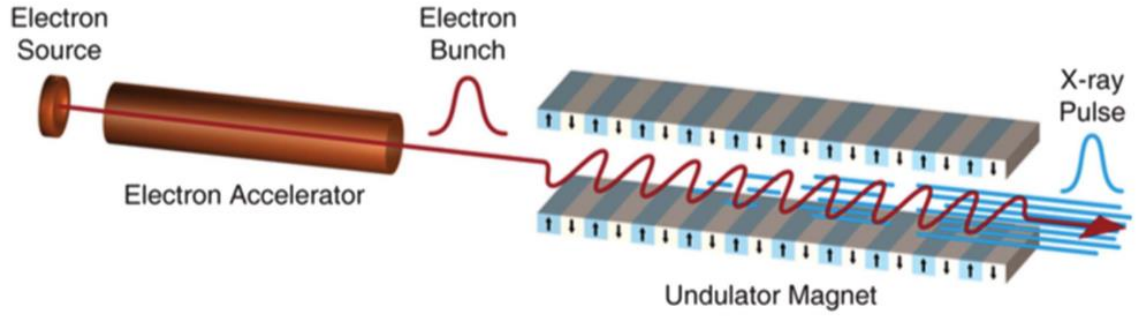

Figure 25 Basic principle of the generation of an X-ray free electron beam (Figure adapted from (251, 258)). The electrons are produced by an electron source, followed by a linear electron accelerator (*linac*) to amplify the energy of the electron beam before it is getting tuned to a short wavelength inside the undulator magnet.

Time resolved serial femtosecond crystallography (TR-SFX)

Structural changes in a biological system like a protein or an enzyme-substrate complex can range on a time-scale from fs (10^{-15} s) to hours. Depending on the change to be monitored, different methods can be used. Figure 26a summarizes the different structural changes, shows which techniques can be used to initiate these changes as well as which methods can be used to monitor them (259). For instant, large conformational changes, like a

hydrophobic collapse, can either destroy the crystalline lattice or the crystal packing would completely prevent this motion. In these cases, X-ray scattering of biomolecules in solution can be used. Small angle X-ray scattering (SAXS) is able to show changes in the overall dimension/mass of protein, whereas wide angle X-ray scattering (WAXS) provides higher resolution information like relative positions of different subunits, domains or secondary structure elements. To follow highly resolved structural changes on a very short time-scale at room temperature, serial femtosecond crystallography (SFX) combined with XFEL is the method of choice (260, 261).

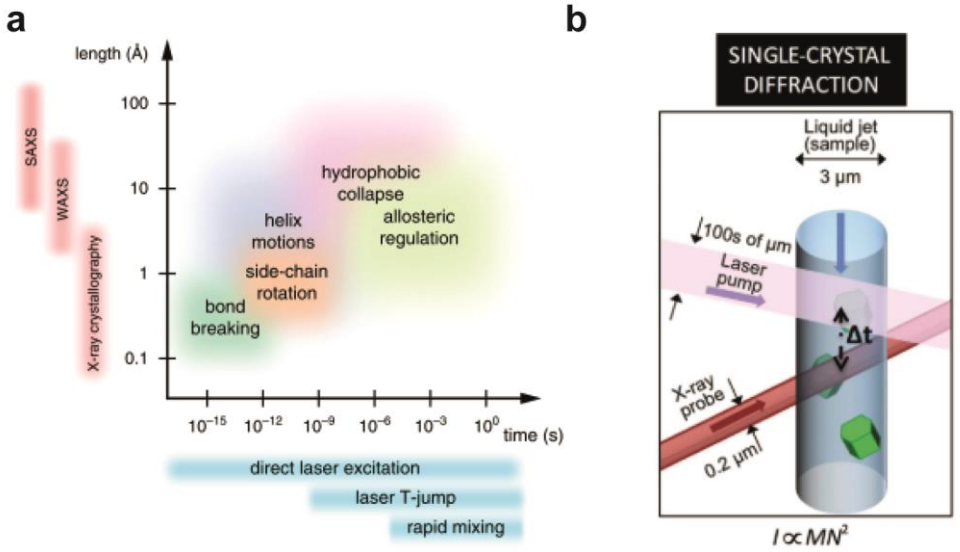

Figure 26 a) Overview of the different changes, that can be observed with time-resolved methods like small angle X-ray scattering (SAXS), wide angle X-ray scattering (WAXS) and X-ray crystallography combined with XFEL. The different excitation methods used for the different time scales are shown in blue (figure adapted from (259)). b) Schematic setup of a time resolved serial femtosecond X-ray experiment with a classical pump-probe design (figure adapted from (249)). Δt describes the delay between the laser flash (pump) and the X-ray (probe) beam hitting the crystal.

For the collection of time-resolved data, a classical pump-probe experiment can be used. First the reaction is initiated inside the crystal by a laser pump pulse and the same crystal gets hit by the X-ray (XFEL) probe after a time-delay Δt. To collect enough diffraction data (minimum of 20,000 images (262)) for all needed crystal orientations and to increase the signal-to-noise ratio, a continuous flow of hydrated crystals is needed. Here, one bottleneck

of the technique is exposed, as the carrier material/solution has to stabilize the crystals but has to be viscous enough not to lose too much sample material. One method uses liquid microjet injection (263), but here only around 0.01 % of the crystals are hit be the XFEL pulse (264). Another method developed at SACLA is the usage of a grease-matrix as carrier, which reduces the required sample amount tremendously (265).

TR-SFX measurements of members of the CPF at SACLA

To increase the knowledge about the structural changes upon photoreduction and the repair reaction in the photolyase/cryptochrome superfamily, two members representing two different classes were chosen to be studied by TR-SFX: the class II CPD photolyase from *Methanosarcina mazei* (*Mm*CPDII) and the animal-like cryptochrome from *Chlamydomonas reinhardtii* (*Cr*aCRY). The crystal structures of both proteins have been solved in the ESSEN lab. Whereas the structure of *Mm*CPDII (2XRZ) was published by Kiontke *et al.* in 2011 (54), the crystal structure of *Cr*aCRY (6FN2) is a major part of the present thesis (142). For both proteins the aim is to gather data sets at different time points of the photoreduction process and to display the structural changes upon DNA-repair, especially inside the DNA binding pocket. The exact experimental conditions will be described in the following publication. The experiments took place at the SACLA inside the DAPHNIS (*diverse application platform for hard X-ray diffraction in SACLA*) system (266). It mainly consists of the sample chamber, injectors and a multi-port charge-coupled device detector (MPCCD) with eight sensor modules (512 x 1024 pixels each) (Figure 27a). The distance between the detector and the sample is adjustable between 50 and 100 mm. The DAPHNIS system is designed to control the temperature and humidity around the sample, so a continuous sample flow can be realized. The sample chamber can be flushed with helium to reduce X-ray scattering by air (Figure 27b). The sample injector is mounted on a motorized manipulator, so it can be moved in x, y and z direction over the control system and is monitored by different cameras (Figure 27c) (266).

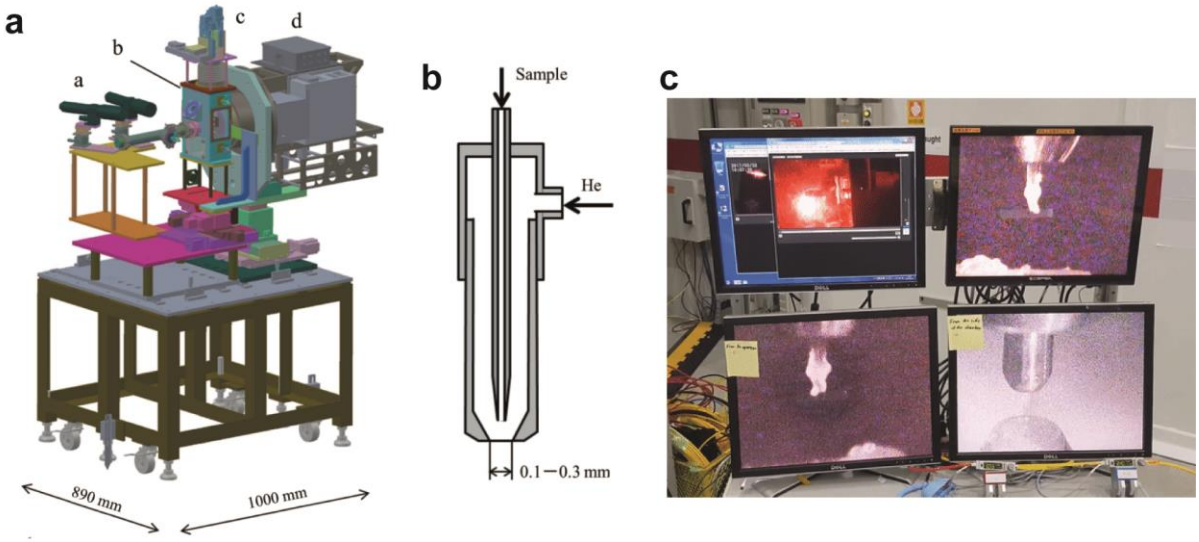

Figure 27 a) Schematic view of the whole DAPHNIS system, which is placed on an adjustable optical table (figure adapted from (266)). The sample chamber (b) is monitored by different cameras (a). On top of the sample changer is an injector manipulator (c), which is regulating the sample flow. In this picture, the X-ray beam is going inside the chamber from the left side and is hitting the MPCCD detector (d) on the right. b) The temperature and flow of the sample is regulated by a constant helium flow inside the sample injector (figure adapted from (266)). c) The flow and beam position is monitored through different cameras, showing the x, y and z positions.

For triggering photoreduction and DNA repair, a 400 nm laser (pump) was connected to the DAPHNIS system to point directly at the sample. Depending on what process should be observed, the delay times before the XFEL (probe) hits the sample varies between 10 ns and 2 ms. To avoid light-contamination of the crystals flowing on top at least one dark measurement between the next light image was taken.

For data processing of SFX at SACLA, Nakane *et al.* (267) developed a processing pipeline that is based on the *Cheetah* (268) and *CrystFEL* (269) software. During 36 h of beam time at SACLA, millions of diffraction images can be produced, but not all contain valuable information. Typically the hit rate, which describes the amount of XFEL pulses that actually hit crystals with useful diffraction, lies under 50 %. In the first step of the processing, *Cheetah* runs parallel to the measurement and analyses all images in real-time. It gives an almost direct feedback about the hit rate, detector saturation and the indexing rate of the collected images. After a run is finished, the offline pipeline runs the spot finding again, converts the hit images into HDF5 files and puts this information into *CrystFEL*.

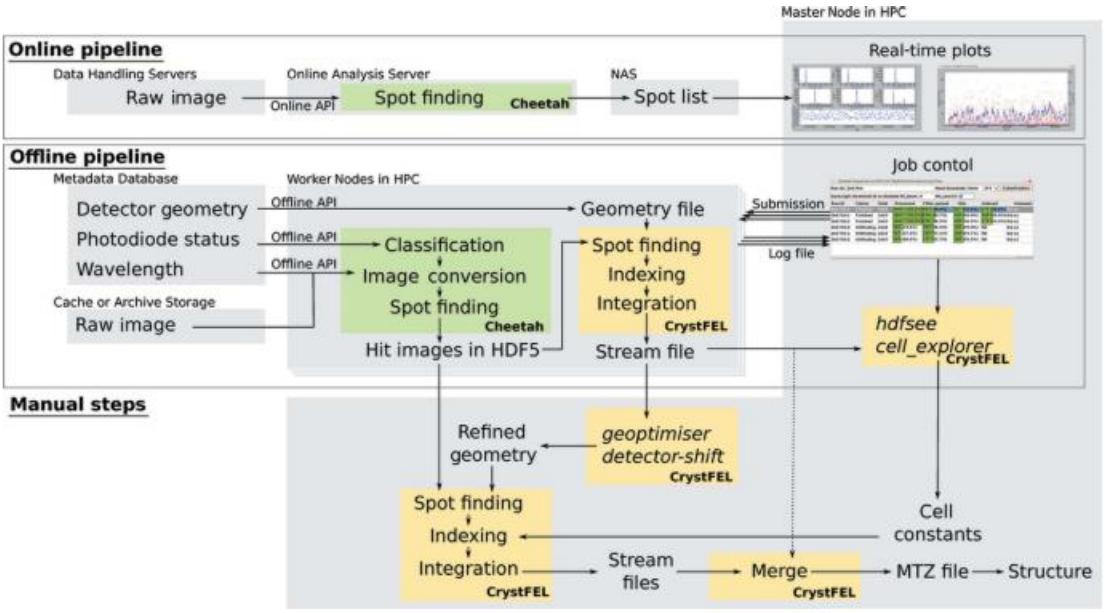

Figure 28 SACLA data processing pipeline (adapted from (267)). The first part of the pipeline finds spots on the diffraction images and provides a real-time feedback on hit rates and detector saturation. The offline part runs spot finding again and generates output files in HDF5 format. These get processed by *CrystFEL*. The user is optimizing parameters based on the pipeline output and re-run *CrystFEL* before the final merging step. If the refined parameters are already known, the stream files from the pipeline can be directly merged (dotted line) to generate the final MTZ file.

After the automatic pipeline is finished, the user is encouraged to optimize various parameters. This optimization can increase the index rate by 5-10 % (267). The data sets can be reduced to one MTZ file comparable to that of a synchrotron data set and the structure solution from this point is straight-forward.

2.3 Hydrogen/deuterium exchange mass spectrometry – HDX-MS

Hydrogen/deuterium exchange (HDX) combined with mass spectrometry (MS) is a method in structural biology to analyze conformational changes as well as protein-protein or protein-ligand interaction sites. The method is based on the principle that only amide hydrogens of the peptide backbone exchange on a time-scale, which can be resolved by HDX-MS (270). Additionally, the exchange rate depends on the accessibility of the hydrogen atoms resulting in a correlation between structural characteristics of a protein and deuterium uptake. Flexible loops or dynamic regions of a protein show a faster deuterium uptake as structured parts or interaction sites. For hydrogens that are really “hidden” inside

the protein, the exchange can take several hours up to several days (271). In the present work, HDX-MS was used to compare structural features of different cryptochrome mutants in their different reduction states.

The work flow of an HDX-MS experiment is illustrated in Figure 29 (272). The protein sample is incubated for a defined time in D_2O buffer. The exchange will be stopped by lowering the temperature to 0 °C and adding a highly acidic quench solution, which shifts the pH to low values. This step already unfolds the protein which is then injected onto a protease column, usually with immobilized pepsin, afterwards. The protease digests the sample into small peptide fragments, which are separated and analyzed by HPLC-MS. By comparison of the spectra of the different fragments with and without deuterium incubation, the deuterium uptake can be calculated. The data can be displayed as a colored uptake chart and the differences between two states are calculated and displayed in a relative fractional uptake chart. For better visualization and analysis, the values can also be mapped on an available structure or structural model in PyMol (273).

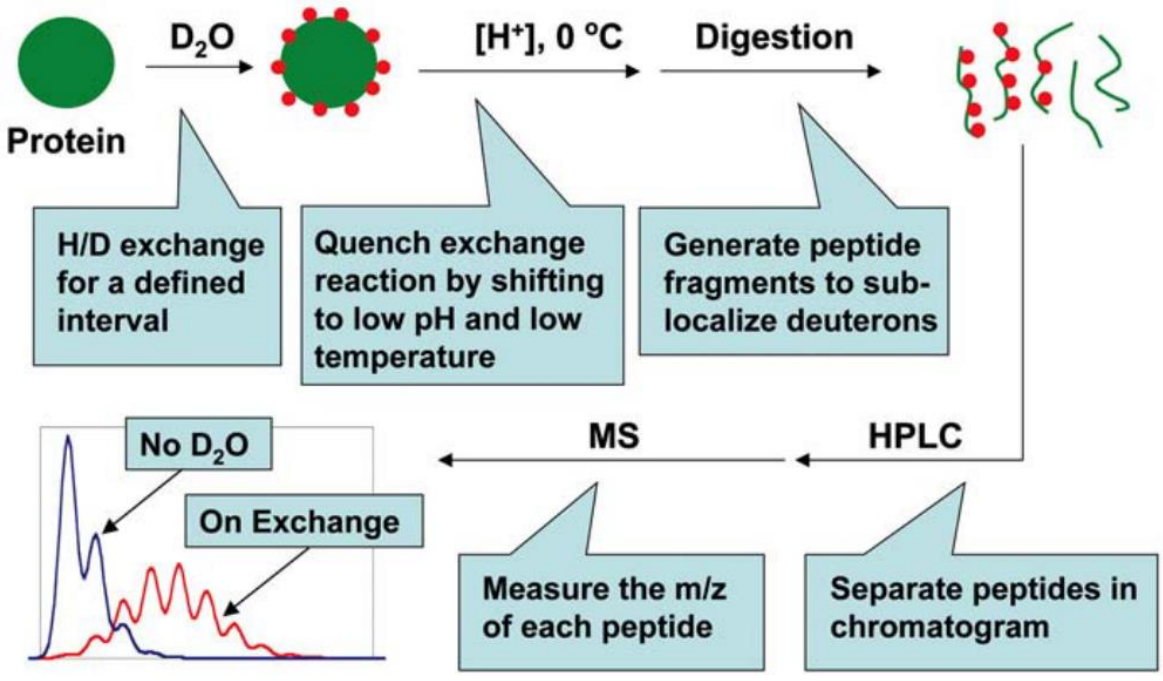

Figure 29 Overview of a typical workflow of a HDX-MS experiment (figure adapted from (272)).

One of the advantages of HDX-MS compared to X-ray crystallography is the measurement of proteins in solution, which takes the dynamic character of proteins into account (274, 275). Additionally, HDX-MS requires only a small amount of the protein of interest and is relatively fast (276). Compared to NMR spectroscopy, there is no principle limitation of sample size for HDX-MS (277, 278).

2.4 Electron paramagnetic resonance (EPR) spectroscopy

Electron paramagnetic resonance (EPR) spectroscopy is basically a method used in structural biology to measure long-range distances inside a protein or a multimeric complex (279). By collecting various distances, information about structural elements, domain arrangements, complex formation and structural changes upon ligand binding can be obtained. This approach can also be combined with molecular dynamic (MD) simulations as a powerful tool to calculate the conformation of large multimeric complexes (280).

EPR spectroscopy is based on the paramagnetic spin of a molecule and the coupling of this spin with nearby nuclear spins. Most proteins are not intrinsically paramagnetic, but some proteins like photoreceptors contain paramagnetic cofactors which can be observed *via* EPR (281, 282). Some also undergo a reaction mechanism where paramagnetic states are generated (283). Additionally, paramagnetic labels can be introduced into the protein of interest. Most commonly used are metastable nitroxide spin labels which can be attached to cysteine residues (284).

In the present work, transient EPR (trEPR) was used to investigate the formation of radicals during the photoreduction process. This method is measuring the EPR signal intensity in a time-resolved manner at a fixed magnetic field (285). To generate the paramagnetic species a nanosecond laser flash is used. Then a series of trEPR signals are recorded from different magnetic-field points, which can be described as a two-dimensional graph of the signal intensity in respect to the time and the magnetic field. The spectral shape of the trEPR signals provides various information about the chemical nature of the individual radicals, their interaction with each other and their environment (282).

3 Objective of the thesis

The main knowledge of cryptochrome structure has derived from their comparison with photolyases, but a lot of questions about their function cannot be answered by this analogy. Cryptochromes have a highly variable C-terminus, which can be involved in signaling, but the underlying mechanism is not clearly described so far. There is only one crystal structure of a full-length CRY so far, which is relatively short (64, 65). A lot of studies are based on this CRY (*Dm*CRY), which might be a good model, but the short CTE and its attachment to the DNA binding site might be more of an exception then the rule. That's why one aim of my thesis was to study the structure of another animal-like cryptochrome with a long CTE to gather more information about this group of proteins. This particular CRY, *Cr*aCRY, was identified in the algae *Chlamydomonas* and demonstrates some interesting behavior *in vivo* and *in vitro* (233, 286). Therefore, alongside the structural characterization, I focused on the photoreduction mechanism and the involved residues. To gain more information about the light-induced processes in *Cr*aCRY, I identified the relevant sidechains through mutagenesis and used different spectroscopic methods. I also worked together with several other research groups with expertise in different analytical methods, to gain a whole picture of this system. This should also address the question, if *Cr*aCRY may be suitable to act as a receptor in the process of magnetoreception.

*Cr*aCRY is also believed to be part of the photoreactivation process in *Chlamydomonas*, *e.g.* be able to repair UV-induced DNA lesions (232). For this reason, we were investigating its photolyase activity and looked further into the repair mechanism itself. One objective for my PhD thesis was to identify the basic requirements of an enzyme to function as a (6-4) photolyase. Additionally, the connection between structure and bifunctionality of *Cr*aCRY should be investigated.

4 Publications

4.1 Spectroscopic characterization of *Cr*aCRY and *Dm*CRY

This research was originally published in Biophysical Journal by *Daniel Nohr, Sophie Franz, Ryan Rodriguez, Bernd Paulus, Lars-Oliver Essen*, Stefan Weber and Erik Schleicher*.* **Extended Electron-Transfer in Animal Cryptochromes mediated by a Tetrad of Aromatic Amino Acids.** *Biophysical Journal.* 2016; 111 (*2*): 301-311. Some preliminary results were already presented in the master thesis (287).

Summary

This publication is focusing on the electron transfer chain in two members of the cryptochrome family: the animal type I CRY from *Drosophila melanogaster* (*Dm*CRY) and the animal-like CRY from *Chlamydomonas reinhardtii* (*Cr*aCRY). In general, the reduction of the FAD cofactor was shown to be catalyzed over a highly conserved tryptophan triad as described in chapter 1.5 (36, 85, 91–95). Müller *et al.* revealed *via* multiple sequence alignment, that there is a fourth tryptophan residue exclusively in animal CRYs and (6-4)PHLs (288). They performed transient absorption spectroscopy with the (6-4)PHL of *Xenopus laevis, Xl*(6-4)PHL, and demonstrated a lifetime of about 40 ms for the $FAD^{\bullet-}$ $Trp_4^{\bullet}$ radical pair. In *Dm*CRY this fourth Trp_4 is also present whereas *Cr*aCRY contains a tyrosine at this particular position. Considering these variations in the electron transfer pathway, we investigated the role of the triad residues (TrpA, TrpB, TrpC; *Cr*aCRY: W399, W376, W322; *Dm*CRY: W420, W397, W342) and several other putative electron donor residues in the direct environment of the triad. As a result, trEPR spectra (Figure 30a) of several point mutants revealed the importance of the Trp triad for radical pair (RP) formation, whereas the mutant of W332, a residue which is expected to be located close to TrpA and TrpB in *Cr*aCRY, showed the same RP formation as the wildtype. For the Y373F mutant, the RP can still be observed, but the spectral shape shows significant differences. This can be assigned to TrpC acting as a terminal electron donor as the spectrum is similar to the trEPR spectra from the CRY-DASH subclade (289–291). The same is observable in the *Dm*CRY-W394F mutant. Remarkably, the $Tyr^{\bullet}$ in *Cr*aCRY demonstrates a lifetime of 26 ms.

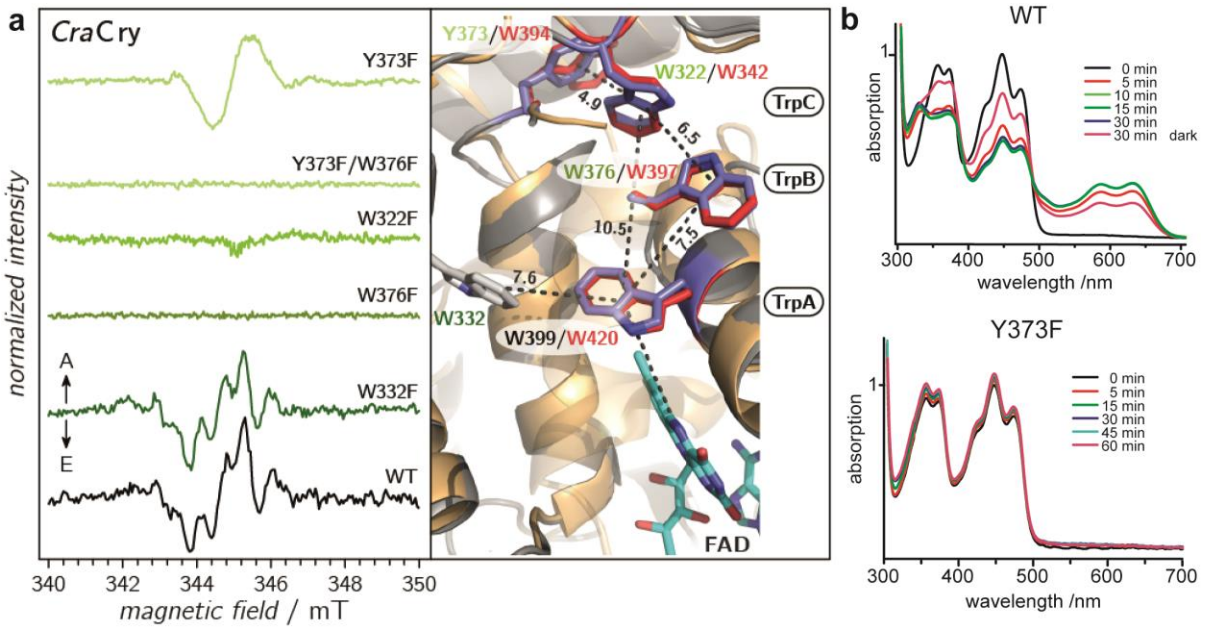

Figure 30 a) TrEPR signals of different *Cra*CRY mutants (green) and wild type (WT, black). A and E arrows indicating enhanced absorption and emissive polarization of resonances. W332F displays the same signature as the WT, whereas Y373F reveals a loss of hyperfine coupling. For the double mutant Y373F-W376F as well as mutants of the triad W322F and W376F no radical pair formation could be detected in trEPR. The middle shows a superimposition of *Dm*CRY (red, 1TEZ) and a structural model of *Cra*CRY (green). b) UV/Vis spectra of *Cra*CRY WT and Y373F when illuminated with blue light (450 nm) for defined times without any reducing agent. The WT displays complete formation of FADH° after 10 min, whereas Y373F shows no difference even after 60 min of illumination.

Contributions

D. Nohr designed experiments, performed trEPR and TA measurements of all proteins, analyzed the data and wrote parts of the manuscript. S. Franz cloned, expressed and purified the different *Cra*CRY mutants, performed stady-state UV/Vis spectroscopy of them, carried out thermo-FAD measurements of all *Cra*CRY and *Dm*CRY variants and wrote parts of the manuscript. R. Rodriguez expressed and purified the *Dm*CRY variants. B. Paulus helped with analyzing the trEPR data. L.-O. Essen, S. Weber and E. Schleicher designed experiments, wrote and revised the manuscript.

Biophysical Journal
Article

Extended Electron-Transfer in Animal Cryptochromes Mediated by a Tetrad of Aromatic Amino Acids

Daniel Nohr,[1] Sophie Franz,[2] Ryan Rodriguez,[1] Bernd Paulus,[1] Lars-Oliver Essen,[2,*] Stefan Weber,[1] and Erik Schleicher[1,*]
[1]Institute of Physical Chemistry, University of Freiburg, Freiburg, Germany; and [2]University of Marburg, Marburg, Germany

ABSTRACT The cryptochrome/photolyase protein family possesses a conserved triad of tryptophans that may act as a molecular wire to transport electrons from the protein surface to the FAD cofactor for activation and/or signaling-state formation. Members from the animal (and animal-like) cryptochrome subclade use this process in a light-induced fashion in a number of exciting responses, such as the (re-)setting of circadian rhythms or magnetoreception; however, electron-transfer pathways have not been explored in detail yet. Therefore, we present an in-depth time-resolved optical and electron-paramagnetic resonance spectroscopic study of two cryptochromes from *Chlamydomonas reinhardtii* and *Drosophila melanogaster*. The results do not only reveal the existence of a fourth, more distant aromatic amino acid that serves as a terminal electron donor in both proteins, but also show that a tyrosine is able to fulfill this very role in *Chlamydomonas reinhardtii* cryptochrome. Additionally, exchange of the respective fourth aromatic amino acid to redox-inactive phenylalanines still leads to light-induced radical pair formation; however, the lifetimes of these species are drastically reduced from the ms- to the μs-range. The results presented in this study open up a new chapter, to our knowledge, in the diversity of electron-transfer pathways in cryptochromes. Moreover, they could explain unique functions of animal cryptochromes, in particular their potential roles in magnetoreception because magnetic-field effects of light-induced radical pairs strongly depend on distance and orientation parameters.

INTRODUCTION

Cryptochromes (Crys) are blue-light photoreceptors found in all domains of life (1,2). They participate in a wide range of regulatory functions such as inhibition of hypocotyl growth, blue-light-dependent flowering, synchronization of the internal clock by ambient light (3,4), and magnetoreception (5–8). Recently, Crys have also been used in the emerging field of optogenetics; several constructs demonstrate the potential of Crys for light-controlled modulation of protein functions (9,10). In addition, Crys are closely related to the photolyase DNA repair enzymes (Pl) (1,2,11–13). Both have similar tertiary structures despite a C-terminal extension that is supposed to control signal transduction in Crys. Crys and Pls harbor a noncovalently bound light- and redox-active FAD as an essential cofactor. Based on structural and functional similarities the Cry/Pl family can be further subdivided into several subclades: class-I to class-III cyclobutane pyrimidine dimer Pls, plant Crys, DASH (*Drosophila, Arabidopsis, Synechocystis, Homo*) Crys, Cry-pros, and animal (animal-like) Crys/(6,4) Pls (2,14,15).

The photoreceptor mechanism of Crys can be separated into at least two parts: the primary photochemistry triggered by blue-light excitation of FAD, and the subsequent secondary light-independent processes followed by downstream signal transduction. In the dark, the FAD cofactor resides in the fully oxidized ground state (FAD_{ox}) (16–19). Upon light excitation, the singlet-state excited flavin abstracts an electron from a close-by tryptophan that is part of the so-called conserved "Trp-triad" (20–22), thus forming an anionic semiquinone radical ($FAD^{\bullet-}$) and concomitantly a short-lived tryptophan radical. Subsequently, stepwise sequential electron transfer (ET) takes place along the Trp-triad until the terminal surface-exposed tryptophanyl cation radical is formed, which corresponds to the $[FAD^{\bullet-}\cdots TrpH^{\bullet+}] \equiv$ RP1 radical pair. RP1 is further stabilized by deprotonation, thus forming the secondary $[FAD^{\bullet-}\cdots Trp^{\bullet}]$ radical pair, RP2 (20,23). RP2 either deactivates by backward electron transfer to regenerate the

Submitted March 16, 2016, and accepted for publication June 10, 2016.
*Correspondence: essen@chemie.uni-marburg.de or erik.schleicher@physchem.uni-freiburg.de
Editor: David Cafiso.
http://dx.doi.org/10.1016/j.bpj.2016.06.009

ground state moieties or the $Trp^{\bullet}$ radical is reduced by an exogenous electron donor; the latter process results in a net reduction of the FAD cofactor. In combination with FAD reduction, protonation of the $FAD^{\bullet -}$ occurs in Pls and plant/DASH Crys. Unlike in Pls, no further (or only partial) reduction of the FAD radical to the fully reduced redox state ($FADH^-$) was observed both in plant and in animal Crys (16–18,24).

In general, the theory of a conserved Trp-triad was widely accepted during the last decade, although its biological relevance is still under discussion (25–27), and various exceptions have been discovered in the past few years. For example, an alternative nonconserved tryptophan that serves as a terminal electron donor in *Synechocystis* sp. Cry DASH was identified (28). Furthermore, in 2012 a new class of prokaryotic cryptochromes was discovered, which lacks the conserved Trp-triad (14). In a recent study of a (6-4) photolyase the existence of a fourth tryptophan involved in ET was proposed based on amino acid sequence similarities (29).

In light of the previously mentioned notions that Cry electron-transfer pathways upon light excitation are essential but may be variable, the focus of this contribution is to provide an in-depth spectroscopic characterization of the fast events in two proteins, *Chlamydomonas reinhardtii* (*Cra*Cry) and *Drosophila melanogaster* Cry (*Dm*Cry), from the animal (and animal-like) Cry subclade. *Dm*Cry is by far the best-investigated protein among the animal Crys: its direct involvement in circadian timing (30) and magnetoreception has been proven (8,31), although the molecular mechanisms of both processes remain largely unexplored, and immediate magnetic field effects have not yet been published. On the other hand, the exact function of *Cra*Cry is still under discussion; studies point in the direction of its function as a red light transcriptional regulator, although the exact mechanism of action remains to be elucidated (32).

To obtain spectroscopic information at a molecular level, steady-state photoreduction experiments of *Cra*Cry, and two complementary time-resolved techniques with nanosecond time resolutions, transient electron-paramagnetic resonance (trEPR) and transient (optical) absorption spectroscopy (TA), were applied to probe the involvement of the Trp-triads comprising the residues W399, W376, and W322 in *Cra*Cry, and W420, W397, and W342 in *Dm*Cry (also denoted as TrpA, TrpB, and TrpC) in the primary photochemistry of animal (and animal-like) Crys. Additionally, various point mutants were investigated to corroborate our conclusions gathered from the wild-type (WT) proteins.

MATERIALS AND METHODS

Preparation of *Cra*Cry mutants

Mutant plasmids were generated via the Round-the-horn site-directed mutagenesis method using phosphorylated back-to-back primers. The plasmids (pET28a vector) were sequenced by GATC (Konstanz, Germany). Expression and purification of all *Cra*Cry variants were carried out following published procedures (32). To get rid of remaining nucleases bound to the protein, additional purification through a heparin affinity column was carried out: after application to the column, the protein was washed with four column volumes of buffer containing 50 mM sodium phosphate pH 7.8, and 20% (v/v) glycerol. Elution was performed using a salt gradient reaching a concentration of 2 M sodium chloride. As a last purification step, size-exclusion chromatography was performed in a buffer containing 50 mM NaH_2PO_4 pH 7.8, and 100 mM NaCl. After a final buffer exchange, the protein was obtained in a buffer containing 50 mM NaH_2PO_4 pH 7.8, 100 mM NaCl, and 35% (v/v) glycerol.

Preparation of *Dm*Cry mutants

The *Dm*Cry W394F mutation was introduced by overlap extension polymerase chain reaction, and the obtained fragment was subsequently ligated into a pET28a vector (Merck Millipore, Darmstadt, Germany) via restriction cloning. The mutation was verified by sequencing (Eurofins Genomics, Ebersberg, Germany). The final plasmid was transformed into SoluBL21 competent *Escherichia coli* cells (Genlantis, San Diego, CA) for protein expression. Protein production was performed using the protocol for the WT (24).

Sample preparation for time-resolved spectroscopy

*Dm*Cry samples for trEPR measurements were prepared in a buffer containing 50 mM HEPES pH 7.0, 100 mM NaCl, 5 mM $K_3[Fe(CN)_6]$, and 35% (v/v) glycerol (24), whereas *Cra*Cry samples were prepared in a buffer containing 50 mM NaH_2PO_4 pH 7.8, 100 mM NaCl, 5 mM $K_3[Fe(CN)_6]$, and 35% (v/v) glycerol. Sample concentrations were determined using ultraviolet-visible (UV-vis) spectroscopy (UV-2450, Shimadzu, Kyoto, Japan) and were adjusted to a final concentration of ~1 mM. *Dm*Cry samples for transient absorption measurements were prepared in a buffer containing 50 mM HEPES pH 7.0, 100 mM NaCl, and 20% (v/v) glycerol (24), whereas *Cra*Cry samples were prepared in a buffer containing 50 mM NaH_2PO_4 pH 7.8, 100 mM NaCl, and 20% (v/v) glycerol. Sample concentrations were determined using UV-vis spectroscopy (UV-2450, Shimadzu) and were adjusted to a final concentration of ~0.05 mM.

Steady-state UV-vis and photoreduction assays

Absorption spectra were recorded using a V-660 spectrometer (Jasco, Easton, MD). The protein samples were measured in buffer containing 50 mM NaH_2PO_4 pH 7.8, 100 mM NaCl, and 20% (v/v) glycerol. The protein solution was incubated for 5 min in the dark before the first spectrum was recorded. Spectra were measured at 10°C after different illumination times using a high-power LED emitting at 450 nm (9.7 mW cm^{-2}, Roithner Lasertechnik GmbH, Vienna, Austria).

Fluorescence spectroscopy

The purified proteins were tested for correct folding and stability via a modified Thermofluor device optimized for flavoproteins (33). 20 μL of protein samples with ~25 μM protein concentration were measured in a reverse transcription-polymerase chain reaction device (Rotor Gene-Q, QIAGEN, Venlo, The Netherlands). The experiment was performed using an excitation wavelength range between 470 and 480 nm and a green emission filter (510–515 nm). Melting curves were generated by a temperature gradient from 25–99°C, detecting fluorescence every 0.5°C. *Cra*Cry mutants were measured in buffer containing 50 mM NaH_2PO_4 pH 7.8, 100 mM NaCl, and 35% (v/v) glycerol, and *Dm*Cry samples in a buffer containing 50 mM HEPES pH 7.0, 100 mM NaCl, and 35% (v/v) glycerol.

X-band trEPR spectroscopy

X-band trEPR spectra of *Cra*Cry and *Dm*Cry samples were recorded following pulsed laser excitation of the sample, which was performed using an OPO system (BBO-355-visible/IR, Opta, Bensheim, Germany) pumped by a Nd:YAG laser (GCR 190-10, Spectra Physics, Santa Clara, CA) at a wavelength of 460 nm and a pulse energy of (1.0 ± 0.2) mJ at a repetition rate of 1 Hz (pulse duration: 6 ns). A laboratory-build spectrometer was used in combination with a Bruker microwave bridge (ER046 MRT, Bruker, Billerica, MA). The sample was placed in a synthetic quartz (Suprasil) tube with an inner diameter of 1 mm, and irradiated in a dielectric resonator (ER 4118X-MD5, Bruker). The resonator was immersed into a laboratory-built nitrogen gas-flow cryostat and EPR data collected at a temperature of (270.0 ± 0.1) K stabilized by a temperature controller (ITC503, Oxford Instruments, Abingdon, UK). The microwave power was set to 2 mW and the microwave frequency controlled by a frequency counter (5352B, Keysight Technologies, Boeblingen, Germany). Signal acquisition was performed with a transient recorder (9354A, Teledyne LeCroy, Chestnut Ridge, NYA) at a bandwidth of 25 MHz. Distortions of the signal baseline introduced by the laser pulse were corrected by subtracting a signal collected at an off-resonant magnetic field position.

Spectral simulation of trEPR data

Simulations of trEPR spectra were performed using a self-written MATLAB (The MathWorks, Natick, MA) routine, based on the radical pair model and the FORTRAN program described previously (34). Additionally, the **g** and **A** tensors as well as the $\mathbf{D}_{rp}$ tensor were included in the fitting process.

Transient absorption spectroscopy

Time-resolved optical absorption spectroscopy was performed at 277 K with a commercially available laser flash photolysis spectrometer (LP920K, Edinburgh Instruments Ltd., Kirkton Campus, UK) and data were recorded with a digital oscilloscope (TDS-3012C, Tektronix, Beaverton, OR). The protein sample was placed in a synthetic quartz (Suprasil) semimicro cell (108F-QS, Hellma GmbH & Co. KG, Muellheim, Germany). The temperature was regulated to (277.0 ± 0.1) K by a temperature controller (Alpha RA 8, Lauda, Lauda-Königshofen, Germany). Optical excitation was carried out using an OPO system (OPO PLUS, Continuum, San Jose, CA) pumped with a Nd:YAG laser (Surelite I, Continuum) at a wavelength of 460 nm, a pulse width of ~6 ns, and a pulse energy of (4.0 ± 0.2) mJ. The repetition rate of the spectrometer was set to 6.67 mHz. To account for background signals, transients were measured alternately with and without optical excitation, and used for calculation of difference absorbance spectra with Beer-Lambert's law.

Global analysis

To test the transient absorption data for a specific kinetic model, a target analysis was performed using the software Glotaran (Version 1.5.1 http://glotaran.org) (35). Errors were calculated by dividing two times the standard error given by Glotaran by the optical absorption of the sample at 448 nm.

RESULTS

TrEPR spectroscopy

TrEPR allows time-resolved observation of short-lived radical pairs (RPs) and triplet states (36) generated by pulsed laser excitation. In contrast to conventional continuous wave EPR spectroscopy, which usually involves magnetic field modulation and lock-in signal amplification to improve the signal/noise ratio, trEPR data are recorded in a high-bandwidth direct-detection mode to maximize the time resolution of the experiment. Consequently, positive and negative signal amplitudes in trEPR correspond to enhance absorptive (A) and emissive (E) electron-spin polarization of the EPR transitions, respectively.

Various proteins from the Cry/Pl family have been investigated previously using time-resolved EPR methods (28,37–40); however, members of the animal (and animal-like) Cry subclade have not yet been examined. To close this gap, two proteins, *Cra*Cry and *Dm*Cry, were produced with their FAD cofactor being fully oxidized (FAD_{ox}), because amino-acid-FAD RPs can only be generated starting from this redox state. Furthermore, it has been shown in *Dm*Cry protein samples and in intact cells that FAD_{ox} is the physiological dark state of the photoreceptor, and thus, the intrinsic starting point of subsequent light-induced reactions (19,41).

Upon illumination with blue light at ambient temperature, both *Cra*Cry and *Dm*Cry exhibit trEPR signatures with widths of ~7 mT that can be attributed to spin-polarized paramagnetic species, and more specifically, to RPs on grounds of their spectral shape and narrow signal width (full contour plots are shown in the Supporting Material as Fig. S1, one-dimensional spectra obtained at maximum signal amplitudes are depicted in Fig. 1, *A* and *C*).

Surprisingly, both WT proteins exhibit pronounced but different spectral shapes with features that have not yet been observed in other Crys. Specifically, the *Dm*Cry spectral shape is rather symmetric at around $g = 2$ and comprises two broad shoulders at 342.5 and 348.0 mT. *Cra*Cry, on the other hand, shows a more asymmetric pattern of approximately the same width but with a pronounced and well-resolved sequence of maxima and minima. To retrieve more information from the spectral shape, and to elucidate whether the signal patterns originate from a second overlapping RP species or from hyperfine couplings (hfcs), the signal kinetics were extracted from the two-dimensional trEPR data sets: Irrespective of the magnetic field position $1/e$ signal decay times of ~9 μs (*Cra*Cry) and ~4 μs (*Dm*Cry) have been obtained by exponential least squares fittings. It should be noted that these values represent relaxation times of the (light-generated) initial electron-spin polarization toward spin-state populations at thermal equilibrium in the presence of 5 mM $K_3[Fe(CN)_6]$; they should not be confused with the RP lifetimes. Additional overlapping RPs could be excluded for both proteins as the lifetime (and the spectral width) of a second RP is expected to be significantly different. Hence, the rather pronounced modulations of the overall E/A spectral shape must arise from hyperfine interactions of magnetic nuclei interacting with the unpaired electron spins on the individual radical pair halves.

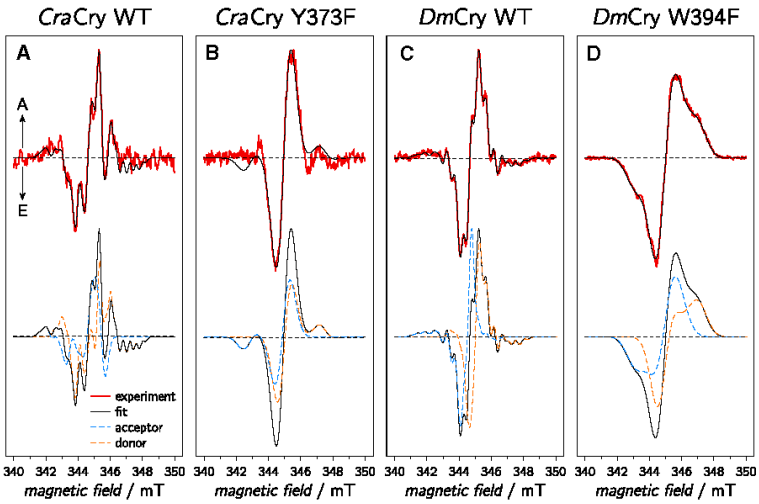

FIGURE 1 trEPR experimental data (*red curves*) including their spectral simulation (*black curves*) of *Cra*Cry WT (*A*), *Cra*Cry Y373F (*B*), *Dm*Cry WT (*C*), and *Dm*Cry W394F (*D*). A and E arrows indicate enhanced absorptive and emissive signals, respectively. Lower panels depict contributions of the individual simulated radicals (donor depicted in *orange*, FAD as acceptor in *blue*) to the overall spectral simulation (drawn *black curves*). Spectra were recorded at microwave frequencies of 9.6650 GHz (*Cra*Cry WT), 9.6741 GHz (*Cra*Cry Y373F), 9.6650 GHz (*Dm*Cry WT), and 9.6756 GHz (*Dm*Cry W394F), respectively. For simulation details, see Table 1. To see this figure in color, go online.

Spectral simulations of the trEPR data are required for an unambiguous assignment of individual hyperfine patterns. For this purpose, our existing trEPR fitting routine (34) had to be extended to include anisotropic hfcs arising from various nuclei. As an initial starting point, published parameters for **g**-tensors, dipolar (*D*), and exchange (*J*) spin-spin couplings, angles between the two radicals ($FAD^{\bullet-}$ and $TrpC^{\bullet(+)}$, the terminal tryptophan residue of the Trp-triad) extracted from the *Dm*Cry structure (42,43), and residual line-width parameters (37) were used, and additional hfcs were successively added to account for the complex hyperfine pattern. However, the rather large electron-electron coupling parameters (*D* and *J*) necessary for a distance of ~19-Å between the proposed electron donor TrpC (W322 in *Cra*Cry and W342 in *Dm*Cry) and the electron acceptor FAD did not yield satisfactory simulations because the calculated spectra were too broad to reproduce the experimental data. Therefore, other amino acids at a larger distance to the FAD were taken into account as additional stepping stones in an extended electron-transfer pathway. Amino acid alignments of the animal Cry/(6,4) Pl subclade and first experimental data from *Xenopus laevis* (6,4) Pl (29) suggested a fourth residue (Y373 and W394 in *Cra*Cry and *Dm*Cry, respectively) that could in principle be involved in electron transfer of some Crys. Using a distance of ~21.5 Å and the orientations of the corresponding amino-acid residues with respect to the flavin's isoalloxazine moiety, both extracted from the *Dm*Cry crystal structure (Protein Data Bank: 4GU5; the orientation of Y373 in *Cra*Cry was assumed to be similar), the spectral shape could be fairly well reproduced using published hfcs for both radicals (albeit in different protein surroundings) as starting values (44). The best fits for both proteins are presented in the upper panels of Fig. 1, *A* and *C*, the contributions of the individual radicals are presented in the respective lower panels, and the respective parameters to calculate the trEPR spectra are summarized in Table 1.

Briefly, only three hfcs (N(5), N(10), and H(8α)) were necessary to reproduce the FAD part, and only one (H(1′)) or two (N(1) and H(5)) for the tyrosine and tryptophan parts, respectively. Specifically, two axial nitrogen hfcs taken from EPR data of a stable $FAD^{\bullet-}$ radical (44) and one isotropic hfc that corresponds to the unrestricted rotation of the 8α methyl group protons at ambient temperatures were required to yield an excellent agreement between experiment and simulation. The hfcs for the FAD part are quite similar for both proteins, thus supporting our general analysis concept (Table 1). Simulation of the tyrosine radical required one nearly axial hfc that accounts for one of the two H(1′) protons (45). As for all β-protons, their hfc values strongly depend on the orientation of the protons with respect to the π-plane of the aromatic ring (46). Here, an angle of 30° has been assumed (47). Finally, one axial and one isotropic hfc tensor that account for tryptophan N(1) and H(5) were included; their values have been taken from the literature (45).

To strengthen our assumption that in *Cra*Cry a tyrosine residue serves as terminal electron donor in FAD photoreduction, we repeated the trEPR experiments with a number of *Cra*Cry point mutants under otherwise identical experimental conditions. In all mutant proteins, redox-inactive phenylalanine residues have been chosen as replacements for tyrosine and/or tryptophan. All mutant proteins have been investigated for comparable stability and correct folding by temperature-dependent fluorescence spectroscopy (see Fig. S4). The resulting trEPR spectra are summarized in Fig. 1 *C* and Fig. 2.

Various *Cra*Cry mutants, namely W376F, W322F, and the double mutant W376F/Y373F, do not show any discernible trEPR signals under the present conditions, thus

TABLE 1 Compilation of Parameters Used to Calculate trEPR Spectra of the Radical Pairs in *Cra*Cry and *Dm*Cry

	*Cra*Cry WT	*Cra*Cry Y373F	*Dm*Cry WT	*Dm*Cry W394F
	FAD	FAD	FAD	FAD
g-tensor				
g_x	2.00435	2.00450	2.00413	2.00413
g_y	2.00370	2.00350	2.00370	2.00370
g_z	2.00220	2.00220	2.00220	2.00220
g_{iso}	2.00342	2.00340	2.00334	2.00334
A(N(5)) / mT				
$A_\parallel$	1.876	2.199	1.933	1.840
$A_\perp$	0.100	0.001	0.015	0.100
A(N(10)) / mT				
$A_\parallel$	0.825		0.997	
$A_\perp$	0.100		0.001	
A(H(8α)) / mT				
A_{iso}	0.380		0.442	
line broadening / mT	0.500	1.067	0.376	1.498
	Y373	W322	W394	W342
g-tensor				
g_x	2.01075	2.00381	2.00449	2.00349
g_y	2.00450	2.00248	2.00258	2.00235
g_z	2.00241	2.00230	2.00216	2.00211
g_{iso}	2.00589	2.00286	2.00308	2.00265
A(H(1′)) / mT				
A_x	2.158		0.050	
A_y	1.992		1.200	
A_z	2.000			
A(N(1)) / mT				
$A_\parallel$			0.050	
$A_\perp$			1.200	
A(H(5)) / mT				
A_{iso}			0.383	
line broadening / mT	0.303	1.020	0.391	1.286
	Radical Pair			
D / mT	–0.285	–0.411	–0.285	–0.491
J / mT	0.002	0.030	0.005	0.015

From Fig. 1.

demonstrating that the bridging tryptophans in the Trp-triad are strictly essential for light-induced ET (Fig. 2). In contrast, substituting phenylalanine for W332, a tryptophan residue that is expected to be located close to W399 and W376 and that could in principle be involved in ET, exhibits a trEPR spectrum similar to that of the WT. Finally, the mutant Y373F exhibits a trEPR signal; however, the spectrum does not show any resolved hyperfine structure and is quite similar in its spectral shape to previously published trEPR data from the Cry-DASH subclade (28,37,38). Spectral simulation using values for W322 (TrpC) as RP partner in a flavin-based radical pair (due to larger D and J values that reflect the shorter distance between the two radicals, all tryptophan hfcs were treated as contributions to inhomogeneous line broadening) fit well with the experimental spectrum (Fig. 1 *B*; Table 1). Respective mutants from the *Dm*Cry protein, *Dm*Cry W394F and W342F, were also investigated under otherwise identical experimental conditions. Although the *Dm*Cry W342F sample did not show any trEPR signal (data not shown), a spectrum similar to the one of *Cra*Cry Y373F was obtained from the *Dm*Cry W394F mutant (Fig. 1 *D*). Again, spectral simulations using the parameters of W342 (TrpC) as electron donor led to very satisfactory agreement with the experiments (*lower panel* of Fig. 1 *D*).

As a first summary, trEPR spectra of WT *Cra*Cry and *Dm*Cry proteins can only be satisfactorily simulated if an aromatic amino acid different from the expected TrpC is taken into account and assumed to act as a terminal electron donor: Y373 in the case of *Cra*Cry and W394 in the case of *Dm*Cry. If these amino acids are replaced with phenylalanine residues, trEPR spectra can nevertheless be detected; however, spectral simulations indicate that TrpC serves as an electron donor in these mutants. On the other hand, disruption of the classical Trp-triad, e.g., by mutating TrpC, inhibits efficient ET in both proteins, and trEPR signals could not be detected.

Transient optical spectroscopy

To yield further insights into the molecular processes upon illumination, we performed TA measurements on *Cra*Cry WT, *Cra*Cry Y373F, and the corresponding *Dm*Cry W394F protein sample; experimental data of *Dm*Cry WT were reproduced from the literature (24). All protein samples were photoexcited, and transient absorbance changes monitored in 4-nm steps over a wavelength range from 370 to 690 nm for either up to 10 μs or up to 10 ms after pulsed laser excitation (full data sets are shown in Fig. S2). Qualitatively, all to date published Cry/Pl difference spectra that were recorded with the flavin being initially fully oxidized, FAD_{ox}, can be divided into different parts, namely a negative band at around 450 nm that has been assigned to FAD_{ox} ground-state bleaching, and positive difference bands in the 375–415 nm and 500–650 nm regions. By global analyses and comparisons with reported spectra (21,23,24,37,48), the difference signals and their kinetics have been assigned to a two-step sequential reaction scheme: a deprotonation of the initially generated (protonated) tryptophanyl radical cation resembles the first species-associated spectrum (SAS) followed by a recombination of the RP2 consisting of $FAD^{\bullet-}$ and (deprotonated) $Trp^{\bullet}$ radicals.

To analyze the spectrum of *Cra*Cry WT, global analysis using an identical kinetic scheme was applied and two SAS (*upper panel* of Fig. 3) with lifetimes of 6 and 26 ms, respectively, were obtained (Table 2). However, both SAS are almost identical despite some minor discrepancies at 390 and 400 nm (see Fig. 3). There is no indication of any $TrpH^{\bullet+}$ deprotonation, which typically exhibits absorption differences at around 550 nm (49). This finding could either be rationalized if an amino acid other than tryptophan acts as terminal electron donor in *Cra*Cry WT, or (more unlikely) if tryptophan deprotonation is too fast for

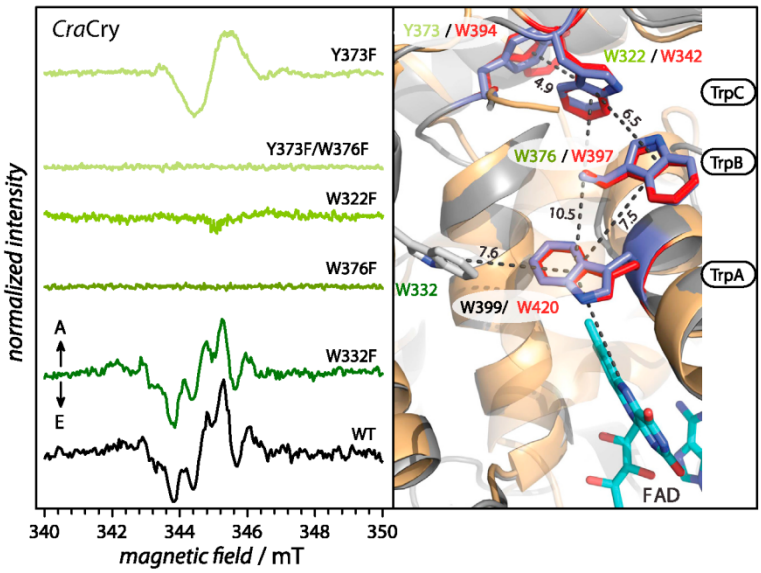

FIGURE 2 TrEPR signals of *Cra*Cry mutants with A and E arrows indicating enhanced absorptive and emissive polarization of resonances, respectively. The experimental WT spectrum is shown in black, spectra of point mutants are shown as a green color gradient, where dark green resembles close and light green a long distance to the FAD cofactor. Spectra were recorded at microwave frequencies of 9.6650 GHz (*Cra*Cry WT), 9.6746 GHz (*Cra*Cry W332F), 9.6748 GHz (*Cra*Cry W376F), 9.6728 GHz (*Cra*Cry W322F), 9.6741 GHz (*Cra*Cry Y373F), and 9.6748 GHz (*Cra*Cry Y373F/W376F), respectively. On the right-hand side, an overlay of the *Dm*Cry structure (42,43) and a *Cra*Cry model structure, including selected residues of the ET pathway, is shown. *Cra*Cry numbering is shown as a green color gradient, *Dm*Cry numbering is shown in red. To see this figure in color, go online.

the time resolution of our TA setup (~5 ns). Consequently, the two mutants *Cra*Cry Y373F and *Dm*Cry W394F were investigated and similar analysis procedures applied (Fig. 3, *second* and *fourth panels*). Again, two SAS, although with different spectra and different lifetimes of 0.48 and 8.46 μs for *Cra*Cry Y373F, and 0.62 and 6.76 μs for *Dm*Cry W394F, were detected. Both more short-lived components have identical broad absorption maxima between 550 and 600 nm, which coincides well with the absorption of a $TrpH^{\bullet+}$ radical species that deprotonates, thus forming RP2. These findings substantiate our notion that in both mutants a tryptophan-based radical is formed upon illumination. It is important to note that in both samples the final component in our model, RP2, decays three orders of magnitude faster as compared to *Cra*Cry WT and *Dm*Cry WT (Table 2).

Steady-state photoreduction of *Cra*Cry

To receive further details of the ET properties of *Cra*Cry under steady-state conditions, photoreduction kinetics were recorded and analyzed (exemplary spectra and kinetics are depicted in Fig. 4, full data sets are depicted as Fig. S3).

By steady-state optical absorption spectroscopy it has been shown previously that *Cra*Cry WT is capable of forming all three biologically relevant FAD redox states, FAD_{ox}, and after blue-light excitation $FADH^{\bullet}$ and $FADH^{-}$ (32). In this contribution, we show that *Cra*Cry WT can be easily reduced to its semiquinone state ($FADH^{\bullet}$) without any reducing agent, such as dithiothreitol (DTT), within a few minutes of blue light illumination, and saturation is reached after ~10 min (Fig. 4, *A* and *F*). Unlike other animal type-1 cryptochromes, *Cra*Cry can be converted to the fully reduced state, $FADH^{-}$, without significant accumulation of an intermediate radical species by adding DTT (Fig. 4 *B*).

To obtain further information on the importance of the Trp-triad for photoreduction, several point mutants were investigated under identical experimental conditions. The distal tryptophan mutant, W322F, which is located close to the protein surface, shows no photoreduction activity even after extended periods of blue light illumination (Fig. 4, *E* and *F*). This lack of photoreduction that is not alleviated by addition of DTT coincides with expectations, as this mutation in the Trp-triad was found to abolish photoreduction completely in other cryptochromes (e.g., (19,24,26,50)). Surprisingly, the medial Trp mutant, W376F, still undergoes photoreduction under the chosen steady-state conditions. Here, formation of the $FADH^{\bullet}$ state proceeds ~20% slower than in the WT (Fig. 4, *E* and *F*). In the presence of DTT, the medial W376F mutant still cannot perform the second reduction step toward $FADH^{-}$, similar to the WT protein, but gets arrested in the $FADH^{\bullet}$ state (Fig. S3). Interestingly, the proximal mutant W399F exhibits also a slight increase of its absorption between 500 and 700 nm upon illumination indicating radical state formation with low efficiency (Fig. 4, *E* and *F*).

Overall, our experiments lead to the assumption that ET in the photoreduction process of *Cra*Cry can occur in vitro via other residues than the conserved Trp-triad. Therefore, the two additional mutants of aromatic residues near the Trp-triad, Y373F and W332F, were also investigated. The photoreduction kinetic of the W332F mutant is fairly similar to that of the WT protein, whereas the tyrosine mutant, Y373F, lacks formation of any flavin radical species even

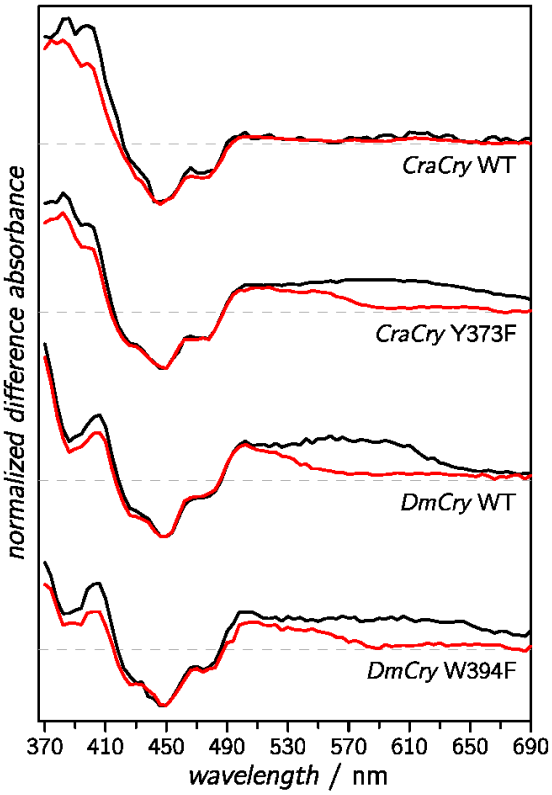

FIGURE 3 Global analyses of transient optical spectra of *Cra*Cry and *Dm*Cry. Species-associated difference spectrum components of RP1 (*black*) and RP2 (*red*) are shown for WT *Cra*Cry and *Cra*Cry Y373F. For comparison, the respective components of WT *Dm*Cry and *Dm*Cry W394F are depicted in the lower panels. To see this figure in color, go online.

after 1 h of blue light illumination (Fig. 4, *E* and *F*). Significant amounts of the neutral radical (including minute amounts of $FADH^-$) can only be generated if 10 mM DTT are added (Fig. S3). Further distortion of the ET pathway by combining the Y373F mutant with the W376F mutant causes a nearly complete loss of photoreduction (Fig. 4, *E* and *F*). These findings show that Y373 and the integrity of the Trp triad are essential for efficient photoreduction, and thus, for any light-induced process in *Cra*Cry.

DISCUSSION

Time-resolved spectroscopic characterization

trEPR spectroscopy has proven to be a valuable tool for the examination of ET pathways in a number of proteins because of its favorable time resolution and spectral sensitivity to molecular properties of the individual RP partner molecules. Hence, it is well suited to gain insight into intraprotein ET processes and their participating amino acids. In detail, trEPR spectra depend on the **g**-tensor, the hfcs, and

TABLE 2 Kinetic Data Extracted from TA Spectra

	Formation of RP2	Decay of RP2
*Cra*Cry WT		
Rate constant/μs^{-1}	$(0.16 \pm 0.04) \times 10^{-3}$	$(0.038 \pm 0.009) \times 10^{-3}$
Lifetime/μs	$(6.1 \pm 1.4) \times 10^{3}$	$(26 \pm 6) \times 10^{3}$
*Cra*Cry Y373F		
Rate constant/μs^{-1}	2.08 ± 0.04	0.118 ± 0.001
Lifetime/μs	0.480 ± 0.008	8.46 ± 0.05
*Dm*Cry WT (24)		
Rate constant/μs^{-1}	0.390 ± 0.009	$(0.147 \pm 0.005) \times 10^{-3}$
Lifetime/ μs	2.56 ± 0.06	$(6.8 \pm 0.3) \times 10^{3}$
*Dm*Cry W394F		
Rate constant/μs^{-1}	1.61 ± 0.05	0.148 ± 0.002
Lifetime/μs	0.620 ± 0.016	6.76 ± 0.09

Rate constants and respective lifetimes for formation and decays of RP2 were extracted from global analyses.

the electron-electron interaction parameters of the paramagnetic species involved. As most of these parameters are orientation-dependent, and their anisotropy does not average out under the present conditions, also spatial information such as the orientation of the radicals with respect to each other, as well as distance estimations can be extracted from spectral simulations. In principle, the amino acids tyrosine and tryptophan exhibit sufficiently different **g**-tensor components to allow for radical discrimination even at X-band microwave frequencies (45), which has been demonstrated on a number of *Xenopus laevis* Cry-DASH mutants (37). However, the spectra of *Cra*Cry and *Dm*Cry presented here are the first ones, to our knowledge, that show pronounced hyperfine patterns, which prevented straightforward assignments to participating radicals exclusively on the basis of their **g**-tensor differences. Consequently, a minimum number of strong hfcs, namely N(5), N(10), and H(8α) for $FAD^{\bullet -}$, N(1) and H(5) for $Trp^{\bullet}$, and H(1′) for $Tyr^{\bullet}$ had to be taken into account to achieve good agreements of experimental data and simulations (Fig. 1; Table 1). Dipolar couplings of −285 μT and exchange interactions of +5 μT for *Dm*Cry and +2 μT for *Cra*Cry, which are far smaller than published values for RPs with TrpC (34,37) (W322 in *Cra*Cry and W342 in *Dm*Cry) and correspond to distances of about ~21.5 Å, complete the necessary fitting parameters for an excellent agreement between experiment and theory. Although structural information is unavailable for *Cra*Cry to date, alignments predict that Y373 is at a similar position as W394 in *Dm*Cry. Nevertheless, this assumption leads to increased uncertainties in the distance and in particular in the orientation parameters of RPs in *Cra*Cry. In addition, it should be noted that the electron-electron interaction parameters that were optimized in the fitting process are just two out of a number of variables, and although many of them (e.g., **g**-tensors and hfcs) are known from independent experiments and had only

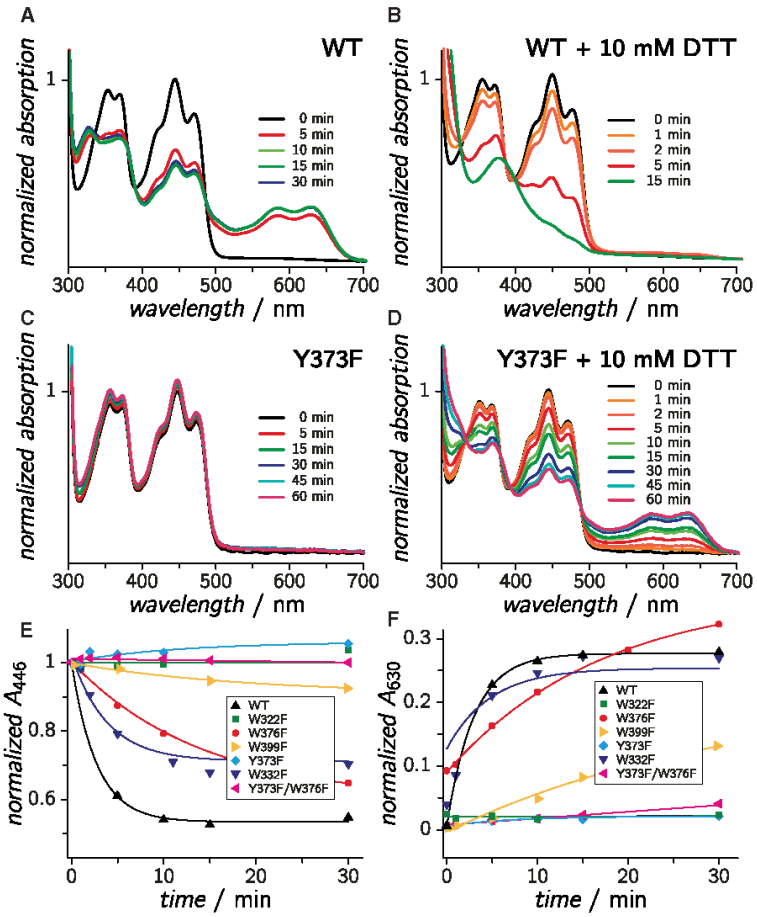

FIGURE 4 Blue light-induced spectral changes in the optical absorptions of WT and mutant *Cra*Crys. Spectral changes in the optical absorptions of WT *Cra*Cry (with or without DTT as the external electron donor) after the indicated illumination times are shown in (*A*) and (*B*), respectively. Spectral changes in the optical absorptions of *Cra*Cry Y373F (with or without DTT) after the indicated illumination times are shown in (*C*) and (*D*), respectively. Absorption changes of all investigated *Cra*Cry samples without DTT, recorded at 446 and 630 nm, are depicted in (*E*) and (*F*). Monoexponential functions have been added as guide to the eye. To see this figure in color, go online.

narrow variability during fitting (see Results section for details), a straightforward error analysis for the derived distance between the radicals in the RP remains almost impossible. However, by manually varying D and J around their optimal values and compensating the resulting changes by spectral line width while keeping all other parameters constant, we are confident that our values are trustworthy within a distance uncertainty of ~1 Å.

Bringing together the remarkably pronounced hyperfine structures and the weak electron-electron interactions led us to the conclusion that in both Crys not TrpC but more distant aromatic amino acids must serve as terminal electron donors. To corroborate this notion on the basis of our trEPR data on the WT proteins, additional experiments were carried out with a number of *Cra*Cry and *Dm*Cry point mutants. Whereas mutants of tryptophans within the conserved Trp-triad did not show any signal at all, the replacement of Y373/W394 lead to a trEPR signature that can be simulated using parameters of a flavin-based radical pair with TrpC (W322/W342, Fig. 1, *B* and *D*), as a terminal electron donor. Consistent results were obtained from transient optical absorption spectroscopy: in contrast to the *Cra*Cry WT protein, a tryptophan deprotonation process could be identified in *Cra*Cry Y373F and in *Dm*Cry W394F mutants (Fig. 3). Although the characteristic rates of this process in the two mutants are very similar, a difference of a factor of ~1000 when compared to the respective WT proteins shows that both RP2s are much more short-lived (Table 2). This finding can be rationalized by the reduced surface exposure of residues W322 and W342: Formation of RP2 requires a proton acceptor close to the tryptophan, but neither an amino acid that could serve as proton acceptor nor pockets that could harbor water molecules can be found in the direct vicinity of TrpC. Therefore, direct recombination of RP1 back to the ground state is favored in these mutants.

Taken together, all experimental data point toward an aromatic amino acid that extends the conserved Trp-triad to a tetrad and is the terminal electron donor in *Cra*Cry and *Dm*Cry. There is one question which arises, and that is

why there is no sign of a tyrosine radical observed in the difference TA data from the *Cra*Cry WT. In principle, a tyrosine radical should show absorptions at around 400 nm (51); however, only minute differences in absorption could be detected in this spectral region (*upper panel* of Fig. 3). One possible explanation is that overlapping difference absorptions from the FAD obscure positive absorptions that are expected for $Tyr^{\bullet}$ formation, in particular as the absorption coefficient of a $Tyr^{\bullet}$, which is around 2 $Lmmol^{-1}cm^{-1}$ (51), is far smaller than that of FAD.

Similarities and differences of *Cra*Cry and *Dm*Cry and their implications for photoreceptor functions

Although the two cryptochromes investigated in this spectroscopic study belong to the same animal (and animal-like) Cry subclade, their proposed functions differ significantly. Therefore, it is surprising that both proteins use an identical tetrad of aromatic amino acids for RP formation and/or flavin photoreduction. Both proteins exhibit fast steady-state photoreduction properties. However, in contrast to *Dm*Cry (24), the FAD in *Cra*Cry can be easily converted into the fully reduced state via the neutral $FADH^{\bullet}$ state (32). In addition, our steady-state photoreduction data show that *Cra*Cry exerts some light-driven electron transfer, when either the proximal or medial tryptophan has been mutated, although only to the radical $FADH^{\bullet}$ state. In this way, *Cra*Cry contrasts *Dm*Cry, where corresponding mutations (W420F, W397F) cause a complete loss of the formation of its signaling active $FAD^{\bullet-}$state (42,52). Complete loss of photoactive behavior can only be achieved in *Cra*Cry by mutation of the distal tryptophan of the Trp-triad, W322. This residue is supposed to be the terminal electron donor (TrpC) of the ET pathway in most other Crys and Pls. This result raises the question, whether there are other determinants for ET in *Cra*Cry apart from the different photochemistry, i.e., formation of $FAD^{\bullet-}$ in *Dm*Cry and $FADH^{\bullet}$ or $FADH^{-}$ in *Cra*Cry, which may allow partial bypassing of the Trp-triad. Among the candidate residues, W332 and Y373, we found that W332, a candidate for an ET side branch, caused only minute effects on the photochemistry of *Cra*Cry, whereas replacement of Y373 abolishes intramolecular ET in the absence of an exogenous reductant. In a model of the *Cra*Cry structure, this residue is only ~4.9 Å distant from W322 and apparently elongates thereby the ET chain of the Trp triad (*right panel* of Fig. 2). The ability of the Y373F mutant to undergo photoreduction in the presence of DTT to the semiquinoid redox state indicates that the remaining Trp-triad is operational as long as the distal tryptophan can be reduced by a reductant during the μs-lifetime of the RP. However, one has to note that further reduction to the fully reduced $FADH^{-}$ state is not possible in the Y373F mutant. One possible explanation is that RP recombination after excitation of the $FADH^{\bullet}$ cofactor outpaces ET from the exogenous reductant to the distal tryptophan W322. A similar inability to perform the second photoreduction step from $FADH^{\bullet}$ to $FADH^{-}$ has been found for the medial tryptophan mutant W376F. In this mutant, excitation of FAD_{ox} under steady-state conditions allows some electron transfer, presumably from the distal tryptophan and the nearby essential residue Y373, but again, no formation of the fully reduced $FADH^{-}$ state can be detected. In this context, it is noteworthy that in some members of the Cry/Pl family, the ET pathway can differ from the conserved Trp-triad (14,28), or use other aromatic residues as side branches, as shown for the *Methanosarcina mazei* class II photolyase (53).

In summary, the length of the ET cascade of *Cra*Cry and *Dm*Cry is extended by ~2 Å; however, steady-state reduction of the FAD cofactor seems to be equally efficient. It should also be mentioned at this point that appearance and kinetics of TA and/or trEPR spectra cannot be directly correlated to steady-state photoreduction kinetics as their experimental conditions are different. Yet, the terminal electron donor is different in both proteins: a tyrosine residue that forms a RP with a pronounced lifetime of 26 ms has been observed in *Cra*Cry. This finding shows that not only tryptophan residues are able to stabilize RP2 within a ms-lifetime, but also tyrosine residues may fulfill this function. Unfortunately, no information on the protonation state of the $Tyr^{\bullet}$ radical can be obtained from our TA and trEPR data as *g*-values, electron-spin density distributions (and hence, hyperfine couplings) and optical absorptions are rather similar for $Tyr^{\bullet}$ and $Tyr^{\bullet+}$ (45). Nevertheless, it can be summarized that both proteins show a surprisingly similar behavior after light excitation.

Are there any advantages for animal Cry function if ET occurs via a Trp/Tyr-tetrad and not via the normal Trp-triad? In principle, the Trp/Tyr-tetrad could be an evolutionary improvement because in animal Crys TrpC is not as surface-exposed as in other proteins of the Cry/Pl family. Here, structural information on *Cra*Cry would definitely help to support (or disprove) the argument. Furthermore, the direct consequences of the Trp/Tyr-tetrad for *Cra*Cry function remain vague. Because the protein is supposed to be involved in red-light photoreception (32), both the FAD_{ox} state and the $FAD^{\bullet-}/Tyr^{\bullet}$ RP may not be the primary light-absorbing states as none of these absorbs in the red-light region. Either the involvement of a second protein that absorbs in this range or the $FADH^{\bullet}$ being the dark state of the photoreceptor seem conceivable for red-light photoreception.

On the other hand, significant consequences are expected for the proposed magnetoreceptor function of *Dm*Cry. In principle, the distance between the RP partners determines the spin-spin coupling parameters. Together with the strengths and anisotropies of hfcs they directly influence the singlet-to-triplet mixing rate, which is crucial for the ability of a molecule to sense magnetic fields (54–57).

Therefore, it is conspicuous that a fourth tryptophan with a different distance and orientation with respect to the flavin differentiates animal Crys from other proteins of the Pl/Cry family. This finding becomes even more important as most calculations of magnetic field effects in Crys have been performed using parameters of a flavin-TrpC radical pair derived from the classical Trp-triad (e.g., (58,59)). Therefore, it will be intriguing to see how altered distance/orientation parameters of the fourth tryptophan—from now on named TrpD—affect the magnetic field effects of light-induced RPs in *Dm*Cry.

CONCLUSIONS

In this contribution, we describe how molecular spectroscopy corroborated by spectral simulations leads to a detailed picture of the ET pathways and photochemical processes in two animal (and animal-like) Crys upon blue-light excitation. Time-resolved spectroscopy with optical detection unravels aspects of the photochemistry, such as rate constants for the decay and transformations of involved radicals. Spectral simulations of trEPR data are well suited not only to distinguish between tryptophan-based and tyrosine-based RPs, but also to allow extracting structural information such as the distances between the RP partners. Therefore, the combination of the two techniques is crucial to obtain a clear picture of light-induced reactions in Crys.

Both Crys show ET along the conserved Trp-triad. However, a fourth aromatic amino acid residue extends this pathway. Whereas a tyrosine residue serves as a surface-exposed terminal electron donor in *Cra*Cry, a tryptophan is found for *Dm*Cry. When the respective fourth aromatic amino acids are exchanged to phenylalanines, RPs with similar TA/trEPR spectra as compared to published FAD-TrpC RPs are detected in both proteins (37); however, their lifetimes are drastically reduced as compared to those of the WT. On the other hand, if TrpC or TrpB are mutated, RP signatures could not be detected, which demonstrates the importance of the Trp-triad in these proteins for efficient ET.

SUPPORTING MATERIAL

Four figures are available at http://www.biophysj.org/biophysj/supplemental/S0006-3495(16)30442-8.

AUTHOR CONTRIBUTIONS

D.N., S.F., R.R., and B.P. gathered and analyzed the data. D.N. and B.P simulated the time-resolved spectroscopic data. S.F. and R.R. produced the samples. D.N., S.F., R.R., B.P., L.-O.E., S.W., and E.S. discussed the data, their interpretation and presentation. L.-O.E., S.W., and E.S. conceived and designed the study. E.S. coordinated the experiments. L.-O.E., S.W., and E.S. wrote the article.

ACKNOWLEDGMENTS

E.S. and S.W. were supported by the Deutsche Forschungsgemeinschaft (DFG RTG1976, project P13), L.-O.E. was supported by the Deutsche Forschungsgemeinschaft (ES152/12-1) and the AFOSR (FA9550-14-1-0409). The authors thank Maria Mittag for providing the original *Cra*Cry plasmid.

REFERENCES

1. Losi, A., and W. Gärtner. 2012. The evolution of flavin-binding photoreceptors: an ancient chromophore serving trendy blue-light sensors. *Annu. Rev. Plant Biol.* 63:49–72.
2. Chaves, I., R. Pokorny, …, M. Ahmad. 2011. The cryptochromes: blue light photoreceptors in plants and animals. *Annu. Rev. Plant Biol.* 62:335–364.
3. van der Horst, G. T. J., M. Muijtjens, …, A. Yasui. 1999. Mammalian Cry1 and Cry2 are essential for maintenance of circadian rhythms. *Nature.* 398:627–630.
4. Stanewsky, R., M. Kaneko, …, J. C. Hall. 1998. The *cry^{b}* mutation identifies cryptochrome as a circadian photoreceptor in *Drosophila*. *Cell.* 95:681–692.
5. Maeda, K., A. J. Robinson, …, P. J. Hore. 2012. Magnetically sensitive light-induced reactions in cryptochrome are consistent with its proposed role as a magnetoreceptor. *Proc. Natl. Acad. Sci. USA.* 109:4774–4779.
6. Ritz, T., S. Adem, and K. Schulten. 2000. A model for photoreceptor-based magnetoreception in birds. *Biophys. J.* 78:707–718.
7. Mouritsen, H., and T. Ritz. 2005. Magnetoreception and its use in bird navigation. *Curr. Opin. Neurobiol.* 15:406–414.
8. Gegear, R. J., A. Casselman, …, S. M. Reppert. 2008. Cryptochrome mediates light-dependent magnetosensitivity in *Drosophila*. *Nature.* 454:1014–1018.
9. Kennedy, M. J., R. M. Hughes, …, C. L. Tucker. 2010. Rapid blue-light-mediated induction of protein interactions in living cells. *Nat. Methods.* 7:973–975.
10. Bugaj, L. J., A. T. Choksi, …, D. V. Schaffer. 2013. Optogenetic protein clustering and signaling activation in mammalian cells. *Nat. Methods.* 10:249–252.
11. Zoltowski, B. D., and K. H. Gardner. 2011. Tripping the light fantastic: blue-light photoreceptors as examples of environmentally modulated protein-protein interactions. *Biochemistry.* 50:4–16.
12. Müller, M., and T. Carell. 2009. Structural biology of DNA photolyases and cryptochromes. *Curr. Opin. Struct. Biol.* 19:277–285.
13. Paulus, B., C. Bajzath, …, E. Schleicher. 2013. Flavoproteins and blue light reception in plants. *In* Handbook of Flavoproteins. Vol. 2: Complex Flavoproteins, Dehydrogenases and Physical Methods. R. Hille, S. Miller, and B. Palfey, editors. Walter de Gruyter GmbH, Berlin/Boston, pp. 361–392.
14. Geisselbrecht, Y., S. Frühwirth, …, L.-O. Essen. 2012. CryB from *Rhodobacter sphaeroides*: a unique class of cryptochromes with new cofactors. *EMBO Rep.* 13:223–229.
15. Mei, Q., and V. Dvornyk. 2015. Evolutionary history of the photolyase/cryptochrome superfamily in eukaryotes. *PLoS ONE.* 10:e0135940.
16. Bouly, J.-P., E. Schleicher, …, M. Ahmad. 2007. Cryptochrome blue light photoreceptors are activated through interconversion of flavin redox states. *J. Biol. Chem.* 282:9383–9391.
17. Banerjee, R., E. Schleicher, …, A. Batschauer. 2007. The signaling state of *Arabidopsis* cryptochrome 2 contains flavin semiquinone. *J. Biol. Chem.* 282:14916–14922.
18. Berndt, A., T. Kottke, …, E. Wolf. 2007. A novel photoreaction mechanism for the circadian blue light photoreceptor *Drosophila* cryptochrome. *J. Biol. Chem.* 282:13011–13021.
19. Hoang, N., E. Schleicher, …, M. Ahmad. 2008. Human and *Drosophila* cryptochromes are light activated by flavin photoreduction in living cells. *PLoS Biol.* 6, e160.1559-e1160.1569.

20. Aubert, C., M. H. Vos, …, K. Brettel. 2000. Intraprotein radical transfer during photoactivation of DNA photolyase. *Nature*. 405:586–590.
21. Henbest, K. B., K. Maeda, …, E. Schleicher. 2008. Magnetic-field effect on the photoactivation reaction of *Escherichia coli* DNA photolyase. *Proc. Natl. Acad. Sci. USA*. 105:14395–14399.
22. Li, Y. F., P. F. Heelis, and A. Sancar. 1991. Active site of DNA photolyase: tryptophan-306 is the intrinsic hydrogen atom donor essential for flavin radical photoreduction and DNA repair in vitro. *Biochemistry*. 30:6322–6329.
23. Giovani, B., M. Byrdin, …, K. Brettel. 2003. Light-induced electron transfer in a cryptochrome blue-light photoreceptor. *Nat. Struct. Biol.* 10:489–490.
24. Paulus, B., C. Bajzath, …, E. Schleicher. 2015. Spectroscopic characterization of radicals and radical pairs in fruit fly cryptochrome - protonated and nonprotonated flavin radical-states. *FEBS J.* 282: 3175–3189.
25. Liu, B., H. Liu, …, C. Lin. 2010. Searching for a photocycle of the cryptochrome photoreceptors. *Curr. Opin. Plant Biol.* 13:578–586.
26. Oztürk, N., S.-H. Song, …, A. Sancar. 2008. Animal type 1 cryptochromes. Analysis of the redox state of the flavin cofactor by site-directed mutagenesis. *J. Biol. Chem.* 283:3256–3263.
27. Ozturk, N., C. P. Selby, …, A. Sancar. 2011. Reaction mechanism of *Drosophila* cryptochrome. *Proc. Natl. Acad. Sci. USA*. 108:516–521.
28. Biskup, T., K. Hitomi, …, S. Weber. 2011. Unexpected electron transfer in cryptochrome identified by time-resolved EPR spectroscopy. *Angew. Chem. Int. Ed. Engl.* 50:12647–12651.
29. Müller, P., J. Yamamoto, …, K. Brettel. 2015. Discovery and functional analysis of a 4th electron-transferring tryptophan conserved exclusively in animal cryptochromes and (6-4) photolyases. *Chem. Commun. (Camb.).* 51:15502–15505.
30. Collins, B., E. O. Mazzoni, …, J. Blau. 2006. *Drosophila* CRYPTOCHROME is a circadian transcriptional repressor. *Curr. Biol.* 16:441–449.
31. Marley, R., C. N. G. Giachello, …, A. R. Jones. 2014. Cryptochrome-dependent magnetic field effect on seizure response in Drosophila larvae. *Sci. Rep.* 4:5799.
32. Beel, B., K. Prager, …, M. Mittag. 2012. A flavin binding cryptochrome photoreceptor responds to both blue and red light in *Chlamydomonas reinhardtii*. *Plant Cell*. 24:2992–3008.
33. Forneris, F., R. Orru, …, A. Mattevi. 2009. ThermoFAD, a Thermofluor-adapted flavin ad hoc detection system for protein folding and ligand binding. *FEBS J.* 276:2833–2840.
34. Weber, S., T. Biskup, …, J. R. Norris, Jr. 2010. Origin of light-induced spin-correlated radical pairs in cryptochrome. *J. Phys. Chem. B.* 114:14745–14754.
35. Snellenburg, J. J., S. P. Laptenok, …, I. H. M. van Stokkum. 2012. Glotaran: a Java-based graphical user interface for the R package TIMP. *J. Stat. Softw.* 49:1–22.
36. Bittl, R., and S. Weber. 2005. Transient radical pairs studied by time-resolved EPR. *Biochim. Biophys. Acta*. 1707:117–126.
37. Biskup, T., B. Paulus, …, E. Schleicher. 2013. Variable electron transfer pathways in an amphibian cryptochrome: tryptophan versus tyrosine-based radical pairs. *J. Biol. Chem.* 288:9249–9260.
38. Biskup, T., E. Schleicher, …, S. Weber. 2009. Direct observation of a photoinduced radical pair in a cryptochrome blue-light photoreceptor. *Angew. Chem. Int. Ed. Engl.* 48:404–407.
39. Weber, S., C. W. M. Kay, …, T. Todo. 2002. Photoactivation of the flavin cofactor in *Xenopus laevis* (6 - 4) photolyase: observation of a transient tyrosyl radical by time-resolved electron paramagnetic resonance. *Proc. Natl. Acad. Sci. USA*. 99:1319–1322.
40. Engelhard, C., X. Wang, …, M. Ahmad. 2014. Cellular metabolites enhance the light sensitivity of *Arabidopsis* cryptochrome through alternate electron transfer pathways. *Plant Cell*. 26:4519–4531.
41. Vaidya, A. T., D. Top, …, B. R. Crane. 2013. Flavin reduction activates *Drosophila* cryptochrome. *Proc. Natl. Acad. Sci. USA*. 110:20455–20460.
42. Czarna, A., A. Berndt, …, E. Wolf. 2013. Structures of *Drosophila* cryptochrome and mouse cryptochrome1 provide insight into circadian function. *Cell*. 153:1394–1405.
43. Levy, C., B. D. Zoltowski, …, D. Leys. 2013. Updated structure of *Drosophila* cryptochrome. *Nature*. 495:E3–E4.
44. Okafuji, A., A. Schnegg, …, S. Weber. 2008. G-tensors of the flavin adenine dinucleotide radicals in glucose oxidase: a comparative multifrequency electron paramagnetic resonance and electron-nuclear double resonance study. *J. Phys. Chem. B*. 112:3568–3574.
45. Bleifuss, G., M. Kolberg, …, F. Lendzian. 2001. Tryptophan and tyrosine radicals in ribonucleotide reductase: a comparative high-field EPR study at 94 GHz. *Biochemistry*. 40:15362–15368.
46. McConnell, H. M. 1956. Indirect hyperfine interaction in the paramagnetic resonance spectra of aromatic radicals. *J. Chem. Phys.* 24: 764–766.
47. Un, S. 2005. The *g*-values and hyperfine coupling of amino acid radicals in proteins: comparison of experimental measurements with ab initio calculations. *Magn. Reson. Chem.* 43:S229–S236.
48. Langenbacher, T., D. Immeln, …, T. Kottke. 2009. Microsecond light-induced proton transfer to flavin in the blue light sensor plant cryptochrome. *J. Am. Chem. Soc.* 131:14274–14280.
49. Bent, D. V., and E. Hayon. 1975. Excited state chemistry of aromatic amino acids and related peptides. III. Tryptophan. *J. Am. Chem. Soc.* 97:2612–2619.
50. Zeugner, A., M. Byrdin, …, M. Ahmad. 2005. Light-induced electron transfer in *Arabidopsis* cryptochrome-1 correlates with in vivo function. *J. Biol. Chem.* 280:19437–19440.
51. Bent, D. V., and E. Hayon. 1975. Excited state chemistry of aromatic amino acids and related peptides. I. Tyrosine. *J. Am. Chem. Soc.* 97:2599–2606.
52. Azarkh, M., and E. J. J. Groenen. 2015. Simulation of multi-frequency EPR spectra for a distribution of the zero-field splitting. *J. Magn. Reson.* 255:106–113.
53. Kiontke, S., Y. Geisselbrecht, …, L.-O. Essen. 2011. Crystal structures of an archaeal class II DNA photolyase and its complex with UV-damaged duplex DNA. *EMBO J.* 30:4437–4449.
54. Schulten, K. 1982. Magnetic field effects in chemistry and biology. *In* Festkörperprobleme. J. Treusch, editor. Vieweg, Braunschweig, pp. 61–83.
55. Rodgers, C. T., and P. J. Hore. 2009. Chemical magnetoreception in birds: the radical pair mechanism. *Proc. Natl. Acad. Sci. USA*. 106:353–360.
56. Efimova, O., and P. J. Hore. 2008. Role of exchange and dipolar interactions in the radical pair model of the avian magnetic compass. *Biophys. J.* 94:1565–1574.
57. Zhang, Y., G. P. Berman, and S. Kais. 2015. The radical pair mechanism and the avian chemical compass: quantum coherence and entanglement. *Int. J. Quantum Chem.* 115:1327–1341.
58. Lee, A. A., J. C. S. Lau, …, P. J. Hore. 2014. Alternative radical pairs for cryptochrome-based magnetoreception. *J. R. Soc. Interface*. 11:20131063.
59. Solov'yov, I. A., D. E. Chandler, and K. Schulten. 2007. Magnetic field effects in *Arabidopsis thaliana* cryptochrome-1. *Biophys. J.* 92:2711–2726.

Extended Electron-Transfer Pathways in Animal Cryptochromes Mediated by a Tetrad of Aromatic Amino Acids

-Supporting Information-

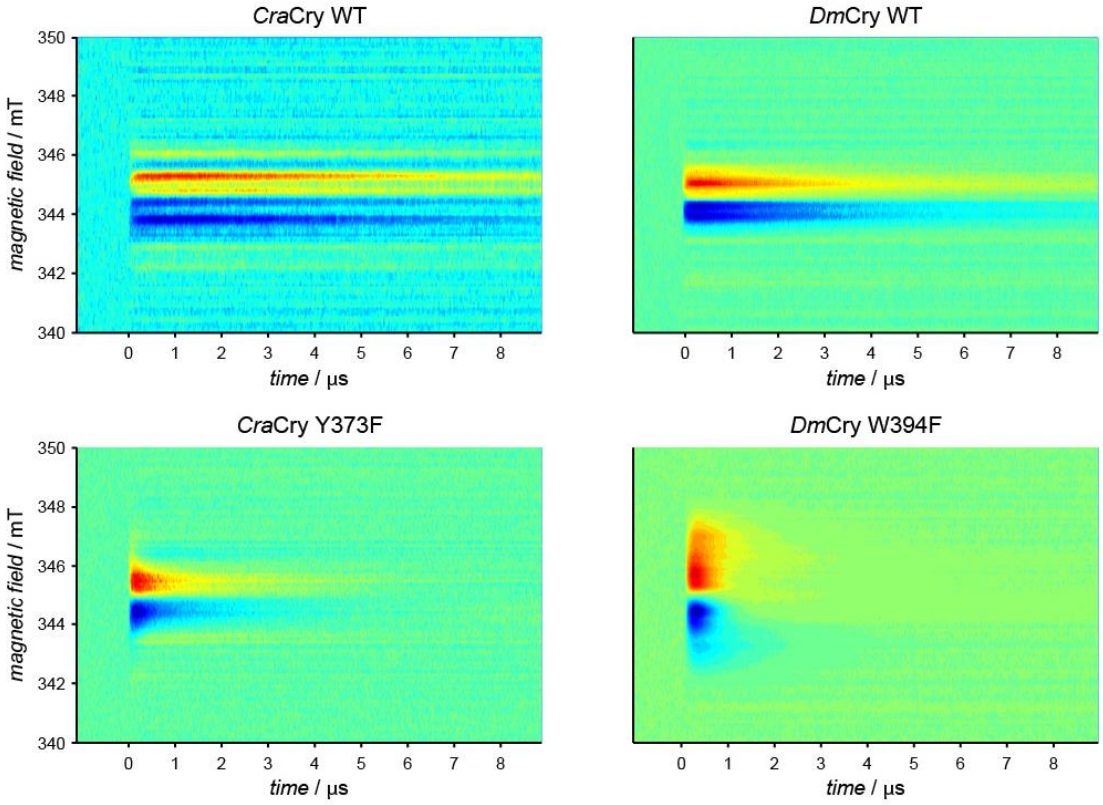

Supporting Figure 1: Complete trEPR data set of *Cra*Cry WT, *Cra*Cry Y373F, *Dm*Cry WT and *Dm*Cry W394F measured at 270 K.
Each time profile is the average of 100 acquisitions recorded with a laser pulse repetition rate of 1 Hz, a microwave frequency of 9.68 GHz, and a power of 2 mW at a detection bandwidth of 25 MHz. A: enhanced absorption; E: emission.

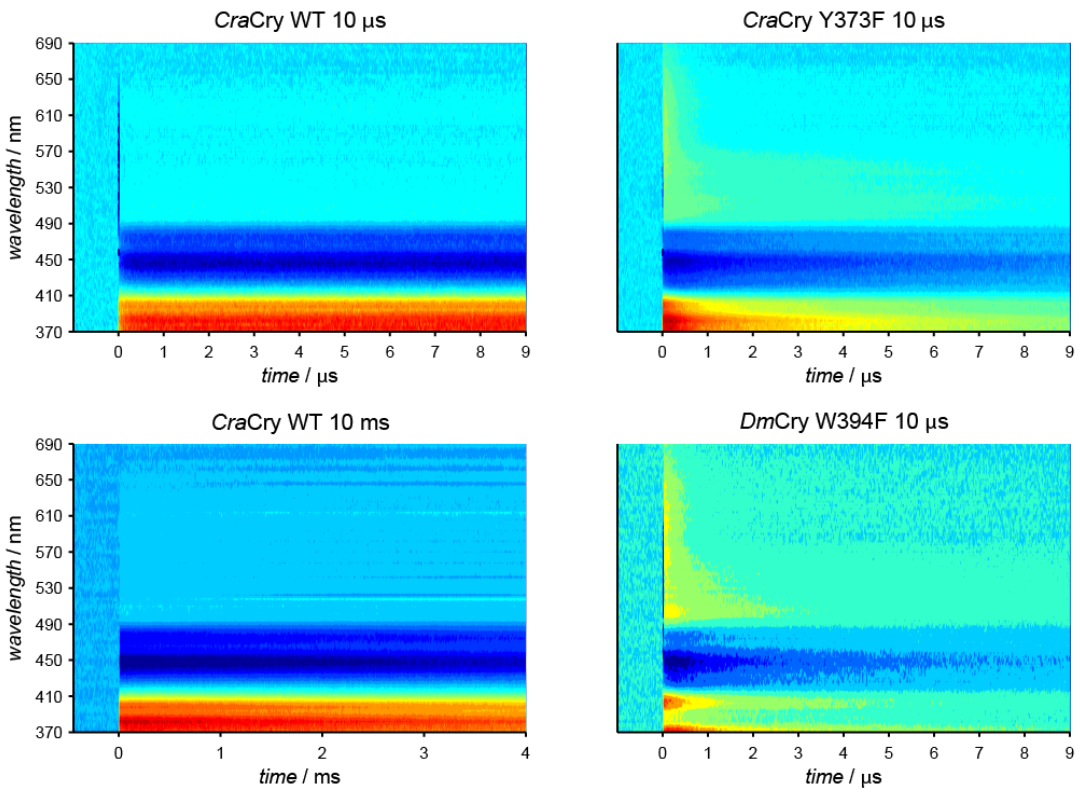

Supporting Figure 2: Transient optical spectroscopy of *Cra*Cry WT, *Cra*Cry Y373F, and *Dm*Cry W394F. Full 2-dimensional plots recorded at different time windows (from 10 µs up to 10 ms) with a laser pulse power of 4 mJ and a repetition rate of 6.67 mHz. Three accumulations have been averaged.

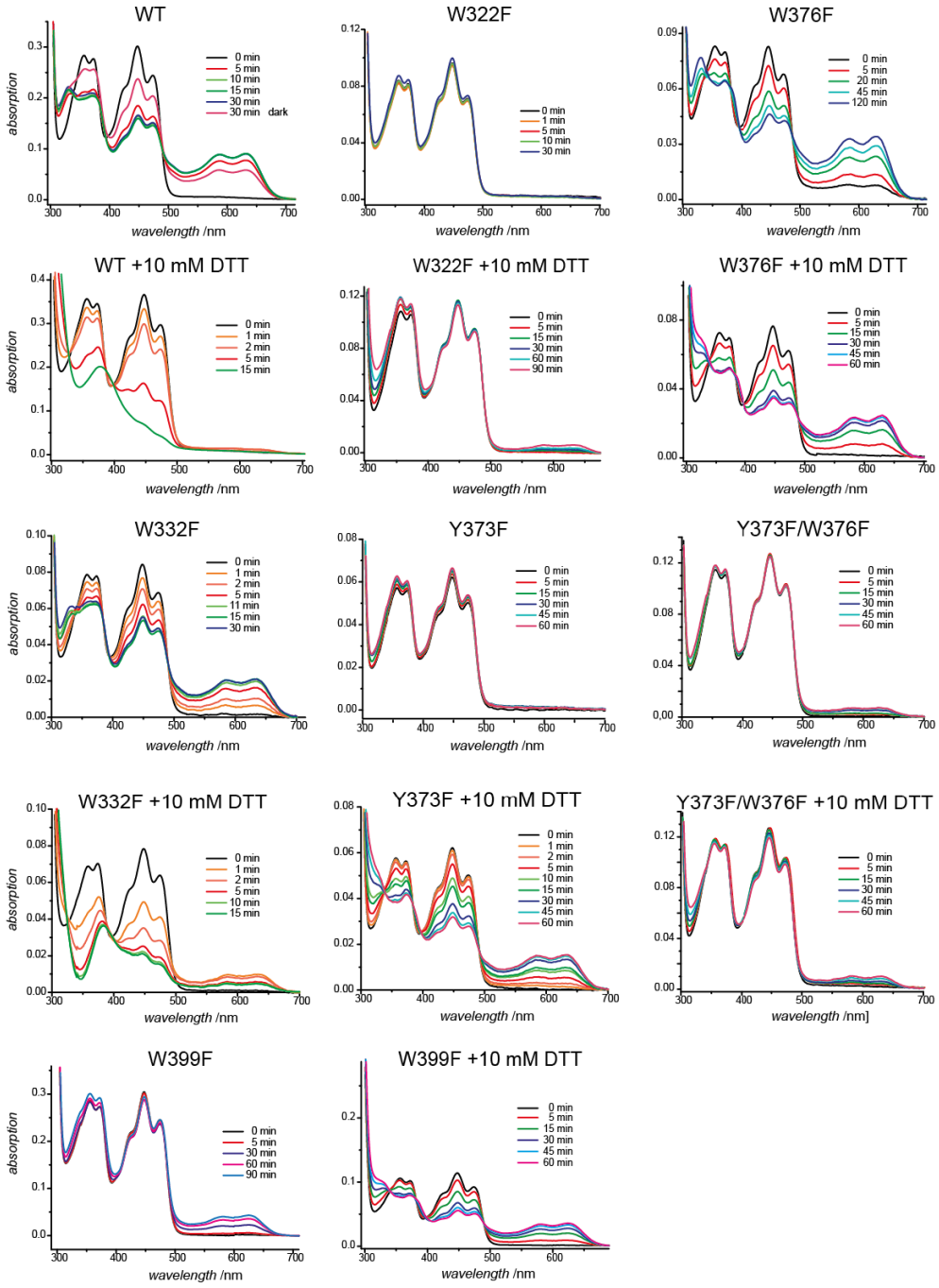

Supporting Figure 3: Blue-light induced spectral changes in the optical absorptions of WT and mutant *Cra*Crys in the absence and presence of DTT as reduction agent. All measurements were performed under aerobic conditions.

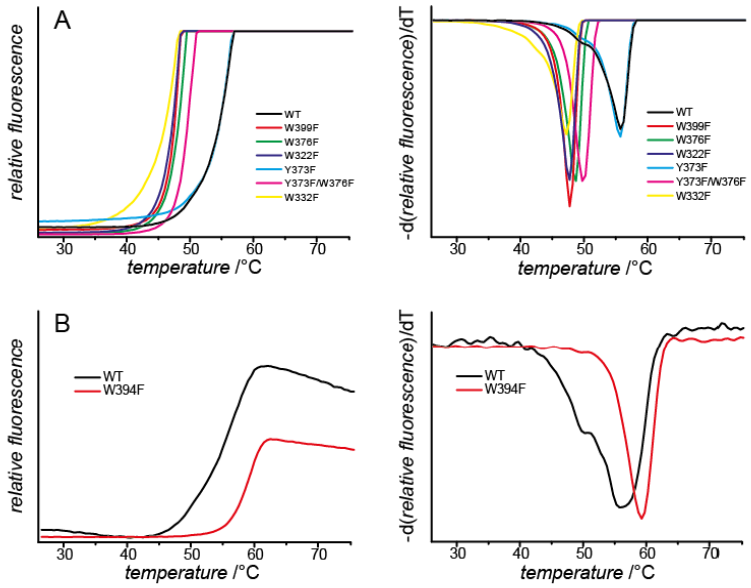

Supporting Figure 4: Thermo fluorescence measurements of *Cra*Cry (A) and *Dm*Cry (B) together with its derivation. For excitation a wavelength range between 470 and 480 nm was chosen and for detection of the FAD fluorescence a green emission filter (510–515 nm) was used. For controlled melting of the protein, the temperature was increased from 25–99 °C in 0.5 °C steps.

4.2 Long-lived Tyrosyl radical under observation

This research was originally published in the Journal of Biological Chemistry by *Sabine Oldemeyer, Sophie Franz, Sandra Wenzel, Lars-Oliver Essen, Maria Mittag, and Tilman Kottke**. **Essential Role of an Unusually Long-Lived Tyrosyl Radical in the Response to Red Light of the Animal-Like Cryptochrome aCRY.** J Biol Chem. 2016; 291 (*27*): 14062-14071.

Summary

This study is focusing on characterization of *Cr*aCRY and several mutants in regard to the red light activity shown by Beel *et al.* (233) and Spexard *et al.* (286). Therefore time-resolved UV/Vis spectroscopy as well as analytical size exclusion chromatography was used. The FAD in the purified protein is present in its oxidized state. For photoreduction, the protein sample was treated with blue light for 5 s to gain the semiquinone FADH°, following a red light laser pulse (630 nm) to achieve the hydroquinone $FADH^-$. The conversion to the latter was followed with time-resolved UV/Vis spectroscopy and besides the absorption peaks characteristic for $FADH^-$, the typical absorption for a tyrosyl radical could be observed, which disappears within a few seconds. By kinetic analysis, the lifetime of the Tyr° as well as of $FADH^-$ was determined to 2.6 s. To verify which tyrosine forms the radical, two mutants were tested. Whereas Y393A did not exhibit any change compared to the WT spectra, Y373F demonstrated some significant change in light sensitivity and Y373 was identified as the residue forming the long-lived radical state.

Another part of this publication is dealing with the oligomerization state of *Cr*aCRY and its dependence on the redox state of the flavin. This was studied using analytical size exclusion chromatography. Therefore all samples were pre-illuminated with BL to convert the FAD to its semiquinone state and the absorbance at 630 nm was detected. For the WT the formation of a dimer was shown, while the truncated variant ΔCTE, which is missing the C-terminal extension, is running as a monomer on the gel filtration column. This leads to the assumption, that the CTE is crucial for dimerization of *Cr*aCRY. Another mutant, C482A, which changed a cysteine residue in close proximity of the Y373 to an alanine, is also running as a dimer like the WT. If all these *Cr*aCRY variants are treated with red light and the

absorbance at 370 nm is detected, the proteins that are in the fully reduced state can be observed. In the WT as well as in the truncated ΔCTE this leads to the appearance of a shoulder at a shorter elution volume, while in C482A no change of the elution profile can be detected. This led to the conclusion, that the cysteine is involved in the light-dependent oligomerization of the cryptochrome, maybe by forming a disulfide bridge to another *Cra*CRY monomer or dimer. Nevertheless, this can only be a side reaction *in vitro* at high protein concentration as only a minor part of the protein sample is engaging in oligomerization. It is rather unlikely that this form of CRY-complex plays any physiological role in the signaling pathway.

Also FOURIER-transform infrared spectroscopy (FTIR) of the *Cra*CRY-ΔCTE was performed and compared to the WT spectra published in Spexard *et al.* (286). In the FTIR of the truncated variant no significant differences to the WT spectra could be observed. Consequently, the differences in the FTIR bands upon light illumination point to a change in the photolyase homology region not involving the CTE.

Contributions

T. Kottke, M. Mittag and L.-O. Essen designed the study. S. Oldemeyer performed and analyzed all the experiments with advice by T. Kottke. S. Franz and S. Wenzel generated plasmids of aCRY variants. S. Oldemeyer and T. Kottke wrote the manuscript with advice by S. Franz, S. Wenzel, L.-O. Essen and M. Mittag. All authors reviewed the results and approved the final version of the manuscript.

THE JOURNAL OF BIOLOGICAL CHEMISTRY VOL. 291, NO. 27, pp. 14062–14071, July 1, 2016

Essential Role of an Unusually Long-lived Tyrosyl Radical in the Response to Red Light of the Animal-like Cryptochrome aCRY*[S]

Received for publication, March 11, 2016, and in revised form, April 29, 2016 Published, JBC Papers in Press, May 9, 2016, DOI 10.1074/jbc.M116.726976

Sabine Oldemeyer[‡], Sophie Franz[§], Sandra Wenzel[¶], Lars-Oliver Essen[§], Maria Mittag[¶], and Tilman Kottke[‡1]

From the [‡]Physical and Biophysical Chemistry, Department of Chemistry, Bielefeld University, Universitätsstr. 25, 33615 Bielefeld, [§]Structural Biochemistry, Department of Chemistry, Philipps University Marburg, Hans-Meerwein Straβe 4, 35039 Marburg, and [¶]Institute of General Botany and Plant Physiology, Friedrich Schiller University, Am Planetarium 1, 07743 Jena, Germany

Cryptochromes constitute a group of flavin-binding blue light receptors in bacteria, fungi, plants, and insects. Recently, the response of cryptochromes to light was extended to nearly the entire visible spectral region on the basis of the activity of the animal-like cryptochrome aCRY in the green alga *Chlamydomonas reinhardtii*. This finding was explained by the absorption of red light by the flavin neutral radical as the dark state of the receptor, which then forms the anionic fully reduced state. In this study, time-resolved UV-visible spectroscopy on the full-length aCRY revealed an unusually long-lived tyrosyl radical with a lifetime of 2.6 s, which is present already 1 μs after red light illumination of the flavin radical. Mutational studies disclosed the tyrosine 373 close to the surface to form the long-lived radical and to be essential for photoreduction. This residue is conserved exclusively in the sequences of other putative aCRY proteins distinguishing them from conventional (6–4) photolyases. Size exclusion chromatography showed the full-length aCRY to be a dimer in the dark at 0.5 mM injected concentration with the C-terminal extension as the dimerization site. Upon illumination, partial oligomerization was observed via disulfide bridge formation at cysteine 482 in close proximity to tyrosine 373. The lack of any light response in the C-terminal extension as evidenced by FTIR spectroscopy differentiates aCRY from plant and *Drosophila* cryptochromes. These findings imply that aCRY might have evolved a different signaling mechanism via a light-triggered redox cascade culminating in photooxidation of a yet unknown substrate or binding partner.

Cryptochromes represent a group of diverse sensory photoreceptors present in all kingdoms of life (1, 2). Together with the UV-light-dependent DNA repair enzymes, the photolyases (3), they constitute the cryptochrome/photolyase family. Members of this family share a highly conserved photolyase homology region (PHR)[2], which comprises ~500 amino acids and carries a non-covalently bound flavin adenine dinucleotide (FAD) as a chromophore. The C-terminal extension (CCT) present in many cryptochromes and photolyases is strongly variable in amino acid composition and length and has been shown to be crucial for signal transduction in the *Arabidopsis* cryptochrome *At*CRY1 (4). The diverse subfamilies of cryptochromes comprise proteins acting as central blue light sensors in bacteria, fungi, plants, and insects (animal type I CRY) (1). Moreover, CRYs are also found as the light-independent, central part of the oscillator of the biological clock in mammals (animal type II CRY) (5) and as a mediator for light-dependent magnetosensitivity in flies (6). Opposed to these findings, DASH cryptochromes have been found to repair lesions in single-stranded DNA and double-stranded loop-structured DNA *in vitro* (7, 8). Therefore, DASH cryptochromes are more similar in terms of functionality to photolyases than cryptochromes. Among the photolyases, two different types are separated depending on their ability to either repair cyclobutane pyrimidine dimers (CPD) (9) or (6–4) photoproducts (10). Animal type II CRY are closely related to eukaryotic (6–4) photolyases whereas plant cryptochromes are homologous to CPD photolyases. In contrast, prokaryotic (6–4) photolyases (11) and bacterial cryptochromes (12) form a distant subfamily.

The paradigm of cryptochromes and other flavoproteins as classical blue light receptors has been challenged recently by the finding that the animal-like cryptochrome (aCRY) from the green alga *Chlamydomonas reinhardtii* strongly influences gene expression not only in response to blue but also to yellow and red light *in vivo* (13). These genes code for proteins involved in chlorophyll and carotenoid biosynthesis, light-harvesting complexes, nitrogen metabolism, cell cycle control, and the circadian clock. The extended spectral sensitivity was explained by the presence of the flavin neutral radical ($FADH^{\bullet}$) in the dark form of the receptor (Fig. 1*A*) (13) as opposed to the oxidized flavin (FAD_{ox}) found in plant cryptochromes (14, 15).

* This work was supported by the Deutsche Forschungsgemeinschaft within the framework of Research Group 1261 (Grants KO3580/1-2, MI373/12-1, MI373/12-2, and ES152/12) and by a Heisenberg Fellowship (KO3580/4-1). The authors declare that they have no conflicts of interest with the contents of this article.

[S] This article contains supplemental Table S1.

[1] To whom correspondence should be addressed: Physical and Biophysical Chemistry, Dept. of Chemistry, Bielefeld University, Universitätsstr. 25, 33615 Bielefeld, Germany. Tel.: 49-521-106-2062; Fax: 49-521-106-2981; E-mail: tilman.kottke@uni-bielefeld.de.

[2] The abbreviations used are: PHR, photolyase homology region; FAD_{ox}, oxidized flavin adenine dinucleotide; CCT, C-terminal extension; *At*CRY1, *Arabidopsis thaliana* cryptochrome 1; CPD, cyclobutane pyrimidine dimers; aCRY, animal-like cryptochrome; $FADH^{\bullet}$, FAD neutral radical; $FADH^{-}$, anionic fully reduced state of FAD; UV-vis, UV-visible; $Trp^{\bullet}$, tryptophan neutral radical; $TyrO^{\bullet}$, tyrosyl radical; SEC, size exclusion chromatography; RNR, ribonucleotide reductase; PSII, photosystem II.

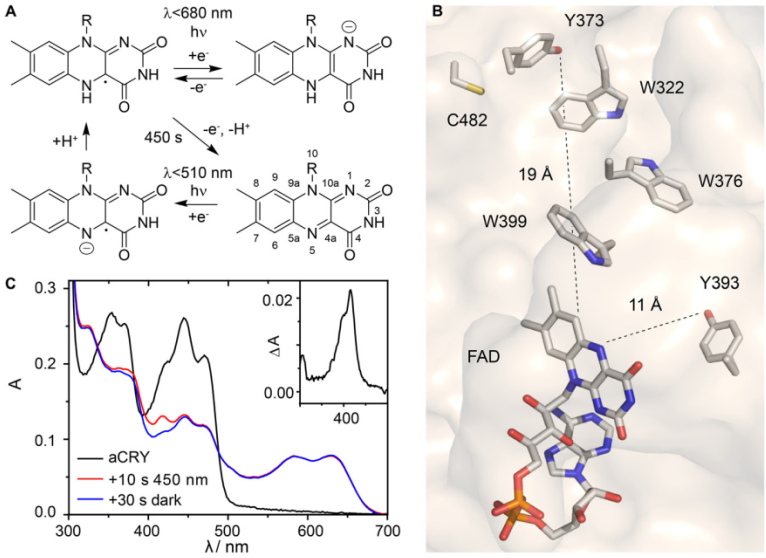

FIGURE 1. **Photoreaction sequence and position of selected residues of aCRY and its response to pre-illumination with blue light.** *A*, FAD neutral radical ($FADH^{\bullet}$, *top left*) represents the dark state *in vivo* and is photoreduced by light of $\lambda < 680$ nm into the anionic fully reduced state of FAD ($FADH^{-}$, *top right*). *In vitro*, $FADH^{\bullet}$ slowly decays into the oxidized state (*bottom right*). It is regenerated by pre-illumination with light of $\lambda < 510$ nm, possibly via the flavin anion radical (*bottom left*). *B*, position of residues tyrosine 373, tyrosine 393, and cysteine 482 investigated in this study relative to the FAD chromophore in aCRY. Tryptophan residues form the classical tryptophan triad. The structural model was derived from the crystal structure of *Arabidopsis* (6–4) photolyase (51). *C*, pre-illumination of aCRY *in vitro* with blue light (450 nm) for 10 s generates $FADH^{\bullet}$ from FAD_{ox}. An additional band is present at 416 nm directly after illumination which is lost within 30 s in the dark. The corresponding absorption difference spectrum is shown in the *inset*.

The absorption spectrum of $FADH^{\bullet}$ covers almost the full visible spectrum of light extending up to 680 nm in agreement with the action spectrum of aCRY (13). *In vitro*, the predominant part of aCRY was found in the oxidized state after purification. Accordingly, formation of $FADH^{\bullet}$ requires a pre-illumination with blue light which was not applied in the *in vivo* experiments (13). However, FTIR spectroscopy revealed structural changes in the protein moiety only in the transition from $FADH^{\bullet}$ to the anionic fully reduced state ($FADH^{-}$) of aCRY providing further support for $FADH^{\bullet}$ as the dark state of the chromophore (16). Strikingly, these changes in turn structures were not detected in the closely related *Xenopus laevis* (6–4) photolyase (17). The lifetime of $FADH^{\bullet}$ state *in vitro* was strongly sensitive to alterations of the pH but not of the oxygen level in contrast to other cryptochromes (18–20).

The molecular mechanisms underlying these extraordinary characteristics of aCRY have remained undisclosed up to now because of missing time-resolved information on the early events after red light illumination. Previously, time-resolved UV-visible (UV-vis) spectroscopy on cryptochromes and photolyases has revealed the involvement of transient radical species formed from FAD, tryptophan, and tyrosine as part of the electron transfer cascade (21–27). Tryptophan neutral radicals ($Trp^{\bullet}$) exhibit a broad band centered at around 510 nm (28), whereas tyrosyl radicals ($TyrO^{\bullet}$) are characterized by two sharp, adjacent bands at 388 and 408 nm (29, 30). Moreover, the formation of these amino acid radicals in the electron transfer cascade has been disclosed by time-resolved EPR studies (31, 32). However, to date the photoreduction process of the $FADH^{\bullet}$ has not been studied time-resolved in the cryptochrome as well as (6–4) photolyase families.

In this study, we focused on resolving the events in aCRY starting from the $FADH^{\bullet}$ state by its selective induction using illumination with red light, because the blue light-induced conversion of FAD_{ox} in aCRY is not considered to be physiologically relevant (13). To elucidate the red light-induced processes, we employed transient UV-vis spectroscopy, size exclusion chromatography (SEC), and FTIR difference spectroscopy on the full-length aCRY as well as on point mutants Y393A, Y373F, C482A (Fig. 1*B*), and aCRYΔCCT lacking the 99 residues of the CCT. We identified the contribution from a remarkably long-lived $TyrO^{\bullet}$ formed by Tyr-373 close to the surface (Fig. 1*B*), which is conserved in aCRY homologues but not in any other subfamily of cryptochromes and photolyases. Furthermore, we investigated the role of the CCT in the light-induced structural response and the oligomerization of aCRY.

Experimental Procedures

Generation of aCRY Mutants—aCRYΔCCT coding for amino acids 1 to 496 of the *aCRY* gene, lacking the 99 amino acids of its CCT, was codon-adapted for *E. coli* (synthesized by Geneart) and cloned into pET28a(+) (Novagen), providing a 6x His-Tag at the C terminus by using the restriction enzyme sites NcoI and HindIII. Mutation Y393A was inserted into the full-length codon-adapted sequence of *aCRY* (synthesized by Geneart (13)) by the replacement of a 739 bp BstEII and HindIII fragment with a fragment containing the codon-adapted sequence for the substituted amino acid Y393A. Full-length aCRY-Y393A was ligated via NcoI and HindIII restriction sites into vector pET28a(+). The Y373F and C482A mutations were inserted into the full-length *aCRY* gene in the pET28a(+) vector using phosphorylated back-to-back primers, of which one

primer contained the mutation. To amplify the whole plasmid, Phusion DNA polymerase (New England Biolabs) was used in the polymerase chain reaction. The reaction products were ligated afterward. The amino acid exchanges in all resulting plasmids were verified by dideoxy sequencing.

Expression and Purification—Expression and purification of aCRY and its variants were conducted following published procedures (13). Finally, the proteins were obtained in a 50 mM sodium phosphate buffer, pH 7.0, 100 mM NaCl, 20% (*v*/*v*) glycerol.

Millisecond Time-resolved UV-Vis Spectroscopy—The concentration of the sample was adjusted to A_{447} = 0.3. An HR2000+ spectrometer with DH-2000-BAL light source (Ocean Optics) was used for experiments in the millisecond to second time regime modified with a mesh filter with 35% transmission to avoid sample conversion by the probe light. For illumination, a 451 nm LED (Luxeon Star, Lumileds) with an intensity of 67 milliwatt/cm^2 (full width at half maximum (FWHM) of 20 nm) and a 632 nm LED (Luxeon Star, Lumileds) with an intensity of 95 milliwatt/cm^2 (FWHM of 15 nm) at the sample were attached to the sample holder perpendicular to the measuring beam. For the generation of FADH$^\bullet$, aCRY was illuminated for 10 s at 451 nm in a 2 × 10 mm fluorescence cuvette (Helma). FADH$^-$ was produced by illuminating the sample for 2 s or 10 s at 632 nm. A continuous series of spectra were recorded before, during and after illumination with an integration time of 2 ms and a time resolution of ~40 ms. Difference spectra were calculated and summarized on a logarithmic time scale to increase the signal-to-noise ratio using MATLAB (The Mathworks).

Nanosecond Time-resolved UV-Vis Spectroscopy—The concentration of the sample was adjusted to A_{447} = 0.5. The experimental setup for time-resolved UV-vis spectroscopy on slowly recovering systems has been described previously (29). aCRY was pre-illuminated for 15 s under stirring to generate FADH$^\bullet$ using a 455 nm LED (Luxeon Star, Lumileds) with an intensity of 10 milliwatt/cm^2 at the sample (FWHM of 20 nm). For excitation of FADH$^\bullet$, a 630 nm pulse with 10 ns duration and 2 mJ/cm^2 energy density was generated by a tunable optical parametric oscillator (Opta), which was pumped by the 355-nm third harmonic of a Nd:YAG laser (Quanta-Ray GCR-12, Spectra Physics). Laser pulses with a repetition rate of (1.6 s)$^{-1}$ were selected by a shutter. Multiple excitations were minimized by rotating a magnetic stirring bar inside the cuvette for 450 ms after each detection. A fast sample exchange within a total volume of 2.5 ml was ensured by a horizontal geometry of the excitation beam. Moreover, contributions from previous excitations were avoided by alternating the recording of reference and signal spectra. All experiments were conducted at 20 °C. Spectra were recorded at 1 μs, 10 μs, 100 μs, and 20 ms after excitation with an integration time of 1 μs, 5 μs, 100 μs, and 100 μs, respectively. Each spectrum was obtained by averaging 10–61 separate experiments, in which each sample was excited 15 times.

For the comparison of the wild type and the Y373F mutant of aCRY, ascorbic acid was added as a reducing agent to a final concentration of 3 mM. The samples were pre-illuminated with blue light for 1 s and 45 s for wild type and Y373F mutant, respectively. For excitation, the 532 nm second harmonic of a Nd:YAG laser (Ultra 100, Quantel) was used at a repetition rate of (1.6 s)$^{-1}$ with a pulse duration of 10 ns and an energy density of 15 mJ/cm^2 and 30 mJ/cm^2 for wild type and mutant, respectively. The integration time was set to 500 ns for the difference spectra recorded at 500 ns. Each spectrum of aCRY was obtained by averaging 8–20 separate experiments, in which each sample was excited 15 times.

FTIR Experiments—The samples were concentrated to an A_{447} ~27 by ultrafiltration using Vivaspin 500 filter devices (Sartorius, 50 kDa cutoff). During centrifugation at 15,000 × *g*, the protein was washed three times with 20 mM sodium phosphate buffer, pH 7.8, 100 mM NaCl, 1% (*v*/*v*) glycerol. A 1.8-μl droplet of the sample solution was applied to a BaF_2 window (20 mm diameter) and kept at 20 °C and atmospheric pressure for up to 30 s to gently reduce the water content. The samples were sealed with a second BaF_2 window. Thus, a well-hydrated film with an absorbance ratio of amide I/water (1650 cm^{-1}) to amide II (1550 cm^{-1}) of 2.3–2.5 was obtained. An appropriate hydration of the sample is essential to ensure that the full extent of changes in secondary structure of the protein is detected.

IR experiments were performed on an IFS 66v spectrometer (Bruker) equipped with a photoconductive mercury cadmium telluride (MCT) detector at a spectral resolution of 2 cm^{-1}. The difference spectra were obtained with a long wave pass filter (OCLI) cutting off infrared light above 2256 cm^{-1}. The experiments were performed at 20 °C. The blue light response of aCRY was induced by illumination for 1 s with a 451-nm LED equipped with a diffusion disc and yielding an intensity of 32 milliwatt/cm^2 at the sample. Red light illumination was conducted for 10 s with a 632-nm LED with an intensity of 40 milliwatt/cm^2 at the sample. To obtain a representative difference spectrum, 512 scans were averaged.

Size Exclusion Chromatography—SEC was performed using an Äkta purifier (GE Healthcare) with a Superdex200 10/300 GL column (GE Healthcare) at 4 °C. For equilibration and elution, 50 mM phosphate buffer at pH 7.0 and 150 mM NaCl were used. Aliquots of 100 μl with a protein concentration of 0.5 mM were centrifuged at 21,400 × *g* for 10 min at 4 °C. For the investigation of aCRY carrying FAD_{ox} and FADH$^\bullet$, loading of the samples and the SEC were performed in the dark. FADH$^\bullet$ was obtained by illuminating the sample for 10 s with two 451 nm LEDs (Luxeon Star, Lumileds) with an intensity of 67 milliwatt/cm^2 each at the sample. The elution profiles were recorded at 447 and 630 nm to ensure that only protein with the flavin bound contributes. For the generation of FADH$^-$, samples were illuminated for 45 s with the two 451 nm LEDs followed by 30 s in darkness and illumination for 20 s with a 451 nm LED and a 632 nm LED with an intensity of 64 milliwatt/cm^2. Alternatively, the latter two LEDs were used to illuminate the sample for 45 s. This variation in illumination did not have any detectable effect on the elution profiles of the proteins recorded at 447 and 370 nm. Standard marker proteins (GE Healthcare) were used to determine the apparent molecular mass of the sample by calibration. Representative traces are shown from the experiments, which were repeated at least three times for each of 2–3 independent preparations.

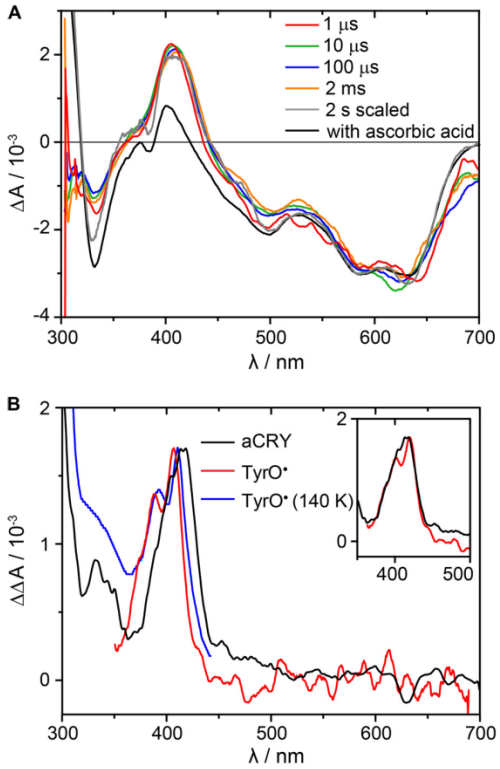

FIGURE 2. **Microsecond time-resolved UV-vis spectra of the red light response in aCRY.** *A*, pre-illuminated samples were excited with 630 nm laser pulses to selectively convert FADH• to FADH⁻. Spectra were recorded at indicated time points. For comparison, a steady state spectrum of the FADH• to FADH⁻ conversion in the presence of 0.1 mM ascorbic acid is shown. *B*, double difference spectrum of the 1 µs spectrum *minus* the steady state spectrum was calculated. The comparison to reference spectra of TyrO• in water (*red*) (29) and at 140 K (*blue*) (30) reveals a red shift. A complete match is obtained by shifting the reference spectrum by 9 nm (*inset*).

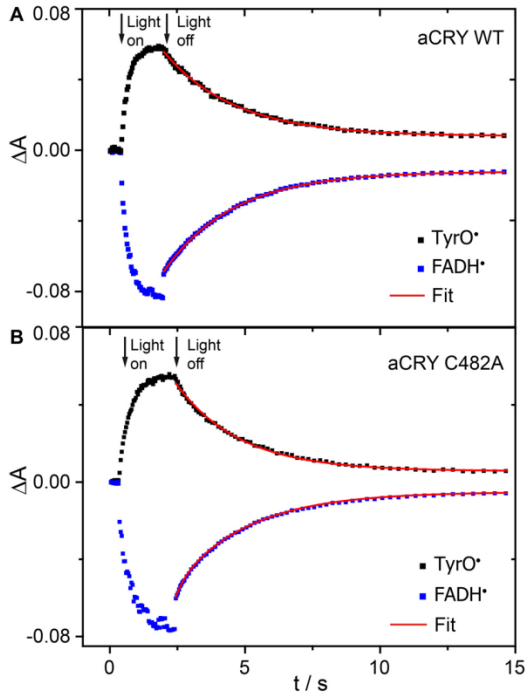

FIGURE 3. **Kinetic analysis of the red light response in aCRY.** *A*, pre-illuminated sample of wild-type aCRY was illuminated for 2 s with 632 nm to selectively convert FADH• to FADH⁻. The recovery of FADH• and the decay of TyrO• were analyzed with a monoexponential fit using the marker bands at 615–643 nm and 395–420 nm, respectively. Both processes show the same time constant of 2.6 s. *B*, these time constants change only slightly to 2.3 s in the C482A mutant of aCRY speaking against an efficient pathway of thiol oxidation by TyrO•.

Phylogenetic Analysis—Phylogenetic analyses were conducted using the MEGA software package version 6 (33). The protein sequences used for the alignment were selected according to the results of the NCBI BLASTP 2.3.0 (34) using the sequences with the highest identity to aCRY. Additionally, sequences of closely related and well characterized cryptochromes and photolyases were included (supplemental Table S1). The protein sequences were aligned with the ClustalW algorithm.

Results

The UV-vis spectrum of aCRY recorded after purification revealed FAD_{ox} to be present in aCRY *in vitro* (Fig. 1*C*). Blue light illumination then generated FADH• with characteristic bands at 585 and 633 nm. We noticed an additional small band at 416 nm with a shoulder at 410 nm in the absorption spectrum after illumination, which was only present for a few seconds (Fig. 1*C*). Such contribution is indicative for transient accumulation of an amino acid radical, but usually detected on a much shorter time scale. Therefore, this finding was scrutinized in a time-resolved manner in the context of the physiologically more relevant reduction of FADH• to FADH⁻.

Microsecond Time-resolved Response to Red Light of aCRY—Time-resolved UV-vis experiments have revealed the involvement of tryptophan and tyrosyl radicals in the photoreaction of cryptochromes *in vitro* starting from FAD_{ox}. Here, flash photolysis was applied to detect possible amino acid radicals involved in the red light-induced photoreduction of FADH• in aCRY. Previous steady-state experiments have shown only the formation of FADH⁻ (16).

Samples containing FAD_{ox} were pre-illuminated with blue light for 15 s to generate a sufficient amount of FADH•, which was stabilized by adjusting the pH to 7.0 (16). To selectively convert FADH• to FADH⁻, nanosecond laser pulses at 630 nm were used. Time-resolved UV-vis difference spectra were recorded at time points from 1 µs to 2 ms (Fig. 2*A*). All difference spectra show the characteristic negative band pattern of the bleaching of FADH• with two broad maxima at 590 nm and 630 nm. Additionally, a small positive contribution from the formation of FADH⁻ is detected at 400 nm. For comparison, spectra after illumination for 2 s with an LED were obtained in the absence and in the presence of 0.1 mM ascorbic acid. This strong reducing agent quenches all contributions by amino acid radicals within a few microseconds. The time-resolved spectra show a pronounced positive band at 416 nm, which is still present 2 s after illumination but is missing in the presence of ascor-

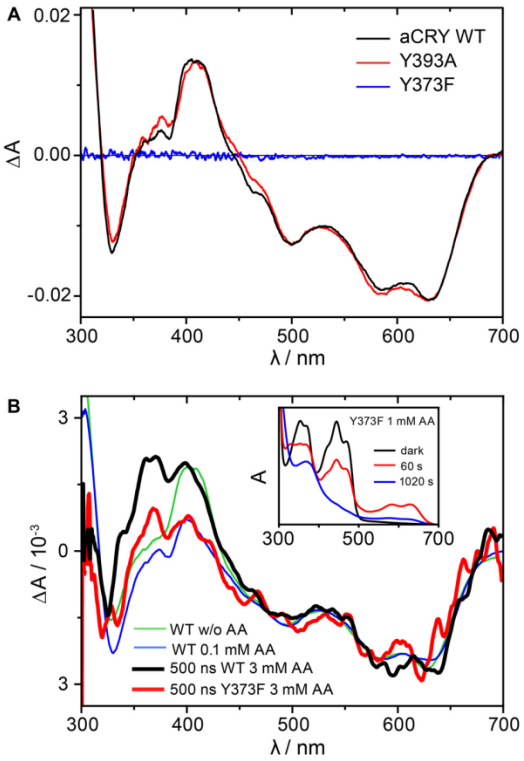

FIGURE 4. **Effects of mutations in tyrosine residues on the red-light response of aCRY.** *A*, red light-induced UV-vis difference spectra of the wild type, the Y393A and Y373F mutants of aCRY. Pre-illuminated samples were illuminated for 10 s with 632 nm. In both the wild type and the Y393A mutant, $FADH^{\bullet}$ is converted to $FADH^{-}$ accompanied by the formation of $TyrO^{\bullet}$. The Y373F mutant does not show any light response. *B*, time-resolved absorption spectra at 500 ns of the Y373F mutant and wild type aCRY in the presence of 3 mM ascorbic acid. Both the Y373F mutant and the wild type show the conversion of $FADH^{\bullet}$ to $FADH^{-}$. In contrast to the wild type, the Y373F mutant does not show an additional contribution of $TyrO^{\bullet}$ at 416 nm identifying Tyr-373 as the origin of this absorption. The conversion of FAD_{ox} to $FADH^{\bullet}$ and $FADH^{-}$ is observed in aCRY-Y373F only in the presence of ascorbic acid (*inset*).

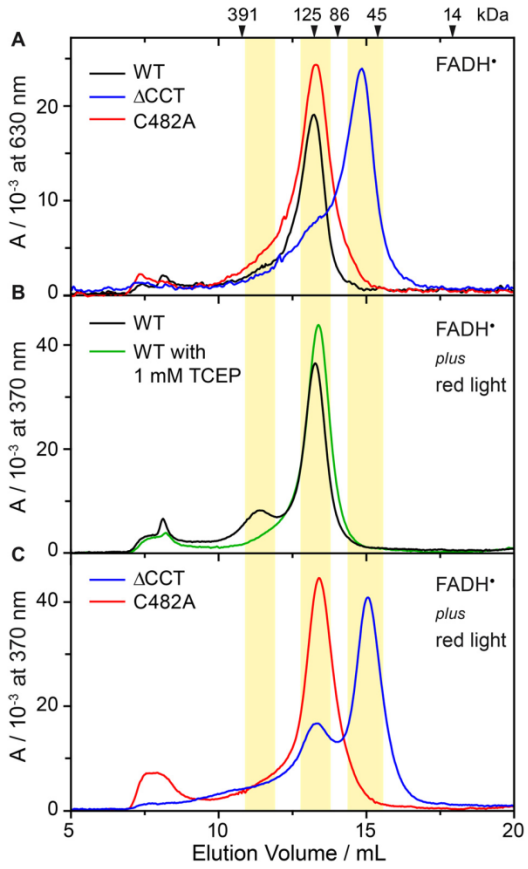

FIGURE 5. **Size exclusion chromatography of wild-type aCRY, aCRYΔCCT and the C482A mutant at injected concentrations of 0.5 mM.** *A*, samples were illuminated for 10 s with 451 nm to convert FAD_{ox} to $FADH^{\bullet}$, which was selectively detected at 630 nm. Wild-type aCRY and the C482A mutant eluted at 13.2 ml, which corresponds to an apparent molecular mass of 130 kDa. Considering a theoretical molecular mass of 66.4 kDa of aCRY, the bands can be assigned to dimers. aCRYΔCCT predominantly eluted at 14.8 ml, which corresponds to an apparent molecular mass of 60 kDa and can accordingly be assigned to a monomer. *B*, samples were illuminated for 45 s with 451 nm and 630 nm to convert FAD_{ox} to $FADH^{\bullet}$ and $FADH^{-}$, which were detected at 370 nm. Wild-type aCRY shows an additional, small peak at 11.4 ml (314 kDa), which indicates a tetrameric species. This light-induced oligomerization can be abolished by the addition of the reducing agent TCEP. *C*, samples were treated as in *B*. In the C482A mutant, light-induced oligomerization is not observed. In contrast, aCRYΔCCT shows an additional peak at 13.3 ml, which can be assigned to a dimeric species. Therefore, some light-induced oligomerization was found for both wild-type aCRY and aCRYΔCCT.

bic acid. This additional contribution is present to an equal extent relative to flavin at all time points.

To reveal the identity of the species contributing at 416 nm, the double difference spectrum of the 1 μs spectrum *minus* the steady-state spectrum was calculated. The resulting spectrum shows a well-defined peak with a maximum at 416 nm and a shoulder at ~400 nm (Fig. 2*B*). The comparison to reference spectra (29, 30) revealed that such a band is characteristic for $TyrO^{\bullet}$. In contrast to the reference spectra obtained in water, $TyrO^{\bullet}$ in aCRY is red-shifted by the protein environment by 9 nm (*inset*, Fig. 2*B*). Any hint for the presence of a tryptophan radical at 1 μs or later was not found.

Kinetic Analysis of the Decay of $TyrO^{\bullet}$ in aCRY after Red Light Illumination—Tyrosyl radicals in proteins usually exhibit maximal lifetimes in the range of a few milliseconds (21, 23, 29, 35). Here, the time-resolved studies on aCRY indicated a much higher lifetime. Therefore, the decay of $TyrO^{\bullet}$ and $FADH^{-}$ after red light illumination was analyzed on a time scale of seconds at 20 °C. The sample was pre-illuminated with blue light and then exposed to 632 nm for 2 s. A continuous series of difference spectra with a time resolution of ~40 ms was recorded for 15 s (Fig. 3). The decay of $FADH^{-}$ was analyzed indirectly using the negative marker bands of the recovery of $FADH^{\bullet}$. The absorbance at 615–643 nm was averaged and subsequently analyzed with a monoexponential fit yielding a time constant of 2.6 s. For the decay of $TyrO^{\bullet}$, changes in absorbance at 395–420 nm were averaged. The monoexponential fit yielded a time constant of 2.6 s for $TyrO^{\bullet}$, implying a mutual decay with $FADH^{-}$.

Candidates for the Tyrosine Residue Involved in the Red Light Response of aCRY—To reveal the identity of the tyrosine residue contributing to the difference spectra, two different

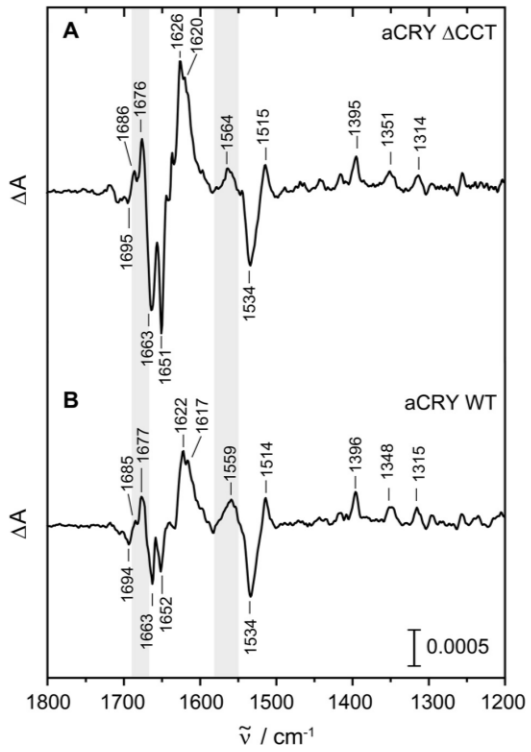

FIGURE 6. **Red light-induced FTIR difference spectra of aCRY ΔCCT as compared with wild-type aCRY.** Samples were pre-illuminated with blue light and then exposed to 632 nm for 10 s to selectively convert $FADH^{\bullet}$ to $FADH^{-}$. Contributions identified in the analysis to originate from changes in secondary structure are highlighted in *gray*. Both samples show very similar responses excluding the CCT as the origin of these structural changes.

mutants of aCRY, Y373F and Y393A were produced. The residues Tyr-373 and Tyr-393 were selected because they are not conserved in other cryptochrome or photolyase families and might therefore provide a basis for the unique photoreceptor properties of aCRY (Fig. 1*B*). Both mutants were expressed and purified as soluble yellow proteins. Samples were pre-illuminated for 10 s with 451 nm to generate $FADH^{\bullet}$, but in Y373F, $FADH^{\bullet}$ was not formed. Difference spectra were then recorded after illumination of the samples for 10 s with 632 nm (Fig. 4*A*). For comparison, the same procedure was repeated with wild-type aCRY. Both the wild type and the Y393A mutant showed the typical pattern of the conversion of $FADH^{\bullet}$ to $FADH^{-}$ accompanied by the formation of $TyrO^{\bullet}$. In contrast, the Y373F mutant did not show any light-induced difference in absorption. These findings lead to the conclusion that in aCRY-Y373F the light sensitivity is strongly reduced by the exchange of the tyrosine residue, whereas Tyr-393 seems not to have any influence on the photoreaction. However, it remained unclear whether Tyr-373 is the residue forming the radical or whether the mutation negatively affected the structural integrity of aCRY.

Identification of Tyr-373 Forming the Long-lived Radical—We have investigated whether there are conditions under which a photoreduction of the Y373F mutant was observable. The protein could be photoreduced from FAD_{ox} to $FADH^{\bullet}$ and further to $FADH^{-}$ by the addition of ascorbic acid, albeit after a much longer light exposure (Fig. 4*B*, *inset*). However, under these harsh conditions $TyrO^{\bullet}$ in the wild type was quenched preventing a direct comparison with the mutant (Fig. 2). Therefore, time-resolved experiments were conducted to capture $TyrO^{\bullet}$ in the wild type before its reaction with ascorbic acid. Conditions had to be established under which the Y373F mutant was sufficiently photoactivated while the wild type showed the signal of $TyrO^{\bullet}$, resulting in time-resolved spectra at 500 ns in the presence of 3 mM ascorbic acid. After pre-illumination with blue light, both samples were excited with laser pulses at 532 nm. The intensity was adjusted so that the difference spectra of the wild type and the Y373F mutant showed both the formation of the $FADH^{\bullet}$ to a similar extent (Fig. 4*B*). The spectrum of the wild type showed the same band pattern as a sample in the absence of ascorbic acid besides an additional band at around 370 nm originating from a reaction intermediate in the oxidation of ascorbic acid. The Y373F mutant, however, does not produce the band at 416 nm of $TyrO^{\bullet}$. In conclusion, Tyr-373 was identified to form the long-lived radical in aCRY.

Size Exclusion Chromatography on aCRY and Its Variants—The oligomerization state of aCRY and its dependence on the redox state of the flavin was studied by SEC at injected concentrations of 0.5 mM. aCRY containing $FADH^{\bullet}$ was analyzed using blue light-illuminated samples. Absorbance was recorded at 630 nm to selectively detect protein with bound $FADH^{\bullet}$. The SEC showed a single peak with a maximum at an elution volume of 13.2 ml (Fig. 5*A*), which corresponds to an apparent molecular mass of 130 kDa. Considering a theoretical molecular mass of 66.4 kDa, the peak can be assigned to a dimer of aCRY. To resolve the functional role of the CCT, aCRY was truncated after amino acid 496. In contrast to the full-length receptor, aCRYΔCCT showed a peak at an elution volume of 14.8 ml, which corresponds to an apparent molecular mass of 60 kDa (Fig. 5*A*). With a theoretical mass of 57.7 kDa of aCRYΔCCT, the peak can be assigned to a monomer. This difference points to the fact that the CCT is necessary for the dimerization of aCRY carrying $FADH^{\bullet}$.

The effects of the formation of $FADH^{-}$ in aCRY were investigated using blue and red light-illuminated samples. Due to the decay of $FADH^{-}$ back to $FADH^{\bullet}$ within a few seconds during the SEC, the detected absorbance at 370 nm mainly represents $FADH^{\bullet}$ in aCRY, but $FADH^{-}$ and FAD_{ox} might absorb as well. Interestingly, aCRY showed the same profile as before, but with an additional peak at 11.4 ml (314 kDa) possibly from a tetrameric species (Fig. 5*B*). Similarly, aCRYΔCCT showed an additional peak at 13.3 ml (122 kDa) after the conversion, which is assignable to the formation of a dimer (Fig. 5*C*). Therefore, it can be concluded that the red light-induced changes in aCRY are persistent even after the fast recovery of $FADH^{\bullet}$ from $FADH^{-}$. The formation of $FADH^{-}$ is accompanied by light-induced oligomerization of aCRY to some extent. This process is abolished by the presence of 1 mM of the strong reducing agent TCEP (Fig. 5*B*). As TCEP is known to reduce disulfide bonds, a potential candidate for such an intermolecular bond was identified as Cys-482 on the basis of its close proximity to

the reactive tyrosine residue Tyr-373 (Fig. 1*B*) as well as its position close to the protein surface. The replacement of Cys-482 with alanine led to a disappearance of the additional peak in the SEC profile of aCRY after red-light illumination (Fig. 5*C*), whereas the profile of aCRY without red light treatment was not altered in the C482A mutant (Fig. 5*A*). Therefore, light-induced oligomerization in aCRY most likely proceeds via disulfide bridge formation at Cys-482.

Red Light-induced FTIR Difference Spectroscopy on aCRYΔCCT—The previously recorded FTIR difference spectrum of the wild type (16) showed changes in turn structures in the light-induced conversion from $FADH^{\bullet}$ to $FADH^{-}$ that are not present in (6–4) photolyase (17). To further investigate a possible involvement of the CCT in the red light response of aCRY, difference spectra of aCRYΔCCT were taken after red light exposure. The reference was recorded after the sample was pre-illuminated for 1 s with blue light. Immediately afterward the sample was illuminated for 10 s at 632 nm to induce the formation of $FADH^{-}$ (Fig. 6*A*). In the resulting difference spectrum, only bands of vibrational modes changing upon red light illumination are detectable. The negative bands represent the dark state with bound $FADH^{\bullet}$ in good agreement with the spectrum of the wild type (Fig. 6*B*), showing marker bands of $FADH^{\bullet}$ at 1663, 1651, and 1534 cm^{-1} (16). The positive bands in the difference spectrum of aCRYΔCCT are also in good agreement with those of the wild type, most of which can be assigned to $FADH^{-}$. Marker bands for $FADH^{-}$ (16) are present in the spectrum of aCRYΔCCT at 1626, 1620, 1515, and 1395 cm^{-1}. The positive band assigned to a change in turn elements is also present in aCRYΔCCT at 1676 cm^{-1}. Only the band at 1564 cm^{-1} originating from both flavin and the amide II band shows an upshift of 5 cm^{-1} as compared with the wild type spectrum. In conclusion, the difference spectrum of aCRYΔCCT is almost identical to that of the wild type taking into account a slight shift of several bands by ~1 cm^{-1}. It can be concluded that the CCT in aCRY does not respond to light by a change in secondary structure, in contrast to the CCT in plant cryptochromes (36, 37). So far, structural changes detected in aCRY are therefore limited to the PHR domain.

Discussion

Unusual Stability of TyrO• in aCRY—Tyrosyl radicals have been observed as part of the electron transfer cascade in other cryptochromes and photolyases than aCRY (21, 23, 29, 32). Lifetimes of these tyrosyl radicals have been determined to range from 1 ms up to >140 ms (21, 23, 29). In contrast, an unusually long-lived TyrO• with a lifetime of 2.6 s is formed in aCRY, implying a high stability of the radical.

A very similar lifetime of TyrO• has been achieved in α3Y, a *de novo* model protein specifically designed for investigating the stabilizing effect of the protein matrix on the lifetime of tyrosyl radicals (38). α3Y does not contain any cofactors and places the reactive tyrosine in a three helix bundle scaffold. Similar to aCRY, αY3 does not carry a covalent modification of tyrosine or a metal center for stabilization of TyrO• (39). However, the residue is buried deeply in a hydrophobic environment in α3Y without any hydrogen bonding partner or access to the solvent (38). Therefore, the surrounding protein matrix is rather different compared with the one present in aCRY, considering the relatively exposed position of Tyr-373 in a cavity on the surface of the protein, as derived from the modeled structure (16).

Interestingly, a system more similar to aCRY was found in the D2 subunit of photosystem II (PSII). Here, Tyr_D forms a radical that is stable for hours under physiological conditions without a metal cluster in close proximity (40). Tyr_D was reported to be deprotonated upon oxidation, because phenolic compounds become strong acids upon oxidation. Such a proton-coupled electron transfer has also been found for other tyrosyl radicals (39). For Tyr_D, it is believed that the kinetics of reprotonation is of considerable importance for the stability of TyrO• (41). The radical is found in a very well-ordered hydrogen bonding network with rather hydrophobic residues, which was postulated to prevent any uncontrolled protonation (41). Additional stability might be provided by the movement of either the proton acceptor (41) or the tyrosine residue away from the proton-donating network upon oxidation, as found for the stable TyrO• coupled to a diiron oxo site in subunit R2 of class I ribonucleotide reductases (RNR) (42). Moreover, it might be important to consider that after oxidation and deprotonation, the phenolic oxygen of the radical might be hydrogen-bonded to an adjacent residue or a coordinated water molecule (43, 44). This hydrogen bond may provide an additional stabilization by delocalizing the spin density of the oxygen, as it has been suggested for the rather hydrophilic environment in mouse RNR (44).

Transferring these findings to aCRY, it seems plausible that TyrO• is also coordinated in a very stable, non-flexible hydrogen bonding network comparable to the one found for Tyr_D in PSII, even if there are not that many adjacent hydrophobic residues in aCRY. In PSII, arginine and aspartate close to Tyr_D form a salt bridge, facilitating the proton transfer during oxidation (41). In the modeled structure of aCRY (16), arginine (Arg-485) and aspartate (Asp-321) also form a salt bridge close to Tyr-373, possibly creating a similar environment as in PSII. Still, it is unclear whether an amino acid residue or a coordinated water molecule is the proton acceptor in aCRY. Furthermore, it needs to be resolved if the phenolic oxygen of TyrO• is also hydrogen bonded as in mouse RNR and PSII-D2. In summary, the lifetime of TyrO• in aCRY can be considered to be unusually long because the protein does not provide the classical environment for stabilization such as a metal center or hydrophobic residues. Furthermore, TyrO• in aCRY does not benefit from possibly stabilizing effects of a membrane-bound complex such as PSII.

Red Shift of TyrO• Absorbance—Another striking feature of TyrO• found in aCRY is its red-shifted absorption pattern. Typically the radical shows absorption maxima at ~390 and ~410 nm (29, 30). In contrast, the maxima in aCRY are found at ~400 and 416 nm, similar to what has been reported previously in mouse RNR (45). An explanation for the shift in both aCRY and the mammalian RNR might be the existence of the hydrogen bond between the phenolic oxygen and a hydrogen bond donor. Interestingly, TyrO• in the *Escherichia coli* RNR is not hydrogen-bonded and shows a non-shifted absorption spectrum in the direct comparison (45). A covalent crosslink of the cysteine to the tyrosine as observed in galactose oxidase (46) can be

ruled out as the absorption difference spectrum of the aCRY-C482A mutant is identical to that of the wild type (data not shown).

Formation of TyrO• from Trp•—Another surprising aspect of the time-resolved UV-vis spectra is the absence of any bands from tryptophan radicals after 1 μs. In other UV-vis-spectroscopic studies on cryptochromes, significant Trp• contributions have been identified in this time region up to milliseconds (23, 24). To our knowledge, the only similar finding has been reported for *Xenopus laevis* (6–4) photolyase, in which TyrO• is already formed within 100 ns after illumination (32). For aCRY, the question arises whether the Trp• decays ultrafast into TyrO• or if the Trp• is not formed in the first place. The latter suggestion is unlikely because a tryptophan triad (23) (Trp-322, Trp-376, Trp-399) is also conserved in aCRY. As such a triad is considered to represent an optimal electron transfer pathway, the electron is most probably guided via this "electron wire" over the distance of ~16 Å, as derived from the model, from the Tyr-373 on the surface to the chromophore. Therefore, the most likely reason for the Trp• band not to be present in the spectra after 1 μs is its ultrafast decay in a time range of pico- to nanoseconds. This short lifetime might be the consequence of a high reactivity of Tyr-373.

Oligomerization State of aCRY—In the dark, SEC at 0.5 mM injected concentration revealed aCRY to form a homodimer whereas the truncated ΔCCT mutant remains predominantly as a monomer. These findings indicate that the CCT may represent the oligomerization site of aCRY in the dark. In the light, SEC revealed some oligomerization for both proteins upon $FADH^-$ formation at a concentration of 0.5 mM. Therefore, the CCT does not play a significant role during red light-induced oligomerization. This conclusion is underlined by the FTIR experiments which do not show any significant differences between red light-induced difference spectra of the wild type and the ΔCCT mutant. These findings are in contrast to events observed in other cryptochromes. In the *Arabidopsis* cryptochrome *At*CRY1, large conformational changes upon photoexcitation were noted by a rearrangement of the CCT (36, 37). In the *Drosophila* cryptochrome dCRY, an increase of proteolytic susceptibility of the CCT upon illumination indicates the involvement of this domain in the light response (47).

Further SEC experiments imply that the light-induced oligomerization originates from the formation of disulfide bridges most likely by Cys-482. From the structural model, Cys-482 was derived to be in close proximity with a 4 Å distance to the reactive Tyr-373. It can be concluded that red light illumination of aCRY triggers a redox cascade with a partial electron transfer from a cysteine to TyrO•. Such transfer has already been observed in class I RNR, in which the cascade does not result in disulfide bridge formation but in the reduction of ribonucleotides to deoxyribonucleotides (48). In aCRY this reaction is inefficient, because the lifetime of TyrO• is not increased in the C482A mutant but even slightly shortened (Fig. 3*B*). Therefore, the formation of disulfide bridges might be regarded as a non-physiological reaction or as a consequence of a missing *in vivo* redox substrate/partner, which might explain the low extent of oligomerization. Alternatively, we may speculate that the covalent linkage of the aCRY dimers constitutes a pathway present

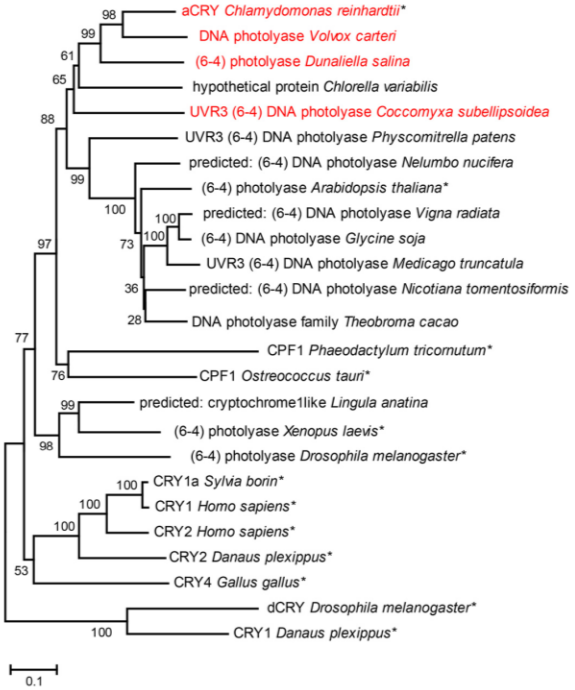

FIGURE 7. **Phylogenetic classification of aCRY and conservation of the tyrosine residue 373.** Three uncharacterized proteins homologous to aCRY were found by BLASTP that all carry the tyrosine residue 373 of aCRY (*red*). These three sequences are among the four closest to aCRY and share more than 63% sequence identity, hinting toward the presence of aCRY-like receptors in these organisms. All other presented sequences lack this tyrosine. Characterized members of other cryptochrome and photolyase subfamilies have been marked with an *asterisk*. Bootstrap values are given after 1000 replications. The scale bar indicates amino acid substitutions per site.

under oxidative stress and high light conditions only, which might lead to an inactivation of aCRY signaling by inhibiting any binding to its signaling partner (49).

Tyr-373 in the Context of Other Cryptochromes and Photolyases—The postulate of a central role of Tyr-373 in the sensory mechanism of aCRY would imply that this residue is conserved in other potential red light receptors. A BLAST search (Fig. 7, supplemental Table S1) revealed that indeed the two closest relatives of aCRY, the putative photolyases from the algae *Volvox carteri* and *Dunaliella salina* share this residue as well as a sequence from *Coccomixa subellipsoidea* but not from *Chlorella variabilis*. These sequences form a subgroup that is well separated in the phylogenetic analysis from other candidates for conventional (6–4) photolyases. Even more convincingly, the next 40 candidates in the alignment of the aCRY homologues and all well characterized members of the cryptochrome/photolyase family to our knowledge do not possess a tyrosine at this position. We consider this finding to be significant as a further support for the crucial role of Tyr-373 in the function of aCRY as light receptor with an extended sensitivity range.

Conclusions—To date, only small conformational changes have been identified for aCRY in the red-light induced photoreduction. In contrast to other full-length cryptochromes, these

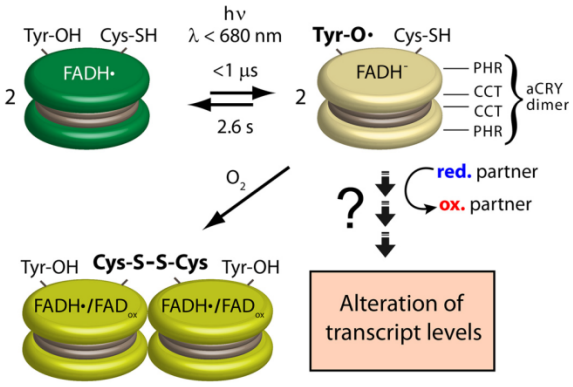

FIGURE 8. **Model of the response to red light of aCRY *in vitro*.** aCRY forms a homodimer (represented by two disks) via its CCT. aCRY carrying FADH• is reduced to FADH⁻ by light with λ < 680 nm. As a result, TyrO• is formed by Tyr-373 within 1 μs with a red-shifted absorption in aCRY compared with water. The lifetime of 2.6 s of TyrO• is unusually high and might allow for an efficient oxidation of a signaling partner *in vivo* finally leading to the changes in the levels of multiple transcripts. The decay of TyrO• proceeds concomitant with that of FADH⁻. Some of the light-activated aCRY oligomerizes via disulfide bridge formation at Cys-482 in the absence of external reductant.

changes resulting from illumination do not involve the CCT. This finding raises the question of how the signal proceeds from the flavin to the protein surface in aCRY if not by such conformational changes. An alternative model would involve a redox cascade starting with the reduction of flavin and proceeding to the surface, where a signal partner or a substrate may then be converted (50).

This study provides insights into the early events of the red light response of aCRY (Fig. 8). We revealed the rapid formation within 1 μs of a tyrosine radical with an unusually long lifetime of 2.6 s, which decays concomitant with FADH⁻. Tyrosine 373 was disclosed to be responsible for the radical formation. This residue is only conserved within a small group of proteins that might be regarded as a new subfamily of the cryptochrome/photolyase superfamily. Partial light-induced oligomerization of the protein was observed and attributed to disulfide bridge formation via cysteine 482 in close proximity to tyrosine 373. These unexpected findings point to an important role of redox reactions in the signaling process of aCRY and imply that aCRY might have evolved a signaling mechanism via a light-triggered redox cascade, which culminates in a photooxidation of a yet unknown substrate or binding partner.

Author Contributions—T. K., M. M., and L. O. E. designed the study. S. O. performed and analyzed all the experiments with advice by T. K. S. F. and S. W. generated plasmids of aCRY variants. S. O. and T. K. wrote the manuscript with advice by S. F., S. W., L. O. E., and M. M. All authors reviewed the results and approved the final version of the manuscript.

Acknowledgments—We thank Benedikt Beel for help in constructing aCRYΔCCT and Mona Lisa Remmers for preliminary experiments with SEC. T. K. thanks Thomas Hellweg for generous support.

References

1. Chaves, I., Pokorny, R., Byrdin, M., Hoang, N., Ritz, T., Brettel, K., Essen, L. O., van der Horst, G. T., Batschauer, A., and Ahmad, M. (2011) The cryptochromes: blue light photoreceptors in plants and animals. *Annu. Rev. Plant Biol.* **62,** 335–364
2. Losi, A., and Gärtner, W. (2012) The evolution of flavin-binding photoreceptors: an ancient chromophore serving trendy blue-light sensors. *Annu. Rev. Plant Biol.* **63,** 49–72
3. Sancar, A. (2003) Structure and function of DNA photolyase and cryptochrome blue-light photoreceptors. *Chem. Rev.* **103,** 2203–2237
4. Yang, H. Q., Wu, Y. J., Tang, R. H., Liu, D., Liu, Y., and Cashmore, A. R. (2000) The C termini of *Arabidopsis* cryptochromes mediate a constitutive light response. *Cell* **103,** 815–827
5. Etchegaray, J. P., Lee, C., Wade, P. A., and Reppert, S. M. (2003) Rhythmic histone acetylation underlies transcription in the mammalian circadian clock. *Nature* **421,** 177–182
6. Gegear, R. J., Casselman, A., Waddell, S., and Reppert, S. M. (2008) Cryptochrome mediates light-dependent magnetosensitivity in *Drosophila*. *Nature* **454,** 1014–1018
7. Pokorny, R., Klar, T., Hennecke, U., Carell, T., Batschauer, A., and Essen, L. O. (2008) Recognition and repair of UV lesions in loop structures of duplex DNA by DASH-type cryptochrome. *Proc. Natl. Acad. Sci. U.S.A.* **105,** 21023–21027
8. Selby, C. P., and Sancar, A. (2006) A cryptochrome/photolyase class of enzymes with single-stranded DNA-specific photolyase activity. *Proc. Natl. Acad. Sci. U.S.A.* **103,** 17696–17700
9. Rupert, C. S. (1960) Photoreactivation of transforming DNA by an enzyme from bakers' yeast. *J. Gen. Physiol.* **43,** 573–595
10. Todo, T., Takemori, H., Ryo, H., Ihara, M., Matsunaga, T., Nikaido, O., Sato, K., and Nomura, T. (1993) A new photoreactivating enzyme that specifically repairs ultraviolet light-induced (6–4) photoproducts. *Nature* **361,** 371–374
11. Zhang, F., Scheerer, P., Oberpichler, I., Lamparter, T., and Krauss, N. (2013) Crystal structure of a prokaryotic (6–4) photolyase with an Fe-S cluster and a 6,7-dimethyl-8-ribityllumazine antenna chromophore. *Proc. Natl. Acad. Sci. U.S.A.* **110,** 7217–7222
12. Geisselbrecht, Y., Frühwirth, S., Schroeder, C., Pierik, A. J., Klug, G., and Essen, L. O. (2012) CryB from *Rhodobacter sphaeroides*: a unique class of cryptochromes with new cofactors. *EMBO Rep.* **13,** 223–229
13. Beel, B., Prager, K., Spexard, M., Sasso, S., Weiss, D., Müller, N., Heinnickel, M., Dewez, D., Ikoma, D., Grossman, A. R., Kottke, T., and Mittag, M. (2012) A flavin binding cryptochrome photoreceptor responds to both blue and red light in *Chlamydomonas reinhardtii*. *Plant Cell* **24,** 2992–3008
14. Banerjee, R., Schleicher, E., Meier, S., Viana, R. M., Pokorny, R., Ahmad, M., Bittl, R., and Batschauer, A. (2007) The signaling state of *Arabidopsis* cryptochrome 2 contains flavin semiquinone. *J. Biol. Chem.* **282,** 14916–14922
15. Bouly, J. P., Schleicher, E., Dionisio-Sese, M., Vandenbussche, F., Van Der Straeten, D., Bakrim, N., Meier, S., Batschauer, A., Galland, P., Bittl, R., and Ahmad, M. (2007) Cryptochrome blue light photoreceptors are activated through interconversion of flavin redox states. *J. Biol. Chem.* **282,** 9383–9391
16. Spexard, M., Thöing, C., Beel, B., Mittag, M., and Kottke, T. (2014) Response of the sensory animal-like cryptochrome aCRY to blue and red light as revealed by infrared difference spectroscopy. *Biochemistry* **53,** 1041–1050
17. Yamada, D., Zhang, Y., Iwata, T., Hitomi, K., Getzoff, E. D., and Kandori, H. (2012) Fourier-transform infrared study of the photoactivation process of *Xenopus* (6–4) photolyase. *Biochemistry* **51,** 5774–5783
18. Berndt, A., Kottke, T., Breitkreuz, H., Dvorsky, R., Hennig, S., Alexander, M., and Wolf, E. (2007) A novel photoreaction mechanism for the circadian blue light photoreceptor *Drosophila* cryptochrome. *J. Biol. Chem.* **282,** 13011–13021
19. Immeln, D., Schlesinger, R., Heberle, J., and Kottke, T. (2007) Blue light induces radical formation and autophosphorylation in the light-sensitive domain of *Chlamydomonas* cryptochrome. *J. Biol. Chem.* **282,** 21720–21728
20. Müller, P., and Ahmad, M. (2011) Light-activated cryptochrome reacts with molecular oxygen to form a flavin-superoxide radical pair consistent with magnetoreception. *J. Biol. Chem.* **286,** 21033–21040

21. Aubert, C., Mathis, P., Eker, A. P., and Brettel, K. (1999) Intraprotein electron transfer between tyrosine and tryptophan in DNA photolyase from *Anacystis nidulans*. *Proc. Natl. Acad. Sci. U.S.A.* **96,** 5423–5427
22. Aubert, C., Vos, M. H., Mathis, P., Eker, A. P., and Brettel, K. (2000) Intraprotein radical transfer during photoactivation of DNA photolyase. *Nature* **405,** 586–590
23. Giovani, B., Byrdin, M., Ahmad, M., and Brettel, K. (2003) Light-induced electron transfer in a cryptochrome blue-light photoreceptor. *Nat. Struct. Biol.* **10,** 489–490
24. Langenbacher, T., Immeln, D., Dick, B., and Kottke, T. (2009) Microsecond light-induced proton transfer to flavin in the blue light sensor plant cryptochrome. *J. Am. Chem. Soc.* **131,** 14274–14280
25. Brazard, J., Usman, A., Lacombat, F., Ley, C., Martin, M. M., Plaza, P., Mony, L., Heijde, M., Zabulon, G., and Bowler, C. (2010) Spectro-temporal characterization of the photoactivation mechanism of two new oxidized cryptochrome/photolyase photoreceptors. *J. Am. Chem. Soc.* **132,** 4935–4945
26. Müller, P., Yamamoto, J., Martin, R., Iwai, S., and Brettel, K. (2015) Discovery and functional analysis of a 4th electron-transferring tryptophan conserved exclusively in animal cryptochromes and (6–4) photolyases. *Chem. Commun.* **51,** 15502–15505
27. Paulus, B., Bajzath, C., Melin, F., Heidinger, L., Kromm, V., Herkersdorf, C., Benz, U., Mann, L., Stehle, P., Hellwig, P., Weber, S., and Schleicher, E. (2015) Spectroscopic characterization of radicals and radical pairs in fruit fly cryptochrome - protonated and nonprotonated flavin radical-states. *FEBS J.* **282,** 3175–3189
28. Solar, S., Getoff, N., Surdhar, P. S., Armstrong, D. A., and Singh, A. (1991) Oxidation of tryptophan and N-methylindole by $N_3^•$, Br_2^-, and $(SCN)_2^-$ radicals in light-water and heavy-water solutions - A pulse-radiolysis study. *J. Phys. Chem.* **95,** 3639–3643
29. Thöing, C., Oldemeyer, S., and Kottke, T. (2015) Microsecond deprotonation of aspartic acid and response of the α/β subdomain precede C-terminal signaling in the blue light sensor plant cryptochrome. *J. Am. Chem. Soc.* **137,** 5990–5999
30. Proshlyakov, D. A. (2004) UV optical absorption by protein radicals in cytochrome *c* oxidase. *Biochim. Biophys. Acta* **1655,** 282–289
31. Biskup, T., Schleicher, E., Okafuji, A., Link, G., Hitomi, K., Getzoff, E. D., and Weber, S. (2009) Direct observation of a photoinduced radical pair in a cryptochrome blue-light photoreceptor. *Angew. Chem. Int. Ed.* **48,** 404–407
32. Weber, S., Kay, C. W., Mögling, H., Möbius, K., Hitomi, K., and Todo, T. (2002) Photoactivation of the flavin cofactor in *Xenopus laevis* (6–4) photolyase: observation of a transient tyrosyl radical by time-resolved electron paramagnetic resonance. *Proc. Natl. Acad. Sci. U.S.A.* **99,** 1319–1322
33. Tamura, K., Dudley, J., Nei, M., and Kumar, S. (2007) MEGA4: Molecular Evolutionary Genetics Analysis (MEGA) Software Version 4.0. *Mol. Biol. Evol.* **24,** 1596–1599
34. Altschul, S. F., Madden, T. L., Schäffer, A. A., Zhang, J., Zhang, Z., Miller, W., and Lipman, D. J. (1997) Gapped BLAST and PSI-BLAST: a new generation of protein database search programs. *Nucleic Acids Res.* **25,** 3389–3402
35. Gauden, M., van Stokkum, I. H. M., Key, J. M., Lührs, D. Ch., van Grondelle, R., Hegemann, P., and Kennis, J. T. (2006) Hydrogen-bond switching through a radical pair mechanism in a flavin-binding photoreceptor. *Proc. Natl. Acad. Sci. U.S.A.* **103,** 10895–10900
36. Kondoh, M., Shiraishi, C., Müller, P., Ahmad, M., Hitomi, K., Getzoff, E. D., and Terazima, M. (2011) Light-induced conformational changes in full-length *Arabidopsis thaliana* cryptochrome. *J. Mol. Biol.* **413,** 128–137
37. Partch, C. L., Clarkson, M. W., Ozgür, S., Lee, A. L., and Sancar, A. (2005) Role of structural plasticity in signal transduction by the cryptochrome blue-light photoreceptor. *Biochemistry* **44,** 3795–3805
38. Glover, S. D., Jorge, C., Liang, L., Valentine, K. G., Hammarström, L., and Tommos, C. (2014) Photochemical tyrosine oxidation in the structurally well-defined α_3Y protein: proton-coupled electron transfer and a long-lived tyrosine radical. *J. Am. Chem. Soc.* **136,** 14039–14051
39. Hoganson, C. W., and Tommos, C. (2004) The function and characteristics of tyrosyl radical cofactors. *Biochim. Biophys. Acta* **1655,** 116–122
40. Pujols-Ayala, I., and Barry, B. A. (2004) Tyrosyl radicals in photosystem II. *Biochim. Biophys. Acta* **1655,** 205–216
41. Saito, K., Rutherford, A. W., and Ishikita, H. (2013) Mechanism of tyrosine D oxidation in Photosystem II. *Proc. Natl. Acad. Sci. U.S.A.* **110,** 7690–7695
42. Lendzian, F. (2005) Structure and interactions of amino acid radicals in class I ribonucleotide reductase studied by ENDOR and high-field EPR spectroscopy. *Biochim. Biophys. Acta* **1707,** 67–90
43. Campbell, K. A., Peloquin, J. M., Diner, B. A., Tang, X. S., Chisholm, D. A., and Britt, R. D. (1997) The τ-nitrogen of D2 histidine 189 is the hydrogen bond donor to the tyrosine radical $Y_D^•$ of photosystem II. *J. Am. Chem. Soc.* **119,** 4787–4788
44. van Dam, P. J., Willems, J. P., Schmidt, P. P., Potsch, S., Barra, A. L., Hagen, W. R., Hoffman, B. M., Andersson, K. K., and Graslund, A. (1998) High-frequency EPR and pulsed Q-Band ENDOR studies on the origin of the hydrogen bond in tyrosyl radicals of ribonucleotide reductase R2 proteins from mouse and herpes simplex virus type 1. *J. Am. Chem. Soc.* **120,** 5080–5085
45. Thelander, M., Gräslund, A., and Thelander, L. (1985) Subunit M2 of mammalian ribonucleotide reductase. Characterization of a homogeneous protein isolated from M2-overproducing mouse cells. *J. Biol. Chem.* **260,** 2737–2741
46. Ito, N., Phillips, S. E., Stevens, C., Ogel, Z. B., McPherson, M. J., Keen, J. N., Yadav, K. D., and Knowles, P. F. (1991) Novel thioether bond revealed by a 1.7 Å crystal structure of galactose oxidase. *Nature* **350,** 87–90
47. Vaidya, A. T., Top, D., Manahan, C. C., Tokuda, J. M., Zhang, S., Pollack, L., Young, M. W., and Crane, B. R. (2013) Flavin reduction activates *Drosophila* cryptochrome. *Proc. Natl. Acad. Sci. U.S.A.* **110,** 20455–20460
48. Minnihan, E. C., Nocera, D. G., and Stubbe, J. (2013) Reversible, long-range radical transfer in *E. coli* class Ia ribonucleotide reductase. *Acc. Chem. Res.* **46,** 2524–2535
49. Lokhandwala, J., Hopkins, H. C., Rodriguez-Iglesias, A., Dattenböck, C., Schmoll, M., and Zoltowski, B. D. (2015) Structural biochemistry of a fungal LOV domain photoreceptor reveals an evolutionarily conserved pathway integrating light and oxidative stress. *Structure* **23,** 116–125
50. Oztürk, N., Song, S. H., Selby, C. P., and Sancar, A. (2008) Animal type 1 cryptochromes. Analysis of the redox state of the flavin cofactor by site-directed mutagenesis. *J. Biol. Chem.* **283,** 3256–3263
51. Hitomi, K., DiTacchio, L., Arvai, A. S., Yamamoto, J., Kim, S. T., Todo, T., Tainer, J. A., Iwai, S., Panda, S., and Getzoff, E. D. (2009) Functional motifs in the (6–4) photolyase crystal structure make a comparative framework for DNA repair photolyases and clock cryptochromes. *Proc. Natl. Acad. Sci. U.S.A.* **106,** 6962–6967

Supplemental Data for

Essential Role of an Unusually Long-Lived Tyrosyl Radical in the Response to Red Light of the Animal-Like Cryptochrome aCRY

Sabine Oldemeyer, Sophie Franz, Sandra Wenzel, Lars-Oliver Essen, Maria Mittag, and Tilman Kottke*

Table 1: NCBI accession numbers of proteins used in the phylogenetic analyses.

Protein	NCBI Accession Nr.
aCRY *Chlamydomonas reinhardtii*	XP_001698054.1
DNA photolyase *Volvox carteri*	XP_002945926.1
(6-4) photolyase *Dunaliella salina*	AAX56342.1
hypothetical protein *Chlorella variabilis*	XP_005843478.1
UVR3 (6-4) DNA photolyase *Coccomyxa subellipsoidea*	XP_005646798.1
UVR3 (6-4) DNA photolyase *Physcomitrella patens*	XP_001754074.1
predicted: (6-4) DNA photolyase *Nelumbo nucifera*	XP_010249985.1
(6-4) photolyase *Arabidopsis thaliana*	BAA24449
predicted: (6-4) DNA photolyase *Vigna radiata*	XP_014515872.1
(6-4) DNA photolyase *Glycine soja*	KHN47785.1
UVR3 (6-4) DNA photolyase *Medicago truncatula*	XP_013454694.1
predicted: (6-4) DNA photolyase *Nicotiana tomentosiformis*	XP_009598181.1
DNA photolyase family *Theobroma cacao*	XP_007023940.1
CPF1 *Phaeodactylum tricornutum*	XP_002180095.1

CPF1 *Ostreococcus tauri*	AAU14280.1
predicted: cryptochrome1like *Lingula anatina*	XP_013420209.1
(6-4) photolyase *Xenopus laevis*	NP_001081421.1
(6-4) photolyase *Drosophila melanogaster*	NP_001260633.1
CRY1a *Sylvia borin*	CAG14931.1
CRY1 *Homo sapiens*	NP_004066
CRY2 *Homo sapiens*	NP_066940
CRY2 *Danaus plexippus*	ABA62409
CRY4 *Gallus gallus*	NP_001034685
dCRY *Drosophila melanogaster*	O77059.1
CRY1 *Danaus plexippus*	EHJ63675.1

4.3 Structural and evolutionary analysis of algal cryptochromes

This review was originally published in the Journal of Plant Physiology by *Lars-Oliver Essen*, Sophie Franz, Ankan Banerjee.* **Structural and evolutionary aspects of algal blue light receptors of the cryptochrome and aureochrome type.** J Plant Physiol. 2017; 217: 27-37.

Summary

This review deals with the current knowledge of blue light receptors of the aureochrome and cryptochrome type in algae. The focus is on the structural and biophysical research on this field that has been done by others and our group. Both photoreceptors, cryptochromes and aureochromes, utilize a flavin chromophore to absorb in the blue range of the visible light spectrum. In algae, several multifunctional cryptochromes have been identified in the last 10 years, namely *Ot*CPF1 from *Ostreococcus tauri*, *Pt*CPF1 from *Phaeodactylum tricornutum* and *Cr*aCRY (57, 58, 232). Multifunctional in the sense, that they can act not only as regulators in gene expression, but also exhibit (6-4) photolyase activity. By structural comparison as well as *in vivo* assays (292), this group was shown to most likely bind 8-HDF as antenna chromophore in their N-terminal domain. The usage of a second chromophore as a light-harvesting antenna is highly advantageous in a marine environment, as the light conditions change within the different depths of water. As shown in the previous publications (293, 294), *Cr*aCRY comprises an extended electron transfer pathway by involving a fourth aromatic residue, Y373, which forms a long-lived radical upon photoreduction. *Pt*CPF1 presents a tryptophan at this particular position, so an elongation of the classical triad is also possible. In *Ot*CPF1, no redox active residue is present at the exact position, but without more structural and biophysical data, the presence of a tetrad cannot be excluded. In a sequence-similarity network analysis of the whole CPF with 13779 orthologs, animal-like cryptochromes and (6-4) photolyases were shown to cluster together in one distinct subfamily. This analysis reveals that the prediction, whether an enzyme acts as a (6-4)PHL or a CRY can not only rely on sequence relationships and there might be even more bifunctional members inside this subfamily. Another distinct group of cryptochromes which is present in algal organisms are the plant-like CRYs. They have been studied in *C. reinhardtii* (CPH1 or pCRY) and *Volvox carteri* (*Vc*CRYp) (226, 295, 296). Plant-like CRYs in

algae were found to bind ATP, just like their relatives in plants (297, 298). ATP-binding boosts the formation of the semiquinone anionic radical state, which is the active form in plant CRYs (295).

Aureochromes are a new type of blue light photoreceptors, which were first described in 2007 in a yellow-green alga *Vaucheria frigida* (299). There, two types of aureochromes could be identified: Aureo1, which regulates BL-induced branching, and Aureo2, which controls the development of the sex organ in *V. frigida*. Till now, aureochromes are exclusively found in aquatic species (300, 301) and they act generally as flavin-dependent photoreceptors for BL-induced transcription regulation. Aureochromes are composed of an N-terminal, DNA-binding basic leucine zipper (bZIP) domain which is linked to the flavin mononucleotide (FMN) binding LOV domain (302). The FMN is non-covalently bound in the dark, but upon BL absorption it forms a reversible C4 photoadduct with a conserved cysteine inside the chromophore binding pocket (5, 303). The C-terminus of the aureochrome LOV is flanked by a Jα-helix (303, 304), which undergoes a movement triggered by blue-light absorption. It was also observed, that aureochrome LOV domains form light-driven stable dimers and display concentration-dependent monomer-dimer equilibria in the dark (305–307). In the available structures, different dimerization modes are present (308–310). However, it is still unclear which mode represents the physiological state. It was shown, that the dimerization of the LOV domain can enhance bZIP domain dimerization and binding to AUREO-box containing DNA (311, 312). In fact, bZIP domains only dimerize when DNA is bound to it (313). The photochemistry in aureochromes is highly controlled by the Jα-helix (308, 309). Through HDX-MS, SAXS, FT-IR and CD spectroscopy the photochemistry of aureochromes has been extensively studied and different models for light-triggered effects on aureochrome/DNA complexes have been proposed (309, 311, 313, 314), which are currently under debate.

Contributions

L.-O. Essen, S. Franz and A. Banerjee wrote and revised the manuscript together.

Journal of Plant Physiology 217 (2017) 27–37

Contents lists available at ScienceDirect

Journal of Plant Physiology

journal homepage: www.elsevier.com/locate/jplph

Review article

Structural and evolutionary aspects of algal blue light receptors of the cryptochrome and aureochrome type☆

Lars-Oliver Essen[a,b,*], Sophie Franz[a], Ankan Banerjee[a]

[a] Department of Biochemistry, Philipps-University, 35043 Marburg, Germany
[b] LOEWE Center for Synthetic Microbiology, Philipps-University, 35043 Marburg, Germany

ARTICLE INFO

Keywords:
Aureochromes
Cryptochromes
Photoreceptor structures
Algae
Blue light
Flavoproteins

ABSTRACT

Blue-light reception plays a pivotal role for algae to adapt to changing environmental conditions. In this review we summarize the current structural and mechanistic knowledge about flavin-dependent algal photoreceptors. We especially focus on the cryptochrome and aureochrome type photoreceptors in the context of their evolutionary divergence. Despite similar photochemical characteristics to orthologous photoreceptors from higher plants and animals the algal blue-light photoreceptors have developed a set of unique structural and mechanistic features that are summarized below.

1. Introduction

The reception of light is an almost ubiquitous feature among organisms of prokaryotic and eukaryotic origin. Especially when their natural habitats *i.e.* aquatic systems, land surfaces or hosts for symbiotic and parasitic life styles are characterized by changing illumination conditions. The reception of blue light (BL) by photosynthetic organisms that thrive in water is of particular importance due to its large penetration depths in open oceans compared to other light qualities (red, green). Altering blue/green or blue/red intensity ratios can furthermore provide positional habitat information, *e.g.* towards coastal waters, where green light is significantly more effective at penetrating the water column.

Terrestrial plants, which originated from green algae about 450 Ma ago (Clarke et al., 2011), have only three different types of BL receptors, cryptochromes, phototropins and members of the Zeitlupe family (Christie et al., 2015). In contrast algae, *i.e.* photosynthetic eukaryotes living in aquatic systems, have originated more than 1500 Ma ago (Yoon et al., 2004). One prominent type of BL photoreceptors is represented here by the flavin-chromophore dependent cryptochrome-photolyase family (CPF). Photolyases, which are ubiquitously found in algae, have an enzymatic function by catalyzing the repair of UV lesions within DNA, namely of cyclobutane pyrimidine dimers (CPD) or (6-4) pyrimidine-pyrimidone photoproducts (Essen, 2006). This makes photolyases essential algal components for maintaining genome integrity due to the unavoidable presence of sun-derived UV radiation. In contrast, the structurally related cryptochromes act just as signaling proteins (Chaves et al., 2011) and are likewise found in all branches of photosynthetic eukaryotes. For comparison phototropins that act as light-activated protein kinase have only been described in green algae, the direct predecessors of land plants (Huang and Beck, 2003; Prochnik et al., 2010; Veetil et al., 2011). Although major parts of phototropin-mediated downstream signaling pathways are still unresolved in plants, the ortholog from the green alga *Chlamydomonas reinhardtii* can functionally replace its plant counterpart (Onodera et al., 2005).

Given their wide occurrence and diversification, additional BL photoreceptors can be found in algae. One example is the blue-light activated adenylyl cyclase PAC from *Euglena gracilis* (Iseki et al., 2002) that is associated with the eyespot of this flagellated species. Its flavin-comprising photoreceptor domain belongs to the BLUF (blue light using FAD) family, whose members otherwise occur in bacterial species (Masuda, 2013). Finally, even non-flavoprotein BL photoreceptors occur in algae. One type of BL photoreceptors actually belongs to the family of canonical phytochromes (Anders and Essen, 2015), which harbor a tetrapyrrole chromophore within their photosensory module. In plants, fungi and bacteria these phytochromes with a complex photosensory module consisting of PAS-, GAF- and PHY-domains are well known for their ability to undergo photochromic transitions between red and far-red light-sensitive states. Instead, orthologs from glaucophytes such as *Cyanophora* and *Gloechaete* show blue/far-red and blue/red transitions, respectively, whereas other algal phytochromes can cover different parts of the visible/near-IR spectrum (Rockwell et al., 2014). Another well-studied type of flavin-independent BL photoreceptors is represented by channelrhodopsins, a class of microbial

☆ This article is part of a special issue entitled: Light driven reactions in model algae published at the Journal of Plant Physiology 217C.

* Corresponding author at: Department of Biochemistry, Philipps-Universität, 35043 Marburg, Germany.
E-mail addresses: essen@chemie.uni-marburg.de, essenl@staff.uni-marburg.de (L.-O. Essen).

http://dx.doi.org/10.1016/j.jplph.2017.07.005
Received 21 May 2017; Received in revised form 5 July 2017; Accepted 5 July 2017
Available online 13 July 2017

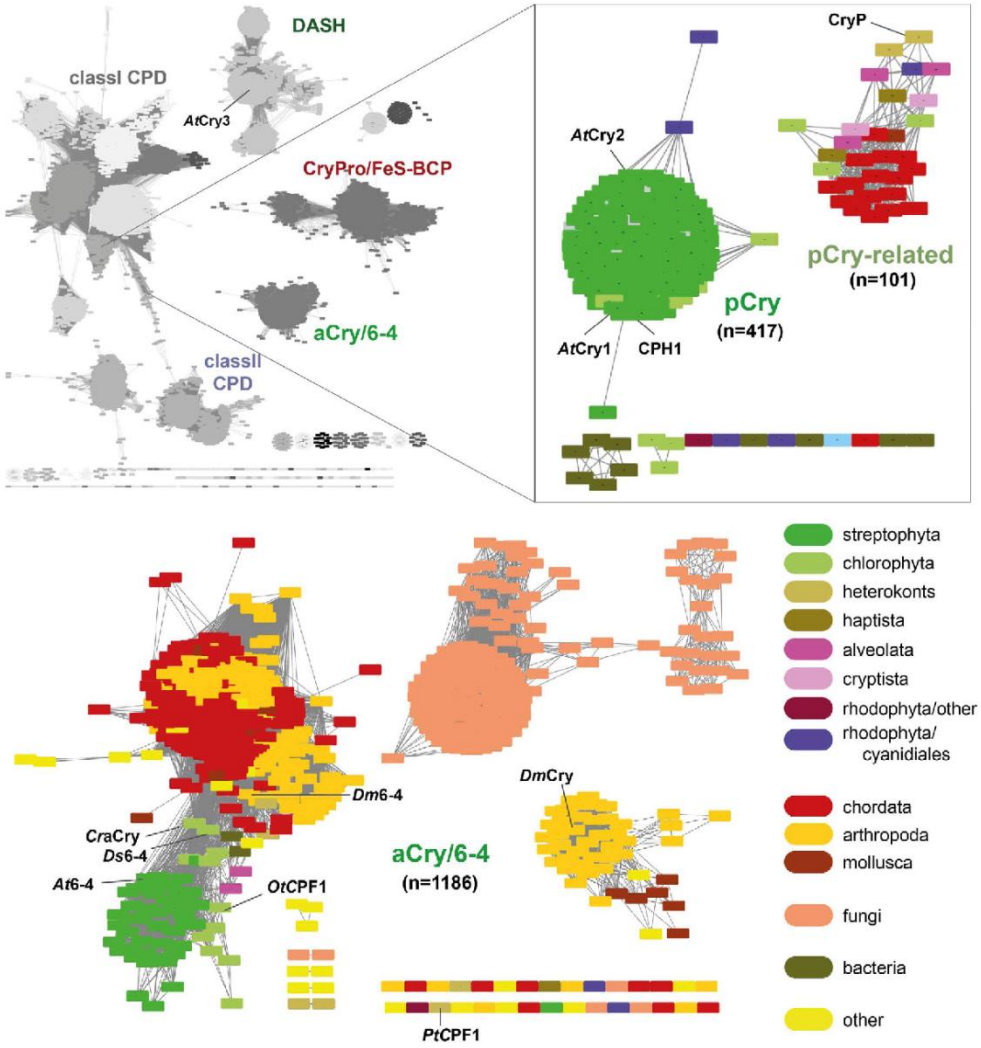

Fig. 1. Sequence-similarity network analysis (Gerlt et al., 2015) of the CPF with 13779 orthologs (Jan. 2017) using PFAM families PF00875 and PF04244. Left, each of the 7503 independent nodes represents sequences with more than 90% sequence identity, the edges correspond to BLAST E-value scores of below 10^{-90}. Obviously, the CPF dissolves in a set of highly distinct subfamilies. Right, view of the pCry and pCry-like cryptochromes after reclustering. Bottom, view on the family of animal-like cryptochromes/6-4 photolyases after decreasing the E-value cutoff to 10^{-150}. Used accession codes including further information are found in the Supplementary Information for the aCry/(6-4) photolyases as well as pCry and pCry-like orthologs.

rhodopsins with a photoisomerizable retinal chromophore that occur in flagellated green algae and mediate mostly proton/cation flow for triggering plasma membrane depolarization (Schneider et al., 2015). Finally, a distinct class of microbial rhodopsins in green algae is fused with a C-terminal histidine kinase domain and a response regulator and apparently function *via* a form of two-component signaling (Luck et al., 2012; Luck and Hegemann, 2017).

In this review, we will focus only on flavin-comprising cryptochromes and aureochromes that have been extensively studied during the last few years by others and us with biophysical and structural approaches. Other aspects of algal photoreceptors, which are not covered in this review, are covered elsewhere in depth (Duanmu et al., 2017; Fortunato et al., 2015; Hegemann, 2008; Arash Kianianmomeni and Hallmann, 2014; Suetsugu and Wada, 2013).

2. Dual function cryptochromes – a new class of photoreceptors found in algae

Cryptochromes have been evolutionary derived multiple times, either from class I CPD photolyases, like the plant and DASH-type cryptochromes, or from (6-4) photolyases as the animal-like cryptochromes (Fig. 1). The common feature between photolyases and cryptochromes is their ability to subject their inbuilt FAD chromophore to BL-induced photoreduction from an oxidized state (FAD) to a semi-reduced form ($FAD\cdot^-$, $FADH\cdot$) and, in the case of photolyases, to the fully reduced $FADH^-$ state (Chaves et al., 2011). The mode of light-dependent downstream signaling by many cryptochromes has not yet been entirely understood in structural terms, although a multitude of light-dependent interactors have been identified for plant- and animal-like cryptochromes (pCry and aCry). For example, the animal type I cryptochrome

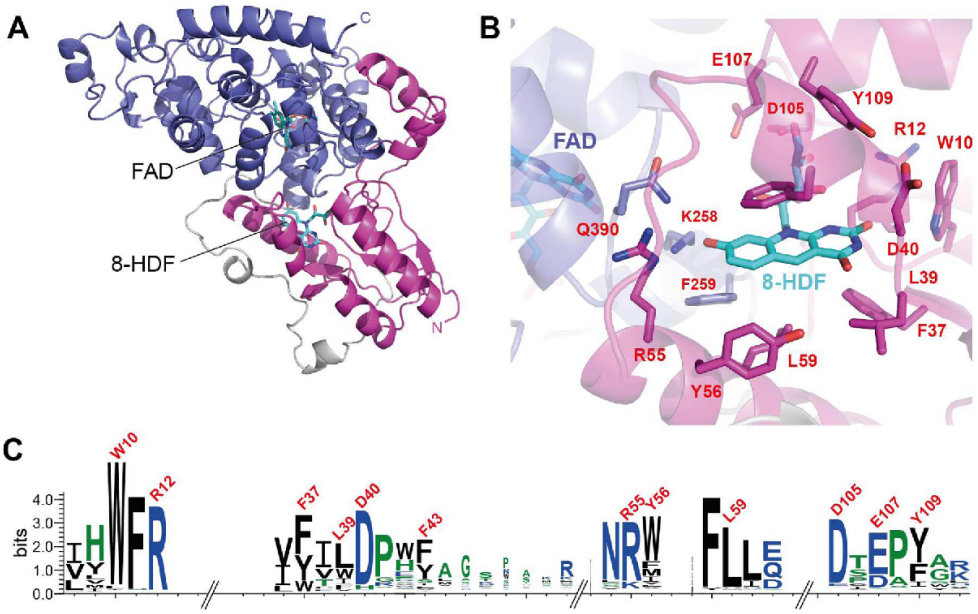

Fig. 2. A, Homology model of *Cra*Cry based on the structure of the *Drosophila melanogaster* cryptochrome (3CVV). The N-terminal antenna-binding domain is shown in magenta, the C-terminal catalytic domain in blue. The grey stretch corresponds to the variable linker between both domains. B, Model of the 8-HDF binding site of *Cra*Cry. C, Weblogo based on the multiple sequence alignment for residues of the 8-HDF binding pocket from 6 to 4 photolyases/animal-like cryptochromes. Residues predicted to be involved in 8-HDF binding by *Cra*Cry are highlighted.

from the insect *Drosophila melanogaster* (*Dm*Cry) depends on a light-dependent interaction between its C-terminal extension (CTE) and photolyase-like domain (Zoltowski et al., 2011).

During the last decade, several multifunctional cryptochromes have been identified in algae (Beel et al., 2013). The first example of this type of blue-light dependent photoreceptors was detected in the marine diatom *Phaeodactylum tricornutum* (Coesel et al., 2009). This cryptochrome, *Pt*CPF1, belongs to the branch of the cryptochrome-photolyase family, whose closely related members are known either to repair (6-4) DNA lesions or to mediate down-stream signaling in higher plants and metazoans. For example, *Dm*Cry synchronizes the circadian rhythm of *Drosophila* to the diurnal cycle, whereas the structurally highly related (6-4) photolyase (r.m.s.d. 0.91 Å for 329 Cα atoms of *Dm*Cry, PDB codes 3CVV *vs* 4GU5) functions as a light-dependent DNA repair enzyme (Maul et al., 2008). Interestingly, *Pt*CPF1 is capable of both, as it not only repairs (6-4) pyrimidine-pyrimidone lesions in double-stranded DNA, but also exerts a significant effect on the regulation of various genes upon homologous overexpression in *P. tricornutum*, specifically those involved in nitrogen metabolism or cell-cycle progression (Coesel et al., 2009). This dual role of *Pt*CPF1 was further confirmed *in vivo* by phenotypic analyses of *Pt*CPF1 knockdown mutants (De Riso et al., 2009). Despite the above-mentioned bifunctionality in algae, the structural and functional similarity of *Pt*CPF1 to metazoan cryptochromes is still high enough to act as transcriptional repressor of the circadian clock in mammalian cell reporter assays. These findings were the first to challenge the notion of a strict functional differentiation between photolyases and cryptochromes within the CPFs. Another member of this subfamily of animal-like cryptochromes with dual function, *Ot*CPF1, was discovered in the green algae *Ostreococcus tauri* (Heijde et al., 2010). Whereas *Ot*CPF2 is a conventional class II CPD photolyase, *Ot*CPF1 exhibits not only (6-4) photolyase activity, but also represses CLOCK:BMAL1-regulated expression in a mammalian reporter model for circadian rhythm control (Heijde et al., 2010).

In the green algae *Chlamydomonas reinhardtii,* several photoreceptors of the CPF were identified. Amongst them were one plant-like (CPH1), an animal-like (*Cra*CRY), two DASH-type cryptochromes and one class II CPD photolyase (Kottke et al., 2017). *Cra*CRY is highly related to *Ot*CPF1 and *Pt*CPF1 (Fig. 1), but also to the (6-4) photolyases of *Dunaliella salina* and *Arabidopsis thaliana* (Beel et al., 2012; Oldemeyer et al., 2016). It shows a different functional behavior than *Pt*CPF1, as it was found not only to be competent in blue light sensing but also to be capable of responding to yellow and red light (Beel et al., 2012). This surprising finding was interpreted to be caused by the broad absorption characteristics of semi-reduced FADH·, as it not only absorbs BL but also orange (λ_{max} 585 nm) and red light (λ_{max} 633 nm). A canonical phytochrome that could instead exert these light-dependent reactions has not been identified so far in the *C. reinhardtii* genome, although the required biosynthetic pathway for a linear tetrapyrrole chromophore has been demonstrated (Duanmu et al., 2013). According to this model, *Cra*Cry might act as a white-light sensor, whose signaling state may be the $FADH^-$ state unlike other cryptochromes, which depend on a semi-reduced redox state for signaling. Given its similarity to *Ot*CPF1, *Cra*CRY can be suspected to show (6-4) repair activity as well, especially since no other ortholog of a (6-4) photolyase exists in the *C. reinhardtii* genome that can ensure genomic DNA integrity. Indeed, its counterpart in the halotolerant green alga *Dunaliella salina*, with which it shares 72% sequence identity, has been characterized as 6-4 photolyase (Yan Lv et al., 2008; Zhang et al., 2011). Likewise, current data from us show a 6-4 photolyase activity for *Cra*Cry (unpublished observation).

These algal cryptochromes are not the only members in the CPF, which show that extent of multifunctionality. Previously described fungal photolyases and cryptochromes such as PHR from *Trichoderma atroviride* (Berrocal-Tito et al., 2007) and others (Bayram et al., 2008; Bluhm and Dunkle, 2008; Tagua et al., 2015) likewise function as DNA repair enzymes and concomitant activity for light-regulated gene expression.

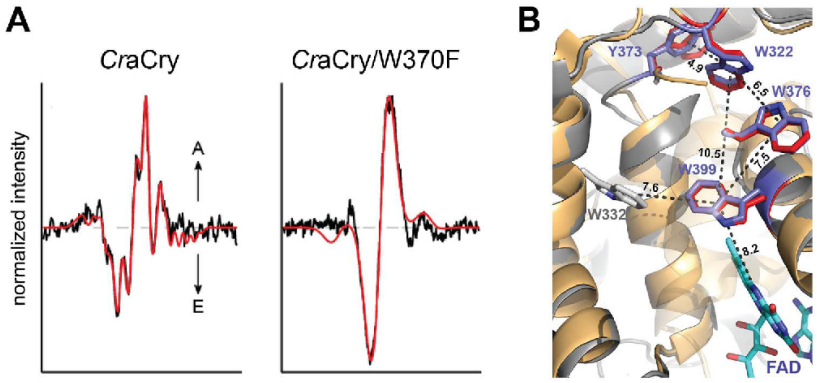

Fig. 3. The aromatic tetrad of the animal-like cryptochrome from *Chlamydomonas reinhardtii* (modified from Nohr et al., 2016). A, The transient-EPR spectra (experimental: black; simulated: red) show the contribution of a tyrosyl radical besides the FAD·⁻ radical. TheW370F mutant shows a signature that is typical for other photolyases/cryptochromes with a conventional tryptophan triad. B, Model of the aromatic tetrad of *Cra*Cry, residues are highlighted as blue sticks. In red, the corresponding aromatic tetrad of *Dm*Cry is depicted. Centroid-centroid distances between aromatic residues are given in Å.

3. Structural aspects of algal cryptochromes

All photolyases and cryptochromes share a conserved bilobal architecture (Fig. 2A), where the FAD chromophore is non-covalently bound to the C-terminal domain in an unusual U-shaped conformation (Mees et al., 2004). The N-terminal domain can bind a second chromophore as light-harvesting antenna to broaden the activity spectrum into the visible region of the light spectrum (Chaves et al., 2011). So far identified antenna chromophores in the CPF include 5,10-methenyltetrahydrofolate (MTHF; Klar et al., 2007; Park et al., 1995), 8-hydroxydeazaflavin (8-HDF; Kiontke et al., 2014), flavin mononucleotide (FMN; Klar et al., 2006), 6,7-dimethyl-8-ribityllumazine (DMLR; Geisselbrecht et al., 2012; Zhang et al., 2013) and a second FAD in its fully oxidized state (Fujihashi et al., 2007). The nature of the antenna chromophore in the multifunctional algal cryptochromes/photolyases is still unknown as the heterologously expressed proteins do not harbor a second chromophore (Beel et al., 2012; Usman et al., 2009), most likely due to a missing biosynthesis pathway, *e.g.* for 8-HDF, or by being lost during purification. By homology modeling of the antenna binding pocket of *Ot*CPF1 with the CPD photolyase of the cyanobacterium *Synechococcus elongatus*, *Ot*CPF1 was proposed to bind most likely 8-HDF *in vivo* (Brazard et al., 2012). FO synthases (7,8-didemethyl-8-hydroxy-5-deazariboflavin synthase) are bifunctional enzymes, which catalyze the biosynthesis of the required 8-HDF in two steps, and are indeed present in green algae and mosses, but not higher plants (Kiontke et al., 2014). In *Chlamydomonas reinhardtii* Petersen et al. showed that the inactivation of the *phr1* gene, which encodes a FO synthase, causes a similar loss of photoreactivation under physiological conditions as deletion of the *phr2* gene that encodes the corresponding class II CPD photolyase (Petersen and Ronan, 2010; Petersen and Small, 2001). Obviously, 8-HDF can act as an antenna chromophore in several members of the CPF from green algae (Fig. 2B, C) as we could also find 8-HDF binding to *Cra*CRY as cognate antenna (unpublished observation).

In cryptochromes, the N-terminal α/β and the C-terminal all-α domain form together the photolyase homology region (PHR). Unlike photolyases, cryptochromes harbor usually elongations at the C-terminus of their PHR. These C-terminal extensions (CTE) are variable in length and mostly disordered without the presence of an interaction partner and have hence been postulated to be key element in cryptochrome-triggered signal transduction cascades (Liu et al., 2011). The animal-like cryptochrome of *Chlamydomonas* shares this structural element, as it holds a C-terminal elongation of about 100 amino acids. Studies of the CTE revealed a function as putative dimerization motif of *Cra*CRY (Oldemeyer et al., 2016) *in vitro*. Direct evidence of a conformational change upon blue or red light illumination still awaits experimental proof.

For the plant-type cryptochrome (CPH1) of *C. reinhardtii*, Reisdorph and Small studied deletion mutants concerning the C-terminal elongation, which is unusually long (530 amino acids). They showed that the CTE is not only posttranslationally modified, but also improves protein stability under both light and dark conditions (Reisdorph and Small, 2004).

4. Electron transfer *via* a tetrad of aromatic residues in animal-like cryptochromes

So far, photoreduction of cryptochromes and photolyases is generally acknowledged to proceed *via* an electron transfer (ET) pathway between the FAD chromophore and the protein surface *via* a highly conserved tryptophan triad (Chaves et al., 2011). In 2015 Müller et al. reported the existence of a fourth aromatic residue, which extends the electron transfer pathway in the *Xenopus laevis* (6-4) photolyase (Müller et al., 2015). The respective tryptophan residue of *Xl*(6-4) photolyase (W370) was identified by sequence alignments to be a common feature of animal-like cryptochromes and (6-4) photolyases including the dual-function photoreceptor *Pt*CPF1 (Müller et al., 2015). Fast-spectroscopy studies on the photoreduction of the *Xl*(6-4) photolyase and its tryptophan mutant W370F showed a highly distinct kinetic behavior. The FAD·⁻/Trp_4· biradical pair in the *Xl*(6-4) wild type had a much longer lifetime of 35 ms in contrast to 50 ms observed for the FAD·⁻/Trp_3· radical pair in the W370F mutant (Müller et al., 2015). The importance of the 4th tryptophan for the formation of stable biradical states was corroborated by polarizable molecular dynamics simulations and constrained density functional theory calculations (Cailliez et al., 2016).

Two studies addressed the aromatic tetrad of *Cra*Cry, which is represented by the ET pathway Y373 → W322 → W376 → W399 → FAD (Nohr et al., 2016). In this algal animal-like cryptochrome transient EPR spectroscopy (Fig. 3A) shows that the terminal electron donor is indeed a tyrosine residue and not a tryptophan as in *Xl*(6-4) or *Dm*Cry (Nohr et al., 2016). The predicted distance between the centroid of the aromatic side chain of Y373 and the next tryptophan, W322, is 4.9 Å and thereby comparable to other Trp–Trp distances within the aromatic tetrad (Fig. 3B). Similar to the *Xl*(6-4) photolyase a lifetime of 26 ms could be assigned to the FAD·⁻/Tyr_4· biradical, whereas the BL-formed Y373F biradical undergoes a fast decay with a lifetime of 8.5 µs. Unlike the wild type, this mutant was incapable to undergo full light-driven reduction to the $FADH^-$ state in the presence of external reductants. The second study focused on the photoreduction step from FADH· to $FADH^-$ using red light for the selective excitation of the semiquinone state (Oldemeyer et al., 2016). Interestingly, the lifetime of the tyrosyl radical is now remarkably long, 2.6 s, although Y373 is predicted to be surface-exposed (Oldemeyer et al., 2016). The longer lifetime of radical states generated in the absence of external reductants may be beneficial for signaling or DNA repair, as the latter relies on the fully reduced $FADH^-$ state (Müller et al., 2015). Y373 of *Cra*Cry is also

present in three other members of the algal, animal-like/(6-4) photolyase subgroup (Oldemeyer et al., 2016), whereas the diatomaceous *Pt*CPF1 harbors here a tryptophan. Interestingly, *Ot*CPF1 is an exception as it shows no suitable electron donor (Tyr, Trp) at this position, but a phenylalanine. Therefore the presence of an aromatic tetrad may not be decisive for the dual functionality as described for *Ot*CPF1 (Heijde et al., 2010). This does not exclude the formation of the $FADH^-$ state that is essential for (6-4) photolyase activity as observed before for the *Cra*Cry/Y373F mutant, because its known that the *in vivo* redox properties of photolyases and cryptochromes can differ significantly from their *in vitro* behavior (Engelhard et al., 2014). Notably, the related type II cryptochromes of vertebrates have further radiated from the branch of animal-like cryptochromes, as they lost the tight binding of the FAD chromophore and thereby their function as photoreceptor. Instead, they remained in these animals as essential components of the internal circadian clock.

5. pCry and pCry-related cryptochomes in algae

In addition to animal-like cryptochromes, cryptochromes of the plant type (pCry) have been analyzed for *Chlamydomonas reinhardtii* (CPH1 or pCRY) and *Volvox carteri* (*Vc*CRYp; Kianianmomeni and Hallmann, 2014). *Chlamydomonas* cells accumulate CPH1 in the dark, which degrades upon illumination with blue or red light (Reisdorph and Small, 2004). The photoreduction mechanism of this plant cryptochrome was studied by femtosecond spectroscopy and validated the importance of the intact tryptophan triad for photoreduction (Immeln et al., 2012). *Vc*CRYp is proposed to be an upstream or downstream regulator in the cell type-specific regulation of photosynthesis and may be involved in apoptosis as well (Kianianmomeni and Hallmann, 2014).

Bioinformatics analysis by sequence-similarity network clustering of the CPF (Fig. 1) shows that cryptochromes of the pCry-type (417 orthologs, Feb. 2017), which cocluster with plant cryptochromes such as cryptochrome 1 and 2 from *A. thaliana*, are restricted to the viridiplantae apart from two exceptions, which belong to red algae. Interestingly, pCry-type cryptochromes appear to share the ability to bind ATP for regulating their photochemistry (Engelhard et al., 2014; Müller et al., 2014), as the ATP-binding site that was structurally characterized for *At*Cry1 (Brautigam et al., 2004) is highly conserved among these cryptochromes. Like its plant relatives CPH1 from *Chlamydomonas reinhardtii* exerts ATP-binding and boosts formation of its radical state that is further augmented by autophosphorylation under *in vitro* conditions (Immeln et al., 2007). This cryptochrome may also be a key to understand the related plant cryptochromes in terms of their redox-dependent signaling. Time-resolved FT-IR spectroscopy shows that formation of the radical state and deprotonation of an aspartate upon BL illumination cause significant secondary structure changes, which have been attributed to an interaction between the CTE and the N-terminal antenna domain (Thöing et al., 2015). Other chlorophytes with such a pCry-type cryptochrome capable of ATP-binding include *Coccomyxa subellipsoidea*, *Volvox carteri*, *Gonium pectorale*, *Auxenochlorella protothecoides, Tetraselmis* sp. and *Monoraphidium neglectum*. Interestingly, red algae from the order of cyanidiales, such as *Galdieria sulphuria* and *Cyanidioschyzon merolae*, harbor also ATP-binding pCry-orthologs.

Interestingly, the subfamily of pCry-related orthologs, of which only *Pt*CryP from the diatom *Phaeodactylum tricornutum* has been characterized, lacks the conserved set of residues in the ATP-binding site. This restricted distribution of pCry orthologs in the green lineage hence indicates that ATP-binding as a "booster" for light-sensitivity may have arisen only in this branch of photosynthetic organisms. Given that pCry orthologs apparently exist *in vivo* predominantly as ATP complexes it cannot be excluded that the bound ATP molecule is involved in interactions with other downstream effector molecules as well. CryP mediates light-dependent regulation of genes encoding light-harvesting proteins of the LhcX type (Juhas et al., 2014; König et al., 2017) and displays like other cryptochromes a CTE of about 70 amino acids. It binds MTHF as antenna chromophore (Juhas et al., 2014), probably in a similar mode as in class I photolyases. However, no affinity to CPD-damaged DNA or repair activity of this lesion has been observed for CryP, indicating towards a monofunctional cryptochrome. Accordingly, expression of CryP under high-light conditions was found not to be up-regulated in contrast to *Pt*CPF1, which repairs (6-4) damaged DNA (Juhas et al., 2014).

6. Aureochromes – a unique type of LOV-domain based blue light receptors

Aureochromes were first described as blue-light photoreceptors in *Vaucheria frigida*, a yellow-green alga, and *Fucus distichus*, a brown alga (Takahashi et al., 2007; Kroth et al., 2017). Before, no member of a known photoreceptor such as plant-like phototropins (Christie et al., 2007) had been identified in *V. frigida*, which could explain its various BL-induced responses (Ishikawa et al., 2009; Takahashi et al., 2001). In *V. frigida* two paralogs of aureochrome have been identified, *Vf*Aureo1 and *Vf*Aureo2. Aureo1 was found to regulate BL-induced branching, whereas Aureo2 controls the development of the sex organ in *V. frigida* (Takahashi et al., 2007).

Subsequent studies showed that aureochromes are found in several species of the superphylum of heterokonts, all of them belong to photosynthetic, but not heteterotrophic stramenopiles (Ishikawa et al., 2009; Suetsugu and Wada, 2013). Heterokonts represent a highly diverse set of aquatic species, which are found as either multicellular or unicellular forms, *e.g.* the diatoms (Adl et al., 2005). So far heterokonts that harbor aureochrome, have more than one aureochrome paralog in their genome (Ishikawa et al., 2009; Schellenberger Costa et al., 2013). In the diatom *P. tricornutum* four aureochrome paralogs were identified *Pt*AUREO1a–1c and *Pt*AUREO2. *Pt*AUREO1a is involved in photoacclimation by regulating the LhcX gene promoter and induces BL-dependent cell division by regulating the promoter of the cyclin dsCYC2 and the transition to the G1 checkpoint of the cell cycle (Huysman et al., 2013; Schellenberger Costa et al., 2013). Furthermore, the expression of *Pt*AUREO1a and *Pt*AUREO1c was found to be regulated in a circadian rhythm while *Pt*AUREO1b is strictly regulated by light. The expression of *Pt*AUREO2, whose gene product is predicted to lack the flavin chromophore, is independent of either circadian rhythm or light conditions (Banerjee et al., 2016b). Together with data for the whole-genome expression patterns of the diatom *Thalassiosira pseudonana* (Ashworth et al., 2013), whose genome likewise includes four aureochromes, one may infer that aureochrome paralogs exert specialized functions in these algae analogous to the situation in *V. frigida*. Interestingly in the evolutionary distant raphidophyte *Heterosigma akashiwo*, a marine bloom-forming alga, a similarly diverse regulatory pattern has been observed for its four aureochrome paralogs *Ha*AUREO1-4 (Ji et al., 2017). In the brown alga *Saccharina japonica* the *Sj*Aureo ortholog was predicted to be associated with BL-dependent photomorphogenesis and early development of the sporophyte (Deng et al., 2014, 2012). Although the precise biological functions have still to be shown for most representatives of the aureochrome family, one can derive from these data that aureochromes generally act as flavin-dependent photoreceptors for BL-dependent transcription regulation. Surprisingly, heterologous expression of *Ng*AUREO1 from *Nannochloropsis gaditana* in the yeast *Saccharomyces cerevisiae* resulted in some degree of lipid accumulation that was apparently caused by changes of the expression of enzymes from the lipid metabolism (Huang et al., 2014).

7. Molecular architecture of aureochromes

Apart from aureochromes, all flavin-dependent photoreceptors studied until now have an N-terminal photosensory domain that precedes a C-terminal effector domain (Herrou and Crosson, 2011; Janovjak, 2016). Phototropins represent a very prominent example, where two

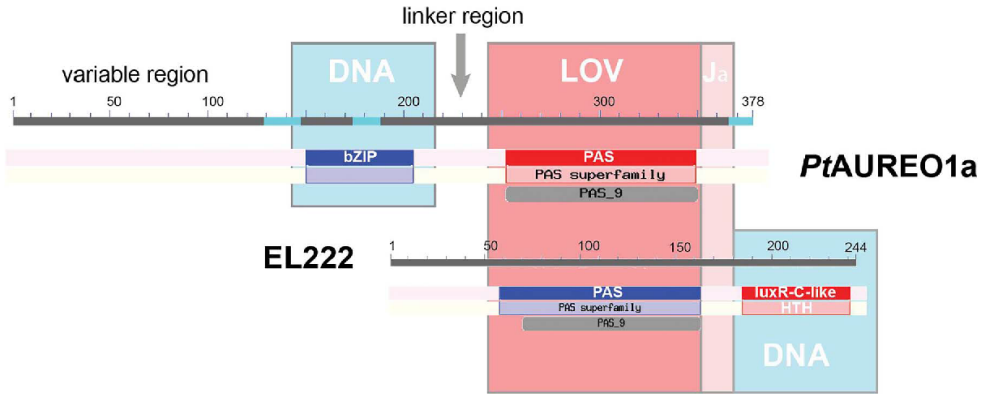

Fig. 4. The inversed topology of aureochromes using *Pt*Aureo1a as example. Among different aureochromes the variable region differs highly in length and sequence; its role for aureochrome-mediated signal transduction is unknown. For comparison, the conventional sensor-effector topology of the bacterial photoreceptor EL222 from *Erythrobacter litoralis* is shown.

light-sensing LOV domains are followed by a Ser/Thr protein kinase domain, but other LOV domain containing photoreceptors like YtvA, EL222 and others have a similar sensor-effector topology (Herrou and Crosson, 2011). By their N-terminal, DNA-binding bZIP domain, which is linked to the flavin mononucleotide (FMN) binding LOV domain, aureochromes are the sole known example which holds a reversed effector-sensor topology for BL-reception (Takahashi, 2016). Given its function as transcription regulator, the simple topology of aureochromes made them to natural candidates as optogenetic tools in transcription regulation. However, compared to the well-studied bacterial counterpart EL222 with its conventional LOV-HLH topology (Nash et al., 2011), whose function is BL-dependent DNA-binding, the inversed topology of aureochromes raises question how and whether at all light-absorption affects binding of cognate DNA motifs (Fig. 4).

Given their simplicity, basic leucine zipper (bZIP) domains appear to be very ancient DNA binding modules found in all three kingdoms of life (Hakoshima, 2005). Their α-helical segment dimerizes at its C-terminus as a coiled-coil along three to five leucine residues, which occupy the fourth position of a heptad motif (Alber, 1992; Hakoshima, 2005). This zipper-like structure is further elongated as helix at its N-terminus, thus that the N-termini can bind the major DNA groove *via* flanking basic residues (Ellenberger, 1994; Ellenberger et al., 1992; Glover and Harrison, 1995). Their strict specificity towards cognate DNA target sequences is a further, striking feature of bZIP domains that is augmented by their ability to change specificity by hetero-dimerization with other bZIP domains (Busch and Sassone-Corsi, 1990; Hakoshima, 2005). The interfaces of the coiled-coil homo- or hetero-dimers are rich in hydrophobic residues and charged residues for forming inter-helical ion bridges. bZIP domains are rather mobile, because DNA binding to the basic N-terminal region induces an increase of the α-helical content of the bZIP domain.

In plants, the recognized DNA sequence motif is often characterized by including a central ACGT motif, the flanking nucleotides then define the specificity (Foster et al., 1994). Using sequence similarity networks, the plant bZIPs (mainly *Arabidopsis thaliana*) were classified into ten different subtypes (A-I and S; Jakoby et al., 2002). The bZIP domain of aureochromes was initially assigned to the corresponding S/D-subtype of bZIP subfamilies (Takahashi et al., 2007), before Isikawa et al. proposed that the aureochrome bZIP domain is better classified by belonging to the G-subtype, which also includes G-box (CACGTG) binding factors (Ishikawa et al., 2009). Interestingly, the bZIP domain of aureochromes can be further classified into two distinct groups. In one group, the dimerization of the bZIP domains, *e.g.* in *Vf*Aureo1, depends on stable intermolecular disulphide bridges between conserved cysteine residues (Hisatomi et al., 2014), whereas the other group, *e.g.* represented by *Pt*Aureo1a, lacks cysteines, but can nevertheless form stable dimers (Banerjee et al., 2016b). Accordingly, mutations of the conserved cysteines in *Vf*Aureo1 (C162, C182) to serine hindered its dimerization and make it plausible that this group of aureochromes might be additionally regulated by a redox mechanism (Hisatomi et al., 2014). The bZIP domains of aureochromes do not only allow homodimer formation, but can also drive heterodimerization as demonstrated for the *Pt*Aureo1a/*Pt*Aureo1c pair (Banerjee et al., 2016b). With a dissociation constant of 0.2 μM the affinity was similarly high as for homodimers and at least for these diatomaceous aureochromes not affected by light. Heterodimerization can clearly widen the *in vivo* function of aureochromes, although this awaits experimental proof.

The Light-Oxygen-Voltage (LOV) domain is a subset of the Per-ARNT-SIM (PAS) superfamily and involved in various blue light-mediated responses such as phototropism, chloroplast relocation, stomatal opening/closing and regulation of circadian rhythm (Herrou and Crosson, 2011). The LOV domain absorbs BL by its non-covalently bound flavin chromophore, mostly FMN, in its oxidized state, *i.e.* in darkness, with absorption maxima of 358, 375 and 448 nm. Upon BL-illumination, the flavin cofactor forms a reversible C4(a) photoadduct (λ_{max} 390 nm) with a cysteine that is conserved in the chromophore binding site (Herrou and Crosson, 2011; Losi and Gärtner, 2011). In terms of signal transduction to effector domains, the N- and C-terminal helices of LOV domains are known to play a critical role. Here, the conserved core that is defined by an Aβ-Bβ-Cα-Dα-Eα-Fα-Gβ-Hβ-Iβ topology is flanked at the N-terminus by an A′α helix and at the C-terminus by the Jα helix (Conrad et al., 2014; Herrou and Crosson, 2011). In aureochromes, the LOV domain shares homology with the LOV2 domain of plant phototropins (Christie, 2007; Takahashi et al., 2007). For both *Vf*Aureo1 and *Pt*Aureo1a their LOV domains have been extensively studied by UV/Vis, FT-IR, TG, and CD spectroscopy as well as by SEC, HDX-MS, SAXS and biomolecular crystallography in both dark and lit states (Banerjee et al., 2016a; Heintz and Schlichting, 2016; Herman et al., 2013; Herman and Kottke, 2015; Toyooka et al., 2011). FT-IR studies on the isolated LOV domain of *Pt*Aureo1a revealed an allosteric trigger for the unfolding of the flanking helices. Here, the adduct formed upon BL-absorption triggers not only Jα helix undocking/unfolding, but also a concomitant unfolding of the N-terminal A′α helix. Another feature of some LOV domains is their ability to dimerize upon BL-illumination. Aureochrome LOV domains indeed show formation of light-driven stable dimers, concentration dependent monomer-dimer equilibria are also evident in the dark state (Herman et al., 2013; Herman and Kottke, 2015; Toyooka et al., 2011).

Five crystal structures of aureochrome LOV domains are currently available, two from *Pt*Aureo1a (PDB codes: 5A8B, 5DKK) and one from

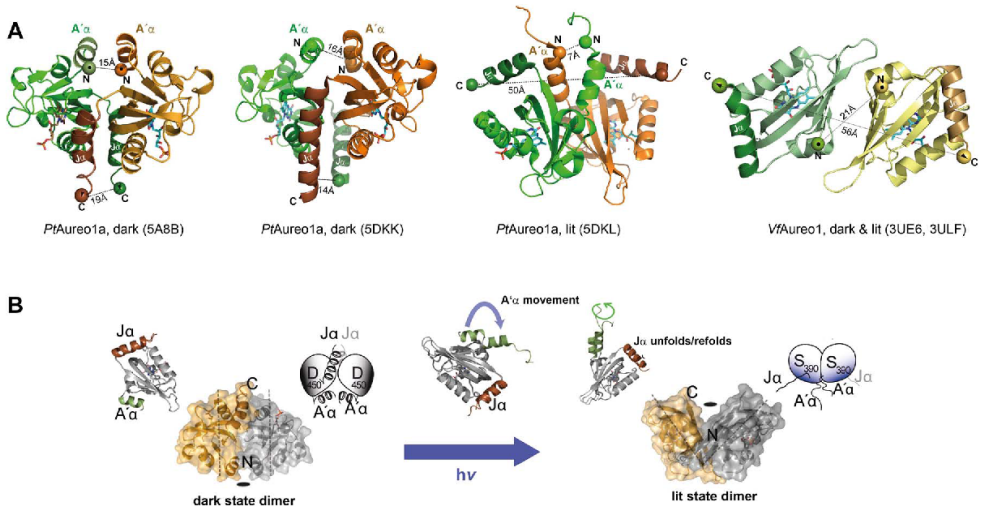

Fig. 5. A, Dimeric structures of aureochrome LOV domains. The lit state structure of the *Pt*Aureo1a LOV domain exhibits some asymmetry at the paired A'α helices. B, Model of light-triggered rearrangement of the LOV dimer within aureochromes.

*Vf*Aureo1 (3UE6) in the dark state as well as one from *Pt*Aureo1a (5DKL) and *Vf*Aureo1 (3ULF) in their lit states (Banerjee et al., 2016a; Heintz and Schlichting, 2016; Mitra et al., 2012), respectively. All of these structures show a dimeric arrangement of the LOV domains in their dark and lit states (Fig. 5A) as exemplified for the dark-state LOV domain of *Pt*Aureo1a, which adopts an almost identical native-like dimeric arrangement despite being analyzed in two different crystal forms (Banerjee et al., 2016b). The *Vf*Aureo1 LOV domain structure shows an antiparallel arrangement (Mitra et al., 2012) in both its dark and lit states although in this case, the lit state was generated by illumination of dark-state crystals. Insofar, no major structural rearrangement apart from FMN-cysteine adduct formation could occur in the crystalline state (Mitra et al., 2012). The *Pt*Aureo1a LOV domain adopts a different dark state arrangement than *Vf*Aureo1 (Banerjee et al., 2016a). Here, the flanking helices, A′α and Jα play crucial roles in stabilizing the dark state dimer interface, whose core mainly consists of paired β-sheets, which contact each other face-to-face. The structure of the *Pt*Aureo1a LOV domain in its lit state was derived from crystals grown under BL conditions (Heintz and Schlichting, 2016). Accordingly, the resulting LOV dimer revealed a new dimerization mode, where the protomers rotated 173° along the symmetry axis (Fig. 5B) when being compared to the dark state dimer (Banerjee et al., 2016b; Heintz and Schlichting, 2016). As expected, the lit state structure shows unfolding of the Jα helix and undocking of the A′α helix, which covered parts of the dimer interface in the dark (Heintz and Schlichting, 2016). The lit state flexibility of the flanking helices was confirmed by FT-IR, SAXS and HDX-MS (Banerjee et al., 2016a; Heintz and Schlichting, 2016; Herman and Kottke, 2015). Post-translational modification of the Jα-helix may be also a pathway for modulation of aureochrome activity, because phosphoproteome data for *P. tricornutum* indicate that at least *Pt*Aureo1b harbors a phosphorylation site in its Jα-helix (Chen et al., 2014).

Aureo2 from the heterokont *V. frigida* lacks a bound flavin cofactor due to replacement of a conserved glutamate by isoleucine, which is required to stabilize the isoalloxazine ring of FMN by hydrogen bonding (Ishikawa et al., 2009; Takahashi et al., 2007). Using homology modeling and mutagenesis analysis based on *Pt*Aureo1a it could be shown that not only the lack of a conserved glutamate, but also the presence of a voluminous methionine in the flavin binding site of *Pt*Aureo2 ablates FMN-binding (Banerjee et al., 2016a). The function of these flavin-less Aureo2-like aureochromes remains to be determined, but given their ability to be involved in heterodimer formation *via* their bZIP domains one may argue that they modulate the function of other, light-dependent aureochromes.

8. DNA binding by aureochromes

The nuclear localization of *Vf*Aureo's and the presence of a bZIP domain prompted Takahashi et al. to perform a random oligonucleotide binding assay, which identified the TGACGT motif as its cognate recognition sequence of *Vf*Aureo1 (Takahashi et al., 2007). Interestingly, no BL-effect on the binding ability of *Vf*Aureo1 to this AUREO-box motif could be then demonstrated. In the case of *Pt*Aureo1a, two studies were conducted using the same functional bZIP-LOV module, but different buffer conditions to delineate the effect of BL. Again, only moderate effects on DNA binding were observed with either a 9.6-fold or twofold increase in affinity upon BL illumination (Banerjee et al., 2016b; Heintz and Schlichting, 2016). Apparently, dimeric PtAureo1a can bind to the AUREO-box even in its dark state. However, BL can induce formation of higher oligomeric species of *Pt*Aureo1a (Banerjee et al., 2016b). Finally, *Pt*Aureo1a can not only interact with the AUREO-box but can also form stable complexes with the G-box motif, which is also widely distributed in the diatom genome (Banerjee et al., 2016b; Ishikawa et al., 2009).

As mentioned above redox-regulation of dimerization has been proposed for the *V. frigida* aureochrome (Hisatomi et al., 2014). Using monomeric cysteine mutants of *Vf*Aureo1, it could be delineated that dimerization of the sensory LOV domain can enhance bZIP domain dimerization and subsequent binding to AUREO-box comprising DNA (Hisatomi et al., 2014, 2013; Hisatomi and Furuya, 2015). Recently a time-resolved approach based on transient grating (TG) method confirmed the conclusion above and indicated that monomeric bZIP domains dimerize only when bound to DNA (Akiyama et al., 2016). The physiological role for this group of aureochromes with cysteine-comprising bZIP domains is presently unknown. Whether these results reflect an *in vivo* situation, where redox conditions depend on environmental conditions and photosynthesis activity, or are only valid *in vitro*, remains to be determined.

9. BL-induced responses of aureochromes and their DNA complexes

The effects of BL-illumination on the LOV-domain comprising aureochromes were studied by UV–vis, FT-IR spectroscopy and HDX-mass spectrometry (Akiyama et al., 2016; Banerjee et al., 2016b; Heintz and Schlichting, 2016; Hisatomi and Furuya, 2015). The N-terminal extension that plays some role in aureochrome oligomerization revealed no or only minor effects on the BL-triggered photocycle of the LOV domain (Banerjee et al., 2016b). In the context of the full-length aureochrome *Pt*Aureo1a, the C-terminal Jα-helix still controls the photochemistry despite its end-standing location. Here, deletion of the Jα-helix caused a fivefold reduction of the dark-state recovery time (Banerjee et al., 2016b). Like other LOV domains the Jα-helix undergoes partial unfolding as traced by HDX-MS and FT-IR spectroscopy (Banerjee et al., 2016b; Heintz and Schlichting, 2016). Furthermore, a sharp increase of deuterium incorporation was noted for the *Pt*Aureo1a aureochrome in its lit state, which corroborates the notion of significant structural changes within the aureochrome dimer (Heintz and Schlichting, 2016). For example, secondary structure changes in the bZIP region upon BL-illumination were interpreted by Heintz et al. to correspond to a dissociation of a direct bZIP-LOV interaction. In contrast, Banerjee et al. interpreted similar spectroscopic data as a rearrangement of a dark-state to a lit-state LOV dimer with a concomitant structural transition of the bZIP domain and an altered H-bonding network along the bZIP dimer interface. This model was further corroborated by SAXS data, where high intrinsic flexibility was assignable to the bZIP domain, that was reduced after DNA binding (Banerjee et al., 2016b; Heintz and Schlichting, 2016). Accordingly, CD spectroscopy indicated that upon DNA binding the helical content of aureochromes increases considerably until an equimolar bZIP dimer/duplex-DNA complex is formed. Another hint favoring a more indirect effect of the LOV domain on the bZIP-dimer is supported by the observation that DNA binding to aureochromes exerts only a very limited effect on its photochemistry (Banerjee et al., 2016b; Kerruth et al., 2014).

Although stable aureochrome-DNA complexes have been studied by a variety of biophysical techniques, there is still a lack for a crystal structure of such a complex. One obstacle for crystallization in the dark or lit state may be the flexibility of the connecting loop between the bZIP and LOV domains. Recent SAXS data to address this issue led to contradictory conclusions. One study showed no significant change for the gyration radius of *Pt*Aureo1a in dark and lit states, both of which adopt a the dimeric states found before by SEC without a large-scale change of the secondary structure (Banerjee et al., 2016b). In contrast, Heintz et al. observed a change of 1–2 nm for the gyration radius upon BL illumination revealing some concentration-dependent change of the volumetric parameter (Heintz and Schlichting, 2016). One reason for the discrepancy in the SAXS parameters may be due to differences in the ionic strength of the buffers used (Banerjee et al., 2016b). In case of the latter study *de novo* modeling from SAXS data led to a model, where the LOV domain interacts in the dark state with the bZIP region and competes with bZIP-dependent DNA-binding (Heintz and Schlichting, 2016). Upon BL-illumination, the LOV domain then releases the bZIP domain and forms instead a LOV dimer. Despite some supportive SEC data, mutational studies on a monomeric *Vf*Aureo1 variant and subsequent analysis by TG methods failed to show any evidence of such a bZIP-LOV interaction (Akiyama et al., 2016). In any case, it is clear that the DNA-bound aureochrome dimer has to undergo a significant conformational change. Banerjee et al. proposed for the dark and lit states of the *Pt*Aureo1a aureochrome dimer that the LOV domains remain pairwise associated. In the dark state, the LOV domain adopts a dimeric arrangement as observed in the LOV domain-only structure (Banerjee et al., 2016a). Upon BL illumination, the LOV domain undergoes a 173° rotation along its LOV–LOV interface without disrupting the aureochrome dimer due to the long linking peptide between the bZIP and LOV domains (Banerjee et al., 2016b).

Similar to other bZIP-DNA interactions, Kerruth et al. showed by FT-IR spectroscopy, that positively charged lysine and arginine residues at the basic region of Vf Aureo1 indeed play a crucial role for cognate DNA binding (Kerruth et al., 2014). These data also showed a significant degree of stretching and deformation of the DNA backbone that is accompanied by structural changes within the bZIP region. SAXS data and MD simulations for *Pt*Aureo1a indicated that the AUREO-box comprising duplex-DNA binds in a tilted orientation to the bZIP dimer rather than the T-shaped orientation found in crystal structures of symmetric bZIP-DNA complexes. Interestingly, this tilted interaction between duplex-DNA and bZIP dimers can be reproduced by molecular dynamic simulations, when using these crystal structures of bZIP-DNA complexes as starting models. Apparently, the tilted orientation may generally be more favored in solution than the T-shaped orientation (Banerjee et al., 2016b) and not only be caused by the non-symmetric AUREO-box recognition motif.

10. Aureochromes – simple architecture, complex mode of action?

Since their discovery, aureochromes were imagined to represent a sort of natural optogenetic tool developed by heterokonts (Takahashi et al., 2007). Their inverted topologies and numerous biophysical, but not so much functional data, has prompted three contrasting hypotheses (Fig. 6), namely the swapping-partner mode (Heintz and Schlichting, 2016), the tilt-twist mode (Banerjee et al., 2016b) and the redox-sensing mode (Akiyama et al., 2016). Interestingly, all these different mechanistic models imply a different function for aureochromes in light-dependent regulation of transcription.

The swapping-partner model as proposed by Heintz et al. implies, that the bZIP and LOV domains interact with each other in the dark state and dissociate in the lit state to unblock the DNA binding site of the bZIP domain with concomitant formation of a stable LOV dimer. Thereby, the bZIP domain can now associate to the cognate DNA. This model is analogous to the EL222 mode of action, where the LOV dimerization surface is hidden by the HTH domain in the dark state and, upon BL-illumination, the LOV domain dimerizes so that the HTH domain becomes free to bind instead the target DNA (Nash et al., 2011). However, in EL222 the effector domain is at the C-terminus of the LOV domain after the Jα-helix. The latter unfolds upon BL illumination and triggers thereby the LOV-HTH dissociation (Nash et al., 2011). In case of aureochromes, the effector bZIP domain is at the N-terminus, although a marked structural change was noted also for the A′α helix in the structure of the lit state LOV domain (Heintz and Schlichting, 2016). Overall, this model predicts a mode of regulation *via* light-dependent DNA-association/dissociation.

In the tilt-twist model, the LOV domain forms a stable dark state dimer due to the high local concentration that is caused by light-independent dimerization of the bZIP domains. C4(a) adduct formation in the lit state promotes adoption of a differently packed LOV domain dimer. Together with an unfolding of the A′α helix, this twist is indirectly transmitted *via* changes in the linker region to the bZIP domain (Banerjee et al., 2016b). This model partly resembles that proposed for bacterial YtvA (Herrou and Crosson, 2011; Möglich and Moffat, 2007). Although some light-driven changes in the bZIP region can be found, they would be relatively modest in terms of DNA-binding compared to the unfolding model. In this context, it was also proposed that aureochromes can form higher oligomeric super-complexes when being bound to DNA (Banerjee et al., 2016b). Indeed, aureochrome-regulated promoter regions (Huysman et al., 2013; Jungandreas et al., 2014) harbor more than one AUREO-box motif at fixed distances of about 100 bp (Banerjee et al., 2016b). Accordingly, it is tempting to speculate whether aureochromes affect DNA structure in a similar way as eukaryotic enhancers by affecting the structure of the promotor region. Alternatively, the LOV domain dimer may recruit or release in its lit

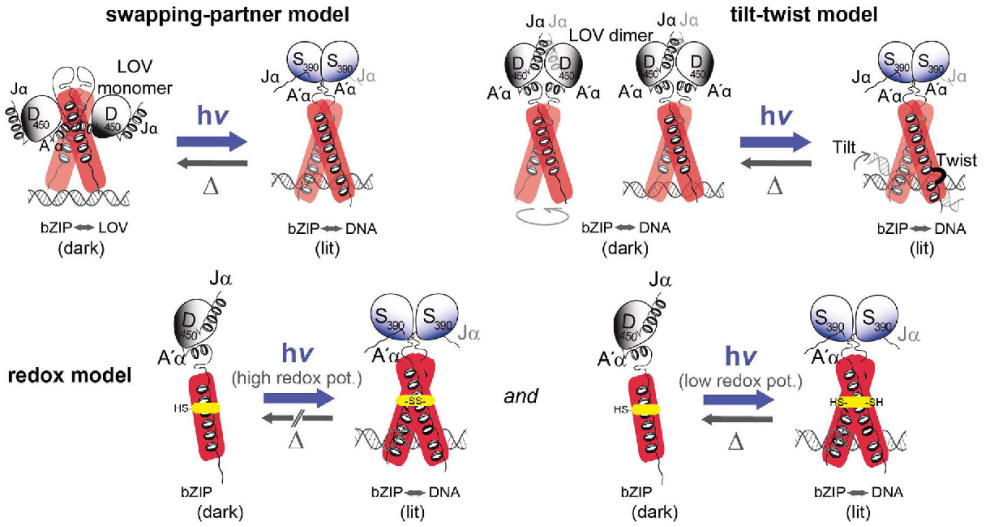

Fig. 6. Three models for light-triggered effects on aureochrome/DNA complexes. The redox model is only applicable to a group of aureochromes like *Vf*Aureo1, which harbor cysteine residues within their bZIP domain.

state other transcription factors. In any case, the relevance of such super-complexes made of aureochrome/DNA complexes or of alternative assemblies with other components of the transcription machinery awaits experimental analysis.

Clearly, the redox-sensing mode is only applicable to the subset of aureochromes, which harbor like *Vf*Aureo1 a set of cysteines capable to covalently stabilize the dimeric state *via* disulphide bridges in the oxidized state (Hísatomi et al., 2013) and thereby promote binding to the AUREO boxes. In a reduced state, *e.g.* under oxygen-depleted conditions, these aureochromes may depend on BL illumination to bind target DNA *via* paired lit state LOV domains.

11. Concluding remark

The large evolutionary distance between different photosynthetic eukaryotes with an estimated split of the different phyla occurring 1.5 billion years ago (Yoon et al., 2004) implies a large degree of functional diversification of the utilized signal transduction systems. As this review on algal photoreceptors shows to some extent, we may be able to derive now certain common features within given photoreceptor families. However, on the other hand, we cannot be sure to what extent these findings can be generalized across the different phyla. Especially, the identity of down-stream interaction partners and the mode of downstream-signaling for algal photoreceptors is almost entirely unknown and we may hence expect that there will be phylum-specific solutions to the problem of algal light-dependent signaling.

Acknowledgment

This work was supported by a grant from the German Research Foundation (DFG, ES152/12) as part of the DFG Research Initiative “Specific Light-Driven Reactions in Unicellular Model Algae”.

Appendix A. Supplementary data

Supplementary data associated with this article can be found, in the online version, at http://dx.doi.org/10.1016/j.jplph.2017.07.005.

References

Adl, S.M., Simpson, A.G.B., Farmer, M.A., Andersen, R.A., Anderson, O.R., Barta, J.R., Bowser, S.S., Brugerolle, G., Fensome, R.A., Fredericq, S., James, T.Y., Karpov, S., Kugrens, P., Krug, J., Lane, C.E., Lewis, L.A., Lodge, J., Lynn, D.H., Mann, D.G., Mccourt, R.M., Mendoza, L., Moestrup, Ø., Mozley-Standridge, S.E., Nerad, T.A., Shearer, C.A., Smirnov, A.V., Spiegel, F.W., Taylor, M.F.J.R., 2005. The new higher level classification of eukaryotes with emphasis on the taxonomy of protists. J. Eukaryot. Microbiol. 52, 399–451.

Akiyama, Y., Nakasone, Y., Nakatani, Y., Hisatomi, O., Terazima, M., 2016. Time-resolved detection of light-induced dimerization of monomeric aureochrome-1 and change in affinity for DNA. J. Phys. Chem. B 120, 7360–7370.

Alber, T., 1992. Structure of the leucine zipper. Curr. Opin. Genet. Dev. 2, 205–210.

Anders, K., Essen, L.-O., 2015. The family of phytochrome-like photoreceptors: diverse, complex and multi-colored, but very useful. Curr. Opin. Struct. Biol. 35, 7–16.

Ashworth, J., Coesel, S., Lee, A., Armbrust, E.V., Orellana, M.V., Baliga, N.S., 2013. Genome-wide diel growth state transitions in the diatom Thalassiosira pseudonana. Proc. Natl. Acad. Sci. U. S. A. 110, 7518–7523.

Banerjee, A., Herman, E., Kottke, T., Essen, L.-O., 2016a. Structure of a native-like aureochrome 1a LOV domain dimer from Phaeodactylum tricornutum. Structure 24, 171–178.

Banerjee, A., Herman, E., Serif, M., Maestre-Reyna, M., Hepp, S., Pokorny, R., Kroth, P.G., Essen, L.-O., Kottke, T., 2016b. Allosteric communication between DNA-binding and light-responsive domains of diatom class I aureochromes. Nucleic Acids Res. 44, 5957–5970.

Bayram, O., Biesemann, C., Krappmann, S., Galland, P., Braus, G.H., 2008. More than a repair enzyme: Aspergillus nidulans photolyase-like CryA is a regulator of sexual development. Mol. Biol. Cell 19, 3254–3262.

Beel, B., Prager, K., Spexard, M., Sasso, S., Weiss, D., Muller, N., Heinnickel, M., Dewez, D., Ikoma, D., Grossman, A.R., Kottke, T., Mittag, M., 2012. A flavin binding cryptochrome photoreceptor responds to both blue and red light in Chlamydomonas reinhardtii. Plant Cell 24, 2992–3008.

Beel, B., Müller, N., Kottke, T., Mittag, M., 2013. News about cryptochrome photoreceptors in algae. Plant Signal. Behav. 8, e22870.

Berrocal-Tito, G.M., Esquivel-Naranjo, E.U., Horwitz, B.A., Herrera-Estrella, A., 2007. Trichoderma atroviride PHR1, a fungal photolyase responsible for DNA repair, autoregulates its own photoinduction. Eukaryot. Cell 6, 1682–1692.

Bluhm, B.H., Dunkle, L.D., 2008. PHL1 of Cercospora zeae-maydis encodes a member of the photolyase/cryptochrome family involved in UV protection and fungal development. Fungal Genet. Biol. 45, 1364–1372.

Brautigam, C.A., Smith, B.S., Ma, Z., Palnitkar, M., Tomchick, D.R., Machius, M., Deisenhofer, J., 2004. Structure of the photolyase-like domain of cryptochrome 1 from Arabidopsis thaliana. Proc. Natl. Acad. Sci. U. S. A. 101, 12142–12147.

Brazard, J., Ley, C., Lacombat, F., Plaza, P., Mony, L., Heijde, M., Zabulon, G., Bowler, C., 2012. Photoantenna in two cryptochrome-photolyase proteins from O. tauri: presence, nature and ultrafast photoinduced dynamics. J. Photochem. Photobiol. A Chem. 234, 135–145.

Busch, S.J., Sassone-Corsi, P., 1990. Dimers, leucine zippers and DNA-binding domains. Trends Genet. 6, 36–40.

Cailliez, F., Müller, P., Firmino, T., Pernot, P., de la Lande, A., 2016. Energetics of photoinduced charge migration within the tryptophan tetrad of an animal (6-4) photolyase. J. Am. Chem. Soc. 138, 1904–1915.

Chaves, I., Pokorny, R., Byrdin, M., Hoang, N., Ritz, T., Brettel, K., Essen, L.-O., van der Horst, G.T.J., Batschauer, A., Ahmad, M., 2011. The cryptochromes: blue light photoreceptors in plants and animals. Annu. Rev. Plant Biol. 62, 335–364.

Chen, Z., Yang, M.K., Li, C.Y., Wang, Y., Zhang, J., Wang, D.B., Zhang, X.E., Ge, F., 2014. Phosphoproteomic analysis provides novel insights into stress responses in Phaeodactylum tricornutum, a model diatom. J. Proteome Res. 13, 2511–2523.

Christie, J.M., Blackwood, L., Petersen, J., Sullivan, S., 2015. Plant flavoprotein photoreceptors. Plant Cell Physiol. 56, 401–413.

Christie, J.M., 2007. Phototropin blue-light receptors. Annu. Rev. Plant Biol. 58, 21–45.

Clarke, J.T., Warnock, R.C.M., Donoghue, P.C.J., 2011. Establishing a time-scale for plant evolution. New Phytol. 192, 266–301.

Coesel, S., Mangogna, M., Ishikawa, T., Heijde, M., Rogato, A., Finazzi, G., Todo, T., Bowler, C., Falciatore, A., 2009. Diatom PtCPF1 is a new cryptochrome/photolyase family member with DNA repair and transcription regulation activity. EMBO Rep. 10, 655–661.

Conrad, K.S., Manahan, C.C., Crane, B.R., 2014. Photochemistry of flavoprotein light sensors. Nat. Chem. Biol. 10, 801–809.

De Riso, V., Raniello, R., Maumus, F., Rogato, A., Bowler, C., Falciatore, A., 2009. Gene silencing in the marine diatom Phaeodactylum tricornutum. Nucleic Acids Res. 37, e96.

Deng, Y., Yao, J., Wang, X., Guo, H., Duan, D., 2012. Transcriptome sequencing and comparative analysis of Saccharina japonica (Laminariales, phaeophyceae) under blue light induction. PLoS One 7, e39704.

Deng, Y., Yao, J., Fu, G., Guo, H., Duan, D., 2014. Isolation, expression, and characterization of blue light receptor AUREOCHROME gene from Saccharina japonica (Laminariales, phaeophyceae). Mar. Biotechnol. 16, 135–143.

Duanmu, D., Casero, D., Dent, R.M., Gallaher, S., Yang, W., Rockwell, N.C., Martin, S.S., Pellegrini, M., Niyogi, K.K., Merchant, S.S., Grossman, A.R., Lagarias, J.C., 2013. Retrograde bilin signaling enables Chlamydomonas greening and phototrophic survival. Proc. Natl. Acad. Sci. U. S. A. 110, 3621–3626.

Duanmu, D., Rockwell, N.C., Clark Lagarias, J., 2017. Algal light sensing and photoacclimation in aquatic environments. Plant. Cell Environ. 1–13.

Ellenberger, T.E., Brandl, C.J., Struhl, K., Harrison, S.C., 1992. The GCN4 basic region leucine zipper binds DNA as a dimer of uninterrupted α Helices: crystal structure of the protein-DNA complex. Cell 71, 1223–1237.

Ellenberger, T., 1994. Getting a grip on DNA recognition: structures of the basic region leucine zipper, and the basic region helix-loop-helix DNA-binding domains. Curr. Opin. Struct. Biol. 4, 12–21.

Engelhard, C., Wang, X., Robles, D., Moldt, J., Essen, L.O., Batschauer, A., Bittl, R., Ahmad, M., 2014. Cellular metabolites enhance the light sensitivity of Arabidopsis cryptochrome through alternate electron transfer pathways. Plant Cell 26, 4519–4531.

Essen, L.-O., 2006. Photolyases and cryptochromes: common mechanisms of DNA repair and light-driven signaling? Curr. Opin. Struct. Biol. 16, 51–59.

Fortunato, A.E., Annunziata, R., Jaubert, M., Bouly, J., Falciatore, A., 2015. Dealing with light: the widespread and multitasking cryptochrome/photolyase family in photosynthetic organisms. J. Plant Physiol. 172, 42–54.

Foster, R., Izawa, T., Chua, N.H., 1994. Plant bZIP proteins gather at ACGT elements. FASEB J. 8, 192–200.

Fujihashi, M., Numoto, N., Kobayashi, Y., Mizushima, A., Tsujimura, M., Nakamura, A., Kawarabayasi, Y., Miki, K., 2007. Crystal structure of archaeal photolyase from Sulfolobus tokodaii with two FAD molecules: implication of a novel light-harvesting cofactor. J. Mol. Biol. 365, 903–910.

Geisselbrecht, Y., Frühwirth, S., Schroeder, C., Pierik, A.J., Klug, G., Essen, L.-O., 2012. CryB from Rhodobacter sphaeroides: a unique class of cryptochromes with new cofactors. EMBO Rep. 13, 223–229.

Gerlt, J.A., Bouvier, J.T., Davidson, D.B., Imker, H.J., Sadkhin, B., Slater, D.R., Whalen, K.L., 2015. Enzyme Function Initiative-Enzyme Similarity Tool (EFI-EST): a web tool for generating protein sequence similarity networks. Biochim. Biophys. Acta 1854, 1019–1037.

Glover, J.N., Harrison, S.C., 1995. Crystal structure of the heterodimeric bZIP transcription factor c-Fos- c-Jun bound to DNA. Nature 373, 257–261.

Hakoshima, T., 2005. Leucine zippers. Encycl. Life Sci. http://dx.doi.org/10.1038/npg.els.0005049.

Hegemann, P., 2008. Algal sensory photoreceptors. Annu. Rev. Plant Biol. 59, 167–189.

Heijde, M., Zabulon, G., Corellou, F., Ishikawa, T., Brazard, J., Usman, A., Sanchez, F., Plaza, P., Martin, M., Falciatore, A., Todo, T., Bouget, F.Y., Bowler, C., 2010. Characterization of two members of the cryptochrome/photolyase family from Ostreococcus tauri provides insights into the origin and evolution of cryptochromes. Plant Cell Environ. 33, 1614–1626.

Heintz, U., Schlichting, I., 2016. Blue light-induced LOV domain dimerization enhances the affinity of Aureochrome 1a for its target DNA sequence. Elife 5, e11860.

Herman, E., Kottke, T., 2015. Allosterically regulated unfolding of the A'α helix exposes the dimerization site of the blue-light-sensing aureochrome-LOV domain. Biochemistry 54, 1484–1492.

Herman, E., Sachse, M., Kroth, P.G., Kottke, T., 2013. Blue-light-induced unfolding of the Jα helix allows for the dimerization of aureochrome-LOV from the diatom Phaeodactylum tricornutum. Biochemistry 52, 3094–3101.

Herrou, J., Crosson, S., 2011. Function, structure and mechanism of bacterial photosensory LOV proteins. Nat. Rev. Microbiol. 9, 713–723.

Hisatomi, O., Furuya, K., 2015. A light-regulated bZIP module, photozipper, induces the binding of fused proteins to the target DNA sequence in a blue light-dependent manner. Photochem. Photobiol. Sci. 14, 1998–2006.

Hisatomi, O., Takeuchi, K., Zikihara, K., Ookubo, Y., Nakatani, Y., Takahashi, F., Tokutomi, S., Kataoka, H., 2013. Blue light-induced conformational changes in a light-regulated transcription factor, aureochrome-1. Plant Cell Physiol. 54, 93–106.

Hisatomi, O., Nakatani, Y., Takeuchi, K., Takahashi, F., Kataoka, H., 2014. Blue light-induced dimerization of monomeric aureochrome-1 enhances its affinity for the target sequence. J. Biol. Chem. 289, 17379–17391.

Huang, K., Beck, C.F., 2003. Phototropin is the blue-light receptor that controls multiple steps in the sexual life cycle of the green alga Chlamydomonas reinhardtii. Proc. Natl. Acad. Sci. U. S. A. 100, 6269–6274.

Huang, Y. Jiang, Wang, L., Zheng, M. Gang, Zheng, L., Tong, Y. Li, Li, Y., 2014. Overexpression of NgAUREO1, the gene coding for aurechrome 1 from Nannochloropsis gaditana, into Saccharomyces cerevisiae leads to a 1.6-fold increase in lipid accumulation. Biotechnol. Lett. 36, 575–579.

Huysman, M.J.J., Fortunato, A.E., Matthijs, M., Costa, B.S., Vanderhaeghen, R., Van den Daele, H., Sachse, M., Inzé, D., Bowler, C., Kroth, P.G., Wilhelm, C., Falciatore, A., Vyverman, W., De Veylder, L., 2013. AUREOCHROME1a-mediated induction of the diatom-specific cyclin dsCYC2 controls the onset of cell division in diatoms (Phaeodactylum tricornutum). Plant Cell 25, 215–228.

Immeln, D., Schlesinger, R., Heberle, J., Kottke, T., 2007. Blue light induces radical formation and autophosphorylation in the light-sensitive domain of Chlamydomonas cryptochrome. J. Biol. Chem. 282, 21720–21728.

Immeln, D., Weigel, A., Kottke, T., Pérez Lustres, J.L., 2012. Primary events in the blue light sensor plant cryptochrome: intraprotein electron and proton transfer revealed by femtosecond spectroscopy. J. Am. Chem. Soc. 134, 12536–12546.

Iseki, M., Matsunaga, S., Murakami, A., Ohno, K., Shiga, K., Yoshida, K., Sugai, M., Takahashi, T., Hori, T., Watanabe, M., 2002. A blue-light-activated adenylyl cyclase mediates photoavoidance in Euglena gracilis. Nature 415, 1047–1051.

Ishikawa, M., Takahashi, F., Nozaki, H., Nagasato, C., Motomura, T., Kataoka, H., 2009. Distribution and phylogeny of the blue light receptors aureochromes in eukaryotes. Planta 230, 543–552.

Jakoby, M., Weisshaar, B., Droge-Laser, W., Vicente-Carbajosa, J., Tiedemann, J., Kroj, T., Parcy, F., bZIP R. Grp, 2002. bZIP transcription factors in Arabidopsis. Trends Plant Sci. 7, 106–111.

Janovjak, H., 2016. Light at the end of the protein: crystal structure of a C-terminal light-sensing domain. Structure 24, 213–215.

Ji, N., Li, L., Lin, L., Lin, S., 2017. Identification and expression analysis of blue light receptor aureochrome in the harmful alga Heterosigma akashiwo (raphidophyceae). Harmful Algae 61, 71–79.

Juhas, M., Von Zadow, A., Spexard, M., Schmidt, M., Kottke, T., Büchel, C., 2014. A novel cryptochrome in the diatom Phaeodactylum tricornutum influences the regulation of light-harvesting protein levels. FEBS J. 281, 2299–2311.

Jungandreas, A., Costa, B.S., Jakob, T., Von Bergen, M., Baumann, S., Wilhelm, C., 2014. The acclimation of Phaeodactylum tricornutum to blue and red light does not influence the photosynthetic light reaction but strongly disturbs the carbon allocation pattern. PLoS One 9, e99727.

König, S., Juhas, M., Jäger, S., Kottke, T., Büchel, C., 2017. The cryptochrome –photolyase protein family in diatoms. J. Plant Physiol. 217, 15–19.

Kerruth, S., Ataka, K., Frey, D., Schlichting, I., Heberle, J., 2014. Aureochrome 1 illuminated: structural changes of a transcription factor probed by molecular spectroscopy. PLoS One 9, e103307.

Kianianmomeni, A., Hallmann, A., 2014. Algal photoreceptors: in vivo functions and potential applications. Planta 239, 1–26.

Kiontke, S., Gnau, P., Haselsberger, R., Batschauer, A., Essen, L.-O., 2014. Structural and evolutionary aspects of antenna chromophore usage by class II photolyases. J. Biol. Chem. 289, 19659–19669.

Klar, T., Kaiser, G., Hennecke, U., Carell, T., Batschauer, A., Essen, L.-O., 2006. Natural and non-natural antenna chromophores in the DNA photolyase from Thermus thermophilus. ChemBioChem 7, 1798–1806.

Klar, T., Pokorny, R., Moldt, J., Batschauer, A., Essen, L.-O., 2007. Cryptochrome 3 from Arabidopsis thaliana: structural and functional analysis of its complex with a folate light antenna. J. Mol. Biol. 366, 954–964.

Kottke, T., Oldemeyer, S., Wenzel, S., Zou, Y., Mittag, M., 2017. Cryptochrome photoreceptors in green algae: unexpected versatility of mechanisms and functions. J. Plant Physiol. 217, 4–14.

Kroth, P.G., Wilhelm, C., Kottke, T., 2017. An update on aureochromes: phylogeny – mechanism – function. J. Plant Physiol. 217, 20–26.

Liu, B., Zuo, Z., Liu, H., Liu, X., Lin, C., 2011. Arabidopsis cryptochrome 1 interacts with SPA1 to suppress COP1 activity in response to blue light. Genes Dev. 25, 1029–1034.

Losi, A., Gärtner, W., 2011. Old chromophores, new photoactivation paradigms, trendy applications: flavins in blue light-sensing photoreceptors. Photochem. Photobiol. 87, 491–510.

Luck, M., Hegemann, P., 2017. The four dark states of the Chlamydomonas sensory photoreceptor histidine kinase rhodopsin 1. J. Plant Physiol. 217, 77–84.

Luck, M., Mathes, T., Bruun, S., Fudim, R., Hagedorn, R., Tran Nguyen, T.M., Kateriya, S., Kennis, J.T., Hildebrandt, P., Hegemann, P., 2012. A photochromic histidine kinase rhodopsin (HKR1) that is bimodally switched by ultraviolet and blue light. J. Biol. Chem. 287, 40083–40090.

Möglich, A., Moffat, K., 2007. Structural basis for light-dependent signaling in the dimeric LOV domain of the photosensor YtvA. J. Mol. Biol. 373, 112–126.

Müller, P., Bouly, J.-P., Hitomi, K., Balland, V., Getzoff, E.D., Ritz, T., Brettel, K., 2014. ATP binding turns plant cryptochrome into an efficient natural photoswitch. Sci. Rep. 4, 5175.

Müller, P., Yamamoto, J., Martin, R., Iwai, S., Brettel, K., 2015. Discovery and functional analysis of a 4th electron-transferring tryptophan conserved exclusively in animal cryptochromes and (6-4) photolyases. RSC Chem. Commun. 15502–15505.

Masuda, S., 2013. Light detection and signal transduction in the BLUF photoreceptors. Plant Cell Physiol. 54, 171–179.

Maul, M.J., Barends, T.R.M., Glas, A.F., Cryle, M.J., Domratcheva, T., Schneider, S., Schlichting, I., Carell, T., 2008. Crystal structure and mechanism of a DNA (6-4)

photolyase. Angew. Chem. Int. Ed. 47, 10076–10080.
Mees, A., Klar, T., Gnau, P., Hennecke, U., Eker, A.P., Carell, T., Essen, L.-O., 2004. Crystal structure of a photolyase bound to a CPD-like DNA lesion after in situ repair. Science 306, 1789–1793.
Mitra, D., Yang, X., Moffat, K., 2012. Crystal structures of Aureochrome1 LOV suggest new design strategies for optogenetics. Structure 20, 698–706.
Nash, A.I., McNulty, R., Shillito, M.E., Swartz, T.E., Bogomolni, R.A., Luecke, H., Gardner, K.H., 2011. Structural basis of photosensitivity in a bacterial light-oxygen-voltage/helix-turn-helix (LOV-HTH) DNA-binding protein. Proc. Natl. Acad. Sci. U. S. A. 108, 9449–9454.
Nohr, D., Franz, S., Rodriguez, R., Paulus, B., Essen, L.O., Weber, S., Schleicher, E., 2016. Extended electron-transfer in animal cryptochromes mediated by a tetrad of aromatic amino acids. Biophys. J. 111, 301–311.
Oldemeyer, S., Franz, S., Wenzel, S., Essen, L.-O., Mittag, M., Kottke, T., Chemistry, B., 2016. Essential role of an unusually long-lived tyrosyl radical in the response to red light of the animal-like cryptochrome aCRY. J. Biol. Chem. 291, 14062–14071.
Onodera, A., Kong, S.G., Doi, M., Shimazaki, K.I., Christie, J., Mochizuki, N., Nagatani, A., 2005. Phototropin from Chlamydomonas reinhardtii is functional in Arabidopsis thaliana. Plant Cell Physiol. 46, 367–374.
Park, H.W., Kim, S.T., Sancar, A., Deisenhofer, J., 1995. Crystal structure of DNA photolyase from Escherichia coli. Science 268, 1866–1872.
Petersen, J.L., Ronan, P.J., 2010. Critical role of 7, 8-didemethyl-8-hydroxy-5-deazariboflavin for photoreactivation in Chlamydomonas reinhardtii. J. Biol. Chem. 285, 32467–32475.
Petersen, J.L., Small, G.D., 2001. A gene required for the novel activation of a class II DNA photolyase in Chlamydomonas. Nucleic Acids Res. 29, 4472–4481.
Prochnik, S.E., Umen, J., Nedelcu, A.M., Hallmann, A., Miller, S.M., Nishii, I., Ferris, P., Kuo, A., Mitros, T., Fritz-laylin, L.K., Hellsten, U., Chapman, J., Simakov, O., Rensing, S.a., Terry, A., Pangilinan, J., Kapitonov, V., Jurka, J., Salamov, A., Shapiro, H., Schmutz, J., Kirk, D., Rokhsar, D.S., 2010. Genomic analysis of organismal complexity in the multicellular green alga Volvox carteri. Science 329, 223–226.
Reisdorph, N.A., Small, G.D., 2004. The CPH1 gene of Chlamydomonas reinhardtii encodes two forms of cryptochrome whose levels are controlled by light-induced proteolysis. Plant Physiol. 134, 1546–1554.
Rockwell, N., Duanmu, D., Martin, S.S., Bachy, C., Price, D.C., Bhattacharya, D., Worden, A.Z., Lagarias, J.C., 2014. Eukaryotic algal phytochromes span the visible spectrum. Proc. Natl. Acad. Sci. U. S. A. 111, 3871–3876.
Schellenberger Costa, B., Sachse, M., Jungandreas, A., Bartulos, C., Gruber, A., Jakob, T., Kroth, P., Wilhelm, C., 2013. Aureochrome 1a is involved in the photoacclimation of the diatom Phaeodactylum tricornutum. PLoS One 8, e74451.
Schneider, F., Grimm, C., Hegemann, P., 2015. Biophysics of channelrhodopsin. Annu. Rev. Biophys. 44, 167–186.
Suetsugu, N., Wada, M., 2013. Evolution of three LOV blue light receptor families in green plants and photosynthetic stramenopiles: phototropin, ZTL/FKF1/LKP2 and aureochrome. Plant Cell Physiol. 54, 8–23.
Tagua, V.G., Pausch, M., Eckel, M., Gutiérrez, G., Miralles-Durán, A., Sanz, C., Eslava, A.P., Pokorny, R., Corrochano, L.M., Batschauer, A., 2015. Fungal cryptochrome with DNA repair activity reveals an early stage in cryptochrome evolution. Proc. Natl. Acad. Sci. U. S. A. 112, 15130–15135.
Takahashi, F., Hishinuma, T., Kataoka, H., 2001. Blue light-induced branching in Vaucheria. Requirement of nuclear accumulation in the irradiated region. Plant Cell Physiol. 42, 274–285.
Takahashi, F., Yamagata, D., Ishikawa, M., Fukamatsu, Y., Ogura, Y., Kasahara, M., Kiyosue, T., Kikuyama, M., Wada, M., Kataoka, H., 2007. AUREOCHROME, a photoreceptor required for photomorphogenesis in stramenopiles. Proc. Natl. Acad. Sci. U. S. A. 104, 19625–19630.
Takahashi, F., 2016. Blue-light-regulated transcription factor, aureochrome, in photosynthetic stramenopiles. J. Plant Res. 129, 189–197.
Thöing, C., Oldemeyer, S., Kottke, T., 2015. Microsecond deprotonation of aspartic acid and response of the α/β subdomain precede C-terminal signaling in the blue light sensor plant cryptochrome. J. Am. Chem. Soc. 137, 5990–5999.
Toyooka, T., Hisatomi, O., Takahashi, F., Kataoka, H., Terazima, M., 2011. Photoreactions of aureochrome-1. Biophys. J. 100, 2801–2809.
Usman, A., Brazard, J., Martin, M.M., Plaza, P., Heijde, M., Zabulon, G., Bowler, C., 2009. Spectroscopic characterization of a (6-4) photolyase from the green alga Ostreococcus tauri. J. Photochem. Photobiol. B Biol. 96, 38–48.
Veetil, S.K., Mittal, C., Ranjan, P., Kateriya, S., 2011. A conserved isoleucine in the LOV1 domain of a novel phototropin from the marine alga Ostreococcus tauri modulates the dark state recovery of the domain. Biochim. Biophys. Acta – Gen. Subj. 1810, 675–682.
Yan Lv, X., Rong Qiao, D., Xiong, Y., Xu, H., You, F.F., Cao, Y., He, X., Cao, Y., 2008. Photoreactivation of (6-4) photolyase in Dunaliella salina. FEMS Microbiol. Lett. 283, 42–46.
Yoon, H.S., Hackett, J.D., Ciniglia, C., Pinto, G., Bhattacharya, D., 2004. A molecular timeline for the origin of photosynthetic eukaryotes. Mol. Biol. Evol. 21, 809–818.
Zhang, F., Xu, H., Cao, Y., Wen, T., Lin, J., Ma, G., Qiao, D., Cao, Y., 2011. Role of Lys281 in the Dunaliella salina (6-4) photolyase reaction. Curr. Microbiol. 62, 146–151.
Zhang, F., Scheerer, P., Oberpichler, I., Lamparter, T., Krauss, N., 2013. Crystal structure of a prokaryotic (6-4) photolyase with an Fe-S cluster and a 6,7-dimethyl-8-ribityllumazine antenna chromophore. Proc. Natl. Acad. Sci. 110, 7217–7222.
Zoltowski, B.D., Vaidya, A.T., Top, D., Widom, J., Young, M.W., Crane, B.R., 2011. Structure of full-length Drosophila cryptochrome. Nature 480, 396–399.

4.4 Structure of the animal-like cryptochrome

This research was originally published in Nucleic Acid Research by *Sophie Franz, Elisabeth Ignatz, Sandra Wenzel, Hannah Zielosko, Eka Putra Gusti Ngurah Putu, Manuel Maestre-Reyna, Ming-Daw Tsai, Junpei Yamamoto, Maria Mittag and Lars-Oliver Essen*.* **Structure of the bifunctional cryptochrome aCRY from *Chlamydomonas reinhardtii*.** Nucleic Acids Res. 2018; 46 (15): 8010-8022.

Summary

This paper is focused on the structure of *Cr*aCRY and its function as a (6-4)PHL. We could solve the structure of the truncated *Cr*aCRY variant, ΔCTE, initially with a resolution of 1.9 Å (6FN3). The achievable resolution was later in optimized to 1.6 Å (5ZM0) *via* the KAMO (315) method. The structure reveals the FAD binding site as well as the antenna binding pocket, which is filled with components of the crystallization condition. The amino acids which compose the catalytic tetrad (W399-W376-W322-Y373) are observable. The structure reveals a VAN-DER-WAALS network through D323, R485 and D321 between the terminal electron donor Y373 and the surface of the protein. This might stabilize the deprotonated TyrO° radical form solvent access and could be a reason for its long lifetime (293, 294). The DNA repair of (6-4)PP was studied *in vitro*, by following the decreasing absorption at 325 nm, which is the specific absorption of the (6-4)PP lesion, and *in vivo* by using an UV-B survival assay of *C. reinhardtii* mutant cells. In both cases, *Cr*aCRY demonstrated efficient DNA repair. *Cr*aCRYΔCTE was also co-crystallized in complex with a double stranded DNA substrate containing the (6-4)PP. This crystal structure provides a lot of information about the overall DNA binding mode as well as the (6-4)PP inside the active pocket. Here, another orientation as in the known *Dm*64 structure (3CVU) of one highly conserved cysteine residue H357, referred as His_1, is present (13). His_1 was shown before to be crucial for (6-4)PP repair and the currently discussed repair mechanism (see section 1.6) are based on the *Dm*64 structure. The discrepancy between the two co-crystal structures 3CVU and 6FN2 leads to the proposed mechanism. Here, the first electron transfer happens in parallel to the protonation of the carbonyl-oxygen of the 3' base. Additionally to DNA-repair, the nature of the antenna chromophore was investigated. The antenna could be identified as 8-

HDF by *in vivo* reconstitution and a co-crystal structure of the *Cr*aCRYΔCTE/8-HDF complex (6FN2) was generated.

Contributions

L.-O. Essen, S. Franz and M. Mittag designed the study. S. Franz performed crystallization experiments, gathered diffraction images and analysed data with advice by L.-O. Essen. E. Ignatz perfomed *in vitro* DNA repair assays, S. Wenzel performed *in vivo* UV-B survival assays. H. Zielosko did initial crystallization experiments. E.P.G.N. Putu and M. Maestre-Reyna optimized the initial X-tal structure by using the KAMO method with advise of M.-D. Tsai. J. Yamomoto generated the DNA substrate. S. Franz and L.-O. Essen wrote the manuscript with help of S. Wenzel and M. Mittag. All authors reviewed the results and approved the final version of the manuscript.

8010–8022 *Nucleic Acids Research, 2018, Vol. 46, No. 15* *Published online 19 July 2018*
doi: 10.1093/nar/gky621

Structure of the bifunctional cryptochrome aCRY from *Chlamydomonas reinhardtii*

Sophie Franz[1], Elisabeth Ignatz[1], Sandra Wenzel[2], Hannah Zielosko[1], Eka Putra Gusti Ngurah Putu[3], Manuel Maestre-Reyna[3], Ming-Daw Tsai[3], Junpei Yamamoto[4], Maria Mittag[2] and Lars-Oliver Essen[1,5,*]

[1]Unit for Structural Biochemistry, Department of Chemistry, Philipps University Marburg, Hans-Meerwein Straße 4, 35032 Marburg, Germany, [2]Matthias Schleiden Institute of Genetics, Bioinformatics and Molecular Botany, Friedrich Schiller University, Am Planetarium 1, 07743 Jena, Germany, [3]Institute of Biological Chemistry, Academia Sinica, 128 Academia Rd. Sec. 2, Taipei 115, Taiwan, [4]Division of Chemistry, Graduate School of Engineering Science, Osaka University, 1–3 Machikaneyama, Toyonaka, Osaka 560-8531, Japan and [5]LOEWE Center of Synthetic Microbiology, Philipps University Marburg, Hans-Meerwein Straße 4, 35032 Marburg, Germany

Received April 05, 2018; Revised June 24, 2018; Editorial Decision June 26, 2018; Accepted July 17, 2018

ABSTRACT

Photolyases and cryptochromes form an almost ubiquitous family of blue light photoreceptors involved in the repair and maintenance of DNA integrity or regulatory control. We found that one cryptochrome from the green alga *Chlamydomonas reinhardtii* (*Cr*aCRY) is capable of both, control of transcript levels and the sexual cycle of the alga in a positive (germination) and negative manner (mating ability), as well as catalyzing the repair of UV-DNA lesions. Its 1.6 Å crystal structure shows besides the FAD chromophore an aromatic tetrad that is indispensable in animal-like type I cryptochromes for light-driven change of their signaling-active redox state and formation of a stable radical pair. Given *Cr*aCRY's catalytic activity as (6-4) photolyase *in vivo* and *in vitro*, we present the first co-crystal structure of a cryptochrome with duplex DNA comprising a (6-4) pyrimidine–pyrimidone lesion. This 2.9 Å structure reveals a distinct conformation for the catalytic histidine His_1, H357, that challenges previous models of a single-photon driven (6-4) photolyase mechanism.

INTRODUCTION

The photolyase/cryptochrome superfamily (PCSf) is a large family of photoactive enzymes, which occurs in all three domains of life. They are roughly classified by their function either as photolyases (PHL) or as cryptochromes (CRY). Photolyases repair UV-induced DNA lesions, namely either cyclobutane-pyrimidine dimers (CPD) or pyrimidine-(6-4)-pyrimidone photoadducts, (6-4)PP. Their close relatives, the cryptochromes, have mostly lost DNA repair functionality and act as signaling proteins for coupling various biological responses to light input, e.g. plant growth and development, initiation of flowering, or as triggers for the entrainment of circadian rhythms in plants and animals (1). CRYs are furthermore separated into the animal types I and II, plant CRYs and CRY-DASH photoreceptors (DASH: *Drosophila, Arabidopsis, Synechocystis, Homo*). During the last decade, several animal-like CRYs (aCRY) have been discovered and characterized outside the animal kingdom, especially in photosynthetic algae (2,3), where they may act not only in signaling, but also as (6-4) photolyases.

The green alga *Chlamydomonas reinhardtii* harbors one aCRY ortholog (*Cr*aCRY) and a plant CRY besides two DASH-type cryptochromes (4,5). Interestingly, although *C. reinhardtii* has a CPD class II photolyase, it lacks a further (6-4) photolyase as well as red light-dependent phytochromes (4–6). The photolyase-homology region (PHR) of *Cr*aCRY shows high sequence identity (40–52%) with the aCRY orthologs *Ot*CPF1 from the green alga *Ostreococcus tauri, Pt*CPF1 from the diatom *Phaeodactylum tricornutum* and an assigned (6-4) photolyase from the green algae *Dunaliella salina* (SI-S1). At least the diatom cryptochrome *Pt*CPF1 is bifunctional as shown by its *in vitro* (6-4) photolyase activity and *in vivo* function as transcriptional regulator (7). Surprisingly, *Cr*aCRY regulates the transcript levels of various genes not only upon blue light due to absorption by its oxidized FAD chromophore but also upon yellow and red light as revealed by *in vivo* studies with a knock-down mutant (5). The latter suggests a light sensor function of the chromophore's semiquinoid $FADH^{\circ}$ state (8). However, till now, there has not yet been identified any

*To whom correspondence should be addressed. Tel: +49 6421/28 22032; Fax: +49 6421/28 22012; Email: essen@chemie.uni-marburg.de

direct interaction partner of *Cra*CRY for downstream signaling. Unlike conventional photolyases, *Cra*CRY harbors like other cryptochromes an elongated C-terminal extension (CTE, A457-E595) as an additional feature besides its light-receptive PHR. These CTE are generally highly variable in length and sequence in cryptochromes and predicted to be mostly disordered in the absence of an interaction partner. CTE are hence generally hypothesized to be key elements of cryptochrome-dependent signal transduction (9). For example, in plant cryptochromes the CTE are targets for extensive blue-light dependent phosphorylation, which is triggered by dimerization of the PHR domain in the lit, i.e. semiquinoid, state (10). Interestingly, the CTE of *Cra*CRY was supposed to fulfill a similar function in homodimerization (11), although no direct evidence of its conformational change upon blue or red light illumination has been shown till now.

Almost all members of the PCSf undergo a blue light mediated reaction called photoactivation (1), in which the catalytically inactive fully-oxidized (FAD_{ox}) or semi-reduced ($FADH^{\circ}$) states abstract an electron from a nearby tryptophan upon photoexcitation. Exceptions may be represented by type-II cryptochromes, which act as light-unresponsive transcription-repressing enzymes in mouse, human and other vertebrates (1,12). Here, photoreduction can be observed under artificial *in vitro* conditions, but has not been proven to be physiologically relevant. In the reduced state the flavin chromophore acts either in DNA repair ($FADH^{-}$) after further light absorption or in triggering signal transduction ($FADH^{\circ}$). In *Cra*CRY the light-dependent photoreduction process can be easily observed *in vitro*, starting from the fully oxidized (FADox) through the neutral radical ($FADH^{\circ}$) up to the fully reduced form ($FADH^{-}$). A common feature of PCSf orthologs is the presence of an aromatic triad for the fast replenishment of an electron from the protein surface. This intramolecular electron transfer (ET) pathway is elongated in *Cra*CRY and related type I animal cryptochromes by a fourth aromatic residue (11,13), which can be either a tyrosine (*Cra*CRY: Y373) or a tryptophan, W394 in the cryptochrome of *Drosophila melanogaster*. This elongated ET pathway is crucial not only for the photoreduction reactions of aCRY orthologs but also for the function of (6-4) photolyases (14). At least in *Cra*CRY, the life time of the terminal Y373-O° radical is unusually long with 26 ms after photoreduction to the $FADH^{\circ}$ state (13) and even 2.6 s upon light-driven formation of the $FADH^{-}$ state (11). As stable tyrosyl radicals such as that of photosystem II or class I ribonucleotide reductases are known to reside in well-shielded protein environments the structural base of the relative longevity of the Y373-O° radical is unclear given its predicted proximity to the protein surface.

All photolyases and cryptochromes share a conserved bilobal architecture, with an FAD chromophore bound to their C-terminal, all α-helical domain in an unusual U-shaped conformation (15). The C-terminal domain is hence responsible for either providing DNA-interaction sites in photolyases or light-dependent/independent interaction sites for CTE or other down-stream signaling partners in cryptochromes. The function of the N-terminal domain appears often to bind a second chromophore as light-harvesting antenna for broadening absorption in the visible spectral region (1). However, this domain has been recently found to provide specific interaction sites for signaling partners in type II cryptochromes (16). Antenna chromophores identified so far include 5,10-methenyltetrahydrofolate (MTHF) (17,18), 8-hydroxydeazaflavin (8-HDF) (19), flavin mononucleotide (FMN) (20), 6,7-dimethyl-8-ribityllumazine (DMLR) (21) and FAD in its fully oxidized state (22). The nature of the antenna chromophore in non-animal aCRYs is still unknown, e.g. *Cra*CRY lacks an additional chromophore besides FAD when overproduced in *Escherichia coli* (5,11,13).

In this study, we show that *Cra*CRY indeed represents a bifunctional cryptochrome due to its additional *in vivo* and *in vitro* function as a (6-4) photolyase. Like for the class II CPD photolyase from *C. reinhardtii* the blue light sensitivity of *Cra*CRY is boostered by its capability to incorporate 8-HDF as antenna chromophore. The co-crystal structure of *Cra*CRY with duplex DNA comprising a (6-4)PP shows not only a higher degree of variable bending of duplex DNA when bound to this type of photolyase, but also a distinct conformation for a catalytically critical histidine within the active site. The latter is clearly inconsistent with several recent theoretical models of the (6-4) photolyase mechanism, but suggests instead a repair reaction via an oxetane intermediate. Furthermore, the structure of *Cra*CRY shows an environment for shielding the terminus of the aromatic tetrad, which rationalizes the unusually long lifetime of the tyrosine radical state formed upon photoactivation.

MATERIALS AND METHODS

Multiple sequence alignment

1186 orthologs of the animal-like cryptochromes/(6-4) photolyases were derived from a sequence-similarity network generated on the whole photolyase-cryptochrome superfamily (23); their pairwise sequence identity for non-redundancy was restricted to <90% leaving 541 sequences for multiple-sequence alignment by Clustal Omega. The resulting alignment was used in WebLogo 3 (24) for visualization with the *Cra*CRY sequence as reference.

Co-expression of CraCRYΔCTE·8-HDF and CraCRY·8-HDF

Escherichia coli BL21(DE3) Gold cells (Stratagene) were transformed with either pET28a-*Cra*CRY (5) or pET28a-*Cra*CRYΔCTE (11) and the cofactor plasmid pCDF-His_6FbiC, encoding the FO synthase (7,8-didemethyl-8-hydroxy-5-deazariboflavin synthase) of *Streptomyces coelicolor*, following published procedures (25).

Expression and purification

Expression and purification of all *Cra*CRY variants were carried out following a published protocol (5). An additional heparin affinity chromatography was performed, which was washed with four column volumes of buffer containing 50 mM sodium phosphate, pH 7.8 and 20% (v/v) glycerol before applying the protein solution. It was eluted with a salt gradient reaching a concentration of 2 M sodium

chloride. For crystallization, the protein was further purified by size exclusion chromatography (Superdex 200, 120 ml CV) in 20 mM Tris, 200 mM NaCl, pH 8.5.

Crystallization and structure determination of *Cr*aCRYΔCTE

For crystallization *Cr*aCRYΔCTE was incubated overnight in the dark and pipetted under safe light using a crystallization robot (Digilab Honey Bee 963™) for screening of different conditions. Initial crystals were grown in 0.1 M 2-(*N*-morpholino)ethanesulfonic acid (MES), pH 5.6 and 35% PEG 4000 at 4°C. Crystals were then further improved by micro-seeding, and grown in 0.1 MES pH 5.6, 35% PEG3350. Crystals were soaked with 30% glycerol as a cryoprotectant and flash-frozen in liquid nitrogen. Diffraction data collection from a single crystal at 100 K was taking place at the BESSY II synchrotron light source in Berlin, or, alternatively, at the Taiwan Photon Source 05A microcrystallography beamline, National Synchrotron Radiation Research Center in Hsinchu. Diffraction images were indexed by *XDS* (26) with datasets derived form different crystals merged via a slightly modified version of the KAMO protocol (27). Briefly, datasets were first manually processed with XDS. Then, datasets were hierarchically clustered by their unit-cell parameters via the BLEND software within the CCP4 software suite. Next, clusters were merged via XSCALE (26). Finally, cluster data quality was assessed hierarchically by their 50% correlation coefficients (28). The structure was solved *via* molecular replacement (*Phaser MR* (29)) using a homology model that derived from the (6-4) photolyase of *Arabidopsis thaliana* (PDB: 3FY4). Refinement was performed by using a combination of REFMAC5 (*CCP4 package* (30,31)), phenix.refine (PHENIX) and COOT (32). Data processing and refinement statistics are presented in Table 1.

Crystallization of *Cr*aCRYΔCTE·8-HDF

Isomorphous crystals of the *Cr*aCRYΔCTE·8-HDF complex were grown in the dark at 18°C in 0.1 M MES, pH 6.0 with 15% PEG 5000. The crystals were mounted with 30% glycerol as cryoprotectant and flash-frozen in liquid nitrogen. Diffraction data were collected at 100 K from a single crystal at beamline ID23-2 in the European Synchrotron Radiation Facility (ESRF). Diffraction images were processed as described before.

Crystallization of *Cr*aCRYΔCTE in complex with DNA

For crystallizing the complex with (6-4)PP damaged DNA a synthetic DNA strand 5′-CAG CGG T(6-4)TG CCG TG-3′ was hybridized with its counter strand 3′-GTC GCC AAC GGC AC-5′ (96°C, shaking 10 min at 300 rpm) resulting in a blunt-ended double strand. Purified *Cr*aCRY was concentrated up to 10 mg/ml and incubated for at least 2 h in the dark, before the ds(6-4)DNA was added in 1.25 folded excess under safe light. Initial crystals grew under conditions with 0.1 M MES, PEG 6000 and different pH as well as precipitant concentrations. These conditions were used for further optimization screens, which resulted in crystals grown in dark at 4°C using 0.1 M MES, pH 5.5 and 10% (w/v) PEG 6000. Crystals were mounted with 30% glycerol as cryoprotectant and flash-frozen in liquid nitrogen. Diffraction data were collected at beamline ID23-1 at the ESRF resulting in 720 processed diffraction images.

Steady-state UV/Vis spectroscopy and photoreduction assay

Absorption spectra of *Cr*aCRY variants were recorded using a V-660 spectrometer (JASCO). The protein solutions were measured in buffer containing 50 mM NaH_2PO_4 pH 7.8, 100 mM NaCl and 20% (v/v) glycerol. The samples were incubated for 5 min in the dark before first spectra were recorded. Spectra were measured after different illumination times using a *high power* LED 450 nm (9.7 mW cm^{-2} at a distance of 10 cm, Roithner Lasertechnik) at 10°C.

Generation of (6-4)PP and *in vitro* photorepair assay

The *in vitro* repair assay of wild type *Cr*aCRY was done following published procedures (33). All steps were carried out under safe light (red) conditions. To generate fully reduced *Cr*aCRY capable of photorepair, samples of 120 μM protein solution were illuminated at a distance of 5.5 cm for 60 min by an LED (λ_{max} = 450 nm, 9.7 mW cm^{-2}; Roithner Lasertechnik) in the presence of 25 mM DTT. The (6-4)PP repair assay was performed with 39.5 μM of the irradiated oligo $(dT)_{18}$, 10 μM of fully reduced *Cr*aCRY and 25 mM DTT. The mixture was illuminated at a λ_{max} of 385 nm (LED, Roithner Lasertechnik; 3.5 mW cm^{-2} at 5.5 cm) and 15°C for 60 min. For control experiments, assays were performed without illumination and without *Cr*aCRY, respectively. A Maya 2000 Pro spectrometer (Ocean Optics) was used for recording of UV/Vis absorption spectra.

In vivo photorepair assay

The following *Chlamydomonas reinhardtii* strains were used: wild type SAG73.72 (mt^+), a knockdown *acry* mutant SAG73.72:acry1A ($acry_{mut}$ (5)) and a complemented strain ($acry_{compl}$) that has been transformed with vector pKP39 (5). The strain $acry_{compl}$, was analyzed by immunoblots using anti-aCRY antibodies and showed a rescue of *Cr*aCRY protein levels of ∼140% as compared to wild-type (100%; SI-S2b). UV-B survival assays were modified from Petersen and Ronan, 2010. Cells were grown under a 12-h light/12-h dark cycle (LD12:12) at a light intensity of 75 μmol photons m^{-2} s^{-1} and 23°C in Tris-acetate phosphate (TAP) medium (Harris, 1989) until they reached a cell density of 4–6 × 10^6 cells/ml. Cells were normalized to 2.6 × 10^6 cells/ml, three tenfold dilutions were made and 10 μl of each dilution were spotted onto TAP plates. The plates were either non UV-B treated or illuminated for 0.5, 2 and 3 min, respectively, with an UV-B lamp (XX-15M model from UVP) at an intensity of 2.2 mW/cm^2 with a peak at 312 nm as experimentally determined. The UV-B lamp was pre-run for 20 min to ensure stability in the UV spectrum and the energy output, which was measured with an UV-X radiometer (UVP). Afterwards the plates were immediately placed under the above described LD conditions with cool-white fluorescent

Table 1. Data collection and refinement statistics

	*Cra*CRYΔ496* 5ZM0	*Cra*CRYΔ496 6FN3	*Cra*CRYΔ496•8-HDF 6FN2	*Cra*CRYΔ496•(6-4) DNA 6FN0
Data collection and processing				
X-ray source, beamline	BESSY II Berlin, 14.3 NSRRC, Hsinchu, 05A	BESSY II Berlin, 14.3	ESRF, Grenoble, ID23-2	ESRF, Grenoble ID23-1
Detector	MX-225 and MX-300	MX-225	Pilatus6m	Pilatus6m
Wavelength (Å)	0.894 and 0.998	0.894	0.992	1.033
Space group	$P2_12_12_1$	$P2_12_12_1$	$P2_12_12_1$	$P4_22_12$
Cell dimensions (*a*, *b*, *c*)	50.21, 65.12, 151.98	151.80, 50.13, 65.07	150.25, 50.53, 64.97	146.24, 146.24, 67.44
Resolution (Å)	39.8–1.60 (1.66–1.60)	75.9–1.9 (2.0–1.9)	29.8–2.3 (2.4–2.3)	103.4–2.9 (3.0–2.9)
Total reflections‡	886 219 (66 592)	74 526 (7462)	43 054 (4233)	33 333 (3269)
Multiplicity‡	13.3 (10.2)	2.0 (2.0)	2.0 (2.0)	2.0 (2.0)
Unique reflections‡	66 645 (6554)	38 187 (3803)	22 003 (2159)	16 737 (1639)
Completeness (%)‡	100 (100)	95.5 (96.6)	96.6 (97.2)	99.8 (99.9)
R_{merge}*,‡	0.275 (1.68)	0.058 (0.211)	0.070 (0.205)	0.050 (0.307)
$CCI/2$*,‡	0.992 (0.506)			
$I/\sigma(I)$‡	8.5 (1.3)	13.7 (4.4)	7.2 (3.5)	12.5 (2.7)
Mosaicity (°)	0.150	0.15	1.53	0.134
Wilson *B*-factor (Å^2)	10.01	11.74	19.75	61.95
Refinement				
Resolution (Å)	39.8–1.6	75.9–1.9	29.8–2.3	61.2–2.9
R_{factor}, R_{free}	0.159, 0.188	0.163, 0.206	0.170, 0.228	0.155, 0.215
Reflections (working, test set)	66 645, 3302	37 003, 1184	21 265, 682	16 201, 536
Completeness for range (%)	100	95.6	96.5	99.8
r.m.s.d. from ideal:				
Bond lengths (Å)	0.008	0.009	0.009	0.010
Bond angles (°)	1.280	1.416	1.436	1.507
Total number of atoms	4907	4527	4306	4754
Mean *B*-value (Å^2)	15.0	13.6	21.5	63.8

*5ZM0 corresponds to a composite dataset based on a total of four crystals collected at BESSY II and NSRRC achieving a multiplicity of 13.29. As described before (28), high multiplicity datasets suffer profoundly from R_{merge}-derived resolution cutoffs. Instead, the 50% correlation coefficient (CC1/2) should be used (28). In this case, the maximum resolution cutoff was determined by a minimal CC1/2 value of 0.5 at the highest resolution shell.
‡Values in parentheses correspond to highest resolution shell.

light at an intensity of 75 μmol photons m^{-2} s^{-1} for recovery. After 7 days of cell growth under these conditions, pictures of the plates were taken.

RESULTS

Overall architecture of *Cra*CRY and its chromophore binding sites

For structure determination of C*ra*CRY, its wild type (WT) and the CTE deletion mutant (*Cra*CRYΔCTE) were screened and optimized for crystallization. Despite its homogenous characteristics full-length *Cra*CRY failed to crystallize, most likely due to a disordered CTE, whereas we obtained well-ordered orthorhombic crystals of *Cra*CRYΔCTE diffracting up to 1.6 Å resolution (Table 1). The *Cra*CRYΔCTE structure (Figure 1) displays the typical two-domain architecture, which is common for all members of the PCSf. In this bilobal structure, a typical ROSSMANN fold is defined by the N-terminal domain (K5-V129). This domain lacks an antenna chromophore but harbors in its putative binding site two additive molecules, 2-(*N*-morpholino)-ethanesulfonic acid (MES) and glycerol (GOL), from the crystallization condition (Figure 1A). The catalytic C-terminal domain harbors the flavin cofactor FAD in a U-shaped conformation like other PCSf members (18,34–36). The N5 nitrogen of the oxidized isoalloxazine moiety forms a rather weak hydrogen bond with N395 as judged by the N5-ND2 distance (3.3 Å). This asparagine or a structurally corresponding residue is known to control the photochemistry of flavins in all photolyases and cryptochromes and to be well conserved within all members of the PCSf capable of DNA repair apart class II and bacterial (6-4) photolyases (17,18,37). Despite this role, N395 is unsuitable to act as a proton donor for the FAD$^{\bullet}$ intermediate formed after photoreduction of the FAD chromophore because of its high pK_a value (~25,5 (38)). As no other deprotonatable residues are close to the N5 nitrogen, the proton is probably derived from the solvent. Here, N395 may be a gate keeper to the solvent because it forms a second H-bond with a surface-bound water that is coordinated to the surface-exposed residues E384 and Q390. This water is conserved in the structure of the *D. melanogaster* (6-4) photolyase as well, but replaced in cryptochromes failing to achieve the semiquinoid FADH$^{\circ}$ state like *Dm*CRY by a hydrophobic leucine moiety.

The tryptophan triad that is commonly found in the PCSf was identified as W399, W376 and W322 by structural comparison and multiple sequence alignment. These three aromatic residues catalyze ET from the surface of the protein to the excited flavin chromophore (39,40). In *Cra*CRY this ET pathway is elongated by Y373 to an aromatic tetrad (Figure 1C) (11,13). The structure shows that Y373, which is only 5.5 Å distant from the third tryptophan, W322, resides close to the protein surface. Its side chain is surrounded

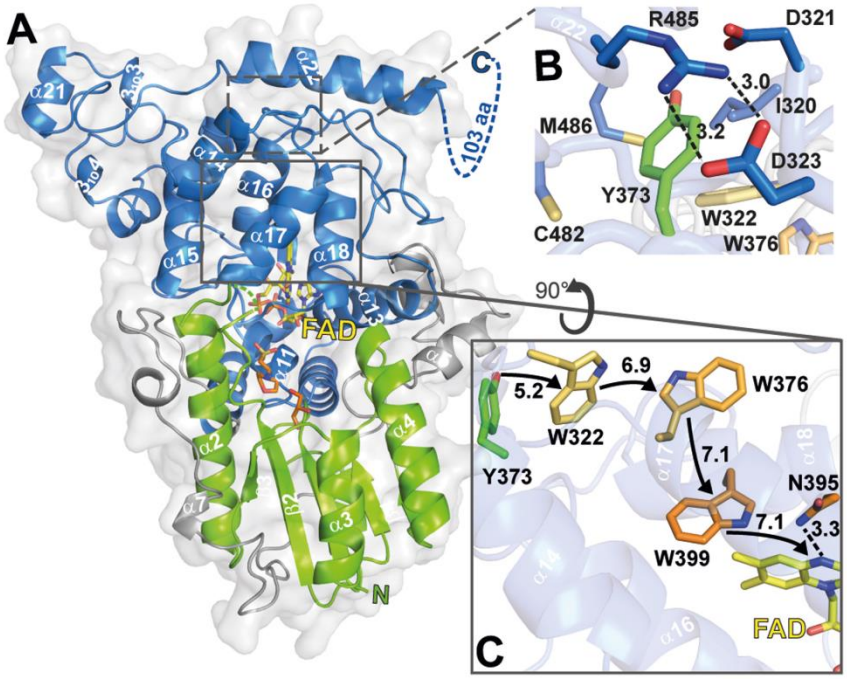

Figure 1. Cartoon representation of *Cr*aCRY structure with highlighted regions of interest. (**A**) Overall structure of *Cr*aCRYΔCTE (6FN3) with FAD (yellow) bound to the C-terminal domain (blue). The C- and N-terminal domain (green) are connected through a flexible loop region (grey). The antenna binding site is occupied by glycerol (GOL, orange) and 2-(*N*-morpholino) ethanesulfonic acid (MES, orange). The C-terminal extension (494–595) is displayed as dotted lines. (**B**) Detail environment of the fourth aromatic residue, Y373. (**C**) The electron transfer pathway of *Cr*aCRY is marked with arrows, centroid-centroid distances are shown in Å. The Trp triad is shown in orange and the fourth aromatic residue, a terminal tyrosine (Y373), is shown in green. Also the potential proton donor of the FAD, N395, is presented as sticks.

by a network of charged residues, most prominently by a salt bridge formed between D323 and R485 (Figure 1B), which appears to stabilize the formation of the long-lived radical by shielding the deprotonated Tyr-O$^{\circ}$ from solvent access. Rapid deprotonation of the terminal tyrosyl radical may be supported by D321 as proton acceptor due to its H-bond formation with the Y373 hydroxyl group (2.9 Å). Like R485, two other residues contacting the phenolic moiety of Y373, C482 and M486 are part of the long C-terminal helix α22 (H475-K494, Figure 1A, B). Mutagenesis of C482 was found to affect red-light dependent, FADH$^{\circ}$ → FADH^{I} driven dimerization of *Cr*aCRY under *in vitro* conditions, maybe due to the ablation of disulfide bond formation (11).

*Cr*aCRY shows DNA repair activity *in vitro* and *in vivo*

To address, whether *Cr*aCRY can act as (6-4) photolyase, we performed *in vitro* repair activity assays as established before (33,41). Incubation of the catalytically competent *Cr*aCRY in its FADH^{I} state with a (6-4)PP comprising oligo(dT)$_{18}$ shows, that illumination at 385 nm causes decreasing absorption at 325 nm, which corresponds to repair of the (6-4)PP (Figure 2A). From the specific decrease, we calculated that after 60 min of illumination almost 70% of the single-stranded DNA with (6-4)PP has been repaired. These data lead to the conclusion that *Cr*aCRY may act as efficient (6-4) photolyase in *Chlamydomonas*.

To analyze the *in vivo* activity of *Cr*aCRY by an UV-B survival assay, we used the following *C. reinhardtii* strains: wild type SAG73.72 (mt^{+}), the knockdown *acry* mutant SAG73.72:acry1A (*acry*$_{mut}$ (5)) and a complemented strain of *acry*$_{mut}$ that has been transformed with vector pKP39 (*acry*$_{compl}$ (5)). The different algae strains were exposed to UV-B light for certain times and grown under white light within a light-dark cycle for 7 days. As predicted, survival of the knockdown mutant (*Cr*aCRY expression level: ∼20% of WT) decreases with longer UV-B illumination times (0.5, 2.0 and 3.0 min) when compared to WT (Figure 2B). In contrast, the complemented strain *acry*$_{compl}$ (*Cr*aCRY expression level: ∼140% of WT) shows WT-like resilience against UV-B light even when illuminated for 3.0 min (SI-S2A). These results correlate with the *in vitro* data and confirm the important role of the animal-like cryptochrome as a repair enzyme for UV-B induced DNA lesions in *C. reinhardtii*.

Structural basis for (6-4)PP repair by *Cr*aCRY

Co-crystals of *Cr*aCRYΔCTE in complex with blunt end 14mer duplex DNA diffracted to a resolution of 2.9 Å. The *Cr*aCRYΔCTE/(6-4)PP-DNA complex shows a highly kinked duplex DNA bound to the C-terminal domain, with the (6-4)PP flipped into the active site (Figure 3A) thus giving rise to a large unpaired bubble within the duplex DNA. With a kinking angle of 60° *Cr*aCRY causes stronger

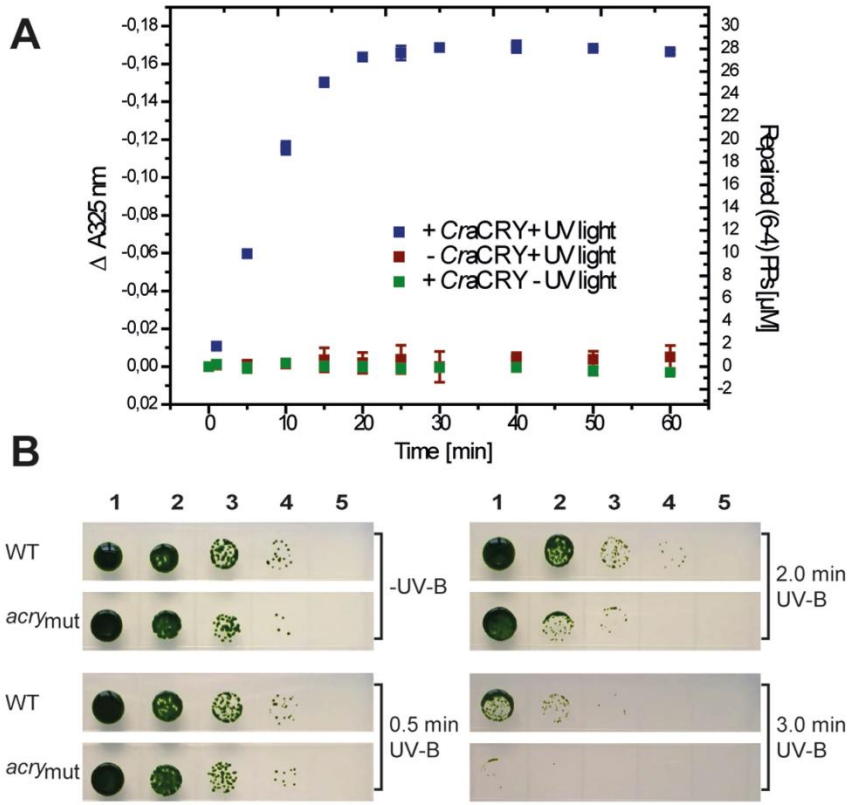

Figure 2. *In vitro* and *in vivo* repair of (6-4)PP by *Cra*CRY. (**A**) *In vitro* DNA repair activity assay with 30 μM of the irradiated oligo-$(dT)_{18}$, abbreviated as (6-4)PPs, 10 μM of *Cra*CRY in the $FADH^-$ state and 25 mM DTT. Controls are shown without *Cra*CRY or illumination. (**B**) UV-B survival of *C. reinhardtii* is reduced in the *acry* mutant compared to WT. Equal numbers of cells starting from 2.6×10^6 cells/ml (lane 1) and three subsequent tenfold dilutions (lanes 2–4) or no cells (lane 5) were spotted onto TAP plates and illuminated for 0.5, 2 and 3 min, respectively, with 2.2 mW/cm^2 UV-B light. Cells from wild type (WT) and an *acry* knockdown mutant ($acry_{mut}$) with a reduced rate down to ~20% compared to WT were used for the assay. A plate with no UV-B treatment was used as growth control (-UV-B). Pictures were taken after 7 days of growth.

bending of (6-4)PP-comprising duplex DNA than the previously characterized structures of *D. melanogaster* (6-4) photolyase/DNA complexes (52°, 3CVU). When comparing *Cra*CRY and the *Dm*(6-4) the conformation of the lesion-comprising DNA strand is almost the same for the bound (6-4)PP and the backbone between the −1 and +3 phosphates (Figure 4A). However, conformational differences between DNA bound to *Cra*CRY and *Dm*(6-4) are not only observed for the flanking ends of the duplexes, but also for the counter bases of the thymines corresponding to the (6-4)PP (SI-S3B).

The wider opening of the double strand along the lesion site in the *Cra*CRYΔCTE/(6-4)PP-DNA complex and the flipping of the damaged DNA is supported by a bubble-intruding region (BIR, S409-R413) that is part of the loop linking the α18 and α19 helices. The BIR intervenes between the double strand by forming hydrophobic interactions between the aromatic side chain of F412 and a cytosine preceding the adenine counter bases (π–π interaction) as well as between R413 and the guanine base (CH–π) that is 3′ of the thymine residues of the (6-4)PP. The latter residue, whose side chain conformation depends on DNA binding (Figure 4B), is highly conserved in most (6-4) photolyases and forms Coulombic interactions with the intralesion and the 3′ phosphate groups. QM/MM calculations and mutagenesis of *Xenopus laevis* (6-4) photolyase, *Xl*(6-4), as shown in an accompanying paper (42) corroborate the notion that the Coulombic R410-phosphate (R410 in *Xl*(6-4) corresponding to R413 in *Cra*CRY) interactions serve as anchor during early formation of the CraCRY/DNA complex, whereas the CH–π interaction with the base following the (6-4)PP are required to form the maturely complex. Due to the local opening of the DNA duplex the (6-4)PP enters the active pocket for interacting directly with the FAD. There, the photoproduct forms a hydrogen bond (2.8 Å) between the C4 carbonyl group of the 5′-thymine moiety with the N6-amino group of the FAD's adenine. A glutamine (Q291) provides specific interactions with the 5′-thymine via hydrogen bonds. The 3′-thymine is stabilized by a water network (Figure 5A) also involving two highly conserved histidine residues (Figure 3C).

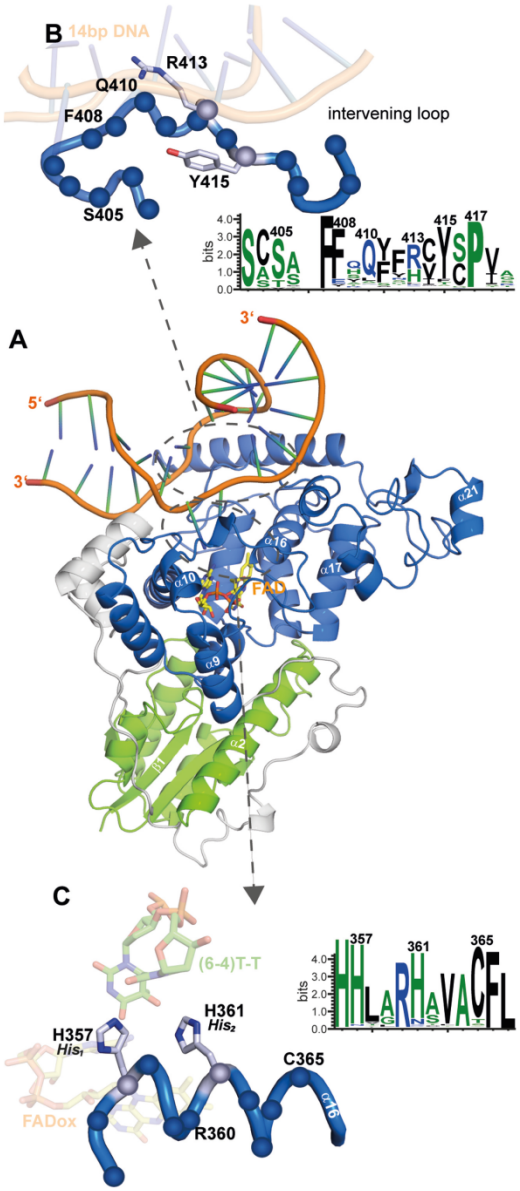

Figure 3. Co-crystal structure of *Cr*aCRY in complex with (6-4)PP comprising duplex DNA. (**A**) Overall structure of *Cr*aCRYΔCTE with 14 bp duplex DNA (6FN0) illustrated as cartoon model. (**B**) Detailed view of the bubble-intruding region of *Cr*aCRY highlighting arginine residue R413. In contrast to *Dm*(6-4) photolyase this residue appears to form only a distant salt bridge (3.9 Å versus 3.1 Å) with the intra-lesion phosphodiester group of the (6-4)PP. Conservation of the BIR within the animal-like cryptochromes/(6-4) photolyases was obtained from 541 non-redundant sequences with less than 90% pairwise sequence identity. The size of the letter correlates with the degree of conservation, for details refer to Supplementary Figure S4. (**C**) Detailed view of helix α16, which harbors the catalytic histidine residues H357 (His_1) and H361 (His_2), nomenclature in parentheses according to Yamamoto *et al.* (43). The HHLARH motif commonly found in (6-4) photolyases is also part of the *Cr*aCRYΔCTE active site.

Both catalytically crucial histidines, H357 (His_1) and H361 (His_2, for nomenclature see Yamamoto *et al.* (43)), and the (6-4)PP are clearly defined by OMIT electron density maps. His_2 of *Cr*aCRY shows the exact position as H369 in *Dm*(6-4) and forms with its imidazole side chain two hydrogen bonds (Figure 5). One is formed via its Nε2 atom to a nearby tyrosine, Y415 (2.7 Å; *Dm*(6-4): Y423), the other via Nδ1 to water molecule WAT2, which is centrally located within the active site by bridging both to the O4 carbonyl and 5-hydroxyl groups of the (6-4)PP as well as to the N6 amino group. The important difference is presented by the conformation of the His_1 side chain. In the *Cr*aCRYΔCTE/(6-4)PP-DNA complex His_1 adopts a *gauche*^{l} rotamer for its χ_1 torsion (77.3°), whereas the corresponding residue in the *Dm*(6-4)/(6-4)PP complex, H365, shows a *trans* conformer (177.2°). Consequently, His_1/H357 points in *Cr*aCRY towards the preceding histidine, H356, and the 3′ base of the (6-4)PP, but away from the adenine moiety of the FAD cofactor. Accordingly, H357 cannot form a hydrogen bond with the O5-hydroxyl of the 5′-base anymore as observed before for His_1 of *Dm*(6-4). Instead it swivels away up to 4 Å from the 5′-base and His_2 into a highly conserved subpocket that is walled by the side chains of K237, T240, H356, L358 and the 3′-base, but unoccupied in *Dm*(6-4). The freed space is instead filled in *Cr*aCRY by water molecule WAT1 that forms an H-bond with His_2. Most importantly, His_1 is now in H-bonding distance to the carbonyl O2 of the 3′-base (NE2-O2: 3.0 Å; Figure 5A). For *Dm*(6-4) it has been shown that the complete triad of His_1-His_2-Tyr (Y423, *Cr*aCRY: Y415) is important for catalysis (36). Especially, His_1 is found to be crucial, because mutagenesis to alanine in the *Xl*(6-4) reduces the quantum yield of repair by ∼500% (43). This triad is also present in *Cr*aCRY, but as the conformation for His_1 is clearly different, our crystal form may have trapped another catalytically competent conformation of the active site.

The antenna chromophore in *Cr*aCRY

As recombinant *Cr*aCRY lacks any antenna pigment, the identity of its light harvesting chromophore was elusive before. Interestingly, Petersen *et al.* showed that not only the phr2 gene coding for a class II CPD-photolyase, but also *phr1* from *Chlamydomonas* is essential for photoreactivation, i.e. light-dependent repair of UV-lesions in DNA (44,45). However, this gene does not code for a photolyase but a bifunctional FO synthase, which catalyzes the synthesis of 8-HDF, a chromophore that serves in many members of the PCSf as antenna and is particularly important for photolyases because of the low blue-light extinction coefficient of the catalytically competent FADH^{l} cofactor. We performed *in vivo* reconstitution using a helper plasmid coding for the bifunctional FO synthase from *Streptomyces coelicolor* (19). UV/Vis spectroscopy reveals a significant peak at 449 nm for a *Cr*aCRY•8-HDF complex (Figure 6A), where the incorporated 8-HDF cofactor is bathochromically shifted by 29 nm relative to free 8-HDF (λ_{max} = 420 nm) (19). Similar shifts of the antenna chromophore absorption have been described for other 8-HDF binding members of the PCSf (25,46–49).

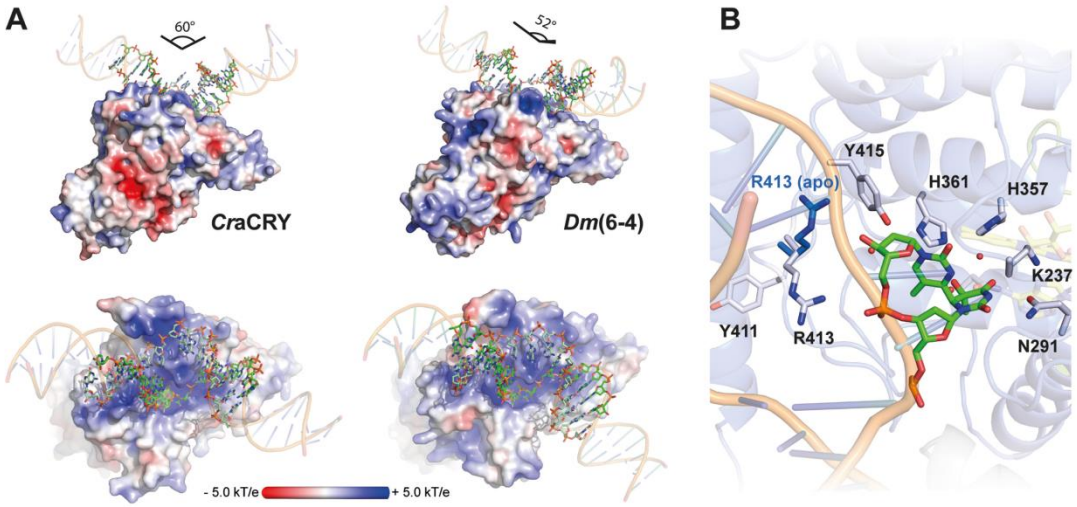

Figure 4. (**A**) Comparison of the (6-4)PP damaged duplex DNA binding to *D. melanogaster* (6-4) photolyase (3CVU) and *Cr*aCRY (6FN0). Electrostatic potentials were calculated with APBS ($c = 0.1$ M, solvent radius = 1.4 Å). The DNA ends were prolonged by regular B-type DNA using PyMOL and the overall binding angles of the DNA therefrom derived. (**B**) Detailed view of the (6-4)PP binding depicting the flipping of R413 upon DNA binding. The side chain of R413 in the unbound *Cr*aCRY structure is shown in blue.

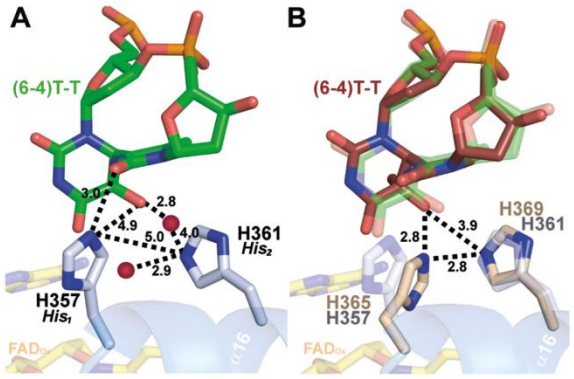

Figure 5. Conformation of the active site histidines in (6-4) photolyases. (**A**) Enhanced view of the (6-4)PP interactions with the two prominent residues H357 (His_1) and H361 (His_2) of *Cr*aCRY (gray). Distances (in Å) were measured between the histidines, the DNA lesion and two water atoms (red). (**B**) Comparison of the active site of *Cr*aCRY (6FN0, gray) with *Dm*(6-4) (3CVU, wheat) (r.m.s.d. 0.658 Å). The (6-4)PP bound to *Dm*(6-4) (red) is slightly tilted compared to the (6-4)PP bound to *Cr*aCRY (green).

To characterize *Cr*aCRY/8-HDF interactions we generated and analyzed the co-crystal structure of the *Cr*aCRYΔCTE/8-HDF complex (Figure 6B). The binding motif within the N-terminal domain that surrounds the ribityl moiety of the 8-HDF is composed of several highly conserved amino acids, namely D105, E107, R113 and D114, which form H-bonds with the ribityl hydroxy-groups. The C2-carbonyl group of the deazaflavin moiety is coordinated by two water molecules, which form H-bonds with W10, the backbone of F11 and D40. The second carbonyl group (C4) forms a hydrogen bond to a water molecule, which is coordinated by Y56 and the carbonyl-group of D40. The deprotonated hydroxy-group of the benzo ring system makes salt bridges to two basic amino acids, R55 and K258, and is further stabilized by Y49. The two basic amino acids are highly conserved in this class of aCRY/(6-4) photolyases as shown in multiple sequence alignments (SI-S4), whereas in class II photolyases the lysine is always replaced by a histidine (19). Unlike the apo-structure, the antenna loop is completely defined by electron density as F43 performs a flip, to engage π-π-stacking interactions with the deazaflavin moiety of 8-HDF. The bottom of the binding pocket is flanked by some small, unpolar amino acids (L59, L39), which are similarly found in other photolyases (25,46).

DISCUSSION

Our study shows that the full length animal-like cryptochrome of *C. reinhardtii* exerts DNA repair activity for (6-4)PP *in vitro* and *in vivo*. Before, *Cr*aCRY has been annotated due to its biological function as a cryptochrome. However, our sequence similarity network analysis (SI-S1) clearly shows that a distinction between (6-4) photolyase and cryptochrome in this common subgroup of the PCSf (1186 sequences) is non-trivial. Only members of the subcluster of insect cryptochromes (89 seq.), including *Dm*CRY, function unambiguously only as signaling proteins due to a cysteine that replaces the conserved asparagine interacting with the N5 nitrogen of FAD (*Cr*aCRY: N395). This replacement is known to arrest insect cryptochromes in the non-protonated FAD^{ox} state after the first photoreduction event, so that these members of the PCSf cannot form the fully reduced and catalytically active $FADH^{\bullet}$ state required for (6-4) photolyase activity (50). In contrast, *Cr*aCRY can be found like other algal

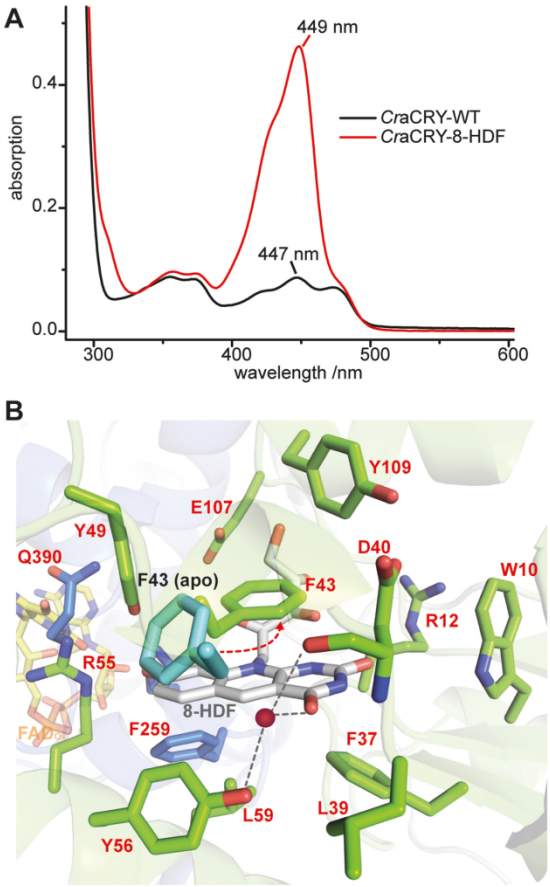

Figure 6. 8-HDF as light harvesting antenna chromophore of *Cra*CRY. (**A**) Comparison of the absorption spectra of WT *Cra*CRY and *Cra*CRY•8-HDF in solution. (**B**) Binding pocket of 8-hydroxydeazaflavin (8-HDF, gray) and comparison of the conformation of F43 in the apo (6FN3) and holo (6FN2) structure. F43 flips to engage a π–π-stacking with the aromatic rings of 8-HDF. A water molecule (red) is present in the pocket.

cryptochromes/(6-4)photolyases between a large subcluster of cryptochromes (480 seq.), mainly of animal origin including vertebrates and mammals, and a subcluster of assigned (6-4) photolyases from plants (77 seq.). In the fungal subcluster (213 seq.) annotations as (6-4) photolyases and cryptochromes are almost evenly split (SI-S1). A prevalence of bifunctional cryptochromes among fungi may be hence similarly given as for algal cryptochromes like *Cra*CRY, e.g. the ortholog from *Trichoderma atroviride* that is designated as cry1 was found to mediate both (6-4) photolyase-dependent photoreactivation and control of gene expression (51). Interestingly, in the plantal subcluster of (6-4) photolyases the forth redox-active residue of the aromatic tetrad is replaced by a phenylalanine. Accordingly, one may suggest that cryptochrome function or bifunctionality depend on the presence of an elongated intramolecular electron transfer chain and thereby increased stabilities of radical pair states, whereas (6-4) photolyase activity may be also driven by a 'conventional' aromatic triad as found in other photolyase families of the PCSf.

The specific repair function for (6-4)PP damaged DNA was observed before in algae for the CPF1 orthologs from *P. tricornutum* and *O. tauri* (7,52). Both CPF1s act as transcriptional regulators and have been therefore assigned as bifunctional photoreceptors (52). *Cra*CRY also shows this bifunctional behavior, as it exerts not only repair of (6-4)PP but also regulates the expression of various genes (5). Recent studies showed that *Cra*CRY controls the sexual life cycle of *C. reinhardtii* together with pCRY (53) at steps affecting mating ability in a negative manner in contrast to PHOT (54). Together with phototropin and pCRY, *Cra*CRY also controls positively zygote germination (55). *Cra*CRY was shown to be enriched in the nucleus during daytime, whereas it is delocalized over the whole cell body at night (55). The latter is consistent with the repair of nuclear (6-4)PP as these are only formed upon exposure to ultraviolet light as provided by sunlight during the day period. Given its red/yellow-light activity (5) that is clearly distinct from other characterized cryptochromes, the signaling function of *Cra*CRY may highly rely on the light-dependent formation of the $FADH^{I}$ state rather than that of the $FADH^{\circ}$ state. Accordingly, bifunctionality as realized by *Cra*CRY may be a highly economic way by exploiting the photoactivation reaction, $FADox \rightarrow FADH^{\circ} \rightarrow FADH^{I}$, 2-fold: First, for monitoring the illumination status of the cell and, secondly, for keeping the (6-4) photolyase in its active fully reduced state. Clearly, such a scheme is expected to give rise to rather complex regulation with down-stream interaction partners under blue/near-UV light as *Cra*CRY binds like other bifunctional cryptochromes/photolyases to UV-damaged DNA also in its oxidized states. Signaling as provided by *Cra*CRY may hence not only simply reflect changes of light exposure, but also the UV-damaging status of the genomic DNA.

Our first crystal structure of a cryptochrome from a green algae, *Cra*CRY, shows besides the essential catalytic FAD cofactor, 8-hydroxydeazaflavin as antenna chromophore. For its biosynthesis the bifunctional synthase, Phr1, is required in *C. reinhardtii* and other green algae. Interestingly, deletion of the PHR1 gene causes loss of photoreactivation in *C. reinhardtii*, which cannot be rescued by high-level overexpression of the PHR2 gene coding for an endogenous class II CPD photolyase, which might harbor 8-HDF (25,44). Given the capability of *Cra*CRY to incorporate 8-HDF in its N-terminal antenna binding domain the loss of photoreactivation by PHR1 deletion may not only be caused by insufficient *in vivo* activity of the class II CPD photolyase Phr2, but also by a loss of (6-4) photolyase activity as provided by *Cra*CRY. Indeed, a multiple sequence alignment covering 541 non-redundant animal-like CRYs and (6-4) photolyases (SI-S4) delineates well conserved residues within the antenna binding site and hence a wide-spread usage of 8-HDF, including several (6-4) PHL from animals (46). Interestingly, the biosynthesis pathway for 8-HDF is preserved in the green lineage also in mosses, but not any more in higher, vascular plants (23). This distribution can be explained by the biological role of the second chromophore, which is to broaden the absorption range

and efficiency of the photolyases especially in their catalytically competent $FADH^{I}$ state, e.g. 8-HDF has an almost tenfold higher extinction coefficient at 400 nm than $FADH^{I}$ ($25\ mM^{-1}\ cm^{-1}$ versus $2.8\ mM^{-1}\ cm^{-1}$). Apparently, algae face a greater challenge than higher plants to collect light at short wavelengths for non-photosynthetic, but essential reactions such as DNA repair, as they have to thrive in aqueous environments.

The photoreduction of the catalytic flavin cofactor *Cra*CRY from the fully oxidized (FAD_{ox}) over the neutral radical ($FADH^{\circ}$) to the fully reduced ($FADH^{I}$) state, is not catalyzed by the canonical tryptophan triad known from other PCSf subfamilies, but by an extended tetrad that depends on a fourth aromatic residue (11,13), in the case of *Cra*CRY ending on a terminal tyrosine, Y373. This extended tetrad is uniquely conserved in the family of animal-like cryptochromes/(6-4) photolyases and was first described for members harboring a terminal tryptophan (56). Upon excitation of the FAD in *Cra*CRY an electron gets abstracted from the proximal tryptophan (W399) resulting in an electron hole at this residue. Then the hole skips towards the surface (W399←W376←W322), where tyrosine (Y373) functions as terminal electron donor. We could show before, that Y373 forms a long-lived deprotonated tyrosyl radical (2.6 s) during formation of the $FADH^{I}$ state (11). *In vivo,* the unusually long lifetime could be physiologically advantageous, because it allows formation of the catalytically competent $FADH^{I}$ cofactor even when extrinsic reductants for reduction of the tyrosyl radical are in scarce supply. Subsequently, *Cra*CRY with accumulated $FADH^{I}$ state can act as photolyase for repairing (6-4)PP lesions. Sequence analysis of 541 non-redundant members of the animal-like cryptochrome/(6-4) photolyase family shows that about 1/3 (162/541) harbor tyrosine as terminal aromatic residue, almost all of them belonging to fungal orthologs and some algae and a few plants including *C. reinhardtii* and *Zea mays*. Those ending their aromatic tetrad with a tryptophan (333/541) mostly belong to animals and a few algae like CPF1 from *P. tricornutum* (11). Interestingly, in the green lineage including most higher plants and also some algae like *O. tauri*, the terminal aromatic residue is replaced by a non-redox active phenylalanine (44/542) indicating that the presence of a catalytic tetrad may have gone lost during further evolution and is dispensible at least for plantal (6-4) photolyase activity. Recent studies on the *Xl*(6-4) photolyase showed that the loss of the fourth redox-active aromatic residue slows indeed photoreduction by up to three orders of magnitude under steady-state conditions and hence impedes recovery of *Xl*(6-4) photolyase from accidental electron loss of its FAD cofactor (14).

Animal-like cryptochromes have apparently evolved a plethora of different docking sites for down-stream signaling partners. In *Dm*CRY the active site itself interacts in a light-dependent manner with the CTE, whereas murine CRY2 uses this site and the emptied FAD-binding pocket for binding to the ubiquitin-ligase FBXL3 (57,58). Another interaction site that has been assigned in type I and type II animal cryptochromes is the 8-HDF binding site of *Cra*CRY, which lost the ability to bind this or another antenna chromophore during their evolution (16). Interestingly, the C-terminal helix α22 acts in animal cryptochromes like murine CRY1 as major docking site for several circadian rhythm factors like TIM, PER2, BMAL1 and FBXL3 (57,59–62). Given that no *Cra*CRY interaction partners have been identified till date, one may suggest that the rather slow light-driven change of the redox and protonation state of Y373 may distort the packing of helix α22 to the photolyase domain, e.g. by proton transfer and subsequent breakage of the hydrogen bond to D321 (3.1 Å). Such a mechanism for an altered interaction with down-stream partners is of some reminiscence to that of phototropin-like LOV domains, where the C-terminal Jα-helix dissociates from the photoreceptor domain upon lit state formation (63).

Although the binding mode of the (6-4)PP in *Cra*CRY resembles that of the (6-4) photolyase from *D. melanogaster*, there are some striking structural differences: First, the overall kinking angle of the DNA duplex differs by ∼8° and coincides with a wider opening of the duplex at the lesion site and formation of specific interactions between the counter bases of the (6-4)PP and the C-terminal helix. The (6-4)PP is likewise positioned in the active site, but an unexpected difference is found for the conformation of His_1 in *Cra*CRY (H357). Although adopting only a different rotamer for its side chain than the corresponding His_1 residue of *Dm*(6-4), H365, this structural detail challenges mechanisms of (6-4) photolyases, which were based on previous structures of *Dm*(6-4) with (6-4) lesion-comprising DNA. In *Cra*CRY, the Nε2 atom of the imidazole moiety of His_1 is in H-bonding distance to the C2 carbonyl group of the 3′-base (Figure 7B). Therefore, we propose that His_1 is protonated and acts as general acid for the C2 carbonyl oxygen after light-driven formation of the radical anion by forward electron transfer (FET). A protonated state of His_1 in the substrate complex is corroborated by earlier studies on *Xl*(6-4) (64,65) and theoretical calculations done for *Dm*(6-4) (66). As a result of FET, which may involve additional intramolecular electron transfer from the electron-rich 5′ ring, the radical anion is formed at 3′ base. Fast proton transfer onto its C2 carbonyl oxygen (PT, step I in Figure 7A) results in formation of the enol form of the 3′-thymine moiety of the (6-4)PP. Through reverse electron transfer (RET, step II) back to $FADH^{-}$, C4 gets highly nucleophilic which may lead to concomitant formation of the oxetane intermediate (step III) under proton transfer (PT) to His_2. Light-driven formation of the oxetane intermediate is accomplished after intramolecular proton transfer to form the final keto-form (step IV). In this model, the first photoactivation and electron transfer step from the $FADH^{-}$ to the (6-4)PP and back is merely required to overcome the high activation barrier for thermal formation of the oxetane intermediate (65). According to this model, DNA repair by (6-4) photolyases requires a second photon to proceed from the bound oxetane intermediate to breaking the C6-C4 and C5-O4 bonds. This second step would be analogous to the single-photon driven repair of CPD lesions by CPD photolyases, where the light-generated CPD radical-anion undergoes almost barrier-free breakage of the C5-C5 and C6-C6 bonds (36,43,67,68).

The shown mechanism is in major parts based on the two-photon mechanism as proposed by Sadeghian *et al.* (66) and Yamamoto *et al.* (43,69) and experimentally supported by recent time-resolved spectroscopy experiments (41). How-

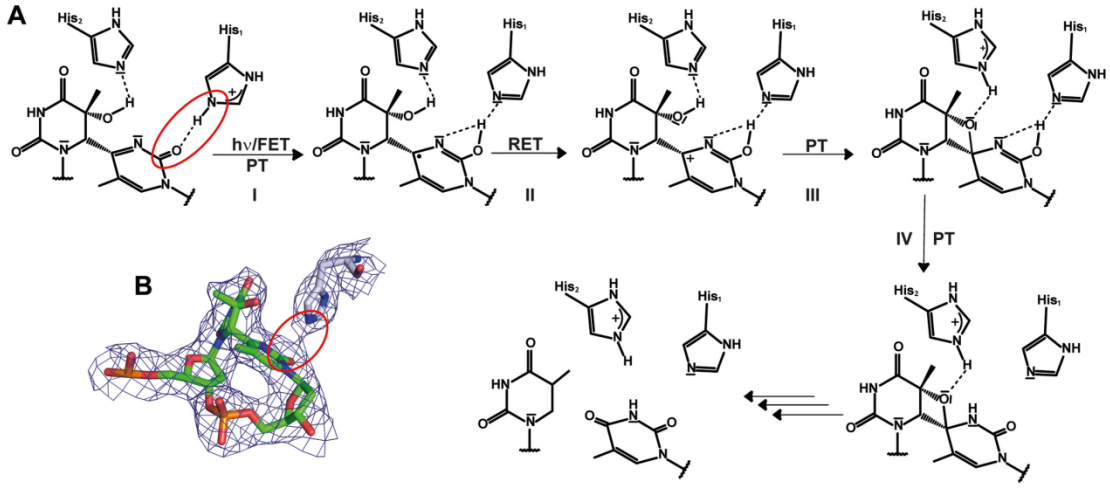

Figure 7. Proposed two-photon mechanism of (6-4)PP repair by *Cra*CRY. (**A**) This mechanism resembles the two photon mechanism suggested by Sadeghian *et al.*(66) without the direct involvement of a water molecule. Both histidine residues are involved in the proton transfer (PT) and the stabilization of the oxetane intermediate. The second forward electron transfer (FET) as well as the return electron transfer (RET) are not shown in detail. (**B**) Given the difference electron density map (F_{obs} - F_{calc}, contoured at 1.25σ) a hydrogen bond between the carbonyl oxygen of the 3′ base and the nitrogen N2 of His_1 can be predicted (3.0 Å distance).

ever, as a consequence of the observed His_1 conformation and hydrogen bonding pattern, a major difference to the model of Schütz and coworkers (66) is the transient proton transfer from His_1 to the C2-carbonyl group of the 3′-thymine instead to the N3 nitrogen. The nucleophilicity of the C2-carbonyl oxygen is apparently higher than that of the nitrogen, as ^{15}N-labeling of the (6-4)PP and NMR-monitored titration showed that the N3 nitrogen lacks any proton accepting properties in the ground state due to a pK_a < 1 (70). Given the limited lifetime of an enzyme-bound oxetane-like intermediate, the high propensity to form the fully reduced and catalytically active $FADH^-$ cofactor by an aromatic tetrade, even when external reductants are limiting, may foster the efficiency of DNA repair under physiological conditions. The contradiction to most previous computational studies on the (6-4)PP repair mechanism, which claim a single-photon based mechanism for (6-4) photolyases, can be now understood by their high reliance on the available structural information for *Dm*(6-4) (36,71). As the same can be assumed for our structure-based two-photon model and to overcome the one- vs. two-photon controversy we require either time-resolved X-ray crystallographic data of the (6-4) lesion repair process or bioanalytical identification of the reaction product as formed after first photon absorption by (6-4) photolyase/(6-4)PP complexes.

DATA AVAILABILITY

The multiple sequence alignment was analyzed with SeaView v3.2 (http://doua.prabi.fr/software/seaview). WebLogo 3.0 was used for the visualization of conserved residues (http://weblogo.threeplusone.com/create.cgi). For structure solution and refinement tools of the CCP4i package were used (www.ccp4.ac.uk). Electrostatic potentials were calculated with APBS (http://www.poissonboltzmann.org). Data sets were merged following the KAMO protocol (https://github.com/keitaroyam/yamtbx/blob/master/doc/kamo-en.md). Atomic coordinates and structure factors for the reported crystal structures have been deposited with the Protein Data bank under accession number 5ZM0, 6FN3, 6FN0 and 6FN2.

SUPPLEMENTARY DATA

Supplementary Data are available at NAR Online.

ACKNOWLEDGEMENTS

We thank Benedikt Beel for plasmids, Tilman Kottke for support of the *in vivo* measurements, Yann Geisselbrecht for initial crystallization experiments and Laura Sinatra, Filipp Bezold and Ralf Pöschke for technical assistance. We thank the beamline staff of Berlin Electron Storage Ring Society for Synchrotron Radiation (BESSY-II, Berlin, Germany), European Synchrotron Radiation Facility (ESRF, Grenoble, France) and the National Synchrotron Radiation Research Center (NSRRC, Hsinchu, Taiwan). We thank Silke von Horsten and Vitali Kalugin for data collection and the group of Alfred Batschauer for help with the *in vitro* assays.

FUNDING

International Max Planck research school for Environmental, Cellular and Molecular Biology [SF]; Deutsche Forschungsgemeinschaft [LOE: FOR 1261-2, ES 152/12-1, MM: Mi373/12-2]; Air Force Office of Scientific Research (AFOSR) [FA9550-14-1-0409]; Taiwanese Ministry for Science and Technology [MOST107-0210-01-19-02]. Funding for open access charge: DFG FOR1261.

Conflict of interest statement. None declared.

REFERENCES

1. Chaves,I., Pokorny,R., Byrdin,M., Hoang,N., Ritz,T., Brettel,K., Essen,L.-O., van der Horst,G.T.J., Batschauer,A. and Ahmad,M. (2011) The cryptochromes: blue light photoreceptors in plants and animals. *Annu. Rev. Plant Biol.*, **62**, 335–364.
2. Kottke,T., Oldemeyer,S., Wenzel,S., Zou,Y. and Mittag,M. (2017) Cryptochrome photoreceptors in green algae: unexpected versatility of mechanisms and functions. *J. Plant Physiol.*, **217**, 4–14.
3. Fortunato,A.E., Annunziata,R., Jaubert,M., Bouly,J. and Falciatore,A. (2015) Dealing with light: the widespread and multitasking cryptochrome/photolyase family in photosynthetic organisms. *J. Plant Physiol.*, **172**, 42–54.
4. Merchant,S.S., Prochnik,S.E., Vallon,O., Harris,E.H., Karpowicz,S.J., Witman,G.B., Terry,A., Salamov,A., Fritz-Laylin,L.K., Maréchal-Drouard,L. *et al.* (2007) The *Chlamydomonas* genome reveals the evolution of key animal and plant functions. *Science*, **318**, 245–250.
5. Beel,B., Prager,K., Spexard,M., Sasso,S., Weiss,D., Müller,N., Heinnickel,M., Dewez,D., Ikoma,D., Grossman,A.R. *et al.* (2012) A flavin binding cryptochrome photoreceptor responds to both blue and red light in *Chlamydomonas reinhardtii*. *Plant Cell*, **24**, 2992–3008.
6. Mittag,M., Kiaulehn,S. and Johnson,C.H. (2005) The circadian clock in *Chlamydomonas reinhardtii*. What is it for? What is it similar to? *Plant Physiol.*, **137**, 399–409.
7. Coesel,S., Mangogna,M., Ishikawa,T., Heijde,M., Rogato,A., Finazzi,G., Todo,T., Bowler,C. and Falciatore,A. (2009) Diatom PtCPF1 is a new cryptochrome/photolyase family member with DNA repair and transcription regulation activity. *EMBO Rep.*, **10**, 655–661.
8. Spexard,M., Thöing,C., Beel,B., Mittag,M. and Kottke,T. (2014) Response of the sensory animal-like cryptochrome aCRY to blue and red light as revealed by infrared difference spectroscopy. *Biochemistry*, **53**, 1041–1050.
9. Liu,B., Zuo,Z., Liu,H., Liu,X. and Lin,C. (2011) *Arabidopsis* cryptochrome 1 interacts with SPA1 to suppress COP1 activity in response to blue light. *Genes Dev.*, **25**, 1029–1034.
10. Sang,Y., Li,Q.-H., Rubio,V., Zhang,Y.-C., Mao,J., Deng,X. and Yang,H.-Q. (2005) N-Terminal domain-mediated homodimerization is required for photoreceptor activity of *Arabidopsis* CRYPTOCHROME 1. *Plant Cell*, **17**, 1569–1584.
11. Oldemeyer,S., Franz,S., Wenzel,S., Essen,L.-O., Mittag,M. and Kottke,T. (2016) Essential role of an unusually long-lived tyrosyl radical in the response to red light of the animal-like cryptochrome aCRY. *J. Biol. Chem.*, **291**, 14062–14071.
12. Ozturk,N. (2017) Phylogenetic and functional classification of the photolyase/cryptochrome family. *Photochem. Photobiol.*, **93**, 104–111.
13. Nohr,D., Franz,S., Rodriguez,R., Paulus,B., Essen,L.-O., Weber,S. and Schleicher,E. (2016) Extended electron-transfer in animal cryptochromes mediated by a tetrad of aromatic amino acids. *Biophys. J.*, **111**, 301–311.
14. Yamamoto,J., Shimizu,K., Kanda,T., Hosokawa,Y., Iwai,S., Plaza,P. and Müller,P. (2017) Loss of fourth electron-transferring tryptophan in animal (6-4) photolyase impairs DNA repair activity in bacterial cells. *Biochemistry*, **56**, 5356–5364.
15. Mees,A., Klar,T., Gnau,P., Hennecke,U., Eker,A.P.M., Carell,T. and Essen,L.-O. (2004) Crystal structure of a photolyase bound to a CPD-like DNA lesion after in situ repair. *Science*, **306**, 1789–1793.
16. Rosensweig,C., Reynolds,K.A., Gao,P., Laothamatas,I., Shan,Y., Ranganathan,R., Takahashi,J.S. and Green,C.B. (2018) An evolutionary hotspot defines functional differences between CRYPTOCHROMES. *Nat. Commun.*, **9**, 1–15.
17. Klar,T., Pokorny,R., Moldt,J., Batschauer,A. and Essen,L.-O. (2007) Cryptochrome 3 from Arabidopsis thaliana: structural and functional analysis of its complex with a folate light antenna. *J. Mol. Biol.*, **366**, 954–964.
18. Park,H.W., Kim,S.T., Sancar,A. and Deisenhofer,J. (1995) Crystal structure of DNA photolyase from *Escherichia coli*. *Science*, **268**, 1866–1872.
19. Kiontke,S., Gnau,P., Haselsberger,R., Batschauer,A. and Essen,L.-O.O. (2014) Structural and evolutionary aspects of antenna chromophore usage by class II photolyases. *J. Biol. Chem.*, **289**, 19659–19669.
20. Klar,T., Kaiser,G., Hennecke,U., Carell,T., Batschauer,A. and Essen,L.-O. (2006) Natural and non-natural antenna chromophores in the DNA photolyase from *Thermus thermophilus*. *ChemBioChem*, **7**, 1798–1806.
21. Zhang,F., Scheerer,P., Oberpichler,I., Lamparter,T., Krauss,N., Krauß,N. and Krauss,N. (2013) Crystal structure of a prokaryotic (6-4) photolyase with an Fe-S cluster and a 6,7-dimethyl-8-ribityllumazine antenna chromophore. *Proc. Natl. Acad. Sci. U.S.A.*, **110**, 7217–7222.
22. Fujihashi,M., Numoto,N., Kobayashi,Y., Mizushima,A., Tsujimura,M., Nakamura,A., Kawarabayasi,Y. and Miki,K. (2007) Crystal structure of archaeal photolyase from *Sulfolobus tokodaii* with two FAD molecules: implication of a novel light-harvesting cofactor. *J. Mol. Biol.*, **365**, 903–910.
23. Essen,L.-O., Franz,S. and Banerjee,A. (2017) Structural and evolutionary aspects of algal blue light receptors of the cryptochrome and aureochrome type. *J. Plant Physiol.*, **217**, 27–37.
24. Crooks,G., Hon,G., Chandonia,J. and Brenner,S. (2004) WebLogo: a sequence logo generator. *Genome Res.*, **14**, 1188–1190.
25. Kiontke,S., Gnau,P., Haselsberger,R., Batschauer,A. and Essen,L.-O. (2014) Structural and evolutionary aspects of antenna chromophore usage by class II photolyases. *J. Biol. Chem.*, **289**, 19659–19669.
26. Kabsch,W. (1993) Automatic processing of rotation diffraction data from crystals of initially unknown symmetry land cell constants. *J. Appl. Crystallogr.*, **26**, 795–800.
27. Yamashita,K., Hirata,K. and Yamamoto,M. (2018) KAMO: towards automated data processing for microcrystals. *Acta Crystallogr. Sect. D Struct. Biol.*, **74**, 1–9.
28. Karplus,P.A. and Diederichs,K. (2012) Linking crystallographic model and data quality. *Science*, **336**, 1030–1033.
29. McCoy,A.J., Grosse-Kunstleve,R.W., Adams,P.D., Winn,M.D., Storoni,L.C. and Read,R.J. (2007) Phaser crystallographic software. *J. Appl. Crystallogr.*, **40**, 658–674.
30. Project,C.C. (1994) The CCP4 suite: Programs for protein crystallography. *Acta Crystallogr. Sect. D Biol. Crystallogr.*, **50**, 760–763.
31. Murshudov,G.N., Vagin,A.A. and Dodson,E.J. (1997) Refinement of macromolecular structures by the maximum-likelihood method. *Acta Crystallogr. Sect. D Biol. Crystallogr.*, **53**, 240–255.
32. Emsley,P., Lohkamp,B., Scott,W.G. and Cowtan,K. (2010) Features and development of Coot. *Acta Crystallogr. Sect. D Biol. Crystallogr.*, **66**, 486–501.
33. Brych,A., Mascarenhas,J., Jaeger,E., Charkiewicz,E., Pokorny,R., Bölker,M., Doehlemann,G. and Batschauer,A. (2016) White collar 1-induced photolyase expression contributes to UV-tolerance of *Ustilago maydis*. *Microbiologyopen*, **5**, 224–243.
34. Zoltowski,B.D., Vaidya,A.T., Top,D., Widom,J., Young,M.W. and Crane,B.R. (2011) Structure of full-length *Drosophila* cryptochrome. *Nature*, **480**, 396–399.
35. Brautigam,C.A., Smith,B.S., Ma,Z., Palnitkar,M., Tomchick,D.R., Machius,M. and Deisenhofer,J. (2004) Structure of the photolyase-like domain of cryptochrome 1 from *Arabidopsis thaliana*. *Proc. Natl. Acad. Sci. U.S.A.*, **101**, 12142–12147.
36. Maul,M.J., Barends,T.R.M., Glas,A.F., Cryle,M.J., Domratcheva,T., Schneider,S., Schlichting,I. and Carell,T. (2008) Crystal structure and mechanism of a DNA (6-4) photolyase. *Angew. Chem. Int. Ed.*, **47**, 10076–10080.
37. Kiontke,S., Geisselbrecht,Y., Pokorny,R., Carell,T., Batschauer,A. and Essen,L.-O. (2011) Crystal structures of an archaeal class II DNA photolyase and its complex with UV-damaged duplex DNA. *EMBO J.*, **30**, 4437–4449.
38. Bordwell,F.G., Bartmess,J.E. and Hautala,J.A. (1978) Alkyl effects on equilibrium acidities of carbon acids in protic and dipolar aprotic media and the gas phase. *J. Org. Chem.*, **43**, 3095–3101.
39. Li,Y.F., Heelis,P.F. and Sancar,A. (1991) Active site of DNA photolyase: Tryptophan-306 is the intrinsic hydrogen atom donor essential for flavin radical photoreduction and DNA repair in vitro. *Biochemistry*, **30**, 6322–6329.
40. Kleine,T., Lockhart,P. and Batschauer,A. (2003) An *Arabidopsis* protein closely related to *Synechocystis* cryptochrome is targeted to organelles. *Plant J.*, **35**, 93–103.

41. Yamamoto,J., Martin,R., Iwai,S., Plaza,P. and Brettel,K. (2013) Repair of the (6-4) photoproduct by DNA photolyase requires two photons. *Angew. Chem. Int. Ed.*, **52**, 7432–7436.
42. Terai,Y., Sato,R., Yumiba,T., Harada,R., Shimizu,K., Toga,T., Ishikawa-Fujiwara,T., Todo,T., Iwai,S., Shigeta,Y. *et al.* (2018) Coulomb and CH – π interactions in (6 – 4) photolyase – DNA complex dominate DNA binding and repair abilities. *Nucleic Acids Res.*, doi:10.1093/nar/gky364.
43. Yamamoto,J., Plaza,P. and Brettel,K. (2016) Repair of (6-4) lesions in DNA by (6-4) photolyase: 20 years of quest for the photoreaction mechanism. *Photochem. Photobiol.*, **38**, 51–66.
44. Petersen,J.L. and Small,G.D. (2001) A gene required for the novel activation of a class II DNA photolyase in *Chlamydomonas*. *Nucleic Acids Res.*, **29**, 4472–4481.
45. Petersen,J.L. and Ronan,P.J. (2010) Critical role of 7,8-Didemethyl-8-hydroxy-5-deazariboflavin for photoreactivation in *Chlamydomonas reinhardtii*. *J. Biol. Chem.*, **285**, 32467–32475.
46. Glas,A.F., Maul,M.J., Cryle,M., Barends,T.R.M., Schneider,S., Kaya,E., Schlichting,I. and Carell,T. (2009) The archaeal cofactor F 0 is a light-harvesting antenna chromophore in eukaryotes. *Proc. Natl. Acad. Sci. U.S.A.*, **106**, 11540–11545.
47. Malhotra,K., Kim,S.T., Walsh,C. and Sancar,A. (1992) Roles of FAD and 8-hydroxy-5-deazaflavin chromophores in photoreactivation by Anacystis nidulans DNA photolyase. *J. Biol. Chem.*, **267**, 15406–15411.
48. Kort,R., Komori,H., Adachi,S.I., Miki,K. and Eker,A. (2004) DNA apophotolyase from *Anacystis nidulans*: 1.8 A structure, 8-HDF reconstitution and X-ray-induced FAD reduction. *Acta Crystallogr. D. Biol. Crystallogr.*, **60**, 1205–1213.
49. Eker,A.P.M., Kooiman,P., Hessels,J.K.C. and Yasui,A. (1990) DNA photoreactivating enzyme from the cyanobacterium *Anacystis nidulans*. *J. Biol. Chem.*, **265**, 8009–8015.
50. Oztürk,N., Song,S.-H., Selby,C.P. and Sancar,A. (2008) Animal type 1 cryptochromes. Analysis of the redox state of the flavin cofactor by site-directed mutagenesis. *J. Biol. Chem.*, **283**, 3256–3263.
51. García-Esquivel,M., Esquivel-Naranjo,E.U., Hernández-Oñate,M.A., Ibarra-Laclette,E. and Herrera-Estrella,A. (2016) The *Trichoderma atroviride* cryptochrome/photolyase genes regulate the expression of blr1 -independent genes both in red and blue light. *Fungal Biol.*, **120**, 500–512.
52. Heijde,M., Zabulon,G., Corellou,F., Ishikawa,T., Brazard,J., Usman,A., Sánchez,F., Plaza,P., Martin,M., Falciatore,A. *et al.* (2010) Characterization of two members of the cryptochrome/photolyase family from *Ostreococcus tauri* provides insights into the origin and evolution of cryptochromes. *Plant, Cell Environ.*, **33**, 1614–1626.
53. Müller,N., Wenzel,S., Zou,Y., Künzel,S., Sasso,S., Weiß,D., Prager,K., Grossman,A., Kottke,T. and Mittag,M. (2017) A plant cryptochrome controls key features of the *Chlamydomonas* circadian clock and its life cycle. *Plant Physiol.*, **174**, 185–201.
54. Huang,K. and Beck,C.F. (2003) Phototropin is the blue-light receptor that controls multiple steps in the sexual life cycle of the green alga *Chlamydomonas reinhardtii*. *Proc. Natl. Acad. Sci. U.S.A.*, **100**, 6269–6274.
55. Zou,Y., Wenzel,S., Müller,N., Prager,K., Jung,E.-M., Kothe,E., Kottke,T. and Mittag,M. (2017) An Animal-Like cryptochrome controls the *Chlamydomonas* sexual cycle. *Plant Physiol.*, **174**, 1334–1347.
56. Müller,P., Yamamoto,J., Martin,R., Iwai,S. and Brettel,K. (2015) Discovery and functional analysis of a 4th electron-transferring tryptophan conserved exclusively in animal cryptochromes and (6-4) photolyases. *Chem. Commun.*, **51**, 15502–15505.
57. Xing,W., Busino,L., Hinds,T.R., Marionni,S.T., Saifee,N.H., Bush,M.F., Pagano,M. and Zheng,N. (2013) SCF(FBXL3) ubiquitin ligase targets cryptochromes at their cofactor pocket. *Nature*, **496**, 64–68.
58. Levy,C., Zoltowski,B.D., Jones,A.R., Vaidya,A.T., Top,D., Widom,J., Young,M.W., Scrutton,N.S., Crane,B.R. and Leys,D. (2013) Updated structure of *Drosophila* cryptochrome. *Nature*, **495**, E3–E4.
59. Engelen,E., Janssens,R.C., Yagita,K., Smits,V.A.J., van der Horst,G.T.J. and Tamanini,F. (2013) Mammalian TIMELESS is involved in period determination and DNA damage-dependent phase advancing of the circadian clock. *PLoS One*, **8**, e56623.
60. Busza,A., Emery-Le,M., Rosbash,M. and Emery,P. (2004) Roles of the two Drosophila CRYPTOCHROME structural domains in circadian photoreception. *Science*, **304**, 1503–1506.
61. Schmalen,I., Reischl,S., Wallach,T., Klemz,R., Grudziecki,A., Prabu,J.R., Benda,C., Kramer,A. and Wolf,E. (2014) Interaction of circadian clock proteins CRY1 and PER2 is modulated by zinc binding and disulfide bond formation. *Cell*, **157**, 1203–1215.
62. Xu,H., Gustafson,C.L., Sammons,P.J., Khan,S.K., Parsley,N.C., Ramanathan,C., Lee,H.W., Liu,A.C. and Partch,C.L. (2015) Cryptochrome 1 regulates the circadian clock through dynamic interactions with the BMAL1 C terminus. *Nat. Struct. Mol. Biol.*, **22**, 476–484.
63. Harper,S.M., Christie,J.M. and Gardner,K.H. (2004) Disruption of the LOV-Jalpha helix interaction activates phototropin kinase activity. *Biochemistry*, **43**, 16184–16192.
64. Schleicher,E., Hitomi,K., Kay,C.W.M., Getzoff,E.D., Todo,T. and Weber,S. (2007) Electron nuclear double resonance differentiates complementary roles for active site histidines in (6-4) photolyase. *J. Biol. Chem.*, **282**, 4738–4747.
65. Hitomi,K., Nakamura,H., Kim,S.T., Mizukoshi,T., Ishikawa,T., Iwai,S. and Todo,T. (2001) Role of two histidines in the (6-4) photolyase reaction. *J. Biol. Chem.*, **276**, 10103–10109.
66. Sadeghian,K., Bocola,M., Merz,T. and Schuütz,M. (2010) Theoretical study on the repair mechanism of the (6–4) photolesion by the (6–4) photolyase. *J. Am. Chem. Soc.*, **132**, 16285–16295.
67. Glas,A.F., Kaya,E., Schneider,S., Heil,K., Fazio,D., Maul,M.J. and Carell,T. (2010) DNA (6-4) photolyases reduce dewar isomers for isomerization into (6-4) lesions. *J. Am. Chem. Soc.*, **132**, 3254–3255.
68. Li,J., Liu,Z., Tan,C., Guo,X., Wang,L., Sancar,A. and Zhong,D. (2010) Dynamics and mechanism of repair of ultraviolet-induced (6-4) photoproduct by photolyase. *Nature*, **466**, 887–890.
69. Yamamoto,J., Hitomi,K., Hayashi,R., Getzoff,E.D. and Iwai,S. (2009) Role of the carbonyl group of the (6-4) photoproduct in the (6-4) photolyase reaction. *Biochemistry*, **48**, 9306–9312.
70. Yamamoto,J., Tanaka,Y. and Iwai,S. (2009) Spectroscopic analysis of the pyrimidine(6-4)pyrimidone photoproduct: insights into the (6-4) photolyase reaction. *Org. Biomol. Chem.*, **7**, 161–166.
71. Dokainish,H.M. and Kitao,A. (2016) Computational assignment of the histidine protonation state in (6-4) photolyase enzyme and its effect on the protonation step. *ACS Catal.*, **6**, 5500–5507.

Supporting Information

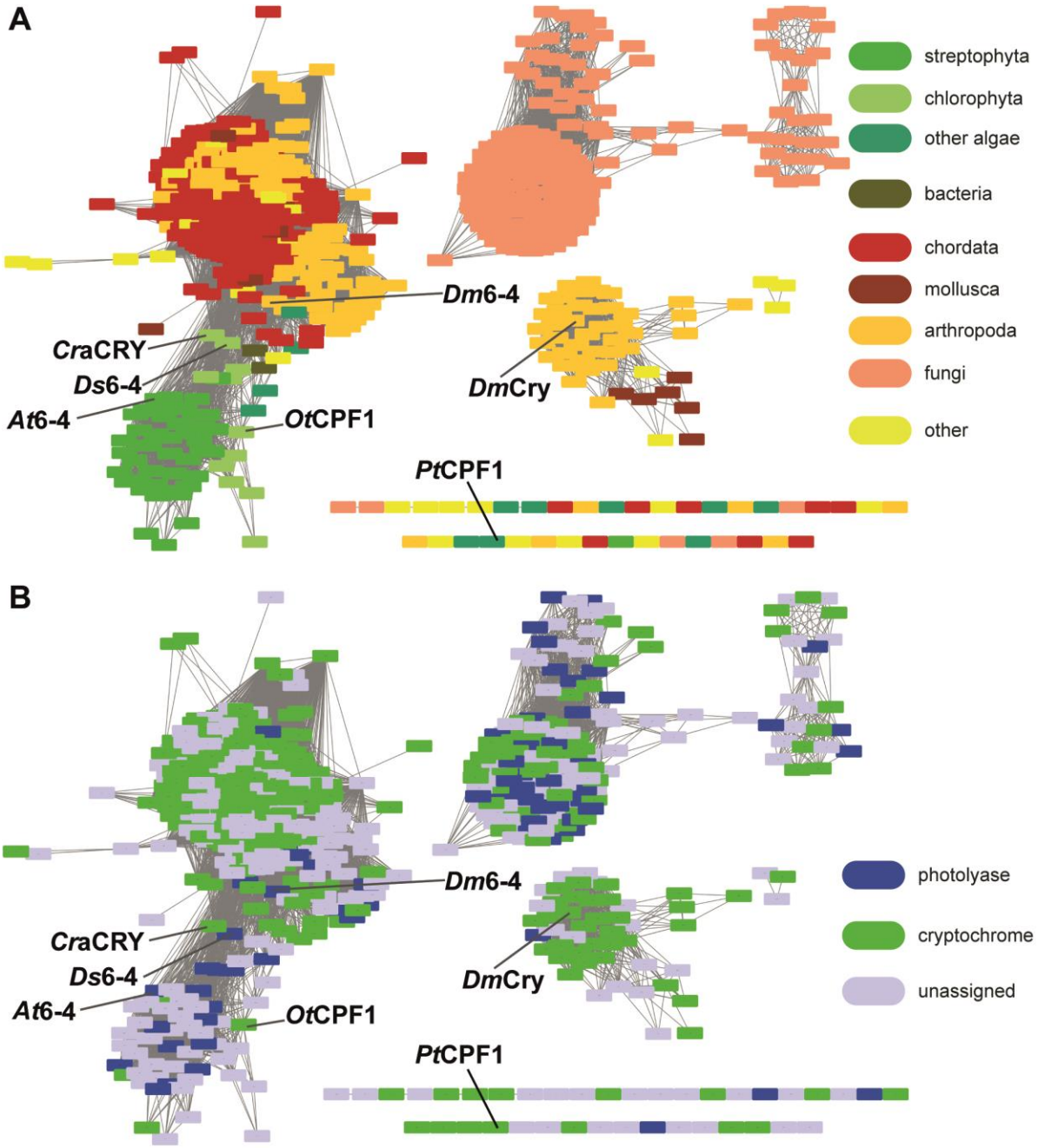

C

	CraCRY	Ds6-4	Dm6-4	At6-4	OtCPF1	PtCPF1	DmCry
CraCRY	100 %						
Ds6-4	51.2 %	100 %					
Dm6-4	51.4 %	98.9 %	100 %				
At6-4	48.8 %	44.5 %	44.4 %	100 %			
OtCPF1	45.2 %	42.7 %	42.4 %	43.5 %	100 %		
PtCPF1	40.6 %	39.1 %	38.6 %	39.1 %	42.5 %	100 %	
DmCry	34.2 %	35.6 %	35.2 %	32.3 %	35.0 %	28.8 %	100 %

Figure S1. Sequence similarity network of based on a multiple sequence alignment of animal-like cryptochromes/(6-4)photolyases after decreasing the E-value cutoff to 10^{-150}. The independent nodes represent sequences with more than 90 % sequence identity. They are colored based on their host organism (A) or their assigned functionality (B). (C) Sequence identities of several cryptochromes in percent. The values were calculated by using the sequence of the photolyase-homology region (PHR) of each cryptochrome (*Cr*aCRY 1-490, *Ds*64 1-534, *Ot*CPF1 1-541, *Pt*CPF1 1-519, *Dm*Cry 1-516) for pairwise sequence alignment via the EMBOSS online tool using the EBLOSUM62 matrix.

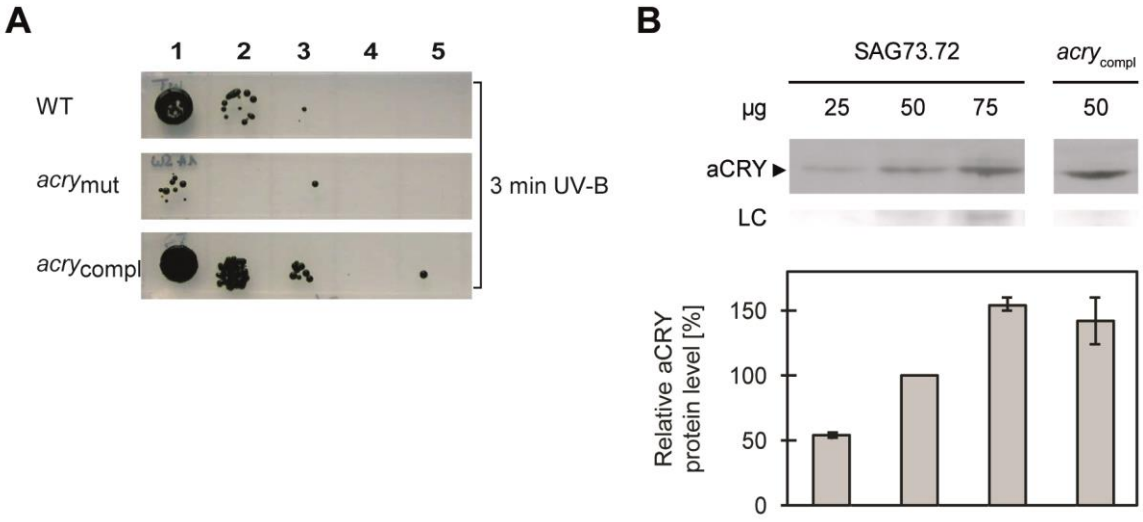

Figure S2. (A) Wild type SAG73.72 (WT), $acry_{mut}$ and a complemented strain $acry_{compl}$ that has a protein level of approximately 140% compared to WT (100%) were treated as described in Figure 2B with UV-B light illumination for 3 min. (B) To check for complementation, different amounts of soluble proteins from crude extracts (25, 50 and 75 µg per lanes) of WT and 50 µg proteins from a crude extract of the complemented *acry* mutant ($acry_{compl}$) were separated on 10% SDS-PAGE along with molecular mass standards and used for immunoblots with anti-aCRY antibodies. The position of aCRY is indicated by the arrowhead. Cells were grown under a LD12:12 cycle and harvested at early day (LD4)4. As loading control (LC) the PVDF membrane was stained with Coomassie Brilliant Blue R 250 after immunochemical detection. From this stain, selected, unspecified protein bands are shown (middle). The quantified aCRY protein levels of three biological replicates are shown in the diagrams (bottom) with standard deviations.

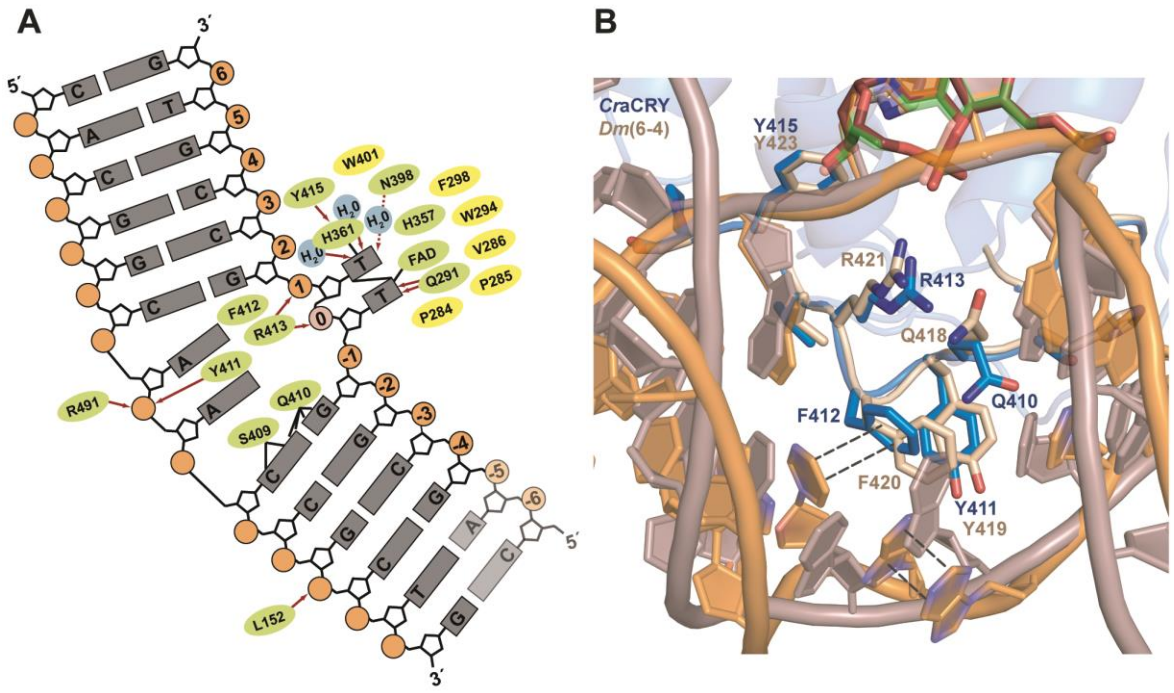

Figure S3. (A) Schematic diagram of the residues of *Cra*CRY interacting with the (6-4)PP comprising DNA (6FN0). Apolar residues of the protein backbone are marked in yellow. Green residues with solid arrows represent direct interactions between protein side chains and DNA. (B) Detailed view of the bubble-intruding region of *Cra*CRY in comparison to *Dm*64. The DNA strain (orange) interacts with *Cra*CRY not only over direct interactions, but also over formation of π-π-stacking (indicated with dotted lines) between F412 and the pyrimidine base.

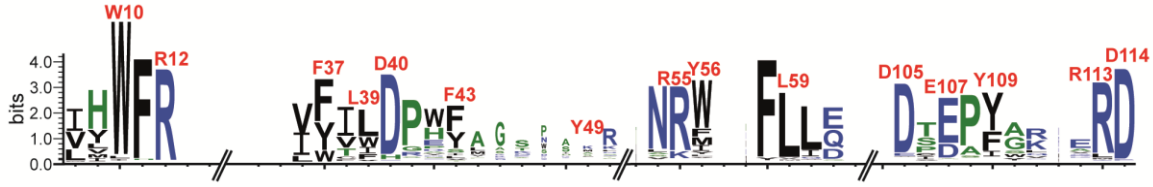

Figure S4. WebLogo based on a multiple sequence alignment of animal-like cryptochromes/(6-4) photolyases. Residues involved in antenna chromophore binding are highlighted. The height at each position corresponds to the residue abundance in aCRY/(6-4)PHL orthologs. Letter coloring follows the default WebLogo 3 hydrophobicity-dependent scheme, with hydrophilic amino-acids in blue, neutral in green, and hydrophobic in black.

4.5 Structural changes in *Cr*aCRY upon blue-light illumination

This research is submitted to Nature Scientific Reports by *Sophie Franz-Badur, Alexander Penner, Simon Straß, Silke von Horsten, Uwe Linne and Lars-Oliver Essen*.* **Structural changes within the bifunctional *Cr*aCRY upon blue-light excitation.** (submitted 2018).

Summary

This publication deals with the question of how *Cr*aCRY can achieve its bifunctionality and wether structural changes are involved. Therefore we studied the protein structure after BL illumination and photoreduction. We chose to use hydrogen-deuterium exchange coupled with mass spectrometry to observe changes in deuterium uptake after specific time points. We were able to get HDX data for the *Cr*aCRY-WT and also the truncated variant ΔCTE with both proteins in their dark state with bound FAD_{OX}. To get data of the fully reduced $FADH^-$ state, a light chamber was designed for the HDX machine, which illuminated the sample with blue light for 5 s in an interval of 20 s. With this device, we were able to gain data for both samples with the hydroquinone state of the cofactor. By comparing the WT with the ΔCTE variant for both, oxidized and reduced samples, four regions with significant differences can be found. In these four regions, the peptide fragments of the WT show a higher deuterium uptake, which correlates with a higher flexibility of these particular regions. We propose that in presence of the CTE, these regions might be unfolded or undergo a conformational change.

Comparison of the oxidized and reduced states of the WT and ΔCTE revealed changes in deuterium uptake in two regions. These could be assigned to a loop between helix α13 and helix α14 (300 – 326) and a short part of helix α18 (399-403) pointing towards this loop. Part of the residues present on this loop are involved in a VAN-DER-WAALS network with the terminal electron donor Y373 (142, 293). We conclude that radical formation at Y373 is triggering a change in this network and therefore a structural change in this region.

Contributions

S. Franz-Badur designed and planned experiments with help of L.-O. Essen and prepared the samples for the HDX experiment. A. Penner analysed the HDX data. S. Straß performed initial experiments and optimized conditions. S. Franz-Badur, S. Straß and S. von Horsten designed the light chamber, which was built by the electronic department of the chemistry department of the Philipps-University of Marburg. W. Steinchen and U. Linne performed the HDX experiment and supervised HDX analysis. S. Franz-Badur and L.-O. Essen wrote the paper. All authors reviewed the results and approved the final version of the manuscript.

Article

Structural changes within the bifunctional cryptochrome/photolyase *Cra*CRY upon blue light excitation

Sophie Franz-Badur[1], Alexander Penner[1], Simon Straß[1,2], Silke von Horsten[1], Uwe Linne[1,3] and Lars-Oliver Essen[1,3]*

[1] Unit for Structural Biochemistry, Department of Chemistry, Philipps University Marburg, Hans-Meerwein Straße 4, 35032 Marburg, Germany

[2] Synovo GmbH, Paul-Ehrlich-Straße 15, 72076 Tübingen, Germany

[3] LOEWE Center of Synthetic Microbiology, Philipps University Marburg, Hans-Meerwein Straße 4, 35032 Marburg, Germany

*Tel: +49 6421/28-22032; Fax: +49 6421/28-22012; Email: essen@chemie.uni-marburg.de

Abstract

Cryptochromes (CRYs) are an ubiquitously occurring class of photoreceptors, which are important for regulating the circadian rhythm of animals *via* a time-delayed transcription-translation feedback loop (TTFL). Due to their protein architecture and common FAD chromophore, they belong to the same superfamily as photolyases (PHLs), an enzyme class that repairs UV-induced DNA lesions upon blue light absorption. Apart from their different functions the only prominent structural difference between CRY and PHL is the highly variable C-terminal extension (CTE) of the former. The nature of the CTE is still unclear and highly speculated. In this study, we show by hydrogen/deuterium exchange and subsequent mass-spectrometric analysis that the CTE of the animal-like cryptochrome from the green algae *Chlamydomonas reinhardtii* (*Cra*CRY) binds to the surface of the photolyase homology region, which flanks the DNA binding site. We also compared the fully oxidized and fully reduced states of the flavoprotein and designed a tool, so called light chamber, for automated HDX-MS measurements of photoreceptors in defined photostates. We could observe some striking differences between the two photostates and propose a model for light-dependent switching of this bifunctional cryptochrome.

Introduction

Trapping dynamic structural changes of a protein between its active/catalytic and inactive/resting state is a difficult task for scientists looking for structure-function relationships. In the last years, several time-resolved methods have been developed, which provided insight into time-dependent structural changes of various photoreceptors, e.g. bacteriorhodopsin (Nango *et al.*[1], TR-SFX) and bacteriophytochrome (Takala *et al.*[2], TR-SAXS). These methods are highly promising, but still expensive and not easily accessible to most users as they rely on advanced synchrotrons and X-ray free electron lasers. Accordingly, to compare different states of a protein, hydrogen/deuterium exchange mass spectrometry (HDX-MS) has attracted attention[3-6], because HDX-MS is a relatively fast method and allows a distinct characterization of structured and unstructured areas of a protein sample in solution. For this the relative deuterium uptakes of peptide fragments are compared, as the exchange rates of structured and unstructured regions significantly differ. Furthermore, this method can also identify the binding site of a substrate or a reaction partner in solution.

In this study we focused on light-induced and redox-state dependent structural changes of the animal-like cryptochrome from the green alga *Chlamydomonas reinhardtii* (*Cr*aCRY)[7,8]. Cryptochromes are flavin-comprising photoreceptors, which utilize for monitoring of available daylight the flavin adenine dinucleotide (FAD) chromophore that is bound to the C-terminal domain of the photolyase-homology region (PHR)[9]. These photoreceptors are found in all three kingdoms of life including animals. Till now, four different types have been assigned[10,11], for example two major and highly related groups are found in insects (type 1)[12] and mammals (type 2)[13,14] The animal cryptochromes (CRY) differ in term of their *in vivo* functionality, because type 1 CRY act as blue-light photoreceptors for resetting the circadian clock. In contrast, type 2 CRY lack any known photosensory function[15], although they are still crucial components of the core of the circadian clock. Two other less related types of cryptochromes include the plant cryptochromes as well as the DASH-type cryptochromes. In terms of their structural features, cryptochromes are highly related to (6-

4) photolyases for type I and II CRY and to class I CPD photolyases for plant and DASH CRY. A common feature that makes them distinct from photolyases is given by their elongated C-terminal extensions (CTEs), which adopt variable lengths. For example, the length of a cryptochrome's CTE varies from 23 amino acids (aa) in the type I cryptochrome of *Drosophila melanogaster* (*Dm*CRY)[16] to 191 aa in CRY1 from the plant *Arabidopsis thaliana*[13] and more. The role of the CTE in affecting the photoreceptor function of CRY is still elusive, as there is only just one example of a successfully analyzed structure of a cryptochrome with CTE, namely *Dm*CRY[16](64)(64)(64). In that case, the CTE is short, 23 aa, and wound up to an α-helix that binds close to the entrance of the FAD binding site. Busza *et al.* showed, that a CTE-truncated *Dm*CRY mutant can still act as a fully functional circadian photoreceptor and is capable to bind TIM, another circadian clock component present in animal cells, as strongly as the wild-type *Dm*CRY[17]. However, the CTE-deficient mutant binds to TIM already in the dark, whereas the wild-type (WT) cryptochrome requires light to enable it for recruiting TIM[18,19]. This lead to the conclusion, that the CTE undergoes a light-dependent conformational change to unblock the TIM binding site in *Dm*CRY. In correlation with the light-dependent binding of Jetlag (JET) to *Dm*CRY[20], Ozturk *et al.* proposed a mechanism combining DmCRY, TIM and JET dependent degradation[21]. For the light-induced change in *Dm*CRY, both Ozturk *et al.*[20] and Ganguly *et al.*[22] proposed a change of the protonation state around the FAD binding pocket, which results in a change of the hydrogen-bonding pattern triggering a movement of the CTE.

The *Dm*CRY ortholog from *C. reinhardtii*, *Cr*aCRY, was shown to regulate the transcription of various genes by different light qualities[7] and plays a significant role in the sexual life cycle of *C. reinhardtii* together with a plant-like CRY and a phototropin orthologs[23-25]. Interestingly, given the close ontogenetic relationship between type 1 CRY and (6-4) photolyases, *Cr*aCRY demonstrates not only a regulatory function but is also capable to repair (6-4)-pyrimidone-pyrimidine lesion comprising DNA[8]. The CTE of *Cr*aCRY is considerably longer than that of *Dm*CRY by comprising 99 aa, which are 17 % of the overall enzyme. The structure of the PHR domain has been recently solved by X-ray crystallographic analysis[8], but the WT protein generated no crystals so far. Accordingly, no structural

information on the long CTE of *Cr*aCRY is available and the role of the C-terminus is hence uncertain. Oldemeyer *et al*. proposed that the WT of *Cr*aCRY forms a heterodimer involving the CTE[26] in the dark state, which we should be able to observe using HDX-MS data.

Results and Discussion

The purified *Cr*aCRY samples were examined by analytical size exclusion chromatography (SEC) under different illumination conditions. We were expecting most of the WT sample to be in the dimeric state according to Oldemeyer *et al.*[26], but our SEC measurements differ significantly, as most of the protein in *Cr*aCRY samples remain in the monomeric state (figure 1a,b). Samples were analyzed before SEC *via* UV/Vis spectroscopy to check the redox state of the FAD (SI-S1). Over 90 % of the fully oxidized as well as the fully reduced state in both variants eluted as monomeric species (SI-S2). SEC data of samples in the semiquinone state are showing the formation of species with a somewhat bigger size, which could be due to dimerization, structural change or unfolding of the protein. As these species show no absorption at 450 nm, it might be a misfolded form of *Cr*aCRY lacking bound FAD. The discrepancy between our SEC data and the data published before indicating higher oligomeric species could be due to differences of the *Cr*aCRY purification scheme. In our improved purification protocol for crystallization and HDX analysis, we used DNase I as well as a heparin affinity column to remove any remaining (oligo)nucleotides that may stuck to the protein as *Cr*aCRY was shown before to bind DNA and repair (6-4)DNA damages[8].

To compare structural changes of *Cr*aCRY in its oxidized (FAD_{OX}/dark) and fully reduced ($FADH^{-}$/light) state by HDX-MS analysis, a suitable buffer condition for HDX and a reducing agent to keep the fully reduced state stable over several hours had to be determined. A Tris-buffer (pH 7.8) with a low salt concentration and without any glycerol was chosen for HDX-MS analysis and various concentrations of different reducing agents were tested (Fig. 1c). For 12.5 mM DTT a significant peak at 376 nm and a local minimum of absorption at 344 nm could be detected. The five characteristic absorption peaks[11] for FAD_{OX} are clearly diminished. As the fully reduced state rapidly reoxidizes in the dark and under aerobic conditions, we developed a light chamber, which fits the specific requirements of the

experimental set-up (SI-S3). In difference-absorption spectra, a clear contrast between a sample which was kept after photoreduction in the dark and a sample that was kept in the light chamber can be seen (Fig. 1d). After 18 h in the light chamber, the protein still shows the typical absorption of the fully reduced $FADH^-$. The HDX-MS measurements for *Cr*aCRY and the deletion variant *Cr*aCRYΔCTE that lacks the C-terminal extension (497-595) and hence comprises only the photolyase-homology region (PHR, 1-496) were performed using the determined conditions.After running the ProteinLynxGlobalServer software (*Waters*) and importing search results into DynamX (*Waters*), 132 peptides could be identified for *Cr*aCRY yielding 75 % coverage at an overall redundancy of 3.43. For the CTE, only four peptides could be found in the *Cr*aCRY dataset with almost no overlaps. Therefore, for further analysis we focused on the PHR domain. Comparing the WT with the truncated ΔCTE, four regions with significant differences in deuterium uptake can be found in the light (Fig. 2) and dark samples (SI-S4). Mapped onto the structure (PDB: 5ZM0) of *Cr*aCRYΔCTE, two loop regions (184-192; 200-211), both located at the long connecting loop between the N-terminal ROSSMAN-like domain and all-α C-terminal domain (Fig. 2), are showing a higher uptake in the WT sample. By rotating the protein 180°, another region with significant difference is shown. Here, a bundle of five helices oriented towards the protein surface with α10 on the top display a much greater uptake in WT protein sample. Namely, peptides covering regions between 225 and 252 as well as between 274 and 293 exhibit the greatest variation. These four identified regions demonstrate the same behavior in light and dark samples. Accordingly, these features are independent of the redox state of *Cr*aCRY. The only difference is the missing C-terminus. So how can we interpret this data? A higher uptake indicates either a more flexible or easily accessible region in one sample or a hidden, maybe through dimerization or interaction, region in the other sample. We already know that ΔCTE is monomeric, so a dimerization site is unlikely. Both proteins are able to bind and repair DNA(142), but during purification DNA contaminants were removed and both samples were treated exactly the same. This leads to the conclusion, that in presence of the CTE, the identified regions underlie a structural change. Looking at a multiple sequence alignment of over 500 sequences (described in Franz *et al*[8]) of animal-like cryptochromes and (6-

4)photolyases, the helix bundle exposes several highly conserved residues. Two of them, K237 and Q291, are involved in formation of the DNA binding site (Fig. 3). We propose, that this binding site might be unfolded or somehow changes it's conformation in the presence of the CTE so it becomes more accessible to the deuterium in the HDX experiment.

Comparing the dark (oxidized) and light (reduced) states of WT and the ΔCTE variant, two regions with significant differences in the uptake can be identified. The differences can be assigned to a loop between helix α13 and helix α14 (300 – 326) and a short part of helix α18 (399-403) pointing towards this loop (Fig. 4a,b). Looking at the specific residues located in this region, one of the essential tryptophans of the highly conserved Trp triad, the distal W322, can be found on the loop (Fig. 4c). In PHLs and CRYs this Trp triad is responsible for the efficient reduction and stabilization of the semireduced ($FAD°^-$ or FADH°) or fully reduced ($FADH^-$) state of the flavin cofactor. *Cra*CRY and other animal CRYs (type 1) and also 6-4 photolyases show an elongation of this Trp triad by a fourth aromatic residue, either tyrosine or another tryptophan. After flavin excitation of *Cra*CRY, an electron is transferred from the proximal tryptophan W399 to FAD, then the electron hole gets filled by the medial tryptophan W376, after that the distal W322 and finally by Y373 as fourth aromate, which forms a relatively stable radical close to the protein surface[8,26,27]. Interestingly, Y373 is not covered by HDX-MS, but the residues D321 and D323, which form a network of charged residues together with R485 and R492 located on helix α22, are also located on the described loop region. As the relative fractional uptake from the reduced state minus the oxidized state is significantly higher at this region, this can be interpreted as a conformational change of the stretch involving these residues from the oxidized to the reduced state. We therefore propose that after the excitation of the flavin and formation of the Y373° radical, the van-der-Waals bond network between D321, D323, Y373, R485 and R492 changes and triggers an overall movement of the loop (300-326). From our analysis, we are not able to show if α22 is moving in some way, as it is only partly covered, but the possibility is not precluded. Also a part of α18, which is in close contact with the relevant loop, seems to be effected from the movement. By comparison of both relative uptake maps to each other, the changes of deuterium uptake in the truncated sample and in

consequence the movement of the specific region are greater. This can be explained by the CTE allowing movement of the α22 only to some extent (Fig. 5). It was shown before that *Cr*aCRY is enriched in the nucleus during the day and delocalized over the whole cell in the night[25]. The proposed mechanism might explain the bifunctional role of *Cr*aCRY, *e.g*. by acting as a photolyase during the day and binding a signaling partner X during the night phase. The yet unknown partner X could be the plant CRY of *C. reinhardtii*, as *Cr*aCRY and *Cr*pCRY have been supposed to form a complex in the dark which results in a loss of mating ability and thus the formation of inactivated gametes[25].

In conclusion, we were able to develop a specific tool to keep photoreceptors in their different photostates during HDX-MS analysis and used it to perform measurements of *Cr*aCRY with and without its CTE. We gained first insights of the structural changes the cryptochrome undergoes upon photoreduction and are a step closer to address the question of how this photoreceptor can perform both DNA repair and regulation of gene transcription.

Materials and Methods

Design of the Light Chamber The light chamber was designed and manufactured in cooperation with the precision mechanics workshop of the chemistry department at the *Philipps University of Marburg*. A detailed schematic representation can be found in the supporting information. The built-in LEDs 450 nm (5.2 cd, ELD-450-525), 625 (60-70 cd, 5RAA5111P) and 735 nm (7.5 cd, ELD-720-524) where purchased from *Roithner LaserTechnik GmbH.* The three sample holders can be programmed separately with two different illumination intervals. Either a long interval with 30 s of illumination and 270 s darkness or a short interval with 5 s of light and 20 s in the dark. The rechargeable battery has a capacity of 2600 mAh and can be charge over a micro-USB port.

Sample Preparation *Cr*aCRY-WT and *Cr*aCRYΔCTE constructs were expressed and purified following published procedures (Beel *et al.*, Franz *et al.*[7,8]) with a heparin column before size exclusion chromatography to remove any DNA contaminants. For HDX-MS, the protein was transferred via PD-10 into a low salt buffer (10 mM Tris, 100 mM sodium chloride, pH 7.8).

To produce the fully reduced $FADH^-$ state, 12.5 mM DTT was added and the samples were illuminated for 30 min with a high power blue light LED (9.7 mW cm-2 at a distance of 10 cm, Roithner Lasertechnik).

Analytical size exclusion chromatography After purification, ΔCTE and WT samples were analyzed with a Superdex 75 increase 10/300 GL which was calibrated at 4°C at 0.5 mL /min (y=-0.15642x+3.29765) prior to use. 200 µL sample (c = 2 mg/mL) was injected at the column and elution was performed in phosphate buffer (50 mM sodium phosphate, 100 mM sodium chloride, pH 7.8). The absorption was detected with a multiwavelength detector. Samples were treated before with blue light (BL) or in combination with red light (RL) or with 12.5 mM DTT.

Steady-state UV/Vis spectroscopy and photoreduction assay Absorption spectra of *Cr*aCRY variants were recorded using a V-660 spectrometer (JASCO). The protein solutions were measured in a low salt buffer (10 mM Tris, 100 mM sodium chloride, pH 7.8) with varying concentrations of dithiothreitol (DTT) and tris(2-carboxyethyl)phospine (TCEP). Spectra were recorded after different illumination times using a high power LED (λ_{max}=450 nm; 9.7 mW cm^{-2} at a distance of 10 cm, Roithner Lasertechnik) at 2 °C. To simulate a HDX-MS measurement samples were put in the light chamber, which was cooled at 4 °C.

Hydrogen-Deuterium-Exchange-Mass Spectrometry (HDX-MS) To promote the light state formation, 12.5 mM DTT was added to *Cr*aCRY samples and they were illuminated for 15 min at 450 nm wavelength and repeatedly illuminated for 5 s at 450 nm wavelength followed by 20 s without illumination prior HDX. The dark state of *Cr*aCRY was facilitated by covering all light-transmissive vessels with aluminum foil. HDX-MS was essentially carried out as described previously[28-30] aided by a robotic two-arm autosampler (LEAP Technologies). 7.5 µl (60 µM) CRY were diluted with 67.5 µl of D_2O-containing buffer (10 mM Tris, 100 mM sodium chloride, pD 7.8) and incubated for 10, 95, 1000 or 10000 s at 25 °C. H/D exchange was stopped by mixing 55 µl of the reaction with an equal volume of quench buffer (400 mM KH2PO4/H3PO4, 2 M guanidine-HCl, pH 2.2) kept at 1 °C and

immediately injected into an ACQUITY UPLC M-class system with HDX technology (*Waters*)[29]. *Cr*aCRY was digested with immobilized pepsin at 12 °C in water + 0.1 % (v/v) formic acid at a flow rate of 100 µl/min and the resulting peptides trapped on a C18 column at 0.5 °C. After 3 minutes, the C18 trap column was placed in line with an ACQUITY UPLC BEH C18 1.7 µm 1.0 x 100 mm column (Waters) and the peptides separated at 0.5 °C with a gradient of water + 0.1 % (v/v) formic acid (eluent A) and acetonitrile + 0.1 % (v/v) formic acid (eluent B) at 30 µL/min flow rate as follows: 0-7 min/95-65 % A, 7-8 min/65-15 % A, 8-10 min/15 % A, 10-11 min/5 % A, 11-16 min/95 % A. Mass spectra were recorded on a G2-Si HDMS mass spectrometer (Waters) *in* High Definition MS (HDMS) *positive ion* mode. *[Glu1]*-fibrinopeptide B (Waters) was used for lock-mass correction. Undeuterated samples of *Cr*aCRY were prepared similarly emplying undeuterated buffer (10 mM Tris, 100 mM sodium chloride, pH 7.8). Here, mass spectra were acquired in *Enhanced High Definition MS (HDMS^E)* positive ion *mode*[28,30]. Between samples, the immobilized pepsin was washed three times with 80 µl of 4% (v/v) acetonitrile and 0.5 M guanidine hydrochloride. All measurements were performed in triplicates. Peptide identification and assignement of deuterium incorporation was done using the PLGS and DynamX 3.0 softwares (*Waters*), respectively, as described elsewhere[31,32]. Statistically significant changes in deuterium uptake were certified by using a two-sided t-test with a 98 % confidence interval (SI-S5/S7). The resulting differences in deuterium uptake were mapped onto the *Cr*aCRYΔCTE structure (PDB: 6FN0) and figures were created using PYMOL 2.0.6 (*DeLano Scientific*).

References

1. Nango, E. et al. A three-dimensional movie of structural changes in bacteriorhodopsin. Science 354, 1552–1557 (2016).
2. Takala, H. et al. Light-induced structural changes in a monomeric bacteriophytochrome. Struct. Dyn. 3, (2016).
3. Zhang, Z. & Smith, D. L. Determination of amide hydrogen exchange by mass spectrometry: A new tool for protein structure elucidation. Protein Sci. 2, 522–531 (1993).
4. Wales, T. E. & Engen, J. R. Hydrogen exchange mass spectrometry for the analysis of protein dynamics. Mass Spectrom. Rev. 25, 158–170 (2006).
5. Hamuro, Y. et al. Rapid analysis of protein structure and dynamics by hydrogen/deuterium exchange mass spectrometry. J. Biomol. Tech. 14, 171–182 (2003).
6. Houde, D., Berkowitz, S. A. & Engen, J. R. The Utility of Hydrogen/Deuterium Exchange Mass Spectrometry in Biopharmaceutical Comparability Studies. J. Pharm. Sci. 100, 2071–2086 (2011).
7. Beel, B. et al. A Flavin Binding Cryptochrome Photoreceptor Responds to Both Blue and Red Light in

Chlamydomonas reinhardtii. Plant Cell 24, 2992–3008 (2012).
8. Franz, S. et al. Structure of the bifunctional cryptochrome aCRY from Chlamydomonas reinhardtii. Nucleic Acids Res. 46, 8010–8022 (2018).
9. Ahmad, M. & Cashmore, A. R. Seeing blue : the discovery of cryptochrome. 851–861 (1996).
10. Michael, A. K., Fribourgh, J. L., Van Gelder, R. N. & Partch, C. L. Animal Cryptochromes: Divergent Roles in Light Perception, Circadian Timekeeping and Beyond. Photochem. Photobiol. 93, 128–140 (2017).
11. Chaves, I. et al. The cryptochromes: blue light photoreceptors in plants and animals. Annu. Rev. Plant Biol. 62, 335–364 (2011).
12. Emery, P., So, W. V, Kaneko, M., Hall, J. C. & Rosbash, M. CRY, a Drosophila clock and light-regulated cryptochrome, is a major contributor to circadian rhythm resetting and photosensitivity. Cell 95, 669–679 (1998).
13. Cashmore, A. R., Jarillo, J. A., Wu, Y.-J. & Liu, D. Cryptochromes: Blue Light Receptors for Plants and Animals. Science 284, 760–765 (1999).
14. Thresher, R. J. et al. Role of mouse cryptochrome blue-light photoreceptor in circadian photoresponses. Science 282, 1490–4 (1998).
15. Ozturk, N. Phylogenetic and Functional Classification of the Photolyase/Cryptochrome Family. Photochem. Photobiol. 93, 104–111 (2017).
16. Zoltowski, B. D. et al. Structure of full-length Drosophila cryptochrome. Nature 480, 396–399 (2011).
17. Busza, A., Emery-Le, M., Rosbash, M. & Emery, P. Roles of the two Drosophila CRYPTOCHROME structural domains in circadian photoreception. Science 304, 1503–1506 (2004).
18. Rosato, E. et al. Light-dependent interaction between Drosophila CRY and the clock protein PER mediated by the carboxy terminus of CRY. Curr. Biol. 11, 909–917 (2001).
19. Ceriani, M. F. et al. Light-Dependent Sequestration of TIMELESS by CRYPTOCHROME. Science 285, 553–556 (1999).
20. Ozturk, N., Selby, C. P., Annayev, Y., Zhong, D. & Sancar, A. Reaction mechanism of Drosophila cryptochrome. Proc. Natl. Acad. Sci. 108, 516–521 (2011).
21. Ozturk, N., VanVickle-Chavez, S. J., Akileswaran, L., Van Gelder, R. N. & Sancar, A. Ramshackle (Brwd3) promotes light-induced ubiquitylation of Drosophila Cryptochrome by DDB1-CUL4-ROC1 E3 ligase complex. Proc. Natl. Acad. Sci. 110, 4980–4985 (2013).
22. Ganguly, A. et al. Changes in active site histidine hydrogen bonding trigger cryptochrome activation. Proc. Natl. Acad. Sci. 113, 10073–10078 (2016).
23. Müller, N. et al. A Plant Cryptochrome Controls Key Features of the Chlamydomonas Circadian Clock and Its Life Cycle. Plant Physiol. 174, 185–201 (2017).
24. Huang, K. & Beck, C. F. Phototropin is the blue-light receptor that controls multiple steps in the sexual life cycle of the green alga Chlamydomonas reinhardtii. Proc. Natl. Acad. Sci. 100, 6269–6274 (2003).
25. Zou, Y. et al. An Animal-Like Cryptochrome Controls the Chlamydomonas Sexual Cycle. Plant Physiol. 174, 1334–1347 (2017).
26. Oldemeyer, S. et al. Essential Role of an Unusually Long-lived Tyrosyl Radical in the Response to Red Light of the Animal-like Cryptochrome aCRY. J. Biol. Chem. 291, 14062–14071 (2016).
27. Nohr, D. et al. Extended Electron-Transfer in Animal Cryptochromes Mediated by a Tetrad of Aromatic Amino Acids. Biophys. J. 111, 301–311 (2016).
28. Li, G. Z. et al. Database searching and accounting of multiplexed precursor and product ion spectra from the data independent analysis of simple and complex peptide mixtures. Proteomics 9, 1696–1719 (2009).
29. Wales, T. E., Fadgen, K. E., Gerhardt, G. C. & Engen, J. R. High-speed and high-resolution UPLC separation at zero degrees celsius. Anal. Chem. 80, 6815–6820 (2008).
30. Geromanos, S. J. et al. The detection, correlation, and comparison of peptide precursor and product ions from data independent LC-MS with data dependant LC-MS/MS. Proteomics 9, 1683–1695 (2009).
31. Steinchen, W. et al. Catalytic mechanism and allosteric regulation of an oligomeric (p)ppGpp synthetase by an alarmone. Proc. Natl. Acad. Sci. 112, 13348–13353 (2015).
32. Schäper, S. et al. AraC-like transcriptional activator CuxR binds c-di-GMP by a PilZ-like mechanism to regulate extracellular polysaccharide production. Proc. Natl. Acad. Sci. 114, E4822–E4831 (2017).

Acknowledgements

We acknowledge support from the DFG-core facility for interactions, dynamics and macromolecular assembly structure at the Philipps-University Marburg. We thank Christine Kupschuss und and Dr. Andreas Mielcarek for technical assistance. SF-B received funding by the Marburg University Research Academy (MARA).

Author Contributions

SF-B designed and planned experiments with help of L-OE and prepared the samples for the HDX experiment. AP analysed the HDX data. SS performed initial experiments and optimized conditions. SF-B, SS, SvH, UL and L-OE designed the light chamber, which was built by the electronic department of the Philipps-University of Marburg. UL performed the HDX experiment and supervised HDX analyzation. SF-B and L-OE wrote the paper. All authors reviewed the results and approved the final version of the manuscript.

Figure 1: Analytical size exclusion of *Cr*aCRY-ΔCTE (**a**) and WT (**b**). In both cases most (80-97%) of the protein sample elute in the monomeric state. **c**) UV/Vis measurement of *Cr*aCRY WT treated with blue light (BL) and different concentrations of dithiothreitol (DTT) or tris(2-carboxyethyl)-phosphine (TCEP). The FAD cofactor was reduced to $FADH^-$ under all conditions (except only BL), but in the sample treated with 12.5 mM DTT less degradation can be observed. **b**) Difference spectra of the photoreduction of *Cr*aCRY with 12.5 mM DTT and 30 min BL as well as reoxidation of $FADH^-$ in- and outside the light chamber. After 18 h the sample outside the light chamber entirely reoxidized to FAD_{OX} (red line), whereas the sample inside the chamber 70 % remains in the $FADH^-$ state with some contributions from FADH° and FAD_{OX} (blue line).

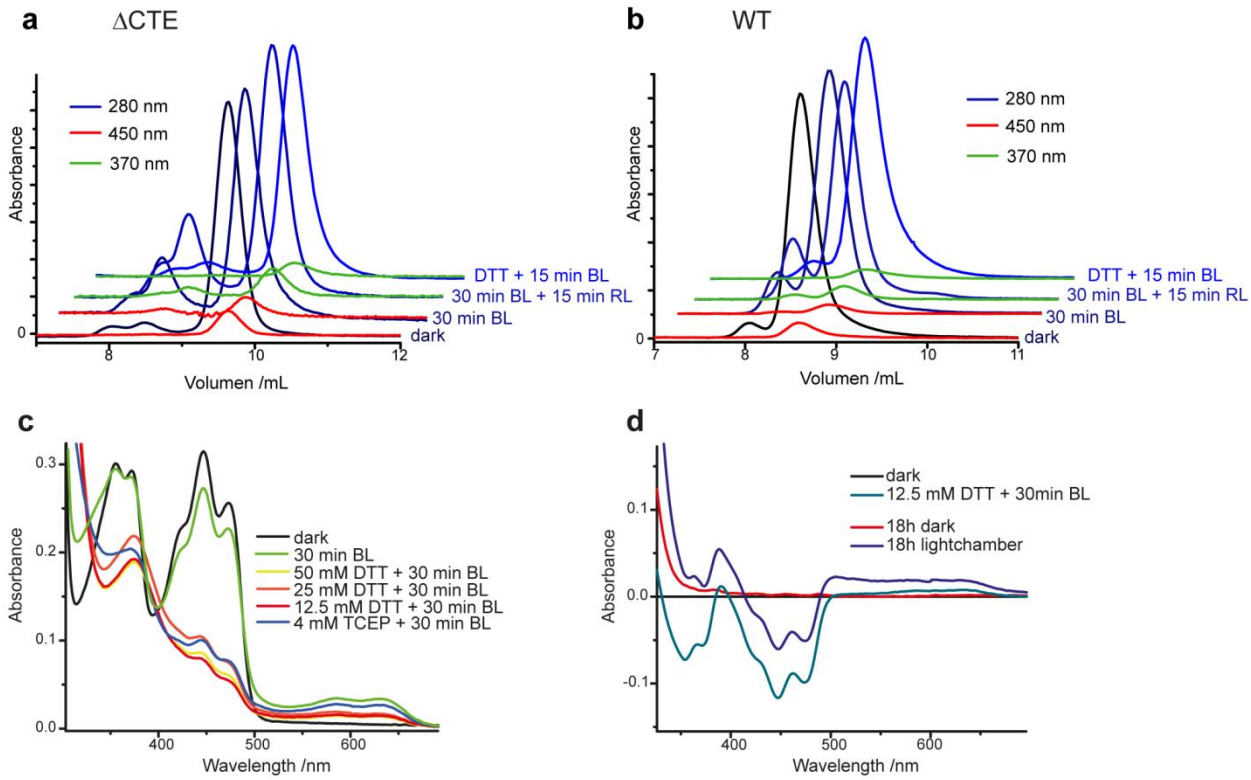

Figure 2: Selected heat maps of the relative fractional deuterium uptake of *Cr*aCRY-WT minus *Cr*aCRYΔCTE. The relative uptake of the FAD_{OX} state at 10 s was mapped onto the *Cr*aCRYΔCTE structure (PDB: 5ZM0). Blue sections correlate with a higher deuterium uptake in the ΔCTE variant than in WT, while red correlates with a higher uptake in full-length *Cr*aCRY. For the black segments no peptides could be assigned by HDX-MS analyses. Changes were observed for the linker between the N- and C-terminal domains and for a helix bundle in the C-terminal domain (α10 to α13) that is exposed at the protein surface. This correlates to a higher flexibility or solvent accessibility of these regions in the WT.

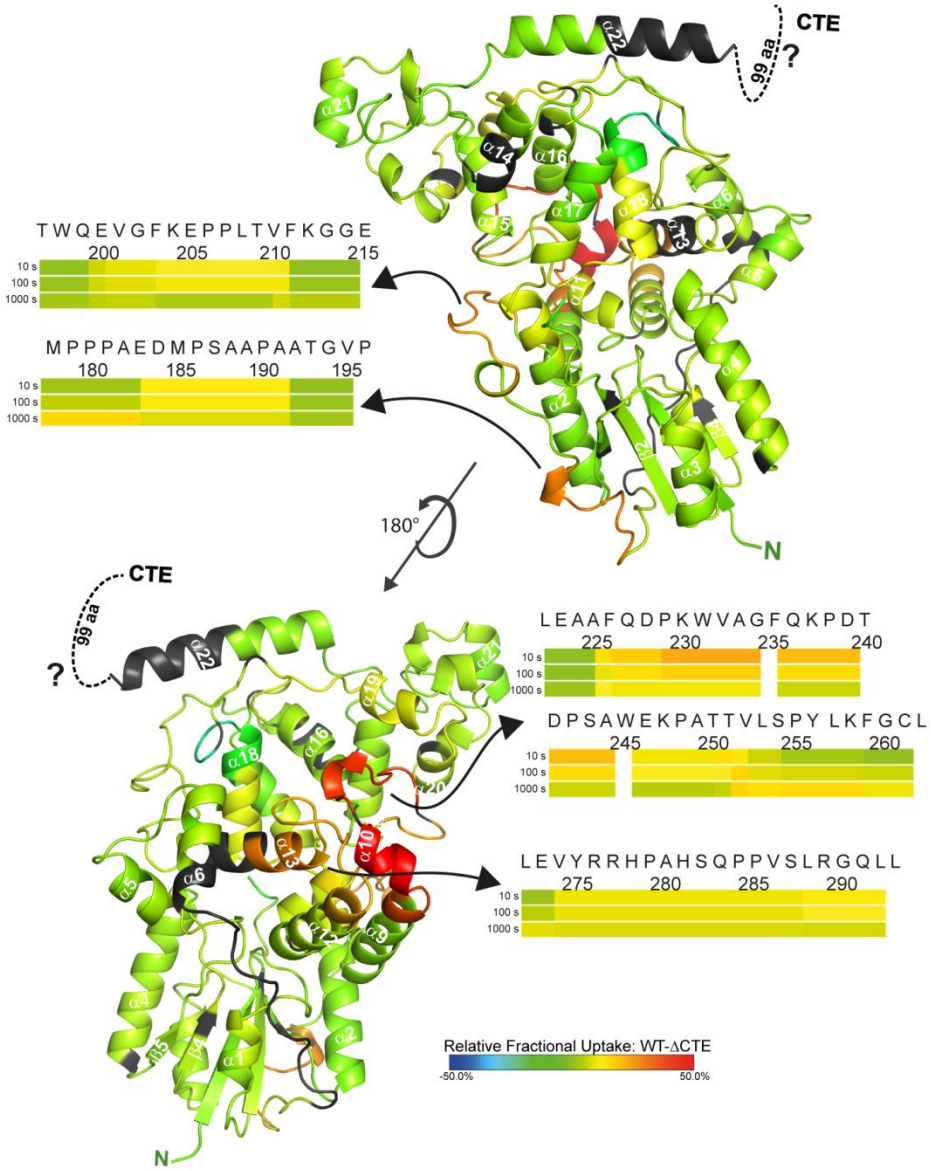

Figure 3: Closer view on the DNA binding site of *Cr*aCRY (PDB: 6FN0). (a) Here, the (6-4) damaged DNA (blue) is bound to the enzyme and the two catalytic histidines (green) are shown. (b) Q291 and K237 play a crucial role in DNA binding and are highly conserved (marked with *) as shown in the WebLogo that was generated from a multiple sequence alignment of animal-like cryptochromes(142). Both residues are located on a stretch with high deuterium uptake in the WT. (c) The overall binding mode of the dsDNA shows no significant differences between *Cr*aCRY-WT and *Cr*aCRYΔCTE comparing HDX analysis without DNA.

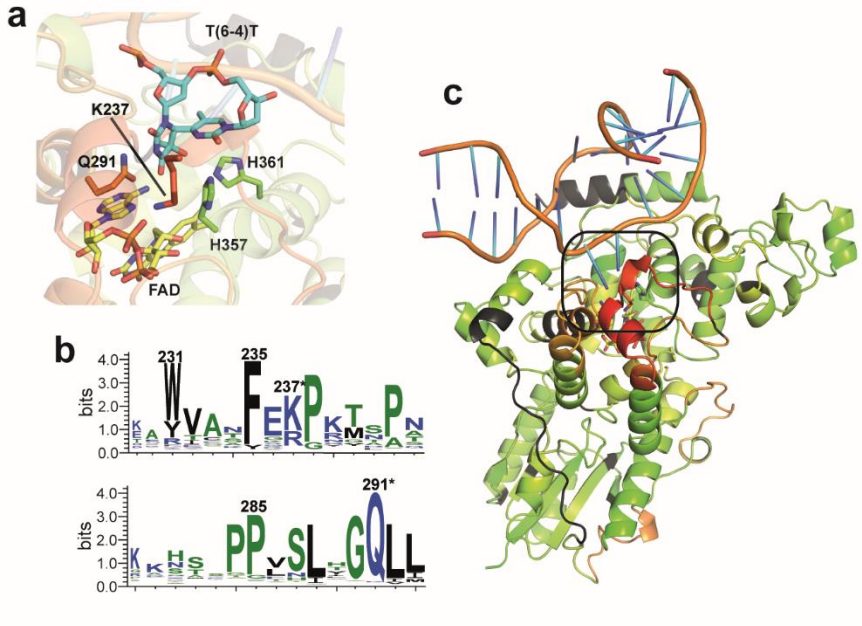

Figure 4: Relative fractional deuterium uptake at 10 s of the reduced ($FADH^-$) minus the oxidized (FAD_{OX}) states of (a) *Cr*aCRY-WT and (b) truncated *Cr*aCRYΔCTE, both are mapped onto the *Cr*aCRYΔCTE structure (PDB: 5ZM0). A highly significant difference can be observed in a loop region close to the C-terminal helix α22. c) The shown loop (300 – 326) presenting the distal tryptophan, W322, is part of the highly conserved Trp triad in photolyases and cryptochromes. W322 is flanked by the polar residues D323 and D321, which form a network of hydrogen bond interactions with the basic residues R485 and R492 from the C-terminal α22 helix. This charged network shields the distal electron donor of the electron transfer cascade, Y373, from exposure at the protein surface. The 320-326 loop exhibits a higher deuterium uptake in the reduced state, which correlates with higher flexibility. We suggest that the tight interaction between D323/D321 and R485/R492 gets disrupted upon formation of the Y373° radical, so that the α22 helix loses conformational restraint by interaction with the PHR.

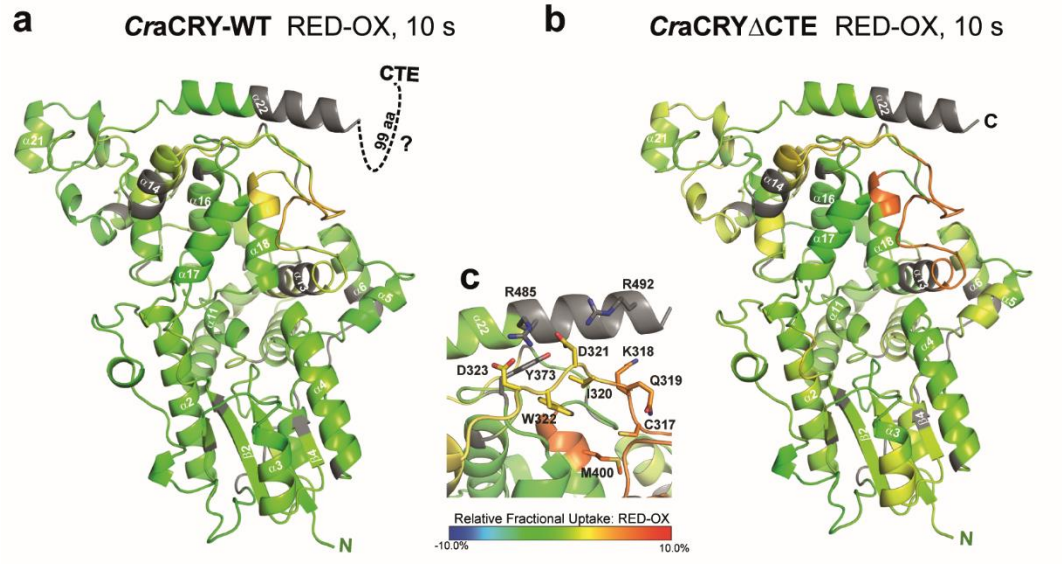

Figure 5: Model of the structural movement in CraCRY from the fully oxidized to the hydroquinone state of the FAD based on the HDX data. In between, the neutral semiquinone state is forming (FADH°), but we have no structural information concerning this. In the shown model, the C-terminal extension (CTE, red) is located over the protein surface and is partly structured. We propose that an unknown signaling partner X (light blue) can bind to CraCRY during the night, when it is located over the whole cell body. During the day, the hydroquinone state is forming ($FADH^-$). Because of the radical pair formation [Y373° and $FADH^{-}$°] during photoreduction, the H-bond network between α22, D323 and D321 is disrupted which leads to a movement of the helix and therefore a change in the CTE. The structured region in the CTE gets unfolded and factor X is getting released.

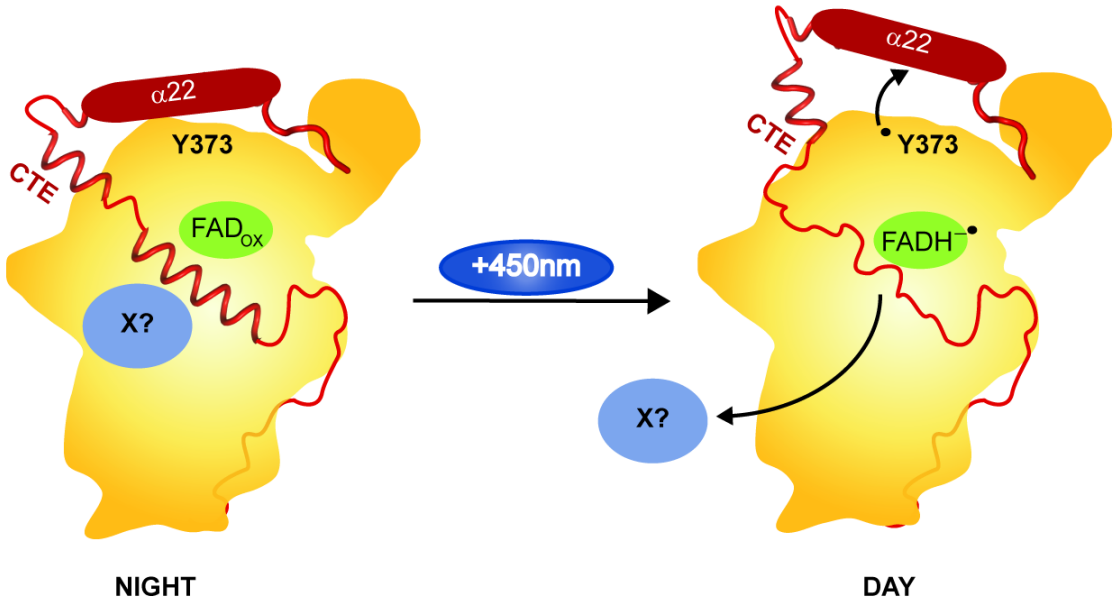

Supplementary Information

SI-S1 UV/Vis absorption spectra of the samples before analytical size exclusion.

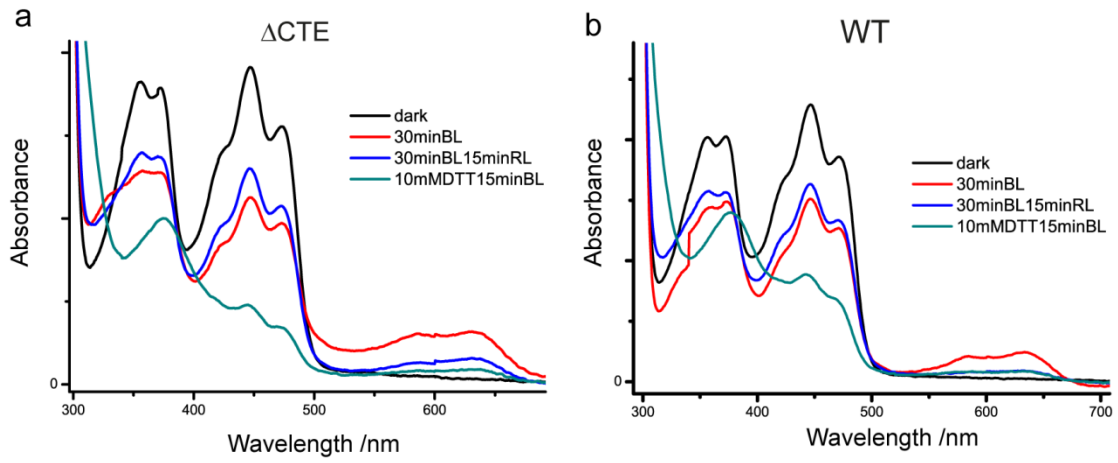

SI-S2 Analytical size exclusion of *Cra*CRY. Apparent mass was calculated in use of the calibration curve (y=-0.15642x+3.29765). Distribution between monomer and dimer were done by using the molecular mass (MM) of *Cra*CRY WT (66.3 kDa) and ΔCTE (57.7 kDa). Ratios between 0.5 and 1.5 are indicating that the protein is a monomer and above 1.5 the protein is probably in a dimeric state. $\%_{Dimer}$ was calculated by adding up the peak integrals and calculating the percentage of the particular peak of the total area.

	Dimer A_{280nm}	**Monomer A_{280nm}**	**Dimer $MM_{app.}$**	**Monomer $MM_{app.}$**	**$\%_{Dimer}$ A_{280nm}**	**$\%_{Dimer}$ A_{450nm}**	**$\%_{Dimer}$ A_{370nm}**	**$\%_{Dimer}^{450nm\ v\ 370nm}$ /$\%_{Dimer}^{280nm}$**
ΔCTE								
dark	8.48	9.63	93.6	61.8	4.4	0	0	0
30 min BL	8.40	9.53	96.3	64.1	17.5	5.5	0	0.31
BL+RL	8.59	9.66	90.0	61.2	21.6	0	17.8	0.82
DTT+BL	8.51	9.66	92.6	61.2	6.6	0	0	0
WT								

dark	8.05	8.60	109.3	89.6	3.7	0	0	0
30 min BL	8.10	8.60	107.3	89.6	11.0	16.0	0	1.45
BL+RL	8.08	8.64	108.1	88.3	16.5	0	38.0	2.30
DTT+BL	8.10	8.70	107.3	86.5	4.1	0	0	0

SI-S3 a) Schematic representation of the light chamber we designed. P1, P2 and P3 are positions of different sample holders, which can be illuminated with three different wavelengths. The 2600 mAh battery can be charged via miniUSB. **b)** Picture of the light chamber. It works completely independently and fits perfectly in the two arm robotic autosampler system (*LEAP Technologies*). **c)** Diagram of the position of the switches to activate the different LEDs. The illumination interval can be regulated over button 5.

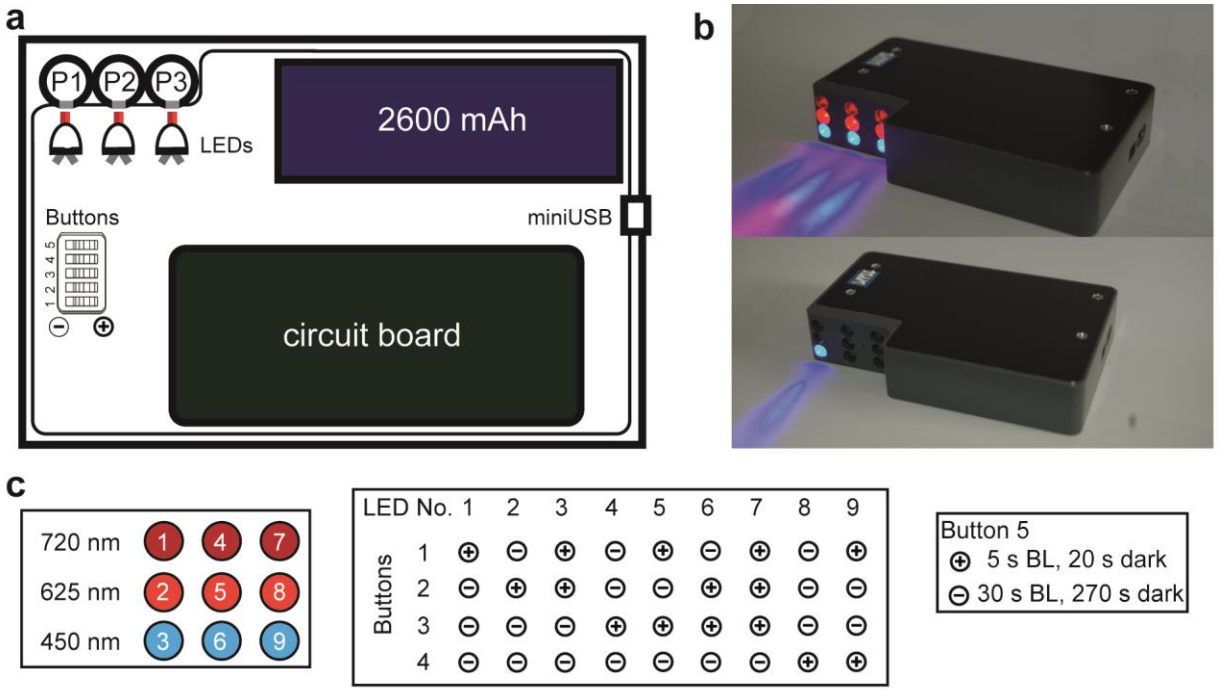

SI-S4 Selected HDX peptides with raw values and standard deviations (SD). Mean relative uptake for WT and ΔCTE for an incubation time of 10 s as well as the percentage uptake.

Start	End	MaxD	Protein	State	Uptake /Da	Uptake SD /Da	Uptake /%
47	59	12	ΔCTE	FAD_{OX}	3.6	0.1	0.83
47	59	12	ΔCTE	$FADH^-$	3.6	0.0	0.15
47	59	12	WT	FAD_{OX}	4.5	0.1	2.37
47	59	12	WT	$FADH^-$	4.4	0.1	1.82
184	202	15	ΔCTE	FAD_{OX}	5.3	0.1	0.48
184	202	15	ΔCTE	$FADH^-$	5.3	0.0	0.63
184	202	15	WT	FAD_{OX}	5.7	0.0	2.52
184	202	15	WT	$FADH^-$	5.7	0.0	2.43
199	211	10	ΔCTE	FAD_{OX}	3.0	0.0	0.82
199	211	10	ΔCTE	$FADH^-$	3.0	0.0	1.93
199	211	10	WT	FAD_{OX}	3.7	0.0	3.65
199	211	10	WT	$FADH^-$	3.6	0.0	4.85
223	234	10	ΔCTE	FAD_{OX}	1.6	0.0	0.38
223	234	10	ΔCTE	$FADH^-$	1.7	0.1	0.30
223	234	10	WT	FAD_{OX}	3.1	0.0	2.45
223	234	10	WT	$FADH^-$	3.0	0.1	1.96
235	244	7	ΔCTE	FAD_{OX}	0.7	0.1	0.84
235	244	7	ΔCTE	$FADH^-$	0.6	0.0	2.69
235	244	7	WT	FAD_{OX}	2.1	0.1	3.04
235	244	7	WT	$FADH^-$	2.1	0.0	8.94
245	250	4	ΔCTE	FAD_{OX}	1.1	0.0	1.13
245	250	4	ΔCTE	$FADH^-$	1.1	0.0	2.51
245	250	4	WT	FAD_{OX}	1.5	0.0	2.49
245	250	4	WT	$FADH^-$	1.6	0.0	8.39
245	259	12	ΔCTE	FAD_{OX}	1.5	0.1	0.41
245	259	12	ΔCTE	$FADH^-$	1.5	0.0	1.56

245	259	12	WT	FAD_{OX}	3.1	0.0	2.66
245	259	12	WT	$FADH^-$	3.1	0.0	3.99
272	293	18	ΔCTE	FAD_{OX}	2.1	0.0	0.64
272	293	18	ΔCTE	$FADH^-$	2.2	0.0	1.84
272	293	18	WT	FAD_{OX}	4.8	0.1	2.34
272	293	18	WT	$FADH^-$	4.8	0.1	5.75
299	317	16	ΔCTE	FAD_{OX}	2.1	0.0	1.25
299	317	16	ΔCTE	$FADH^-$	2.9	0.0	0.86
299	317	16	WT	FAD_{OX}	2.2	0.0	1.86
299	317	16	WT	$FADH^-$	2.7	0.1	3.00
318	328	9	ΔCTE	FAD_{OX}	1.8	0.1	0.56
318	328	9	ΔCTE	$FADH^-$	2.1	0.1	0.54
318	328	9	WT	FAD_{OX}	1.9	0.0	2.44
318	328	9	WT	$FADH^-$	2.0	0.0	2.23
399	404	5	ΔCTE	FAD_{OX}	0.6	0.0	0.71
399	404	5	ΔCTE	$FADH^-$	0.9	0.0	3.82
399	404	5	WT	FAD_{OX}	0.4	0.0	3.94
399	404	5	WT	$FADH^-$	0.5	0.0	9.73

SI-S5 Statistically significant changes in deuterium uptake from selected peptides between ΔCTE and WT were certified by using a two-sided t-test with a 98 % ($|t|>1.94$).

Start	End	Protein	State	s^2	s	t	Significant?
47	59	ΔCTE	FAD_{OX}	$7.29 \cdot 10^{-3}$	$8.54 \cdot 10^{-2}$	-11.9	+
47	59	WT	FAD_{OX}				
47	59	ΔCTE	$FADH^-$	$2.56 \cdot 10^{-3}$	$5.06 \cdot 10^{-2}$	-19.4	+
47	59	WT	$FADH^-$				
184	202	ΔCTE	FAD_{OX}	$1.73 \cdot 10^{-3}$	$4.16 \cdot 10^{-2}$	-13.8	+
184	202	WT	FAD_{OX}				

184	202	ΔCTE	$FADH^-$	$1.12 \cdot 10^{-3}$	$3.35 \cdot 10^{-2}$	-14.6	+
184	202	WT	$FADH^-$				
199	211	ΔCTE	FAD_{OX}	$1.09 \cdot 10^{-4}$	$1.04 \cdot 10^{-2}$	-79.9	+
199	211	WT	FAD_{OX}				
199	211	ΔCTE	$FADH^-$	$8.94 \cdot 10^{-4}$	$2.99 \cdot 10^{-2}$	-25.8	+
199	211	WT	$FADH^-$				
223	234	ΔCTE	FAD_{OX}	$5.51 \cdot 10^{-4}$	$2.35 \cdot 10^{-2}$	-76.2	+
223	234	WT	FAD_{OX}				
223	234	ΔCTE	$FADH^-$	$2.95 \cdot 10^{-3}$	$5.43 \cdot 10^{-2}$	-30.4	+
223	234	WT	$FADH^-$				
235	244	ΔCTE	FAD_{OX}	$3.28 \cdot 10^{-3}$	$5.73 \cdot 10^{-2}$	-30.0	+
235	244	WT	FAD_{OX}				
235	244	ΔCTE	$FADH^-$	$9.15 \cdot 10^{-4}$	$3.02 \cdot 10^{-2}$	-60.6	+
235	244	WT	$FADH^-$				
245	250	ΔCTE	FAD_{OX}	$5.99 \cdot 10^{-4}$	$2.45 \cdot 10^{-2}$	-21.0	+
245	250	WT	FAD_{OX}				
245	250	ΔCTE	$FADH^-$	$2.42 \cdot 10^{-4}$	$1.56 \cdot 10^{-2}$	-35.4	+
245	250	WT	$FADH^-$				
245	259	ΔCTE	FAD_{OX}	$3.80 \cdot 10^{-3}$	$6.16 \cdot 10^{-2}$	-33.0	+
245	259	WT	FAD_{OX}				
245	259	ΔCTE	$FADH^-$	$1.36 \cdot 10^{-3}$	$3.68 \cdot 10^{-2}$	-53.2	+
245	259	WT	$FADH^-$				
272	293	ΔCTE	FAD_{OX}	$2.71 \cdot 10^{-3}$	$5.21 \cdot 10^{-2}$	-63.5	+
272	293	WT	FAD_{OX}				
272	293	ΔCTE	$FADH^-$	$2.01 \cdot 10^{-3}$	$4.48 \cdot 10^{-2}$	-70.5	+
272	293	WT	$FADH^-$				
299	317	ΔCTE	FAD_{OX}	$6.89 \cdot 10^{-4}$	$2.62 \cdot 10^{-2}$	-7.47	+
299	317	WT	FAD_{OX}				

299	317	ΔCTE	$FADH^-$	$2.56 \cdot 10^{-3}$	$5.05 \cdot 10^{-2}$	5.82	+
299	317	WT	$FADH^-$				
318	328	ΔCTE	FAD_{OX}	$3.14 \cdot 10^{-3}$	$5.60 \cdot 10^{-2}$	-1.75	-
318	328	WT	FAD_{OX}				
318	328	ΔCTE	$FADH^-$	$2.21 \cdot 10^{-3}$	$4.70 \cdot 10^{-2}$	1.56	-
318	328	WT	$FADH^-$				
399	404	ΔCTE	FAD_{OX}	$5.06 \cdot 10^{-4}$	$2.25 \cdot 10^{-2}$	11.8	+
399	404	WT	FAD_{OX}				
399	404	ΔCTE	$FADH^-$	$7.10 \cdot 10^{-4}$	$2.66 \cdot 10^{-2}$	18.0	+
399	404	WT	$FADH^-$				

SI-S6 Difference map of the relative fractional uptake for the FAD_{OX} (dark) state WT minus ΔCTE. Selected peptides were marked with either a plus (|t|>1.94) or minus (|t|<1.94).

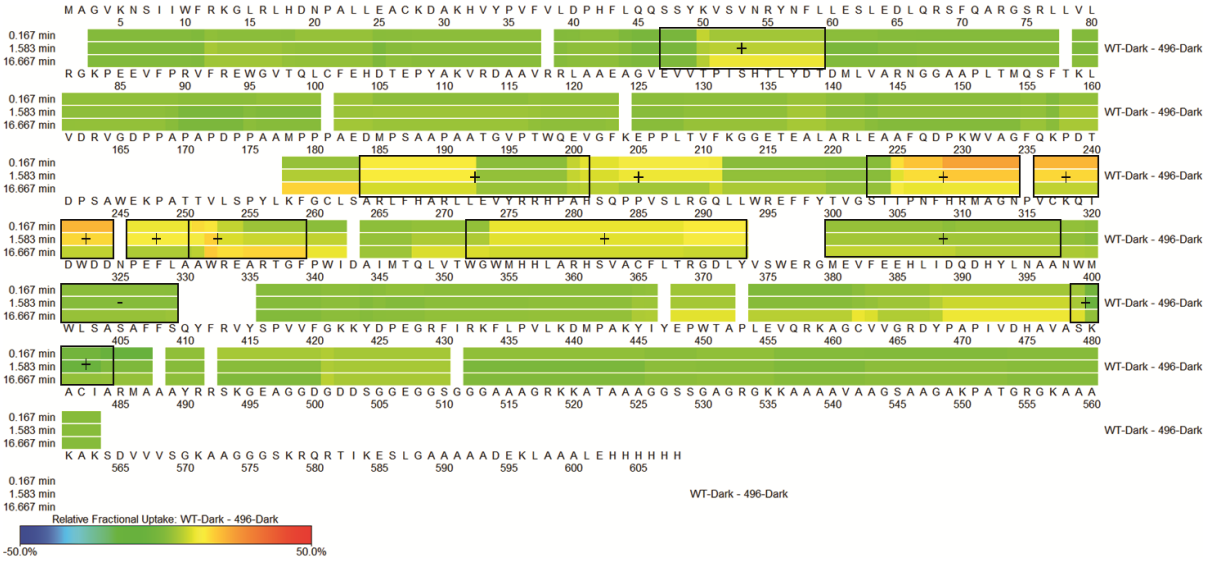

SI-S7 Statistically significant changes in deuterium uptake from selected peptides between FAD_{OX} and $FADH^-$ were certified by using a two-sided t-test with a 98 % (|t|>1.94).

Start	End	Protein	State	s^2	s	t	Significant?
47	59	ΔCTE	FAD_{OX}	$3.08 \cdot 10^{-3}$	$5.55 \cdot 10^{-2}$	0.88	-
47	59	ΔCTE	$FADH^-$				
47	59	WT	FAD_{OX}	$6.78 \cdot 10^{-3}$	$8.23 \cdot 10^{-2}$	1.04	-
47	59	WT	$FADH^-$				
184	202	ΔCTE	FAD_{OX}	$1.50 \cdot 10^{-3}$	$3.87 \cdot 10^{-2}$	-1.27	-
184	202	ΔCTE	$FADH^-$				
184	202	WT	FAD_{OX}	$1.36 \cdot 10^{-3}$	$3.68 \cdot 10^{-2}$	0.10	-
184	202	WT	$FADH^-$				
199	211	ΔCTE	FAD_{OX}	$6.97 \cdot 10^{-5}$	$8.35 \cdot 10^{-3}$	4.40	+
199	211	ΔCTE	$FADH^-$				
199	211	WT	FAD_{OX}	$9.33 \cdot 10^{-4}$	$3.05 \cdot 10^{-2}$	3.21	+
199	211	WT	$FADH^-$				
223	234	ΔCTE	FAD_{OX}	$1.69 \cdot 10^{-3}$	$4.11 \cdot 10^{-2}$	-2.38	+
223	234	ΔCTE	$FADH^-$				
223	234	WT	FAD_{OX}	$1.81 \cdot 10^{-3}$	$4.25 \cdot 10^{-2}$	0.86	-
223	234	WT	$FADH^-$				
235	244	ΔCTE	FAD_{OX}	$1.86 \cdot 10^{-3}$	$4.31 \cdot 10^{-2}$	1.51	-
235	244	ΔCTE	$FADH^-$				
235	244	WT	FAD_{OX}	$2.34 \cdot 10^{-3}$	$4.84 \cdot 10^{-2}$	-1.01	-
235	244	WT	$FADH^-$				
245	250	ΔCTE	FAD_{OX}	$4.06 \cdot 10^{-4}$	$2.02 \cdot 10^{-2}$	0.61	-
245	250	ΔCTE	$FADH^-$				
245	250	WT	FAD_{OX}	$4.35 \cdot 10^{-4}$	$2.09 \cdot 10^{-2}$	-1.17	-
245	250	WT	$FADH^-$				
245	259	ΔCTE	FAD_{OX}	$4.16 \cdot 10^{-3}$	$6.45 \cdot 10^{-2}$	-0.76	-

245	259	ΔCTE	$FADH^-$				
245	259	WT	FAD_{OX}	$9.87 \cdot 10^{-4}$	$3.14 \cdot 10^{-2}$	0.78	-
245	259	WT	$FADH^-$				
272	293	ΔCTE	FAD_{OX}	$1.01 \cdot 10^{-3}$	$3.17 \cdot 10^{-2}$	-2.70	+
272	293	ΔCTE	$FADH^-$				
272	293	WT	FAD_{OX}	$3.72 \cdot 10^{-3}$	$6.10 \cdot 10^{-2}$	1.00	-
272	293	WT	$FADH^-$				
299	317	ΔCTE	FAD_{OX}	$1.12 \cdot 10^{-3}$	$3.35 \cdot 10^{-2}$	-29.6	+
299	317	ΔCTE	$FADH^-$				
299	317	WT	FAD_{OX}	$2.12 \cdot 10^{-3}$	$4.61 \cdot 10^{-2}$	-10.9	+
299	317	WT	$FADH^-$				
318	328	ΔCTE	FAD_{OX}	$3.70 \cdot 10^{-3}$	$6.08 \cdot 10^{-2}$	-5.44	+
318	328	ΔCTE	$FADH^-$				
318	328	WT	FAD_{OX}	$1.65 \cdot 10^{-3}$	$4.07 \cdot 10^{-2}$	-3.92	+
318	328	WT	$FADH^-$				
399	404	ΔCTE	FAD_{OX}	$1.04 \cdot 10^{-3}$	$3.22 \cdot 10^{-2}$	-11.9	+
399	404	ΔCTE	$FADH^-$				
399	404	WT	FAD_{OX}	$1.77 \cdot 10^{-4}$	$1.33 \cdot 10^{-2}$	-12.7	+
399	404	WT	$FADH^-$				

SI-S8 Difference map of the relative fractional uptake for ΔCTE (Δ496) $FADH^-$ (light) minus FAD_{OX} (dark) . Selected peptides were marked with either a plus (|t|>1.94) or minus (|t|<1.94).

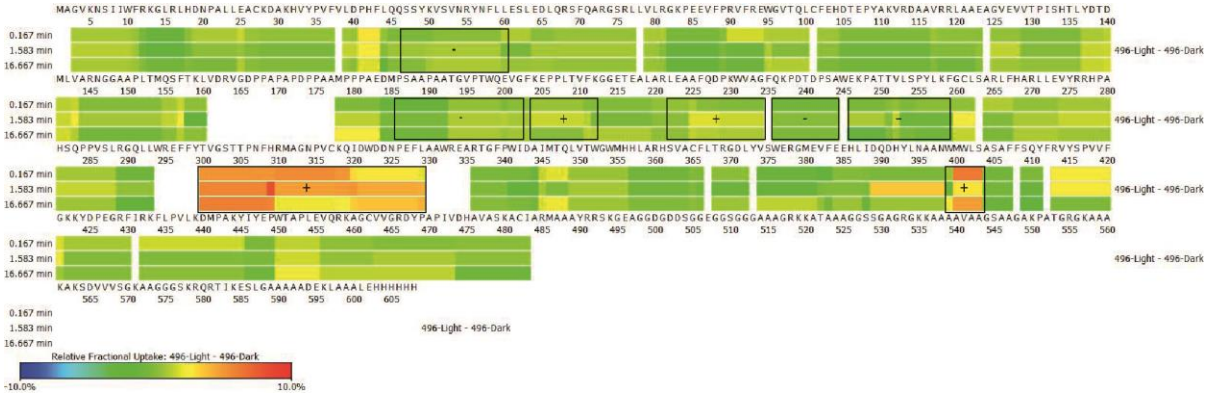

4.6 The FAD observed by TR-SFX

This research is part of the cooperation between the Philipps University Marburg (Germany), the Academia Sinica Taipei (Taiwan)**,** the Osaka University (Japan) and the *RIKEN Harima Institute* (Hyogo Prefecture, Japan). Authors are *Manuel Maestre-Reyna, Cheng-Han Yang, Wei-Cheng Huang, Eka Putra Gusti Ngurah Putu, Sophie Franz-Badur, Wen-Jin Wu, Hsiang-Yi Wu, Po-Hsun Wang, Jiahn-Haur Liao, Cheng-Chung Lee, Kai-Fa Huang, Yao-Kai Chang, Jui-Hung Weng, Michihiro Sugahara, Shigeki Owada, Yasumasa Joti, Rie Tanaka, Kensuke Tono, Eriko Nango, Stephan Kiontke, Junpei Yamamoto, So Iwata, Lars-Oliver Essen*, Yoshitaka Bessho*, Ming-Daw Tsai*.* **Serial femtosecond X-ray dissection of photolyase FAD structure tuning by an electrostatic gate** (submitted 2018).

Summary

During the course of time resolved experiments with *Mm*CPDII we could observe the conformation of FAD in different oxidation states. The structures published so far are showing the FAD in an ill-defined state as X-rays at 100 K already trigger the photoreduction of the cofactor. In this study, we combine damage free TR-SFX under anaerobic conditions, *in crystallo* UV/Vis spectroscopy and molecular dynamics simulation to show and analyse structures of the oxidized, semiquinone and hydroquinone states of the photolyase. The structures reveal a quasi-planar isoalloxazine ring in the oxidized state, whereas the hydroquinone state exhibits a strong buckling of the ring along the N10-N5 axis. The semiquinone FAD demonstrates a longitudinally twist of the isoalloxazine ring as well as a rotation of Asn403 in close proximity to the FAD N5 atom. These results are reflected in the accompanying MD simulations. Surprisingly, the most prominent change in the surrounding area of the isoalloxazine ring is not the flip of Asn403, but an alteration of a salt-bridge between Arg378 and Asp409. This salt-bridge acts as electrostatic gate which is closed in the oxidized state, forcing the FAD into a fully planar conformation. In the reduced structure, the gate is open or weakened, allowing Arg378 to stabilize the reduced isoalloxazine moiety. Although this salt bridge is fully conserved in the CPF, it has never been identified before as key player in the mechanism of photoreduction.

Author contributions

M. Maestre-Reyna, S. Iwata, L.-O. Essen, Y. Bessho and M.-D. Tsai conceived the research and designed experiments. M. Maestre-Reyna, Y. Joti, E. Nango, S. Kiontke, L.-O. Essen, and M.-D. Tsai analyzed the data. M. Maestre-Reyna and C.-H. Yang performed MD simulations and analyzed them. M. Maestre-Reyna, W.-C. Huang, E. P. G. N. Putu, S. Franz-Badur, W.-J. Weng, H.-Y. Wu, Po.-Hsun Wang, J.-H. Liao, C.-C. Lee, K.-F. Huang, Y.-K. Chang, J.-H. Weng, M. Sugahara, S. Owada, R. Tanaka, K. Tono, J. Yamamoto, and L.-O. Essen performed experiments. M. Maestre-Reyna, L.-O. Essen, Y. Bessho, and M.-D. Tsai wrote the manuscript.

Title: An arginine-aspartate electrostatic gate tunes the photolyase flavin chromophore

Authors: Manuel Maestre-Reyna[1], Cheng-Han Yang[1], Wei-Cheng Huang[1], Eriko Nango[2,3], Eka Putra Gusti Ngurah Putu[1], Sophie Franz-Badur[4], Wen-Jin Wu[1], Hsiang-Yi Wu[1], Po-Hsun Wang[1], Jiahn-Haur Liao[1], Cheng-Chung Lee[1], Kai-Fa Huang[1], Yao-Kai Chang[1], Jui-Hung Weng[1], Michihiro Sugahara[2], Shigeki Owada[2], Yasumasa Joti[2,5], Rie Tanaka[2], Kensuke Tono[5], Stephan Kiontke[4], Junpei Yamamoto[6], So Iwata[2,3], Lars-Oliver Essen[4,7,*], Yoshitaka Bessho[1,2,*], Ming-Daw Tsai[1,8,*]

Affiliations:

[1]Institute of Biological Chemistry, Academia Sinica, 128 Academia Rd. Sec. 2, Nankang, Taipei, 115, Taiwan.

[2]RIKEN SPring-8 Center, 1-1-1 Kouto, Sayo, Hyogo, 679-5148, Japan.

[3]Department of Cell Biology, Graduate School of Medicine, Kyoto University, Yoshidakonoe-cho, Sakyo-ku, Kyoto, 606-8501, Japan.

[4]Department of Chemistry, Philipps University Marburg, Hans-Meerwein Strasse 4, Marburg 35032, Germany.

[5]Japan Synchrotron Radiation Research Institute, 1-1-1 Kouto, Sayo, Hyogo, 679-5198, Japan.

[6]Division of Chemistry, Graduate School of Engineering Science, Osaka University, 1-3 Machikaneyama, Toyonaka, Osaka 560-8531, Japan.

[7]LOEWE Center of Synthetic Microbiology, Philipps University Marburg, Hans-Meerwein Straße 4, 35032 Marburg, Germany.

[8]Institute of Biochemical Sciences, National Taiwan University, 1, Roosevelt Rd. Sec. 4, Taipei 106, Taiwan.

*e-mail: mdtsai@gate.sinica.edu.tw ; bessho@sinica.edu.tw ; essen@chemie.uni-marburg.de

Abstract:

DNA photolyases catalyze two ultrafast, blue light-dependent reactions: DNA repair and photoreduction. However, as these reactions are also induced by X-rays, the FAD containing active site is ill-defined in previous photolyase structures, leaving the mechanism of photoreduction unclear. By combining radiation damage-free serial femtosecond crystallography, data collection under controlled reductive conditions, *in crystallo* spectroscopy, and molecular dynamics simulation, we now show the undisturbed structures of a photolyase in the three stages of its photoreactive FAD co-factor, i.e. its oxidized, radical, and fully reduced states. We find differences to reported photolyase structures due to structural changes underlying light-driven FAD reduction, including a strictly conserved arginine-aspartate pair that is adjacent to the FAD chromophore and acts as an electrostatic gate. We show that this Arg-Asp gate modulates the flavin's geometry and redox potential, and propose that this is a common mechanism for priming the flavin for light-driven DNA repair in photolyases and signaling by cryptochromes.

One Sentence Summary: Free electron laser X-ray uncovers an electrostatic gate that tunes FAD geometry and photoreduction activity of photolyase.

Main Text:

DNA photolyases are one of only four types of light-driven enzymes to have been characterized (1). Along with cryptochromes, they form the photolyase-cryptochrome family (PCF) (2), which is ubiquitous in all domains of life (3) and involved in a wide variety of functions including DNA repair by photolyases, circadian clock regulation, and even magnetoreception by cryptochromes(4). PCF members adopt a common, highly conserved two-domain topology (2,4-7), with a uniquely U-shaped, catalytic flavin adenine dinucleotide (FAD) cofactor bound to the C-terminal domain (6). As a central feature of the PCF, the catalytic FAD chromophore is activated by light, and participates in one or two one-electron transfer steps, yielding respectively the radical semiquinone ($FAD^{\bullet-}$ or $FADH^{\bullet}$) or the fully reduced, deprotonated hydroquinone state ($FADH^{-}$) (Fig. 1A) (8). Furthermore, the heteroaromatic, chromogenic isoalloxazine moiety (8) confers the redox-dependent spectroscopic properties of the FAD cofactor (9). Upon excitation of the

oxidized/semiquinone cofactor by blue light (FAD*/$FADH^{\bullet}$*), an intramolecular chain of aromatic residues donates one electron to the flavin, leading to $FADH^{\bullet}$/$FADH^{-}$ and an oxidized, solvent-exposed, tryptophanyl or tyrosyl radical ($Ar^{\bullet}$) (10-12). In most cryptochromes, transient formation of the semiquinone/$Ar^{\bullet}$ radical pair constitutes the photoreceptor's signaling state and causes its magnetic field susceptibility (Fig. 1A) (4). Conversely, in bifunctional cryptochromes and photolyases, where only the fully reduced $FADH^{-}$ is catalytically active (Fig. 1A) (4), subsequent reduction of $Ar^{\bullet}$ by external reducing agents renders the intramolecular electron transfer permanent (13).

Theoretical studies have shown that the isoalloxazine geometry is expected to undergo redox-dependent changes. In the oxidized and semiquinone states, it is planar, although flexibility is increased in the latter (14, 15). In the hydroquinone state, it buckles along the N5 to N10 axis, resulting in 10° to 28° deviation from planarity in solution (15-17), but -34° to 34° when bound to protein (18). Previous crystallographic studies of photolyase structures failed to provide undistorted views of the FAD chromophore, as X-ray irradiation causes unwanted reduction of the flavin's isoalloxazine moiety in photolyases, even under cryogenic conditions (5, 6, 19). Accordingly, all available structures of photolyases including the highly related cryptochromes are compromised by showcasing a mixed redox status, in which different proportions of each state (FAD, $FADH^{\bullet}$ and $FADH^{-}$) coexist (5, 6, 20, 21). Furthermore, as cryo-conditions severely hamper protein motion, it remains unclear whether the protein environment surrounding the cofactor, as determined in previous studies, fully represents the PCF's native mode of FAD binding.

We collected X-ray diffraction data from the *Methanosarcina mazei* class II CPD photolyase (*Mm*CPDII) in its three redox states via radiation damage-free serial femtosecond crystallography (DF-SFX) at the Spring-8 Angstrom Compact free electron Laser (SACLA). *In crystallo* UV/VIS spectroscopy allowed us to establish FAD and $FADH^{-}$ occupancies of higher than 99%, while the semiquinone state adopted an $FADH^{\bullet}/FAD_{ox}$ composition of 2:1 (65% $FADH^{\bullet}$ occupancy, Fig. S1A). Isomorphous difference electron density maps (IDEDM) (22) were used to compare the different redox states, i.e. $IDEDM_{OS}$ were calculated from $|F_{obs}|_{FAD} - |F_{obs}|_{FADH\bullet}$, $IDEDM_{SH}$ from $|F_{obs}|_{FADH\bullet} - |F_{obs}|_{FADH^-}$, and

IDEDM$_{OH}$ from $|F_{obs}|_{FAD}-|F_{obs}|_{FADH^-}$ coefficients. The observed experimental changes were then further analyzed via molecular dynamics simulations (MD), as well as quantum mechanical calculations.

The undistorted *Mm*CPDII structures, refined at 2.1, 2.7, and 2.3 Å resolution for the oxidized, semiquinone, and hydroquinone states, respectively (Table S1), reveal the characteristic PCF fold with its two-domain topology (Fig. 1B and Fig. S1B). In terms of the apoprotein, RMSD deviations were below 0.15 Å for all pair-wise combinations for 433 common Cα atoms and only very few significant IDEDM peaks could be found outside the FAD binding site (Fig. 1B). This invariance of the global *Mm*CPDII structure is additionally mirrored by very low overall atomic fluctuations in our 60 ns MD production trajectories (trajectory RMSDs of 1.01, 1.17, and 1.22 Å, respectively). A serendipitous marker for *Mm*CPDII's redox state is represented by a DTT molecule in the active site (Fig. S1C), because high DTT concentrations were required to generate both the semiquinone and hydroquinone states in crystalline samples, while no DTT was added during sample preparation under oxidizing conditions. Accordingly, in the oxidized state the DTT site remains unoccupied, providing a good benchmark for our IDEDM calculations (8.4 and 7.2 σ-contour peaks for IDEDM$_{OS}$, and IDEDM$_{OH}$, respectively). In conclusion, our structures and simulations agree with previous studies (23), which stated that, due to the overall rigidity of the PCF two-domain topology, no large scale, redox-dependent structural changes are to be expected. Nevertheless, the statistical weight conferred by SFX allowed us to achieve a high degree of crystal isomorphism between states, overcoming the significant, and well known, photolyase crystal variability (24).

A different scenario is represented by the binding site of the FAD cofactor, where significant IDEDM$_{OS}$, IDEDM$_{SH}$ and IDEDM$_{OH}$ peaks could be unambiguously delineated (Fig. 1B). For monitoring the noise level, each experimental data set was split into two control subsets to derive corresponding IDEDM (Fig. S2), which showed little noise. Thus, IDEDM peaks in Fig. 1B indicate changes in the active site structure upon light-driven redox change. Based on the comparison between the active site structures of the oxidized and reduced states (Fig. 2A), some residues are almost unaffected, e.g. Trp381, the closest tryptophan of

the intramolecular electron transfer chain of class II photolyases and acting as the primary electron donor during the photoreduction reaction. However, local conformational changes are observed for the isoalloxazine ring, the Asn403 side-chain, and the Arg378-Asp409 salt bridge. In the following sections we elaborate on how these differences were derived, and address the key roles they are expected to play in the mechanism of photoreduction of *Mm*CPDII.

Previously the different redox states of the FAD cofactor of photolyases could only be deduced by UV/Vis microspectroscopy. Since our *Mm*CPDII structures are damage-free structures, the isoalloxazine dihedral angles ρ_C and ρ_N (Fig. 2B) mirroring buckling and twisting could be determined for each state. A multiple refinement approach (Supplementary material and methods, Tables S2-4, Fig. S3A and S4) led us to fit the oxidized FAD structure by a quasi-planar isoalloxazine ring showing minor ρ_C and ρ_N distortion parameters of -2.0° and -2.1°, respectively (Fig. 2C, Table 1, Fig. S3B). The data for the semiquinone $FADH^{\bullet}$ yielded a longitudinally twisted isoalloxazine system with moderate planarity deviations of ρ_C = -6.1° and ρ_N = -5.1° (Fig. 2D, Table 1), whereas the hydroquinone isoalloxazine indicative of $FADH^-$ buckled strongly along the N5-N10 axis, with ρ_C = -14.3° and ρ_N = -14.5° (Fig. 2E, Table 1). Furthermore, very significant peaks (σ level > 4) could be identified in the corresponding IDEDM within the van-der-Waals radius of the FAD cofactor (Fig. 2D and E). Although the $IDEDM_{OS}$ and $IDEDM_{OH}$ peaks are comparable in position, the latter is more pronounced than the former (8.0 and 8.7 σ peaks, overview in Fig. 1B, in detail in Fig. 2D and E, respectively). In both cases, the IDEDM indicate a movement of the N5 nitrogen out of the isoalloxazine plane, which is consistent with the $FADH^{\bullet}$ twist in the extrapolated model (Fig. 2D) and the $FADH^-$ buckling (Fig. 2E). The twist in the former is representative of an expanded conformational space (Fig. S3C), and had been proposed to significantly contribute to the rapid relaxation of the photoexcited semiquinone during the photocycle of cryptochromes (8, 14). However, these studies were limited to theoretical calculations resulting from the interpretation of kinetic data, as PCF semiquinone structures had been impossible to obtain before.

The residue that forms the H-bond with the N5-nitrogen of FAD's isoalloxazine is the key factor for the different photochemistries of photolyases and cryptochromes. In photolyases it is an asparagine, e.g. Asn403 in *Mm*CPDII, whereas plant and animal cryptochromes, which lack further photoreduction from their semiquinoid $FADH^{\bullet}$ and $FAD^{\bullet-}$ states, harbor here an aspartate or cysteine instead (4). Accordingly, the N403D mutant of *Mm*CPDII and the N378D variant of the class I photolyase from *Escherichia coli* (*Ec*CPDI) fail to photoreduce further from their radical states (5, 25). FTIR spectroscopic studies on *Ec*CPDI showed that its asparagine interacts in a redox-state dependent manner with the FAD N5 atom (26). Given the X-ray mediated reduction of the FAD chromophore during data collection (5, 27), no changes of the conformation of the conserved asparagine side chains could be derived from previous studies of photolyase structures. Here, we could characterize such changes, with the oxidized state closely resembling previously published data (5), as the Asn403 Nδ and Oδ atoms are roughly equidistant from the FAD N5 atom (3.7 and 3.3 Å, respectively, Table 1, Fig 2C). In the refined semiquinone structure $IDEDM_{OS}$ peaks are consistent with a swivel of the Asn403 side-chain, with the Oδ atom approaching the $FADH^{\bullet}$ N5, thus becoming *proximal*, whereas Nδ moves to a *distal* position with distances of 2.7 and 4.1 Å, respectively (Fig. 2D). In contrast, in the hydroquinone state only a single negative $IDEDM_{OH}$ peak appears around the Asn403 distal δ-atom (Fig. 2E), which we refined as the Nδ atom, while the entirety of the side-chain shows increased thermal motion. The resulting structure is somewhat in-between the semiquinone and oxidized states, with Asn403 δ-atom distances being 3.1 and 4.0 Å for Oδ and Nδ, respectively (Fig. 2E, Table 1). The behavior of Asn403 in the refined structures is faithfully reflected in our MD simulations (Fig. S5, Table 1), including the swiveling motion of the Asn403 side-chain. Therefore, redox-dependent structural changes within the FAD cofactor appear to be stabilized to varying degrees by Asn403 as suggested by spectroscopic studies (26), and now being demonstrated by DF-SFX.

The most prominent change in the IDEDM peak intensities in immediate vicinity of the isoalloxazine ring is not, however, the swivel of the Asn403 side-chain, but one involving the end-on symmetric salt bridge (28) between Arg378 and Asp409 (Figs. 2A, 3A). Around

Arg378, $IDEDM_{semi}$ shows a very strong positive peak proximal to the isoalloxazine ring and a negative peak in distal location (σ peak levels: 6.8 and -5.0, respectively, Fig. 3B). This clearly indicates that Arg378 recedes and/or rotates during the FAD→$FADH^{\bullet}$ step of photoreduction in *Mm*CPDII. Furthermore, in $IDEDM_{OH}$ corresponding to the two-step FAD→$FADH^{-}$ transition, these peaks show an even stronger difference between the two states (6.4 and -6.0, Fig. 3C), and are accompanied by similar, albeit weaker, peaks surrounding Asp409 (3.8 and -5.0, Table 1).

The refined models show that, in the oxidized state, Arg378 interacts strongly with the almost coplanar Asp409 carboxylate *via* two H-bonds from the former's η-nitrogens, Nη1 and Nη2. In this end-on interaction the proximal Nη1 of Arg378 approaches the isoalloxazine ring (Fig. 3A, Table 1). Quantum mechanical calculations of the isoalloxazine/Arg378-Asp409 salt bridge system revealed that there is significant charge transfer between this doubly H-bonded salt bridge and the isoalloxazine, with the latter attaining a partial negative charge (isoalloxazine Δq = -0.07, Table S5). Accordingly, in our MD simulations of the oxidized state, the experimentally observed ρ_N and ρ_C values were often achieved, but only when Arg378 was within charge transfer distance (Table S5, Fig. S3B). Meanwhile, in the $FADH^{\bullet}$ state, Arg378 recedes away from the isoalloxazine ring, while flipping the orientation of the guanidinium group, which causes equidistance of the proximal Nη2 and Nε atoms to the N5 atom of the isoalloxazine (3.9 Å, Fig. 3B). Additionally, the interaction between Arg378 and Asp409 is now twisted, as the distal Arg378 Nη1 is swiveled 3.7 Å away from the nearest Asp409 Oδ2 oxygen, whereas the Nη2 forms a tight H-bond with Oδ1 (2.6 Å).

Upon further photoreduction to the fully reduced $FADH^{-}$ state, the Arg378 guanidinium group stays flipped, but further approaches the isoalloxazine ring (Fig. 3C, Table 1). Arg378 Nε becomes now the main interaction partner with the N5 nitrogen of $FADH^{-}$ with a distance of 3.3 Å (FAD: 4.8 Å; $FADH^{\bullet}$: 3.9 Å), while the isoalloxazine's proximal Nη2 atom remains close. As with the semiquinone state, the distal Arg378 Nη1 atom shifts away from Asp409. Under these conditions, no charge transfer between the salt bridge and

the isoalloxazine could be predicted from QM calculations of the hydroquinone state (isoalloxazine Δq = 0, Table S5).

Although our data leave no doubt regarding the Arg378-Asp409 pair swiveling, the base for the underlying molecular trigger of the conformational change is not immediately evident. Clearly, the photoreduction of the nearby isoalloxazine system and its change of conformation and charge distribution must play a key role. Quantum-mechanical studies on Arg-Asp side chain pairs and arginine dimers showed that the nature of guanidinium-carboxylate group interactions highly depends on the electrostatic environment, as the energy difference between an ionic salt-bridge and a neutral, hydrogen bonded Arg-Asp pair can be relatively low, with a few kcal/mol (29, 30). Our quantum mechanical dipole moment calculations of the FAD isoalloxazine system, as derived from the oxidized and fully reduced *Mm*CPDII DF-SFX structures, revealed that the dipole moment increases by two orders of magnitude (10.9 vs. 531.7 D). Deconvolution of the dipole moment into its main components clearly indicates that the in plane component acting colinearly on the Arg378-Asp409 pair gets reversed between the two states (Fig 4A), with a partial negative charge attracting the Nε-Hε group of Arg378 towards the reduced tricyclic system. By this, the reduced isoalloxazine co-planar component tends to separate the Arg-Asp pair by exposing Arg378 to its δ+ end, while Asp409 to δ-, encouraging proton transfer and/or repulsion (Fig. 4A). Most interestingly, the isoalloxazine conformation in the observed hydroquinone state can only be modeled by running a set of MD simulations where both Arg378 and Asp409 were set to the uncharged protonation states, i. e. proton transfer from cationic Arg378 to anionic Asp409 was assumed to have happened. In the presence of a singly H-bonded Arg-Asp pair, which corresponds to a twisted conformation of the guanidinium-carboxylate pair of Arg378-Asp409, the ρ_N and ρ_C values for the isoalloxazine moiety closely reproduce the experimentally observed parameters (Fig. 3D, Table 1). However, when setting the Arg378-Asp409 pair to a conventional salt bridge during MD simulation, very strong over-buckling takes place (Fig 2E, Fig. S3D).

Only three of 446 non-redundant class II photolyase sequences (cut-off for sequence identity: 90%) lack the Arg378 counterpart by harboring instead an uncharged residue, e.g.

the blind fish *Astyanax medicago* (Uniprot entry: W5K2W8; I425). Interestingly, in several Plasmodium species, e.g. *P. malariae* (A0A1A8X734; K697), but not *P. falciparum*, the arginine is exchanged by a lysine. In *Mm*CPDII the corresponding conservative R378K mutation resulted in low levels of bound FAD uptake as compared to the wild type (<20%, Fig. S6A), and a lack of general stability and ability for photoreduction (Fig. S6B). Accordingly, we propose that the profound changes in the electronic structure of FAD are strongly coupled to the Arg378-Asp409 pair, which transitions from a salt bridge-like character in the oxidized FAD state to a neutral H-bonded pair upon full photoreduction (Fig. 4B). Furthermore, the severe perturbation of the stability and function upon the conservative R378K mutation can also explain why the function of this highly conserved pair has never been reported previously.

Taken together, our results suggest that, in the oxidized state, the Arg378-Asp409 pair acts as a closed electrostatic gate by forming an end-on salt bridge for enforcing a non-planar conformation of the oxidized cofactor. The isoalloxazine ring of flavin cofactors is known to be fully planar in the relaxed oxidized form. Given that isoalloxazine buckling is known to affect the redox potential (31), *Mm*CPDII appears to bend the oxidized isoalloxazine ring slightly (Fig. 4B), likely to prime it for electron uptake during the $FAD \rightarrow FADH^{\bullet}$ photoreduction step. Conversely, in the catalytically competent $FADH^{-}$ state, the Arg378-Asp409 electrostatic gate is opened by adopting a twisted, neutral conformation, thus allowing the side-chain of Arg378 to stabilize the reduced isoalloxazine moiety (Fig. 4B). In this case, the buckling angles within the protein matrix are smaller than in solution, suggesting that the photolyase enforces the cofactor toward the oxidized form, most likely to prime it for light-driven forward electron transfer during DNA repair.

By way of these subtle changes, the active site of a photolyases is capable of not only accommodating different flavin redox species, but also optimizing the site for its different enzymatic activities. By the very nature of the SFX technique, we were able to observe dynamics and conformational changes which are inaccessible to traditional protein crystallography methods, including the buckling angles of the bound FAD cofactor and the conformational change of Asn403 at each state. Most crucially, the results suggest that the

Arg378-Asp409 pair, which is fully conserved within the PCF, but its function has never been reported before, plays a central role in the mechanism of DNA photolyases as an electrostatic gate which senses and reacts to the overall redox status and geometry of the cofactor, thus tuning the catalytic activities of photolyases. We propose that this is a common mechanism for light-driven DNA repair by photolyases and for signalling by cryptochromes, and it remains to be seen whether neutral Arg-Asp pairs may also play crucial mechanistic roles in other biological systems.

References and Notes:

1. D. Sorigué et al., An algal photoenzyme converts fatty acids to hydrocarbons. Science. 357, 903–907 (2017).
2. S. Franz et al., Structure of the bifunctional cryptochrome aCRY from Chlamydomonas reinhardtii. Nucleic Acids Res. 46, 8010–8022 (2018).
3. J. I. Lucas-Lledo, M. Lynch, Evolution of Mutation Rates: Phylogenomic Analysis of the Photolyase/Cryptochrome Family. Mol. Biol. Evol. 26, 1143–1153 (2009).
4. I. Chaves et al., The Cryptochromes: Blue Light Photoreceptors in Plants and Animals. Annu. Rev. Plant Biol. 62, 335–364 (2011).
5. S. Kiontke et al., Crystal structures of an archaeal class II DNA photolyase and its complex with UV-damaged duplex DNA. EMBO J. 30, 4437–49 (2011).
6. A. Mees et al., Crystal structure of a photolyase bound to a CPD-like DNA lesion after in situ repair. Science. 306, 1789–93 (2004).
7. M. J. Maul et al., Crystal structure and mechanism of a DNA (6-4) photolyase. Angew. Chem. Int. Ed. Engl. 47, 10076–80 (2008).
8. Y.-T. Kao et al., Ultrafast Dynamics of Flavins in Five Redox States. J. Am. Chem. Soc. 130, 13132–13139 (2008).
9. B. Liu, H. Liu, D. Zhong, C. Lin, Searching for a photocycle of the cryptochrome photoreceptors. Curr. Opin. Plant Biol. 13, 578–586 (2010).
10. D. Nohr et al., Extended Electron-Transfer in Animal Cryptochromes Mediated by a Tetrad of Aromatic Amino Acids. Biophys. J. 111, 301–311 (2016).
11. C. Aubert, M. H. Vos, P. Mathis, a P. Eker, K. Brettel, Intraprotein radical transfer during photoactivation of DNA photolyase. Nature. 405, 586–590 (2000).
12. S. Oldemeyer et al., Essential Role of an Unusually Long-lived Tyrosyl Radical in the Response to Red Light of the Animal-like Cryptochrome aCRY. J. Biol. Chem. 291, 14062–14071 (2016).
13. Z. Liu et al., Determining complete electron flow in the cofactor photoreduction of oxidized photolyase. Proc. Natl. Acad. Sci. 110, 12966–12971 (2013).
14. Y.-T. Kao et al., Ultrafast Dynamics and Anionic Active States of the Flavin Cofactor in Cryptochrome and Photolyase. J. Am. Chem. Soc. 130, 7695–7701 (2008).
15. Y.-J. Z. and, R. L. Ornstein*, A Theoretical Study of the Structures of Flavin in Different Oxidation and Protonation States (1996), doi:10.1021/JA9608151.
16. D. A. Dixon, D. L. Lindner, B. Branchaud, W. N. Lipscomb, Conformations and Electronic Structures of Oxidized and Reduced Isoalloxazine1" Biochemistry. 18, 5770–5 (1979).
17. J. Hahn, M.-E. Michel-Beyerle, N. Rösch, Conformation of the Flavin Adenine Dinucleotide Cofactor FAD in DNA-Photolyase: A Molecular Dynamics Study. J. Mol. Model. 4, 73–82 (1998).
18. Å. K. Røhr, H.-P. Hersleth, K. K. Andersson, Tracking Flavin Conformations in Protein Crystal Structures with Raman Spectroscopy and QM/MM Calculations. Angew. Chemie Int. Ed. 49, 2324–2327 (2010).

19. R. Kort, H. Komori, S. Adachi, K. Miki, A. Eker, DNA apophotolyase from Anacystis nidulans : 1.8 Å structure, 8-HDF reconstitution and X-ray-induced FAD reduction. Acta Crystallogr. Sect. D Biol. Crystallogr. 60, 1205–1213 (2004).
20. H. W. Park, S. T. Kim, A. Sancar, J. Deisenhofer, Crystal structure of DNA photolyase from Escherichia coli. Science (80-.). 268, 1866–1872 (1995).
21. Å. K. Røhr, H.-P. Hersleth, K. K. Andersson, Tracking Flavin Conformations in Protein Crystal Structures with Raman Spectroscopy and QM/MM Calculations. Angew. Chemie Int. Ed. 49, 2324–2327 (2010).
22. M. A. Rould, C. W. Carter, Isomorphous Difference Methods. Methods Enzymol. 374, 145–163 (2003).
23. K. Brettel, M. Byrdin, Reaction mechanisms of DNA photolyase. Curr. Opin. Struct. Biol. 20, 693–701 (2010).
24. R. Kort, H. Komori, S. Adachi, K. Miki, A. Eker, DNA apophotolyase from Anacystis nidulans: 1.8 A structure, 8-HDF reconstitution and X-ray-induced FAD reduction. Acta Crystallogr. D. Biol. Crystallogr. 60, 1205–13 (2004).
25. P. Müller, K. Brettel, L. Grama, M. Nyitrai, A. Lukacs, Photochemistry of Wild-Type and N378D Mutant E. coli DNA Photolyase with Oxidized FAD Cofactor Studied by Transient Absorption Spectroscopy. ChemPhysChem. 17, 1329–1340 (2016).
26. I. M. M. Wijaya, T. Domratcheva, T. Iwata, E. D. Getzoff, H. Kandori, Single Hydrogen Bond Donation from Flavin N 5 to Proximal Asparagine Ensures FAD Reduction in DNA Photolyase. J. Am. Chem. Soc. 138, 4368–4376 (2016).
27. S. Kiontke, P. Gnau, R. Haselsberger, A. Batschauer, L.-O. Essen, Structural and evolutionary aspects of antenna chromophore usage by class II photolyases. J. Biol. Chem. 289, 19659–69 (2014).
28. J. B. Mitchell, J. M. Thornton, J. Singh, S. L. Price, Towards an understanding of the arginine-aspartate interaction. J. Mol. Biol. 226, 251–62 (1992).
29. Y. Feng, L. Liu, T.-W. Mu, Q.-X. Guo, Influence of a Hydrophobic Environment on the Structure of Arginine-Carboxylate Salt Bridge. Chinese J. Chem. 20, 958–962 (2010).
30. Ryan R. Julian, and J. L. Beauchamp, W. A. G. III*, Cooperative Salt Bridge Stabilization of Gas-Phase Zwitterions in Neutral Arginine Clusters (2001), doi:10.1021/JP013205I.
31. Justin J. Hasford, and William Kemnitzer, C. J. Rizzo*, Conformational Effects on Flavin Redox Chemistry (1997), doi:10.1021/JO9703865.
32. M. Sugahara et al., Grease matrix as a versatile carrier of proteins for serial crystallography. Nat. Methods. 12, 61–63 (2014).
33. K. Tono et al., Diverse application platform for hard X-ray diffraction in SACLA (DAPHNIS): application to serial protein crystallography using an X-ray free-electron laser. 22 (2015), doi:10.1107/S1600577515004464.
34. D. von Stetten et al., In crystallo optical spectroscopy (ic OS) as a complementary tool on the macromolecular crystallography beamlines of the ESRF. Acta Crystallogr. Sect. D Biol. Crystallogr. 71, 15–26 (2015).
35. M. Kondoh et al., Light-Induced Conformational Change and Product Release in DNA Repair by (6−4) Photolyase. J. Am. Chem. Soc. 133, 2183–2191 (2011).
36. T. Nakane et al., Data processing pipeline for serial femtosecond crystallography at SACLA. J. Appl. Crystallogr. 49, 1035–1041 (2016).
37. T. A. White et al., CrystFEL : a software suite for snapshot serial crystallography. J. Appl. Crystallogr. 45, 335–341 (2012).
38. U. K. Genick et al., Science (80-.)., in press (available at http://science.sciencemag.org/content/275/5305/1471.abstract).
39. A. McCoy et al., Phaser Crystallographic Software. J. Appl. Crystallogr. 40, 658–674 (2007).
40. The CCP4 suite: programs for protein crystallography. Acta Crystallogr D Biol Crystallogr. 50, 760–763 (1994).
41. M. D. Winn et al., Overview of the CCP4 suite and current developments. Acta Crystallogr. D. Biol. Crystallogr. 67, 235–42 (2011).
42. G. N. Murshudov et al., REFMAC5 for the refinement of macromolecular crystal structures. Acta Crystallogr. D. Biol. Crystallogr. 67, 355–67 (2011).

43. P. Emsley, B. Lohkamp, W. G. Scott, K. Cowtan, Features and development of Coot. Acta Crystallogr D Biol Crystallogr. 66, 486–501 (2010).
44. P. D. Adams et al., PHENIX : a comprehensive Python-based system for macromolecular structure solution. Acta Crystallogr. Sect. D Biol. Crystallogr. 66, 213–221 (2010).
45. P. V. Afonine et al., Towards automated crystallographic structure refinement with phenix.refine. Acta Crystallogr. Sect. D Biol. Crystallogr. 68, 352–367 (2012).
46. D. M. Y. and P. A. K. D.A. Case, D.S. Cerutti, T.E. Cheatham, III, T.A. Darden, R.E. Duke, T.J. Giese, H. Gohlke, A.W. Goetz, D. Greene, N. Homeyer, S. Izadi, A. Kovalenko, T.S. Lee, S. LeGrand, P. Li, C. Lin, J. Liu, T. Luchko, R. Luo, D. Mermelstein, K.M. Merz, G. Monard, H., Amber 2017 (2017).
47. J. A. Maier et al., ff14SB: Improving the Accuracy of Protein Side Chain and Backbone Parameters from ff99SB. J. Chem. Theory Comput. 11, 3696–3713 (2015).
48. J. Wang, R. M. Wolf, J. W. Caldwell, P. A. Kollman, D. A. Case, Development and testing of a general amber force field. J. Comput. Chem. 25, 1157–74 (2004).
49. C. Mller, M. S. PLEsSET, “Note on an Approximation Treatment for Many-Electron Systems” (1934), (available at https://journals.aps.org/pr/pdf/10.1103/PhysRev.46.618).
50. T. V Russo, R. L. Martin, P. J. Hay, Effective Core Potentials for DFT Calculations. J. Phys. Chem. 99, 17085–17087 (1995).
51. W. L. Jorgensen, J. Chandrasekhar, J. D. Madura, R. W. Impey, M. L. Klein, Comparison of simple potential functions for simulating liquid water. J. Chem. Phys. 79, 926–935 (1983).
52. P. Li, K. M. Merz, Taking into Account the Ion-induced Dipole Interaction in the Nonbonded Model of Ions. J. Chem. Theory Comput. 10, 289–297 (2014).
53. S. Miyamoto, P. A. Kollman, Settle: An analytical version of the SHAKE and RATTLE algorithm for rigid water models. J. Comput. Chem. 13, 952–962 (1992).
54. U. Essmann et al., A smooth particle mesh Ewald method. J. Chem. Phys. 103, 8577–8593 (1995).
55. D. R. Roe, T. E. Cheatham III, PTRAJ and CPPTRAJ: software for processing and analysis of molecular synamics trajectory data. J Chem Theory Com. 9, 3084–3095 (2013).
56. W. Delano, The PyMOL molecular graphics system (2008).
57. J. W. Pitera, M. Falta, W. F. van Gunsteren, Dielectric Properties of Proteins from Simulation: The Effects of Solvent, Ligands, pH, and Temperature. Biophys. J. 80, 2546–2555 (2001).

Acknowledgments:

We would like to thank Tzu-Chun Hsiao, and Miu-lun Wu for their assistance in sample preparation. We are also grateful to Yuhei Hosokawa, Tomoyuki Tanaka, Toshi Arima, Yoshinori Matsuura, Hisashi Naitow, Naoki Kunishima, Tetsukon Kin, and the members of Engineering Support Team of SACLA for help during our X-ray experiments, as well as to Takanori Nakane for his introduction to CrystFEL. We thank all staff members of the TPS05A beamline, NSRRC, a national user facility supported by MOST, ROC, and in particular Chien-Chang Tseng and Chung-Kuang Chou for their help in setting up non-standard conditions for crystal testing. Also, Hui-Lin Shr (Crystallization Facility of the Institute of Biological Chemistry, Academia Sinica) provided the location for crystallization under non-standard conditions. We would also like to thank Antoine Royant and Guillaume Gotthard for their assistance in acquiring the redox-dependent *in crystallo* spectra at the ID29S Cryobench

laboratory, ESRF, France. Finally, we would like to thank Mr. Alvaro Maestre Reyna for his help in setting up the necessary scripts and macros for calculating extrapolated structure factors.

Funding:

The project was supported by Academia Sinica and the Taiwan Protein Project funded by MOST (Grant No. AS-KPQ-105-TPP). This work was also supported in part by JSPS KAKENHI (16K01942) and Air Force Office of Scientific Research (AFOSR; Grant No. FA9550-14-1-0409). The XFEL experiments were performed at the BL2 of SACLA with the approval of the Japan Synchrotron Radiation Research Institute (JASRI) (Proposal No. 2017A8019, 2017B8052, 2018A8008).

Author contributions:

MMR, SI, LOE, YB, and MDT conceived the research and designed experiments. MMR, EN, YJ, SK, LOE, YB, and MDT analyzed the data. MMR and CHY performed MD simulations and analyzed them. MMR, WCH, EN, EPGNP, SF, WJW, HYW, PHW, JHL, CCL, KFH, YKC, JHW, MS, SO, RT, KT, JY, YB, and LOE performed experiments. MMR, LOE, YB, and MDT wrote the manuscript.

Competing interests: The authors declare no conflict of financial interest.

Data and materials availability: Structural models, along with structure factors presented here can be found under PDB accession codes 6IWX, 6IX0, and 6IWZ.

Supplementary Materials:

Materials and methods

Figures S1-S6

Tables S1-S5

References (32-57)

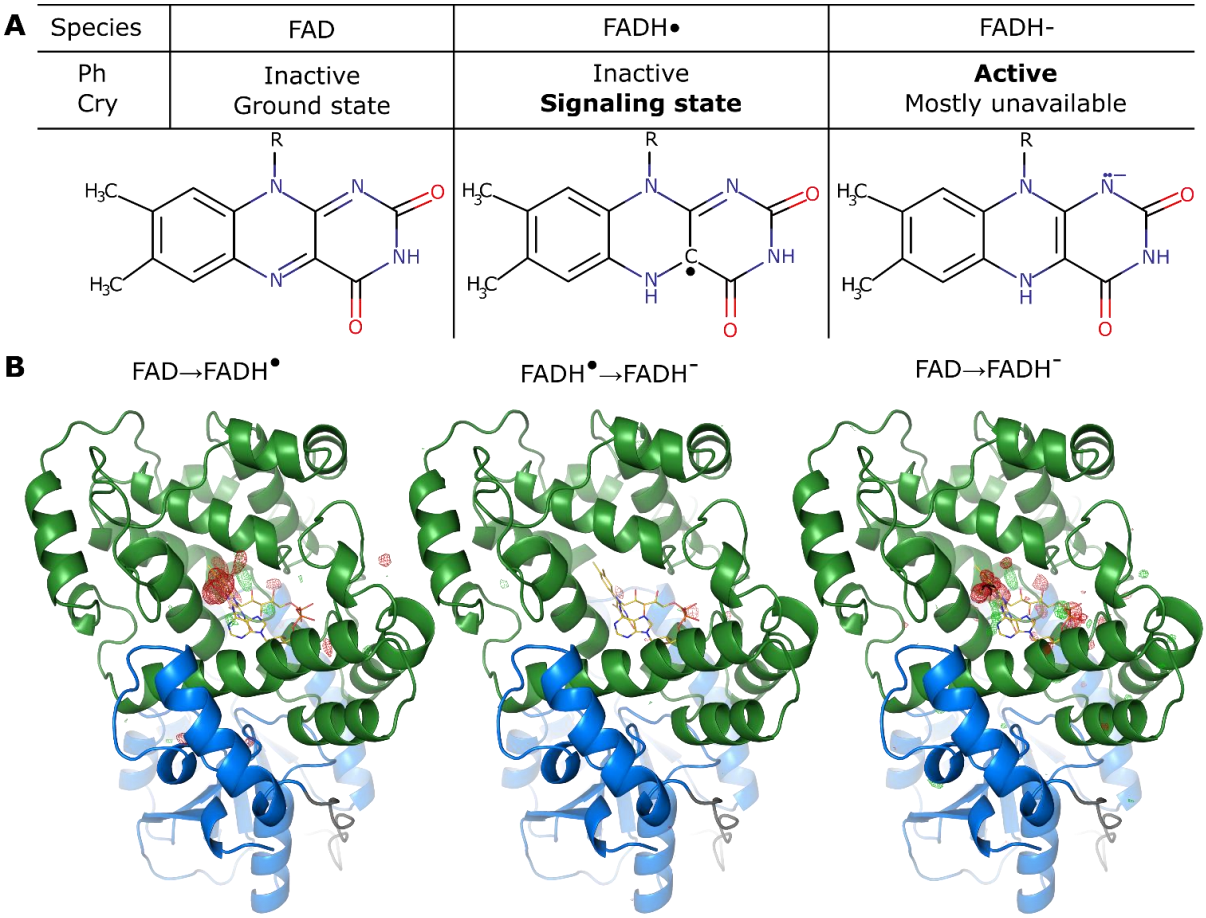

Fig. 1. The three redox states of photolyases. (A) The tricyclic isoalloxazine moiety that is part of flavin-based cofactors is capable of accommodating three redox states in PCF members: oxidized (FAD, left), reduced by a single electron (semiquinone, $FADH^{\bullet}$, middle), and fully reduced by two electrons (hydroquinone, $FADH^{-}$, right). The function of each of these states in photolyases (Ph) and cryptochromes (Cry) is highlighted. (B) Overall structures of the oxidized (left), semiquinone (middle), and fully reduced hydroquinone (right) states of *Mm*CPDII. The N-terminal domain is depicted in blue, the catalytic C-terminal domain in green, and the DTT ligand in black. The $IDEDM_{OS}$ corresponding to the $FAD \rightarrow FADH^{\bullet}$ transition is superposed to the oxidized structure (left), $IDEDM_{SH}$ to the semiquinone structure (middle), and $IDEDM_{OH}$ to the hydroquinone structure (right). Positive and negative difference electron densities (green and red, respectively; contouring level: 4 σ) are almost exclusively located in the binding site of FAD (gold).

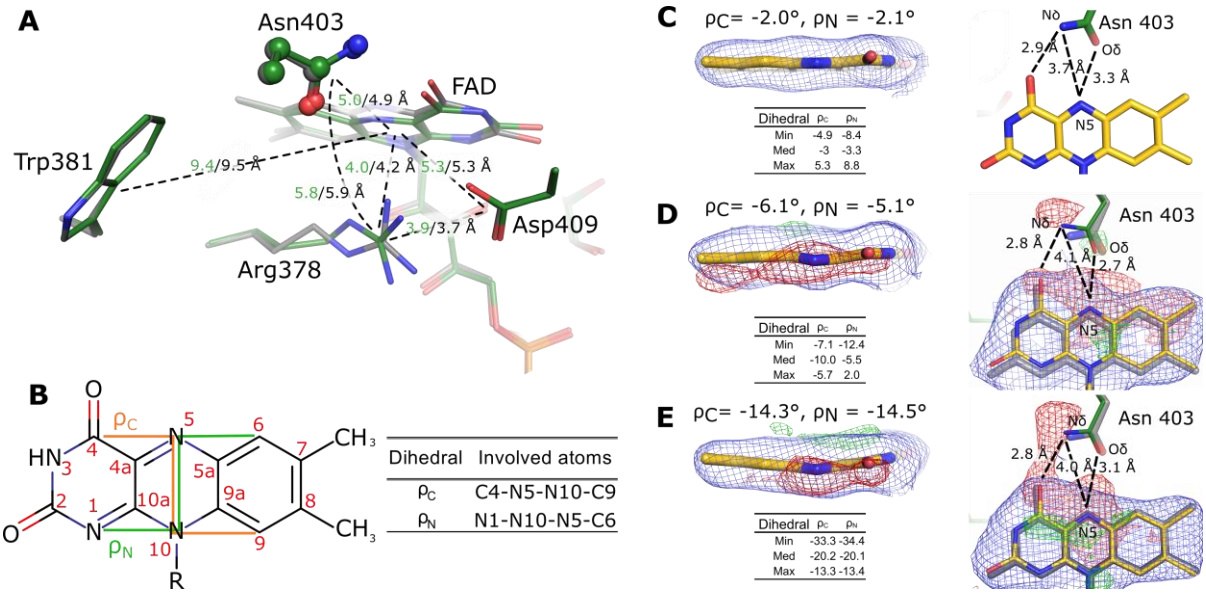

Fig. 2. Redox-dependent conformational changes in the FAD binding site of the *Mm*CPDII photolyase. (A) Stereo view of the superimposed active site structures of *Mm*CPDII in the oxidized (grey) and hydroquinone state (green). Center-of-mass distances between the different elements of the site are highlighted by dotted lines. (B) Definition of dihedral angles ρ_C and ρ_N for describing redox-dependent changes of FAD including its atom nomenclature. ρ_C (orange) and ρ_N (green) values reflect the degree of buckling and twisting within the flavin's isoalloxazine ring. In case of pure butterfly-like buckling, ρ_C equals ρ_N; unequal values of ρ_C and ρ_N indicate twisting of the isoalloxazine moiety. Negative ρ values indicate buckling towards the conserved Arg378-Asp409 pair, while positive values towards the hydrophobic surface of the α16 helix of *Mm*CPDII. (C-E) DF-SFX shows prominent differences for the isoalloxazine moieties of the FAD cofactor as indicated by its ρ_C and ρ_N values in the oxidized (C), semiquinone (D), and hydroquinone (E) states (left panels), including a swivelling motion of the sidechain of Asn403 (right panel). Structures (stick representation) are surrounded by composite omit maps (blue; contouring level: 1σ) and their corresponding IDEDM (green: positive, red: negative peaks; contouring level: 4σ). The ranges of ρ_C and ρ_N values, as derived from MD simulation (table inlays showing minimum, maximum and median values) correlate very well with experimental SFX data for the oxidized and semiquinone data. Under the assumption of a closed electrostatic gate, i. e. salt bridge character of the Arg378-Asp409 pair, the simulation for the $FADH^-$ state produces an over-buckled isoalloxazine moiety, which can be corrected by opening the gate (see Fig. 3).

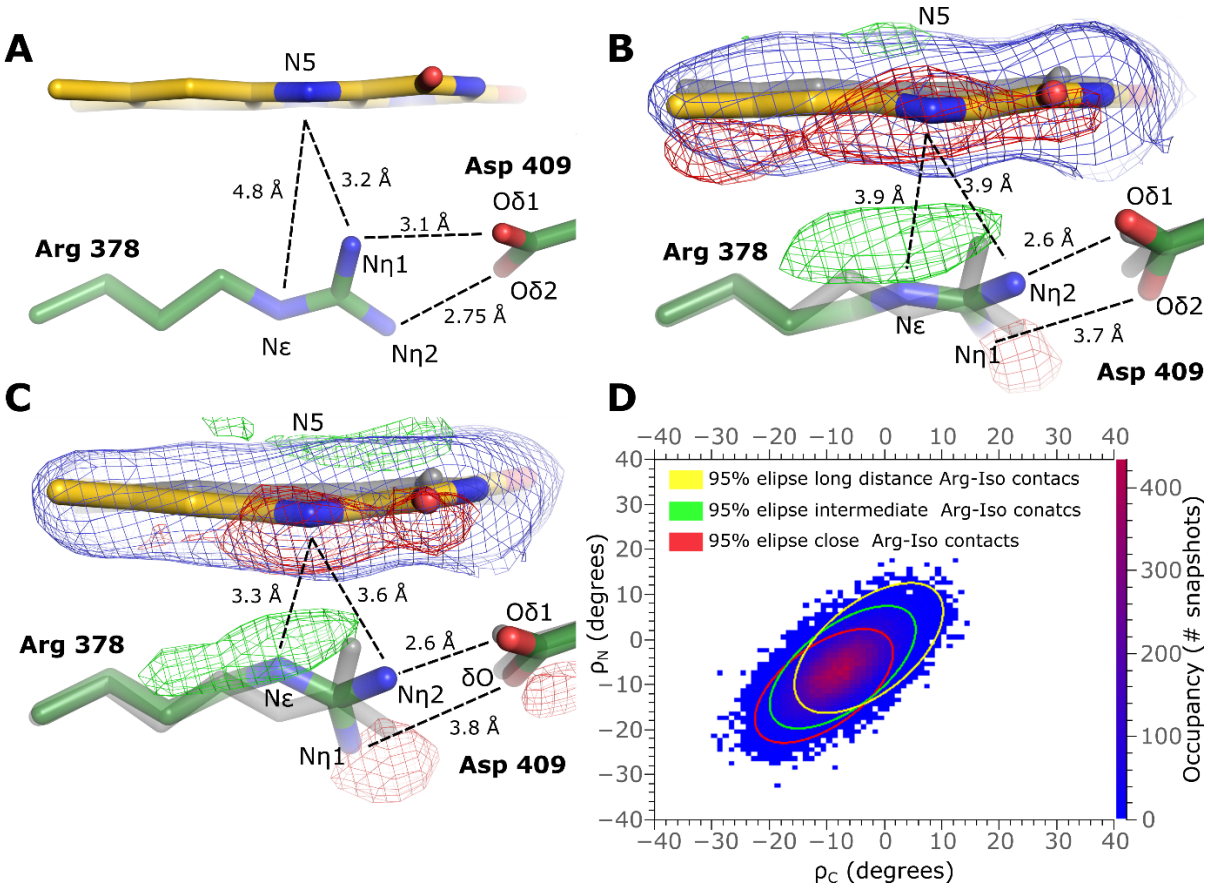

Fig. 3. The redox-dependent interactions between the electrostatic gate formed by the Arg378-Asp409 pair and the FAD isoalloxazine. (A-C) Close-up view of the isoalloxazine group (gold), Arg378 and Asp409 (green) interaction network in the *Mm*CPDII SFX structures in the oxidized (A), the semiquinone (B) and the hydroquinone (C) states. For comparison, (B) and (C) show the conformation of the oxidized *Mm*CPDII structure (grey) as well; the composite omit and IDEDM maps are depicted as in Fig. 2. (D) Correlation between isoalloxazine buckling and isoalloxazine-Arg378 interactions in the hydroquinone MD simulation assuming a neutral Arg378-Asp409 pair. In the 2D heat plot, a histogram of the available buckling conformational space for the simulation is shown (low occupancy in blue, highest occupancy in red). 95% confidence ellipses delineating the presence of close (less than 3.2 Å, red), intermediate (between 3.2 and 4 Å, green), and relaxed (more than 4 Å, yellow) isoalloxazine-Arg378 interactions reveal correlations between the strength of interaction, and the degree of buckling in the isoalloxazine ring. For comparison with oxidized and semiquinone state trajectories, as well as for the hydroquinone state, where a salt bridge is imposed instead for the Arg378-Asp409 pair, refer to Fig. S3B-D.

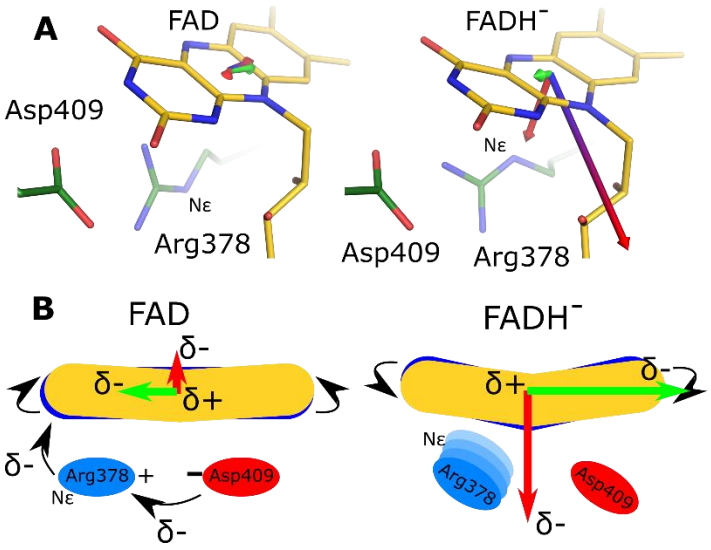

Fig. 4. The isoalloxazine-electrostatic gate feedback loop. (A) Detail of the isoalloxazine moiety and the electrostatic gate in the oxidized (left) and fully reduced (right) states. The isoalloxazine dipole moment is shown for both states as a blue (δ+) to red (δ-) gradient arrow. The dipole moment was decomposed into a component normal to the isoalloxazine plane (red arrow) and a coplanar component that is collinear to the electrostatic gate formed by Arg378-Asp409 (green arrow). Vectors in the oxidized state are shown in a 1:10 scale, while in the fully reduced in a 1:100 scale. (B) Schematic view of the isoalloxazine (yellow for the observed conformation, dark blue for assuming a Arg378-Asp409 salt bridge) and electrostatic gate (blue and red) interactions. In the oxidized state (left) the weak dipole moment, as well as the direction of its principal components (green and red arrows) facilitate a double H-bonded salt bridge between the charged Arg378 and Asp409. In the reduced state (right) the highly increased dipole moment is reversed. Accordingly, the end-on salt bridge is disfavored, causing Arg378 to swivel under proton transfer to form a neutral Arg378-Asp409 pair and interacting now in a side-on fashion with the isoalloxazine moiety. Accordingly, the observed buckling is less than expected in the presence of a charged Arg378-Asp409 pair (yellow vs. blue).

Table 1. Redox-dependent parameters for *Mm*CPDII and its flavin co-factor in the different structures and simulations performed in this work.

		Oxidized (FAD)		Semiquinone ($FADH^{\bullet}$)		Hydroquinone ($FADH^{-}$)	
		DF-SFX	MD	DF-SFX	MD	DF-SFX	MD
Distances (Å)	**Arg378 – Isoalloxazine**						
	Guanidinium-Isoalloxazine	4.2	3.7±0.2	4.2	4.2±0.2	4.0	4.8±0.3
	Nε-N5	4.8	3.7±0.2	3.9	4.6±0.2	3.3	3.5±0.2
	Nη proximal-N5	3.2	3.2±0.2	3.9	3.4±0.2	3.6	3.8±0.3
	Asn403-Isoalloxazine						
	Oδ-N5	3.3	4.1±0.3	2.7	5.8±0.3	3.1	7.5±0.6
	Nδ-N5	3.7	4.2±0.3	4.1	3.9±0.2	4.0	5.8±0.5
	Nδ-O4	2.9	3.0±0.2	2.8	2.9± 0.2	2.8	5.4±0.6
	Arg378-Asp409						
	Nη proximal - Oδ proximal	3.1	2.8±0.1	2.6	3.0±0.2	2.6	5.3±0.8
	Nη distal - Oδ distal	2.8	2.9±0.2	3.7	3.9±0.5	3.8	6.7±1.2
Dihedral angle (degrees)	ρ_C	-2.0°	-1.7±1.5°	-6.1°	-6.6±1.7°	-14.3°	-12.8±2.4°
	ρ_C MAR restraint	-1.5±4.0°	NA	-3.6±5.9°	NA	-14.3±6.3°	NA
	ρ_N	-2.1°	-2.7±1.5°	-5.1°	-5.3±1.6°	-14.5°	-12.3±2.5°
	ρ_N MAR restraint	-1.8±4.4°	NA	-5.6±6.34°	NA	-17.3±3.8°	NA

Science
AAAS

Supplementary Materials for

An arginine-aspartate electrostatic gate tunes the photolyase flavin chromophore

Manuel Maestre-Reyna, Cheng-Han Yang, Wei-Cheng Huang, Eriko Nango, Eka Putra Gusti Ngurah Putu, Sophie Franz-Badur, Wen-Jin Wu, Hsiang-Yi Wu, Po-Hsun Wang, Jiahn-Haur Liao, Cheng-Chung Lee, Kai-Fa Huang, Yao-Kai Chang, Jui-Hung Weng, Michihiro Sugahara, Shigeki Owada, Yasumasa Joti, Rie Tanaka, Kensuke Tono, Stephan Kiontke, Junpei Yamamoto, So Iwata, Lars-Oliver Essen*, Yoshitaka Bessho*, Ming-Daw Tsai*

*Correspondence to: mdtsai@gate.sinica.edu.tw ; bessho@sinica.edu.tw ; essen@chemie.uni-marburg.de

This PDF file includes:

Materials and Methods

Protein production and purification

Protein production and purification followed established guidelines (5). Briefly, *Escherichia coli* BL21(DE3) was transformed with a pET-28-based construct containing the *Mm*CPDII gene (Genbank ID AAM30548.1). Protein was produced via autoinduction in TB medium at 25 °C, with yields above 100 mg of protein per liter of culture. Cell pellets were resuspended in buffer (50 mM Phosphate buffer pH 8.0, 300 mM NaCl), and lysed. After removal of cell debris via a second centrifugation step, the supernatant was loaded into a self-packed 10 mL Nickel-NTA column, with protein eluted via addition of 250 mM imidazole to the running buffer. As a final polishing step, the protein was loaded onto a size exclusion chromatography column containing Superdex 200 material (GE life sciences) equilibrated with gel filtration buffer (10 mM Tris/Hcl pH 8.0, 100 mM NaCl).

Site directed mutagenesis

The *Mm*CPDII R378K mutant was constructed by using the above mentioned construct as a template and a forward primer with sequence 5'- GCACGGTTACACG AAG ATGTACTGGGC-3' and its complementary sequence as the reverse primer. Production and purification of the mutant took place as above.

In solution photoreduction

*Mm*CPDII wild type and its R378K counterpart were photoreduced by mixing a 10 mg/mL protein solution in gel filtration buffer with a 50 mM DTT solution in a 1:1 ratio. Samples were then exposed to a bright white light source for 30 minutes (Leica KD300), and centrifuged for 3 minutes at 18000 g. UV/Vis spectra were then immediately taken in either a Nanodrop 1000 or a Nanodrop One C spectrophotometer (Thermo Scientific, Fig. S6B).

Obtaining free FAD spectra

Oxidized samples from the same stock as those used for photoreduction were boiled for 10 minutes at 99 °C, after which they were centrifuged for 3 minutes, 18000 g. Spectra were acquired as above (Fig. S6B).

Analytical gel filtration

Directly after preparative protein purification, both wild type and R378K samples were concentrated to 5 mg/mL. 10 µL of the concentrated protein sample was injected onto a 2.4 mL Superdex 200 Increase 3.2/300 analytical size exclusion chromatography column (GE Healthcare). The run was

then monitored at both 280 and 450 nm. 50 µL fractions were collected during the run, and further analysed by SDS-PAGE (Fig. S6A).

Protein crystallization and sample preparation

Protein crystals were obtained by optimizing previously published conditions (5)(54)(54)(54). Here, a 14 mg/mL *Mm*CPDII solution was mixed in a 1:1 ratio with a crystallization solution (0.5-0.65 M Li_2SO_4, 10-15% (W/V) PEG8000). 20 µL aliquots of the crystallization mix were pipetted in 96-well ultra-clear u-bottom polystyrene microplates (Basic Life) under 100 µL Al's oil (1:1 paraffin to silicone oil mix). The plates were then incubated at 4 °C for between 24 to 48 hours. Drops containing crystals smaller than 100 µm were finally harvested and concentrated by centrifugation at 6000 g for 6 minutes. For obtaining a fully oxidized dataset, the crystal slurry was then embedded in a hydrophobic grease matrix in a 1:9 crystal:matrix ratio, as described elsewhere (32). After this point, the sample was maintained under far red light (650 nm) at all times to avoid in-situ photoreduction.

For obtaining the semiquinone structure, the crystal slurry was concentrated again as above, and resuspended in a 1:1 crystallization solution: gel filtration buffer mix supplemented with 50 mM DTT. The crystal slurry was then exposed to bright white light (Leica KD300) for 5 minutes, and then to air for another 20 minutes, followed by embedding in grease matrix. After this point, the sample was maintained under far red light (650 nm) at all times to avoid further in situ photoreduction. Embedded crystals were loaded into an injector cartridge that was then mounted into a SACLA extruder device (33) tipped with a 150 µm nozzle.

The production and handling of fully photoreduced *Mm*CPDII crystals for determining the hydroquinone structure was analogous to the semiquinone ones. The crucial difference, however, was performing the entire photoreduction, embedding, etc. under anaerobic conditions within a vinyl anaerobic chamber (Coy Lab Products). Samples were transported to the SACLA hutch in air-tight injectors sealed with grease, which were stored in air-tight, opaque, containers.

In crystallo UV/Vis spectroscopy

In crystallo UV/Vis spectroscopy was performed at the cryobench, ID29S, ESRF, Grenoble, France (34). Here, crystals were treated as for DF-SFX experiments (see above) to photoreduce them into the different redox states (oxidized, semiquinone, hydroquinone). Crystal slurry samples were then frozen in liquid nitrogen under aerobic (oxidized and semiquinone states) and anaerobic conditions

(hydroquinone state), without the addition of any cryoprotectant. Samples were then directly mounted on the cryobench goniometer at 100 K under constant nitrogen gas flow. All data was acquired with a 100 µm focal point for the probing beam, while 200 µm for the detector optics. Individual acquisition times were 200 ms, with ten acquisitions being averaged per spectrum.

Additionally, single oxidized crystals were soaked in photoreduction buffer for one minute and mounted at room temperature under constant humidity (99%). By exposing these to bright white light for five minutes (Leica KD300), and taking spectra periodically afterwards, we determined oxidation kinetics, showing that the semiquinone state was stable under aerobic conditions for at least 2 hours.

Once all spectra had been collected, they were corrected for scattering. As the pathlength for any given spectrum is not known, only relative concentrations of each species were determined via their characteristic wavelengths and extinction coefficients (35). Equations 1 to 3 were used in this process, resulting in relative concentrations of >99.9% for the oxidized and hydroquinone states, while 66% for the semiquinone state.

$$A_{632nm} = E_{632nm,semi} * C_{semi} \quad \text{(eq. 1)}$$

$$A_{450nm} = E_{450nm,semi} * C_{semi} + E_{450nm,ox} * C_{ox} + E_{450nm,hydro} * C_{hydro} \quad \text{(eq. 2)}$$

$$A_{360nm} = E_{360nm,semi} * C_{semi} + E_{360nm,ox} * C_{ox} + E_{360nm,hydro} * C_{hydro} \quad \text{(eq. 3)}$$

A: absorbance

E: extinction coefficient

C: concentration

Data acquisition and on-site processing at the SACLA XFEL

Images were obtained at SACLA using a 30 Hz pulse frequency and 7 keV pulse strength. Camera length corresponded to 50 mm; extrusion speed was set to 1.59 µL/min. Hits vs. misses were identified via the on-site Cheetah pipeline (36), while on-site processing to determine dataset maximum resolution, completeness, redundancy and correlation coefficient was performed with CrystFEL (37).

Based on the estimates for redox species distribution as obtained before by *in crystallo* spectroscopy, which showed >99% enrichment for the oxidized and hydroquinone states, the corresponding datasets were used without further processing. However, as the semiquinone concentration was estimated at 66%, extrapolated structure factors (38) ($F_{ext,semi}$) with a weight factor of 1.5 were calculated according to previously described methods and equation 4.

$$F_{ext,semi}=W(|F_{semi}|-|F_{ox}|)+|F_{ox}| \qquad \text{(eq. 4)}$$

F: structure factor; W: weighting term, corresponding to the inverse of semiquinone occupancy

As, due to error propagation, the signal to noise (I/σ) ratio decreases dramatically during F_{ext} construction, an acceptance criterion of $I/\sigma \geq 1$ was employed as cut-off for the extrapolated structure factors. Accordingly, the resolution of the extrapolated semiquinone dataset was reduced from 2.2 to 2.7 Å in order to maintain a completeness of 98%.

As a quality control for the observed changes in the processed datasets, each individual dataset (oxidized, semiquinone, and hydroquinone) was randomly split into two, with each half being processed independently. The resulting structure factors were then employed to produce $|F_{obs1/2}|-|F_{obs2/2}|$ coefficients for calculation of IDEDMs (Fig. S2), which showed possible artefactual and noise difference electron density.

Structure solution and refinement

All datasets were solved via molecular replacement by Phaser (39), using the previously published *Mm*CPDII crystal structure as a search model (5) (PDB accession code 2XRY). Initial refinement took place with the CCP4 suite (40, 41) using refmac5 (42), and Coot (43). Additional refinement was performed with phenix (44). Data collection, processing and refinement details can be found in Table S1.

Multiple refinement approach to determine the optimal FAD isoalloxazine parameters

FAD geometry was optimized for each redox state by performing a series of refinements of *Mm*CPDII containing a mildly buckled FAD molecule (unrestrained $\rho_N = \rho_C = -10°$) via phenix.refine

(45), with different dihedral geometric restraints for modelling the deviation from planarity as given by ρ_C and ρ_N values. For maximum and minimum ρ_C and ρ_N values, the ρ_C and ρ_N extremes from the corresponding MD trajectory were chosen (Fig. 2, Fig. S3A and S4). After five refinement macrocycles, effective ρ_C and ρ_N values (ρ_{Ceff} and ρ_{Neff}) were individually determined in coot (43), as well as the maximum F_{obs}-F_{calc} σ contour level value in the immediate vicinity of the isoalloxazine ring (Fig. S4, Tables S2 to S4). A fit was considered *good*, and its ρ_{Ceff}/ρ_{Neff} pair was accepted, if its corresponding peak F_{obs}-F_{calc} σ contour level was equal or below 3.5. All *good* ρ_{Ceff}/ρ_{Neff} pairs for a given redox state were then averaged, and standard deviations calculated. These were then used to construct a cofactor library which closely mimicked the observed behavior for each dataset. Finally, data from good fits were used to determine 95% confidence interval covariance matrix ellipsoids (Fig. S3A) to compare with the ones derived from MD calculations (Fig. S3B-D and Fig. 3D).

Generating difference electron density maps

Isomorphous difference electron density maps (IDEDM) were calculated via the phenix tool of the same name using the multiscaling method.

Molecular dynamics simulations

All simulations were conducted using the Amber 16 package (46). Starting coordinates were taken from each of the refined X-ray structural models presented in this work. Simulations were based on the Amber ff14SB protein force field (47), and a set of GAFF (48) parameters was adopted for the description of FAD, $FADH^{\bullet}$ and $FADH^{-}$. The partial charges of the atoms were calculated by QM/MM optimization at the MP2 level (49) of theory. The 6-311G* basis sets were used on the organic atoms and an effective core potential (ECP) (50). The FAD Mulliken charges were added to the force field, and the residue Mulliken charges were based on the amino acid libraries in the Amber 16 package. In order to parameterize a neutral arginine residue, partial charges were calculated analogously, while other parameters were taken from the corresponding ff14SB entry for arginine. Periodic boundary conditions were imposed for solvent–solute systems of *Mm*CPDII in parallel piped boxes. The box lengths of each system, 98.3 × 83.6 × 80.1 $Å^3$, contained 455 amino acids with 16,000 TIP4P water molecules (51). The solvated systems held 102,000 atoms and were neutralized by addition of in appropriate number of Na^+ ions (52).

The initial protein structure was primarily constrained with a force constant (~50 kcal/mol) in the explicit water solvation box for at least 100,000 energy minimization steps, followed by cycles

of full structural relaxation, until the total system energy converged within 0.01 kcal/mol. The system then underwent a 60 ns annealing NPT ensemble with equilibrated steps from 0 K to 300 K under a constant pressure of 1.0 bar. A Langevin thermostat was used to maintain the system temperature by controlling the collision frequency at 1 ps^{-1}. As a result of optimization cycles, the box lengths converged, and the system density was stabilized at ~1.03 g/cm^3 with temperature varied within ± 3 K from the target temperature of 300 K. After the full optimization processes, 60 ns of production MD simulations were carried out in the canonical ensemble (NVT) ensemble with the heat bath of 300 K at a collision frequency in 1 ps^{-1} by using a Langevin thermostat to maintain the system temperature. The SHAKE algorithm (53) was implemented to constrain the covalent bond involving hydrogen atoms. Fourier-based Ewald summation utilized Fourier transforms to replace the summation of interaction energies in real space with an equivalent summation in Fourier space. The Smooth Particle Ewald method (54) was adapted to calculate the reciprocal sum. In our system, long-range electrostatic interactions are carried out using the smoothed particle mesh Ewald algorithm with a real space cut-off length of 10 Å. Numerical integration was performed with a time-step of 1 fs for all MD simulations.

Data analysis

Trajectories and structures were analysed either via cpptraj (55), pymol (56), or Coot (43). Data filtering was performed with cpptraj, while covariance analysis was performed via a Microsoft Excel macro. 2D binning and plotting of the corresponding heat maps was performed in qtiplot.

QM calculations

Initial structures for charge transfer calculations were taken either directly from the experimental structures, or from MD trajectory snapshots corresponding to maximum and minimal values of the short and long Arg-isoalloxazine distance covariance spheroids (Fig. S4). Each QM system included Arg378, Glu407, Asp409 and the isoalloxazine moiety. Amino and carboxy groups of each amino acid were neutralized by capping, while the isoalloxazine system was closed by a methyl group being bound to N10. The ESP charges of the atoms were calculated by QM/MM at the MP2/6-311G* level. *In vacuo* calculations were performed to account for the low protein core dielectric constant (~2), which is much more similar to the former (1) vs that of an ionic liquid (~80) (57). The total charge for the oxidized system is -1 and for the hydroquinone one is -2. Charge transfer difference (Δq) was calculated as the QM calculated ESP charge of the isoalloxazine system minus its expected charge (0

for the oxidized state, -1 for the hydroquinone state). Dipole moments for the isoalloxazine moiety in the oxidized and hydroquinone states were additionally calculated at the same level as above.

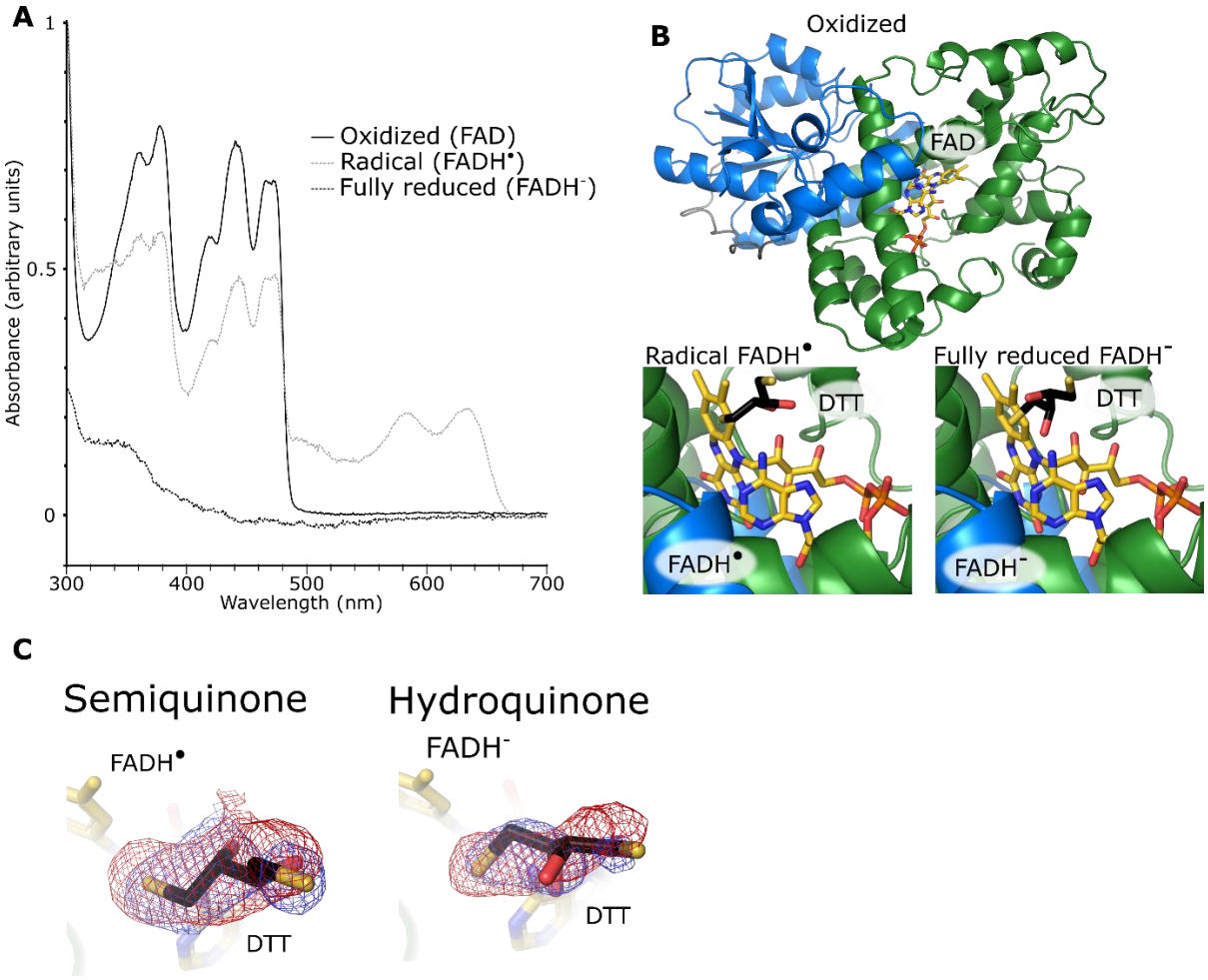

Fig. S1.

Properties of *Mm*CPDII crystals and structures at different states. (A) *In crystallo* spectra of the oxidized (dotted black line), semiquinone (grey dotted line), and hydroquinone (black line) state adopted by *Mm*CPDII crystals. Using supplementary equations 1-3, we estimated species occupancies for each state. (B) Overall structure of oxidized *Mm*CPDII (top), and details of the FAD binding site bound to DTT for the semiquinone and hydroquinone structures (bottom). The *Mm*CPDII N- and C-terminal domains are shown in blue and green, respectively, while the U-shaped FAD/ $FADH^{\bullet}$/ $FADH^{-}$ in yellow. The DTT carbons are shown in black. (C) Details of the bound DTT. The 1σ contoured composite omit map is shown in blue, and the corresponding $IDEDM_{OS}$ or $IDEDM_{OH}$ contoured to 4σ are rendered in red.

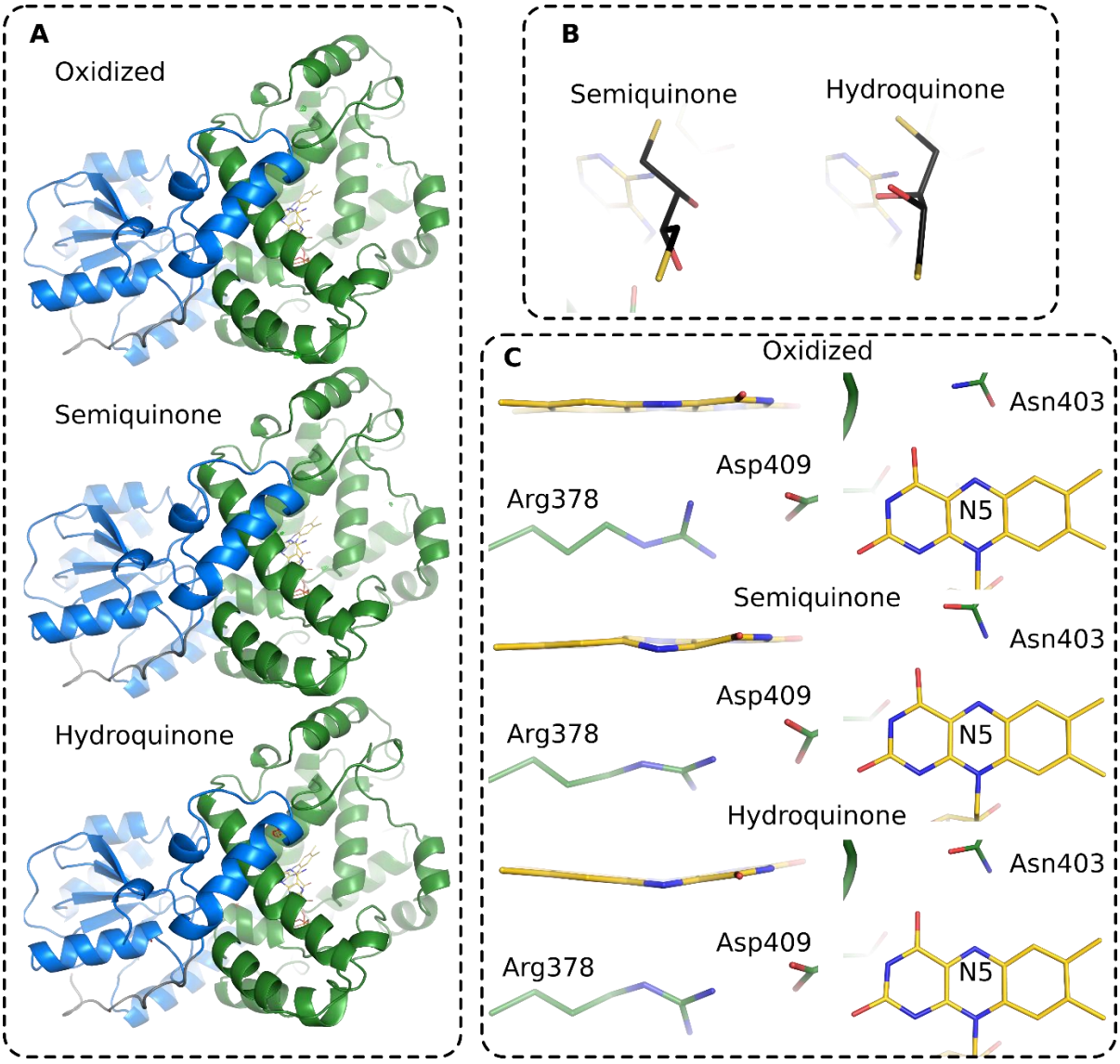

Fig. S2.

Control analysis of the SFX obtained datasets. Each of the datasets was randomly divided in half, then processed and solved independently. Next, $|F_{obs,1/2}|$-$|F_{obs,2/2}|$ maps were generated for each of them. Here, the corresponding IDEDMs are shown with a 4 σ-cut-off for (A) the full proteins, (B) the bound DTT for the semiquinone and hydroquinone datasets, and (C) the active site. As expected, only very few peaks, and all of them outside the active site, can be observed.

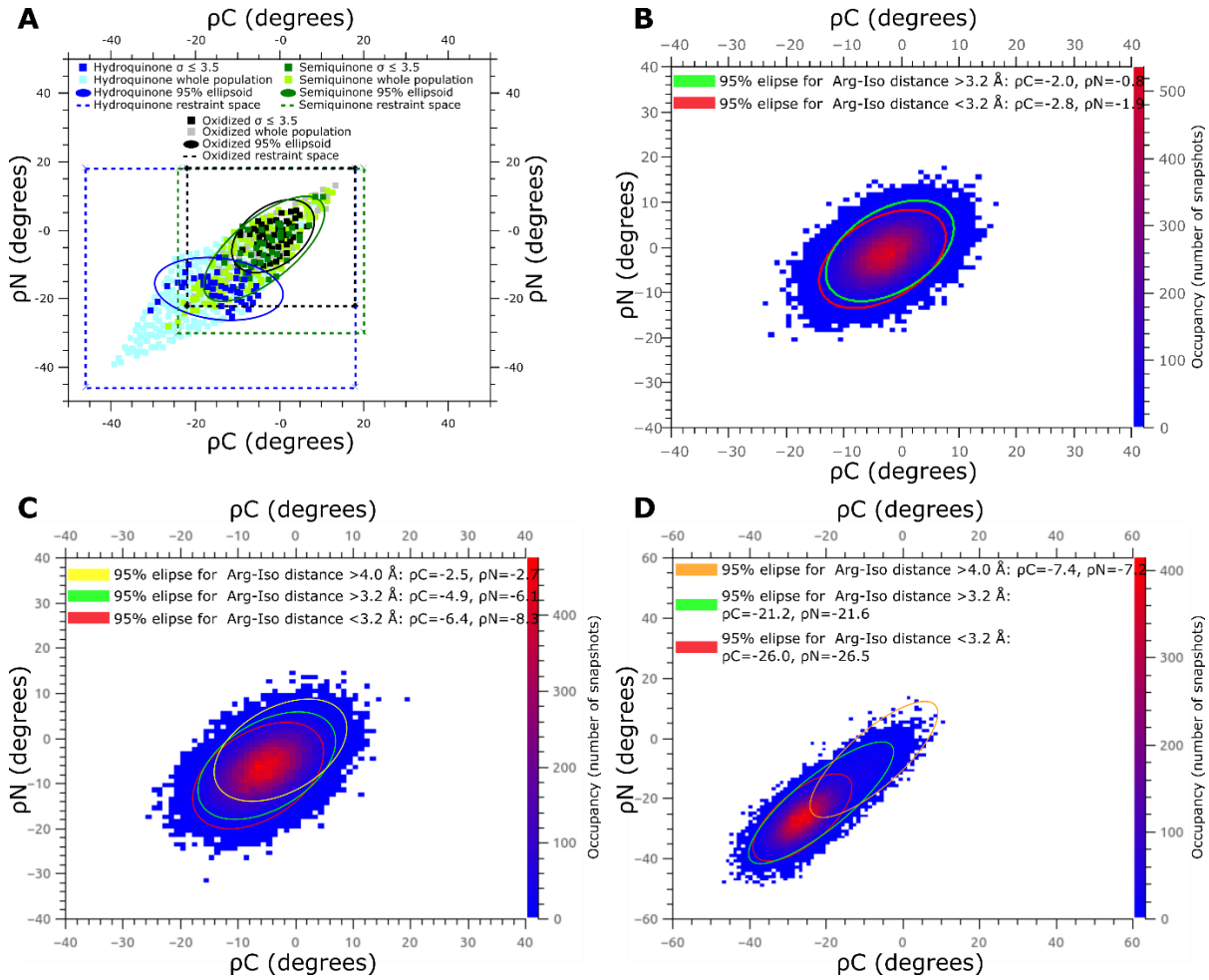

Fig. S3.

Redox-dependent behaviour of MRA and MD distributions. (A) Superposition of all three MRA processes (oxidized in shades of grey, semiquinone in shades of green, and hydroquinone in shades of blue). The overall restraint space is shown as a dotted square surrounding the actual data. Individual data points represent the actual ρ_N and ρ_C values obtained from the refined structures. Values corresponding to good fits (σ-peak below 3.5) are highlighted by a darker shade. Ellipsoids represent the 95% confidence interval (CI) region for the corresponding good fit. (B, C, and D) 2D ρ_N vs ρ_C heat maps for the initial MD simulations. Occupancy of each bin is shown in a blue (low occupancy) to red (high occupancy) scale. Correlation between buckling and interactions between the isoalloxazine central ring and Arg378 (arg-Iso distance) are highlighted by ellipsoids corresponding to 95% CI region in which snapshots presenting a given arg-Iso distance could be found. Overall the heat map was divided into three possible arg-Iso distances. Those indicating a strong interaction (below 3.2 Å, shown in red), those representative of a medium strength

interaction (between 3.2 Å and 4 Å, green), and those with a weak interaction (above 4 Å, yellow) (B) Oxidized state MD simulations. (C) Semiquinone state MD simulations. (D) Initial hydroquinone state MD simulations, where the Arg378-Asp409 was at full strength.

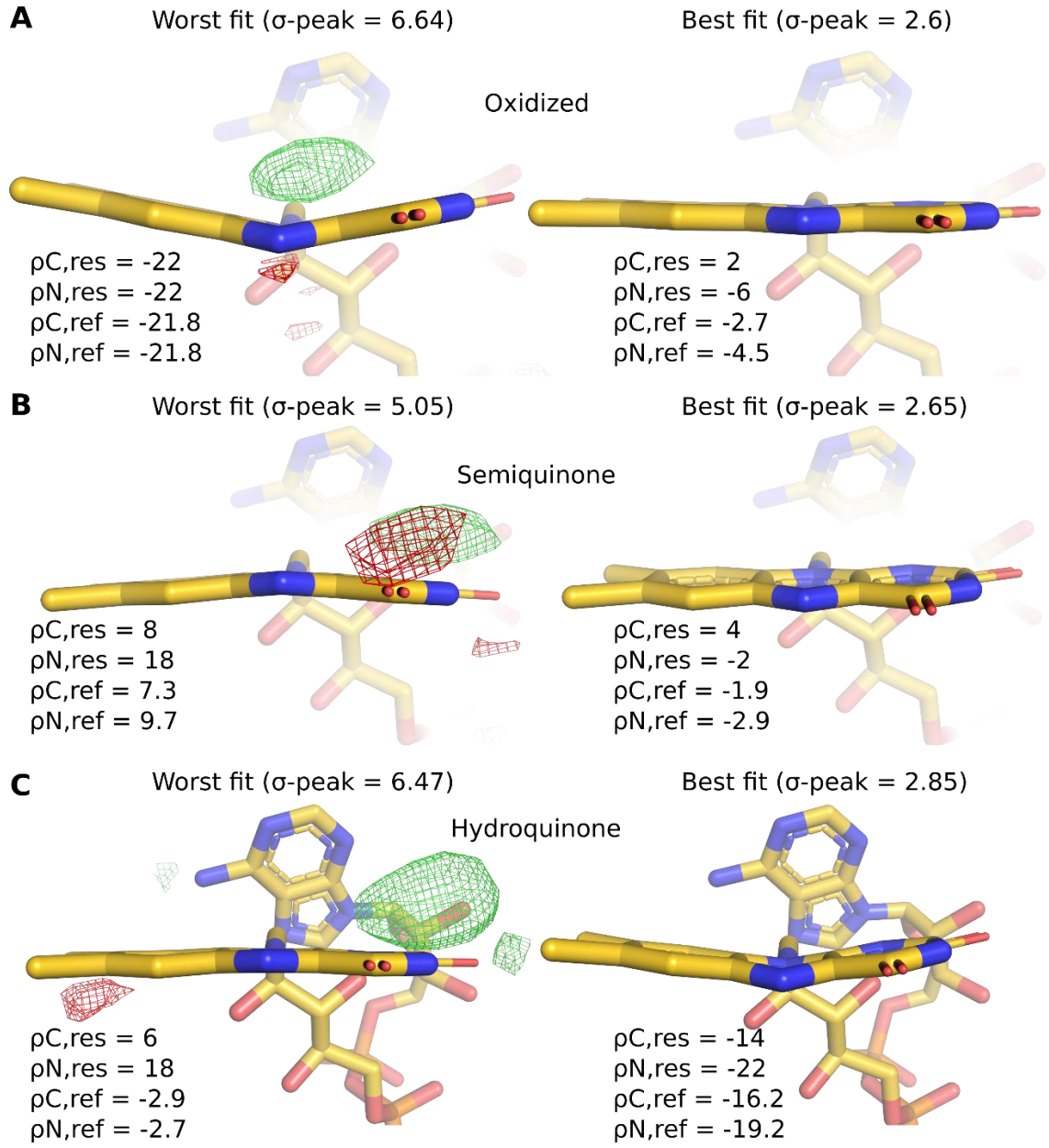

Fig. S4.

Multiple Refinement Approach for determining best isoalloxazine refinement restraints. (A), (B), and (C) show the worst (left) and best (right) fit for isoalloxazine moiety in the oxidized, semiquinone,

and hydroquinone states, respectively. A fit was considered bad, if there was at least one difference electron density peak with a σ magnitude of 3.5 or larger. These are shown for each of the representative structures at a 3.5 σ contour level, where applicable. Below each of the isoalloxazine structures, the applied dihedral restraints are shown ($\rho_{C,res}$ and $\rho_{N,res}$), as well as the dihedral angles resulting from refining with them ($\rho_{C,ref}$ and $\rho_{N,ref}$). The final restraints employed for the deposited structures were based on the average and standard deviation of the $\rho_{C,ref}$ and $\rho_{N,ref}$ values of all good fits for the corresponding redox state.

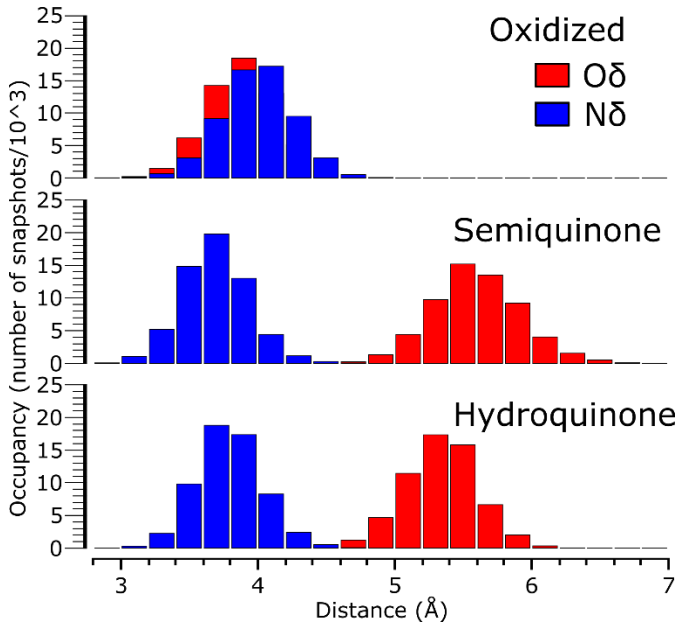

Fig. S5.

MD trajectory population analysis of the Asn403 Nδ- and Oδ-atoms towards the isoalloxazine N5 nitrogen.

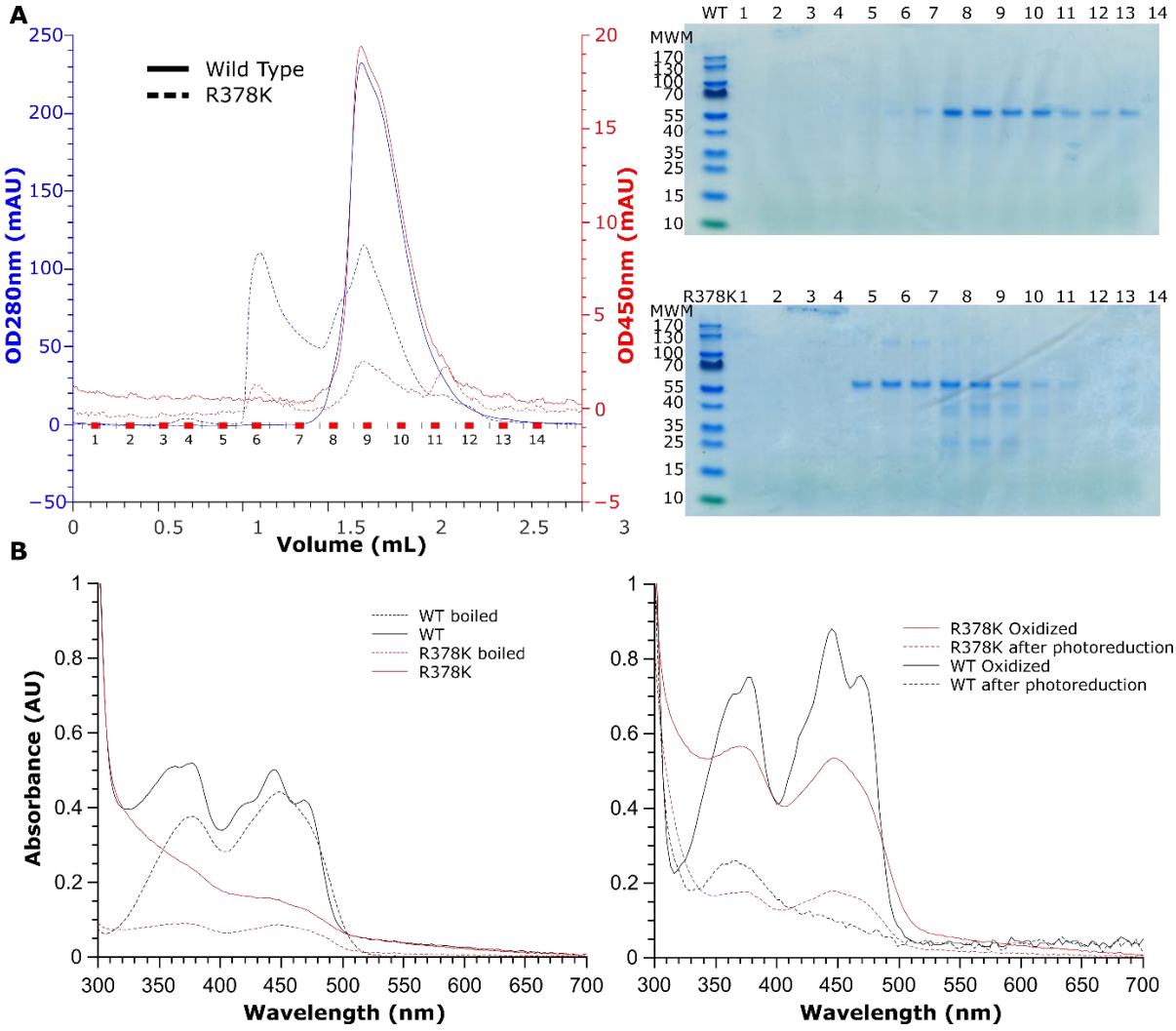

Fig. S6.

The R378K mutant of *Mm*CPDII. (A) Analytical size exclusion chromatography of wild type and R378K *Mm*CPDII (solid and dashed lines, respectively). The left panel shows a chromatogram, in which the main protein and FAD wavelengths (280 nm in blue, 450 nm in red, respectively) are shown. Note the difference in 280 nm vs 450 nm ratio between WT and R378K, which is indicative of low FAD content in the mutant. The right panel shows SDS-PAGE analyses for both the WT (top) and R378K mutant (bottom). For the wild type, only one major absorbance peak could be detected, which corresponds to the characteristic 55 kDa *Mm*CPDII band. Conversely, for the R378K mutant, one peak appeared in the column's exclusion volume (1 mL), while the second aligned well with WT. Here, the SDS-PAGE analyses revealed both to be *Mm*CPDII, indicating that the mutant is prone to aggregation. (B) Spectroscopic comparison between WT and R378K. Left, oxidized *Mm*CPDII wild type spectra were collected before and after boiling (black solid vs. dashed lines). Here, the

characteristic fine structure of the FAD is lost after boiling as a result of the protein denaturing and liberating the FAD. Conversely, the R378K mutant showed a spectrum which is characteristic of a high degree of aggregation before boiling (red solid line). After boiling the sample, *Mm*CPDII denatured, thus precipitating and freeing the FAD into the solution. The result (dashed red line) is a characteristic free FAD spectrum that lacks any aggregated protein contribution. Right: When WT *Mm*CPDII was exposed to both DTT and bright white light, its flavin cofactor transitioned from its oxidized state (solid black line) to its fully reduced state (dashed black line), which is characterised by a single peak at 360 nm, and a slope between 400 and 500 nm. On the other hand, when the R378K mutant was exposed to the same conditions, the protein did not photoreduce. Instead, the initial oxidized, aggregated protein (solid red line) precipitated and denatured. The result, as when the sample was boiled, was a free, oxidized FAD spectrum and a large protein pellet.

Table S1.

SFX data statistics. Numbers in parenthesis describe the highest resolution shell.

*Mm*CPDII Redox states	Oxidized (FAD)	Semiquinone ($FADH^{\bullet}$/FAD)*	Semiquinone ($FADH^{\bullet}$, extrapolated)*#	Hydroquinone ($FADH^{-}$)
PDB code	6IWX		6IX0	6IWZ
Space group	$P4_32_12$			
Unit cell	$a = b = 70.55$ Å, $c = 245.7$, $\alpha = \beta = \gamma = 90º$			
	Data collection statistics			
Total number of crystals	32815	26335	N/A	22191
Number of indexed crystals	20901	16488	N/A	13028
Indexing rate (%)	63.7	62.6	N/A	58.7
Resolution range	42.6-2.1 (2.14-2.10)	40.32-2.09 (2.13-2.09)	N/A	42.6 – 2.13 (2.18 – 2.13)
	Merging Statistics			
Completeness (%)	100 (100)	100 (100)	99 (98)	100 (100)
Multiplicity	620.8 (137.9)	438.4 (57.4)	N/A	339.53 (66.6)

CC1/2	0.99 (0.57)	0.99 (0.51)	N/A	0.98 (0.51)
I/σ	7.63 (0.56)	5.54 (0.49)	N/A	4.56 (0.49)
		Refinement statistics		
Resolution range (Å)	42.6-2.1 (2.14-2.10)	N/A	40.32-2.7 (2.797 – 2.70)	42.6 – 2.3 (2.382 – 2.3)
Unique reflections	37362 (3630)	N/A	17790 (1705)	28652 (2796)
I/σ	7.63 (0.56)	N/A	7.15 (2.39)	4.56 (1.59)
Rwork (%)	18.3	N/A	20.96	19.6
Rfree (%)	21.8	N/A	25.7	23.7
Ramachandran outliers	0	N/A	0	0
RMS (bonds, Å)	0.004	N/A	0.002	0.002
RMS (angles, deg)	0.99	N/A	0.42	0.42
Average B factor	64.66		71.50	74.16
Extrapolation weighting term	N/A	N/A	1.5	N/A

* Extrapolated structure factors were calculated as described in the Supplementary materials and methods, using the oxidized and raw semiquinone datasets. No refinement was performed on the raw semiquinone structure factors.

Maximum resolution was selected by choosing an extrapolated structure factor completeness of 98% in the highest resolution shell and $F/\sigma \geq 1$.

Table S2A.

Multiple Refinement Approach (hydroquinone *Mm*CPDII) maximum σ-peak within 2 Å of the isoalloxazine ring resulting from applying torsion angle restraints (axis, $\rho_{N,res}$ $\rho_{C,res}$). Good fits (i.e. σ peak ≤ 3.5σ) are highlighted by a yellow background.

$\rho_{N,res}$: torsion angle restraint (degrees) \ $\rho_{C,res}$: torsion angle restraint (degrees)	-46	-42	-38	-34	-30	-26	-22	-18	-14	-10	-6	-2	2	6
-46	6.14	5.78	5.46	6.59	5.32	5.09	5.1	4.64	4.5	4.34	4.23	4.23	3.81	3.8
-42	4.74	5.36	5.62	5.44	5.29	5.32	4.64	4.65	4	4.13	4.13	3.81	3.66	3.38
-38	5.29	4.62	5.07	5.15	4.77	4.95	4.59	4.32	4.09	4.26	3.68	3.61	3.12	3.31
-34	5.62	5.08	5.07	4.58	4.87	4.64	4.28	4.08	4.02	3.8	4.22	3.49	3.47	3.27
-30	5.09	4.97	4.76	4.49	4.49	4.32	4	3.69	3.62	4.11	3.62	3.47	3.72	3.13
-26	5.01	4.86	4.59	4.51	4.35	4.15	4.08	3.76	3.54	3.74	3.29	3.49	3.2	3.54
-22	4.83	4.79	4.48	3.76	4.27	3.93	3.83	3.72	2.85	3.36	3.27	3.44	3.14	3.8
-18	4.61		4.28	4.13	3.93	3.72	3.54	3.59	3.3	3.31	3.52	3.37	3.39	3.99
-14	4.59	4.17	3.97	4.18	3.8	4.08	3.21	3.31	3.24	3.78	3.51	3.58	3.33	3.6
-10	4.19	3.91	3.9	3.82	3.61	3.53	3.28	3.26	3.74	3.78	3.48	3.67	3.8	4.29
-6	3.96	3.85	3.91	3.42	3.8	3.53	3.26	3.08	3.62	3.8	4.06	3.84	4.43	4.59
-2	3.31	3.78	3.47	3.25	3.37	3.23	3.59	4.02	3.79	3.73	3.56	4.12	4.21	4.4
2	3.76	3.55	3.67	4.12	3.83	3.8	3.72	3.73	4.03	4.07	4.59	4.51	4.43	4.77
6	3.72	3.55	3.31	4.02	3.91	3.79	3.4	4.59	4.52	4.57	4.44	4.18	4.64	5.28
10	3.71	4.11	3.46	3.52	4.1	3.97	3.59	4.11	4.1	4.73	4.93	4.68	4.74	5.74
14	3.65	3.99	4.05	3.57	3.87	3.93	4.2	4.41	4.82	5.22	4.73	5.2	5.29	5.87
18	4.38	4.18	3.84	3.82	4.1	4.16	4.68	4.39	4.8	5.52	5.56	5.33	5.15	6.47

Table S2B.

Multiple Refinement Approach (hydroquinone MmCPDII) actual ρC torsion angles resulting from applying torsion angle restraints (axis, ρN,res ρC,res). Good fits (i.e. σ peak ≤ 3.5σ) are highlighted by a yellow background.

$\rho_{N,res}$: torsion angle restraint (degrees) \ $\rho_{C,res}$: torsion angle restraint (degrees)	-46	-42	-38	-34	-30	-26	-22	-18	-14	-10	-6	-2	2	6
-46	-39.3	-37.7	-33.9	-34	-31.9	-29.4	-27.7	-25.5	-23.5	-21.7	-19.4	-17.2	-15.3	-13.3
-42	-38.2	-35	-34.6	-32.7	-30.6	-28.7	-26.3	-24.6	-21.6	-20.3	-18.3	-16	-14.2	-12.3
-38	-36.2	-36.1	-33.2	-31.5	-29.2	-27.7	-25.5	-23.4	-21.5	-19.3	-17.3	-15	-30.8	-11.4
-34	-36.7	-34	-32.5	-30.5	-28.4	-26.7	-24.3	-22.2	-20.5	-18.1	-16	-13.9	-29	-10.2
-30	-35.5	-33.1	-31.7	-29.5	-27.7	-25.6	-23.5	-19.9	-19.1	-17.1	-14.9	-12.9	-10.8	-9.35
-26	-34.3	-32.4	-30.5	-28.6	-26.3	-24.2	-22.3	-20.3	-18.5	-16.3	-14.2	-11.8	-10.3	-7.95
-22	-33.6	-31.8	-29.5	-26.1	-25.4	-23.4	-21.2	-19.2	-16.2	-15.4	-12.9	-11.2	-9.21	-7.55
-18	-32.6	-180	-28.7	-26.6	-24.4	-22.2	-20.4	-18.4	-16	-14	-12.3	-10.3	-8.37	-6.44
-14	-32	-29.6	-27.6	-25.6	-23.3	-21.2	-18.1	-17.2	-15.4	-12.9	-11.4	-9.15	-7.37	-5.67
-10	-30.8	-26.7	-26.5	-24.6	-22.2	-20.2	-18.1	-16.3	-13.9	-12.1	-10.1	-8.11	-6.56	-4.35
-6	-29.6	-27.6	-25.3	-23.2	-21.2	-19.2	-17.1	-15	-13	-11.1	-9.54	-24.9	-5.46	-3.6
-2	-26.8	-26.8	-24.1	-22.6	-20.4	-18.6	-16.1	-14	-11.9	-10.3	-8.65	-6.31	-4.72	-2.91
2	-27.4	-25.3	-23.2	-21.2	-19.3	-16.9	-15.4	-13.4	-13.5	-9.2	-7.17	-5.48	-21.3	-1.59
6	-26.7	-24.1	-22.4	-19.9	-17.9	-16.1	-14.3	-12.2	-9.86	-8.52	-6.49	-4.84	-9.6	-0.61
10	-25.6	-23.2	-21.6	-19.4	-17.2	-15.3	-12.7	-10.9	-9.52	-7.19	-5.38	-3.76	-1.3	0.93
14	-24.3	-22.4	-20.5	-17.4	-16.3	-14.2	-12	-10.2	-8.4	-6.5	-4.93	-2.72	-0.84	-1.41
18	-23.1	-21.4	-19.7	-17.4	-15.2	-13.1	-11.2	-9.76	-7.66	-5.59	-3.34	-2.1	-0.28	-2.69

Table S2C.

Multiple Refinement Approach (hydroquinone *Mm*CPDII) actual ρ_N torsion angles resulting from applying torsion angle restraints (axis, $\rho_{N,res}$ $\rho_{C,res}$). Good fits (i.e. σ peak ≤ 3.5σ) are highlighted by a yellow background.

$\rho_{C,res}$: torsion angle restraint (degrees)

$\rho_{N,res}$: torsion angle restraint (degrees)	-46	-42	-38	-34	-30	-26	-22	-18	-14	-10	-6	-2	2	6
-46	-39.1	-38.5	-35.4	-36.8	-35.7	-34.2	-34.3	-32.5	-31.2	-30.3	-29.1	-28	-27	-25.9
-42	-37.3	-34.6	-35.4	-35.4	-34.2	-33.2	-31.9	-30.4	-28.5	-28.2	-27	-26.1	-26	-24.1
-38	-34.7	-35.7	-33.2	-32.4	-31.1	-30.5	-29.3	-28.2	-28.3	-27.1	-25.2	-24.1	-23.2	-22.7
-34	-34.3	-32.3	-31.5	-30.5	-29.3	-29.6	-28.2	-26.1	-26.3	-24.1	-23	-22	-21	-20.1
-30	-31.6	-30.6	-30.5	-28.5	-27.8	-27.3	-25.4	-22.9	-24	-22.1	-20.9	-20	-19	-18.4
-26	-29.4	-28.6	-27.6	-26.5	-25.3	-24.4	-23.3	-22.4	-21.3	-20.4	-19.2	-17.5	-18.1	-16
-22	-27.7	-27.8	-25.6	-23.2	-23.4	-22.3	-21.5	-20.2	-19.1	-19.2	-16.9	-16.6	-16.2	-14.4
-18	-25.8	-180	-23.7	-22.5	-21.5	-20.3	-19.5	-19.3	-17.1	-16.2	-15.4	-14.2	-14.4	-13.4
-14	-23.9	-22.6	-21.6	-20.5	-19.4	-18.4	-16	-16.5	-15.4	-14.1	-13.5	-13.1	-12.3	-10.7
-10	-21.8	-19.1	-19.5	-19.4	-17.3	-16.1	-15.3	-15.3	-13.1	-13	-11.9	-10.4	-9.63	-8.52
-6	-19.6	-18.7	-17.4	-16.4	-15.1	-14.4	-13.5	-12.4	-11.2	-11	-9.84	-8.6	-7.68	-6.74
-2	-16.4	-17.4	-15.4	-15.2	-14.1	-13.5	-12	-10.5	-9.23	-9.33	-8.88	-6.8	-5.85	-4.93
2	-15.7	-14.8	-13.6	-12.7	-11.5	-10.3	-9.85	-9.45	-8.28	-6.53	-5.69	-4.75	-21.2	-2.77
6	-14.2	-12.5	-12.3	-10.5	-9.1	-8.52	-7.91	-7.11	-5.45	-4.85	-4.25	-4.08	-2.6	-1.2
10	-12.1	-11.1	-10.2	-9.11	-7.74	-7	-5.69	-4.46	-4.67	-2.7	-1.96	-3.94	-0.33	1.5
14	-10.1	-9.14	-8.17	-6.4	-6.43	-4.82	-3.37	-3.3	-1.88	-0.94	-0.72	0.69	1.64	2.61
18	-7.49	-7.01	-6.57	-5.8	-4.05	-2.76	-2.49	-2	-0.16	1	1.51	1.8	-2.81	-4.87

Table S3A.

Multiple Refinement Approach (semiquinone *Mm*CPDII) maximum σ-peak within 2 Å of the isoalloxazine ring resulting from applying torsion angle restraints (axis, $\rho_{N,res}$ $\rho_{C,res}$). Good fits (i.e. σ peak ≤ 3.5σ) are highlighted by a yellow background.

$\rho_{C,res}$: torsion angle restraint (degrees)

$\rho_{N,res}$: torsion angle restraint (degrees)	-24	-20	-16	-12	-8	-4	0	4	8	12
-30	4.79	4.55	4.16	4.21	3.94	4.26	4.08	3.63	4.01	3.53
-26	3.76	4.61	4.33	4.32	3.83	3.99	3.33	2.85	3.85	3.77
-22	3.75	3.73	3.71	4.25	4.13	4.04	3.43	3.93	3.82	3.84
-18	4.27	3.82	3.9	3.72	3.94	3.57	3.28	3.66	4.01	3.61
-14	3.84	3.82	3.44	4.27	4.03	3.76	3.43	3.16	3.32	3.49
-10	4.42	4.21	4.11	4.17	3.45	3.48	3.44	2.96	3.3	3.57
-6	4.22	3.78	3.76	3.78	3.35	3.18	3.67	3.58	3.86	3.62
-2	3.96	2.73	3.46	3.01	3.77	3.18	2.77	2.65	2.86	3.27
2	4.1	3.77	4.24	3.8	3.87	3.44	3.11	3.4	3.54	2.77
6	4.14	3.66	3.61	3.78	4.06	3.56	3.55	3.2	3.52	3.72
10	3.86	4.21	3.87	3.65	3.49	3.59	3.48	3.78	3.77	3.86
14	4.04	3.86	2.83	3.73	3.87	3.73	4.16	4.52	4.78	4.92
18	3.58	3.38	3.96	4.22	3.73	4.39	4.31	4.64	5.05	3.21

Table S3B.

Multiple Refinement Approach (semiquinone *Mm*CPDII) actual ρ_C torsion angles resulting from applying torsion angle restraints (axis, $\rho_{N,res}$ $\rho_{C,res}$). Good fits (i.e. σ peak ≤ 3.5σ) are highlighted by a yellow background.

$\rho_{N,res}$: torsion angle restraint (degrees)	$\rho_{C,res}$: torsion angle restraint (degrees)									
	-24	-20	-16	-12	-8	-4	0	4	8	12
-30	-26.5	-24.1	-19.8	-17.2	-16	-15.3	-12.2	-8.53	-7.65	-4.68
-26	-20.5	-22.7	-20.7	-17.9	-15.5	-13.6	-10.7	-7.11	-7	-4.48
-22	-20.8	-19.7	-16.8	-16.6	-14.1	-12.8	-8.8	-7.47	-5.13	-2.95
-18	-23	-19.3	-17.4	-15	-12.8	-10	-8.06	-6.58	-3.68	-1.91
-14	-19.7	-18.6	-15.9	-14	-11.9	-9.3	-6.88	-4.72	-2.87	-0.51
-10	-20.5	-17.4	-15.7	-13	-9.8	-8.48	-6.24	-3.89	-1.83	0.32
-6	-19.5	-15.2	-14.6	-12.1	-9.56	-6.95	-4.56	-2.5	-0.36	1.54
-2	-15.9	-12.9	-13	-9.47	-8.02	-5.64	-3.8	-1.91	0.12	2.05
2	-15.8	-12.8	-11.1	-8.87	-6.61	-4.89	-2.6	0.12	1.34	2.88
6	-15.2	-11.7	-10.6	-7.72	-5.48	-3.37	-1.16	0.18	2.71	5.23
10	-13.4	-11	-9.11	-6.82	-4.45	-2.37	-0.42	-362	4.2	6.27
14	-12.6	-10.2	-7.75	-5.47	-3.19	-1.28	1.47	3.62	6.08	8.22
18	-11	-8.79	-6.57	-4.02	-2.49	-360	2.77	4.87	7.33	8.31

Table S3C.

Multiple Refinement Approach (semiquinone *Mm*CPDII) actual ρ_N torsion angles resulting from applying torsion angle restraints (axis, $\rho_{N,res}$ $\rho_{C,res}$). Good fits (i.e. σ peak ≤ 3.5σ) are highlighted by a yellow background.

$\rho_{N,res}$: torsion angle restraint (degrees)	$\rho_{C,res}$: torsion angle restraint (degrees)									
	-24	-20	-16	-12	-8	-4	0	4	8	12
-30	-28.1	-26.7	-23.2	-21.7	-21.4	-22.1	-20.1	-17	-17.6	-15.2
-26	-20.3	-24.4	-23.4	-21.7	-19.9	-19.2	-17.2	-14.2	-15.9	-14.4
-22	-20	-20	-18.2	-19.3	-17.9	-17.6	-14.4	-14.4	-13.1	-11.9
-18	-21.2	-18.6	-17.9	-16.4	-15.5	-13.5	-12.6	-12.4	-10.6	-9.5
-14	-17	-17.1	-15.2	-14.7	-13.6	-12	-10.6	-9.32	-8.42	-7.06
-10	-17	-15	-14.3	-12.6	-10.2	-10.1	-8.99	-7.43	-6.29	-4.65
-6	-15	-13.5	-12.1	-10.7	-9.14	-7.42	-6.05	-5.16	-4.05	-3
-2	-10.3	-7.88	-9.57	-6.81	-6.67	-5.09	-3.83	-2.91	-1.87	-1.07
2	-9.21	-7.18	-6.6	-5.37	-4.24	-3.42	-2.03	-0.55	0.14	0.7
6	-7.66	-5.07	-5.05	-3.28	-2.05	-0.86	0.29	1.42	2.18	3.72
10	-4.84	-3.42	-2.56	-1.33	0.19	1.18	2.12	3.85	4.67	5.7
14	-3.01	-1.57	0.13	1.09	2.31	3.32	5	6.04	7.51	8.61
18	-0.41	1.04	1.97	3.46	4.15	5.98	2.77	8.33	9.73	9.78

Table S4A.

Multiple Refinement Approach (oxidized *Mm*CPDII) maximum σ-peak within 2 Å of the isoalloxazine ring resulting from applying torsion angle restraints (axis, $\rho_{N,res}$ $\rho_{C,res}$). Good fits (i.e. σ peak ≤ 3.5σ) are highlighted by a yellow background.

$\rho_{N,res}$: torsion angle restraint (degrees)	$\rho_{C,res}$: torsion angle restraint (degrees)									
	-22	-18	-14	-10	-6	-2	2	6	10	14
-22	6.64	4.48	4.93	4.01	5.78	3.8	3.6	3.36	3.08	3.08
-18	6.43	6.1	4.81	4.3	3.68	3.24	3.41	4.38	3.59	2.79
-14	4.39	4.3	3.41	5.41	4.83	3.81	3.71	3.48	3.66	3.81
-10	5.54	4.72	5.01	4.33	4.63	3.04	4.22	2.69	2.71	3.32
-6	3.69	5.11	3.58	4.6	3.68	4.97	2.6	3.72	2.81	3.44
-2	3.55	4.66	3.48	4.01	3.27	3.1	4.46	3.87	2.79	3.11
2	5.51	4.63	3.61	3.97	3.22	2.71	2.75	2.84	3.2	2.89
6	4.94	3.93	3.83	3.63	2.82	3.77	3.38	3.37	3.11	3.76
10	3.94	3.31	3.21	2.7	2.99	4.47	2.56	2.77	3.29	3.77
14	3.38	4.1	3.32	3.01	3.21	2.7	3.47	3.11	3.61	4.03
18	4	3.81	2.9	3.68	3.63	3.23	3.96	3.8	4.63	4.97

Table S4B.

Multiple Refinement Approach (oxidized *Mm*CPDII) maximum σ-peak within 2 Å of the isoalloxazine ring resulting from applying torsion angle restraints (axis, $\rho_{N,res}$ $\rho_{C,res}$). Good fits (i.e. σ peak ≤ 3.5σ) are highlighted by a yellow background.

$\rho_{N,res}$: torsion angle restraint (degrees)	$\rho_{C,res}$: torsion angle restraint (degrees)									
	-22	-18	-14	-10	-6	-2	2	6	10	14
-22	-21.8	-14.7	-15.1	-11	-12.5	-7.62	-5.86	-3.92	-2.33	-0.81
-18	-20.2	-18.8	-13.7	-12.2	-8.42	-6.24	-4.99	-4.45	-1.96	-0.12
-14	-14.8	-13	-10.1	-11.9	-9.93	-6.95	-5.27	-2.88	-1.61	0.44
-10	-18.5	-14.7	-13.4	-10.6	-8.48	-4.94	-5.18	-1.93	-0.35	1.6
-6	-13.1	-14.3	-9.73	-9.77	-6.85	-5.5	-2.7	-1.44	0.5	3.18
-2	-11.9	-12.6	-8.86	-8.38	-5.41	-3.73	-2.03	0.04	1.35	0.71
2	-16.1	-12.3	-9.3	-7.87	-4.88	-3.04	-1.34	0.26	3.38	3.64
6	-13.6	-10.6	-7.45	-6.73	-4.05	-2.07	-0.3	2.13	3.66	6.75
10	-11.4	-9.29	-7.07	-5.04	-3.31	-0.61	-0.19	1.52	4.7	7.57
14	-9.32	-8.87	-6.15	-4.33	-2.36	-0.94	2.69	3.8	6.65	10.97
18	-9.32	-7.25	-5.21	-3.05	-0.88	0.42	3.55	5.83	8.34	10.05

Table S4C.

Multiple Refinement Approach (oxidized *Mm*CPDII) actual ρ_N torsion angles resulting from applying torsion angle restraints (axis, $\rho_{N,res}$ $\rho_{C,res}$). Good fits (i.e. σ peak ≤ 3.5σ) are highlighted by a yellow background.

$\rho_{N,res}$: torsion angle restraint (degrees)	$\rho_{C,res}$: torsion angle restraint (degrees)									
	-22	-18	-14	-10	-6	-2	2	6	10	14
-22	-21.8	-15.4	-17	-13.7	-16.7	-12.3	-11.4	-10.5	-9.72	-9.19
-18	-19.2	-18.9	-14.6	-14.1	-13	-9.88	-9.53	-10.7	-8.81	-7.54
-14	-19.3	-11.8	-9.56	-13	-12.1	-9.95	-9.22	-7.73	-7.7	-6.77
-10	-15.6	-12.7	-12.4	-10.6	-9.61	-6.64	-8.33	-5.56	-4.74	-4.32
-6	-9.01	-11.4	-7.49	-8.87	-6.79	-6.67	-4.46	-4.62	-3.09	-2.01
-2	-6.86	-8.69	-5.69	-6.41	-4.25	-3.53	-3.24	-2.16	-1.33	-0.32
2	-8.09	-7.33	-5.41	-4.86	-2.1	-2.02	-1.24	-0.61	1.19	1
6	-6.62	-4.71	-2.54	-2.8	-0.98	-0.14	0.61	2	3.66	4.55
10	-3.52	-1.33	-1.12	-0.01	0.75	2.27	1.97	2.76	4.6	9.96
14	-0.59	-0.96	0.57	1.55	2.52	3.03	5.3	5.59	7.53	6.38
18	-0.64	-1.69	2.57	3.92	5.04	5.25	7.48	8.76	10.25	11.86

Table S5.

Salt-bridge to isoalloxazine charge transfer (Δq*) and trajectory occupancy (D#) in oxidized and fully reduced *Mm*CPDII simulations.

	Oxidized		Fully reduced	
	DF-SFX	MD	DF-SFX	MD
Short Iso-Arg distance Δq*	-0.07	-0.03	NA	0.08
Short Iso-Arg distance D#	NA	0.51	NA	0.007
Long Iso-Arg distance Δq*	NA	-0.05	0	0
Long Iso-Arg distance D#	NA	0.49	NA	0.993

* Charges were calculated via MP2 quantum mechanical calculations based on either the experimental structures, or snapshots from the MD trajectories corresponding to the extremes of each corresponding population (i.e. either for the shortest, or the longest possible distances). Charge transfer (Δq) was obtained as the difference between the calculated isoalloxazine charge and its expected value (0 for oxidized, -1 for hydroquinone). Note that no calculations were performed for the semiquinone system, as the open system would not converge.

Trajectory occupancy was calculated as the number of snapshots which fit the selection criteria divided by the total number of snapshots in the trajectory. As the experimental data corresponds to a single snapshot, occupancy cannot be calculated for them.

5 Discussion and Conclusion

*Cr*aCRY as a regulatory Enzyme

The animal-like cryptochrome (*Cr*aCRY) displays (6-4) DNA repair activity *in vitro* and *in vivo* as well as playing a role in maintaining the sexual life cycle of *Chlamydomonas* (227). Zou *et al.* presented in immunolocalization studies, that *Cr*aCRY is located all over the cell in the dark and accumulates in the nucleus during the day. During the night phases, a high amount of *Cr*aCRY is membrane-associated. Through size exclusion chromatography from the crude extract followed by Western-Blot, Zou *et al.* could show that *Cr*aCRY is present as a monomer, but there are also oligomeric species present during day (200 – 400 kDa) and during night (130 to 140kDa) phases. It is contrary to our *in vitro* SEC experiments (316) where *Cr*aCRY is mainly present as a monomer. This could be explained by the possibility of DNA binding to *Cr*aCRY from the crude extract as we use DNase I as well as an additional affinity chromatography step to remove any remaining nucleic acids. There is apparently also a modified *Cr*aCRY present in late zygotes, which is not due to phosphorylation of the enzyme. Zou *et al.* was able to study the role of *Cr*aCRY in the sexual life cycle of *Chlamydomonas* by performing several assays for mating ability, mating maintenance and germination. The results are summarized in Figure 31. Together with the plant CRY (pCRY), *Cr*aCRY negatively regulates the mating pathway as lower aCRY levels equal an increase in mating ability (227, 228). In the zygote germination step, *Cr*aCRY acts as a positive regulator together with pCRY and the phototropin PHOT. As blue and red light have an influence on the process of germination, the semiquinone state of *Cr*aCRY might be the main photoreceptor of this step. The semiquinone state of *Cr*aCRY is the only photoreceptor known in *Chlamydomonas* which is capable to absorb light in the red range of the visible spectrum (Figure 31b) (228, 233).

Besides the involvement of *Cr*aCRY in the sexual life cycle of *Chlamydomonas*, it displays influence on the transcription levels of various genes after cells were treated with blue, yellow and red light (233). Some of them are clock-relevant genes encoding for proteins of the carotenoid and chlorophyll biosynthesis, cell cycle control or nitrogen metabolism.

Studies show that some genes are more strongly upregulated in BL than RL, whereas other genes show the exactly opposite behavior (233). Beel *et al.* propose, that both, the oxidized and semireduced state, are present inside the cell and both regulatory responses are possible. It is speculated that *Cr*aCRY might be the main RL receptor, as no other typical RL receptor like a phytochrome has been identified in *Chlamydomonas*.

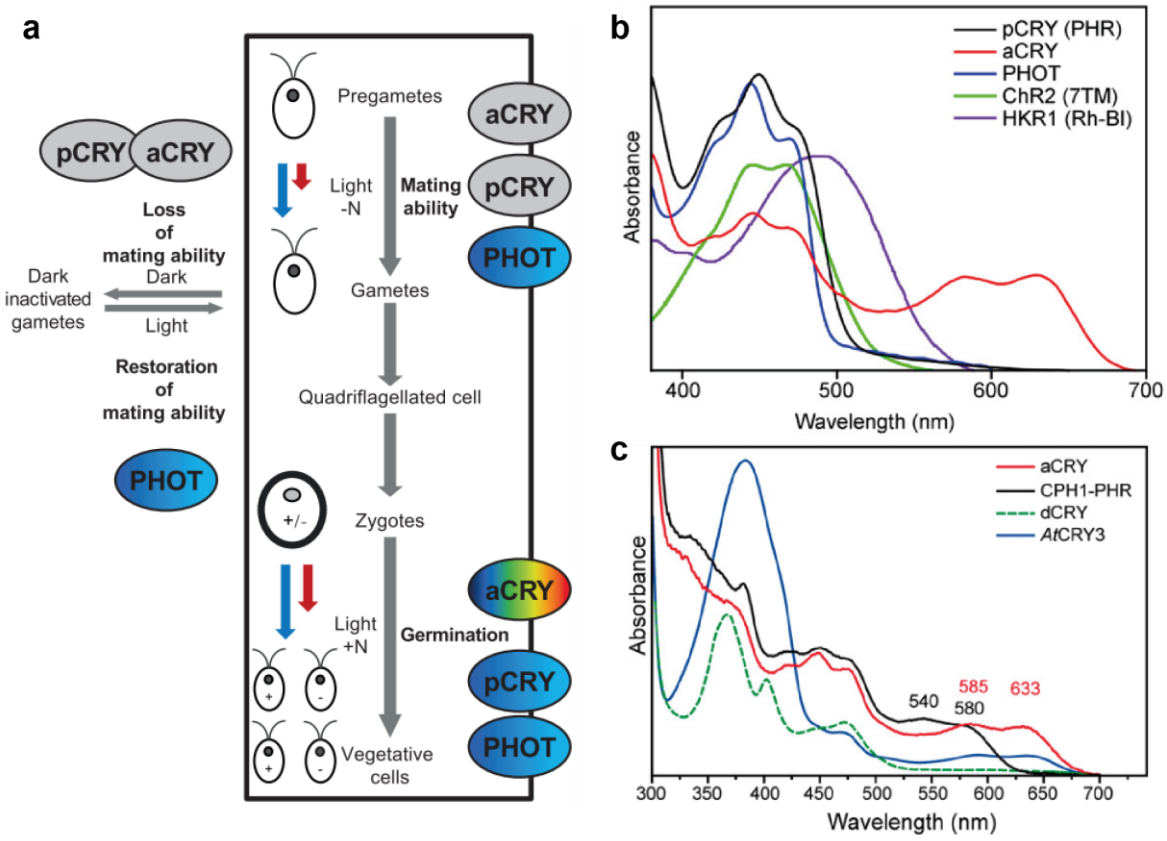

Figure 31 a) Role of aCRY, pCRY and PHOT in the *Chlamydomonas* sexual life cycle as shown by Zou *et al*. (227). The colors of the ellipses indicate the absorbed light spectrum of the particular photoreceptor. aCRY and pCRY act as negative regulators of gametogenesis in the dark, so they are colored in grey. Gametogenesis and germination are the two light-dependent steps which is indicated with blue and red arrows. The length of the arrows indicates the extent to which these pathways are affected by the specific light. **b)** Absorption spectra from the blue light receptors identified in *Chlamydomonas* (228). For pCRY only the photolyase homology region (PHR) is shown. *Cr*aCRY absorption is shown with the neutral radical state of the flavin as it is proposed to be the dark state *in vivo*. The other blue light receptors found are phototropin (PHOT), the seven-transmembrane helix domain of ChR2 and the UV-illuminated rhodopsin fragment of HKR1. **c)** Comparison of absorption spectra of different CRYs (233). CPH1 also named pCRY from *Chlamydomonas* shows a blue shift compared to *Cr*aCRY. The *Drosophila* dCRY (*Dm*CRY) forms the anionic radical state and *Arabidopsis At*CRY3 has a MTHF antenna chromophore bound.

Classification inside the superfamily

As described in section 1.2 of the introduction, the classification inside the cryptochrome/photolyase family (CPF) is non-trivial. In the latest phylogenetic analysis, OZTURK (35) describes 10 classes of photolyases and cryptochromes whereas Scheerer *et al.* (50) is defining 7 and Oliveri *et al.* (56) is dividing the family into 4 superclasses with a total of 11 subgroups. In a sequence-similarity network (SSN) (317) done by Lars-Oliver Essen in 2017 (318) 13779 orthologs using the *Pfam protein families database* (319) (families PF00875 and PF04244) were analyzed.

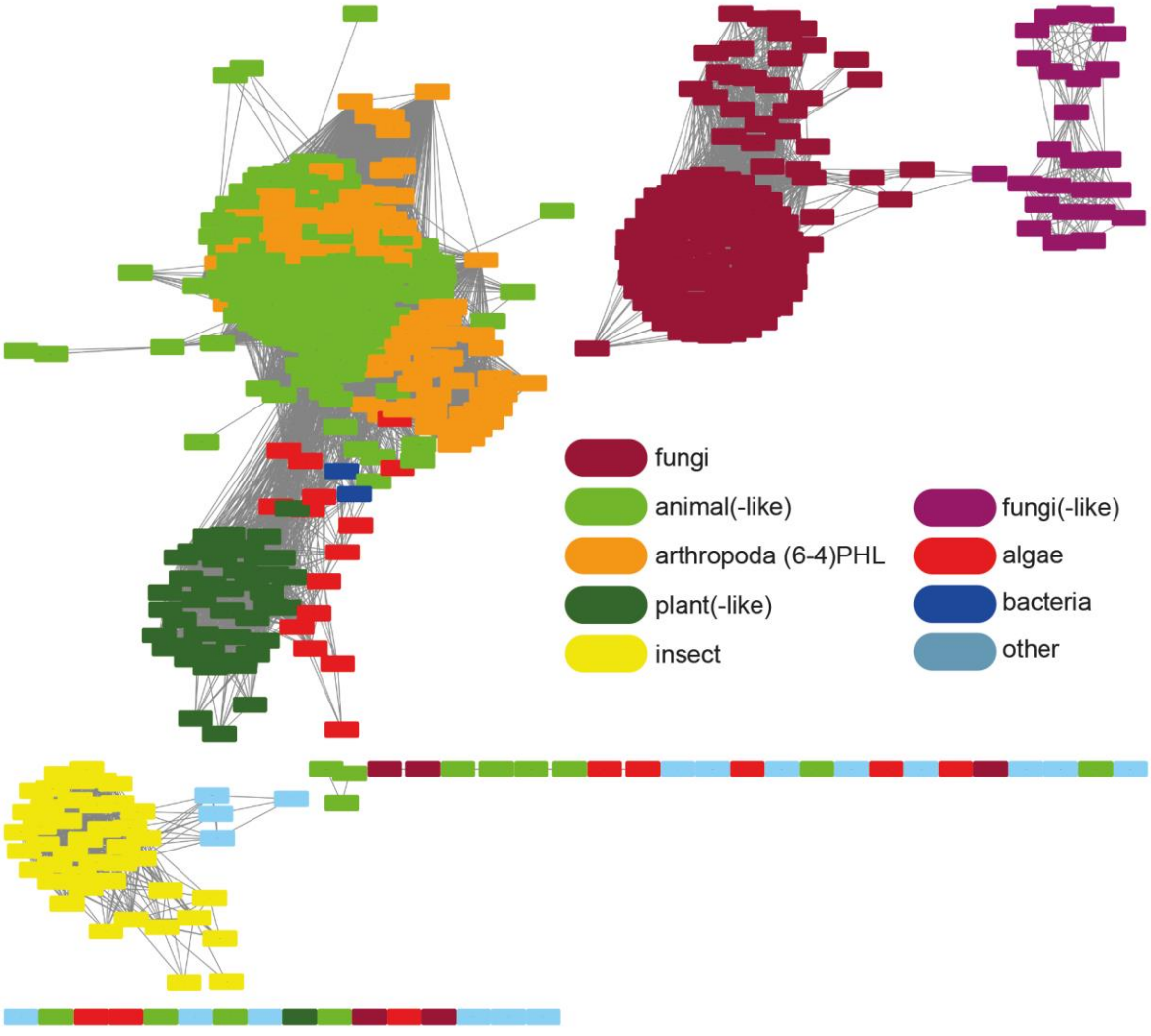

Figure 32 Sequence-similarity network analysis (317) of the CPF with 13770 orthologs using PFAM families PF00875 and PF04244 done by L.-O. Essen in Jan. 2017 (318). Each of the 7503 independent nodes represents sequences with more than 90 % sequence identity; the edges correspond to BLAST

E-values of below 10^{-90}. The CPD class I photolyases is the biggest class, which is composed of class I CPDs of different organisms (*Actino: Actinomyces, Proteo: Proteobacteria*). Plant cryptochromes (pCRY) show high sequence identity to CPD class I. DASH cryptochromes also known as ssDNA photolyases form their own group as well as class II CPD PHLs. Another subclass is the CryPro or FeS bacterial cryptochromes and photolyases (FeS-BCP) (52). Interestingly, animal cryptochromes (aCRY) and (6-4) photolyases cluster as one group.

In a SSN, each member of a family is illustrated as a node (symbol) connected with an edge (line) to neighboring nodes that share a sequence similarity over a user-defined value. In our case (Figure 32), each of the 7503 independent nodes represents sequences with more than 90 % pairwise sequence identity and the connecting lines (edges) were specified to a BLAST E-value score below 10^{-90}. In the SSN, six major groups can be identified as well as several minor groups. The biggest group turns out to be the class I CPD PHLs that clusters into several subgroups depending on the covered organisms. The plant CRYs are in a high relationship to class I CPD PHLs and also include pCRY-related proteins, like CryP from *Phaeodactylum tricornutum* (318). Class II CPD PHLs form another distinct group, which is much smaller than class I. This finding is not surprising, as the genome of far more unicellular organisms has been sequenced so far. DASH cryptochromes or ssDNA repairing enzymes are clustering together as well as CryPro or FeS-cluster containing bacterial CRYs and PHLs (FeS-BCP). Exceptions are the plantDASH CRYs, which form their own group. A class of not yet characterized proteins can be identified and annotated as “newCRYs” but will be described elsewhere. Interestingly, animal CRYs and (6-4)PHLs show high sequence identity to each other and form thereby a single group. In Figure 33, a more detailed view of the SSN of this subgroup with a E-value cutoff at 10^{-150} is displayed (142). The figure also shows the assignment of the different family members as either a photolyase or a cryptochrome in the protein family database. There are also a lot of unassigned proteins, which are mainly present in the cluster in the lower left corner. This cluster consists of sequences coming from streptophyta and chlorophyta, *i.e.* plants and algae. The node representing *Cr*aCRY is located between one cluster of mainly photolyases in plants and algae and another cluster with cryptochromes from animal species (e.g. chordata, arthropoda *etc.*). This might already indicate the role of *Cr*aCRY as a bifunctional photoreceptor. On the upper middle and right corner are two clusters, which are connected

to each other. Both are highly diverse in their assigned functionality. All the sequences inside both groups are from fungal organisms. The presence of PHL and CRYs in fungi is only poorly studied compared to other organisms, so there are only a few members of the CPF identified so far (40, 320–323).

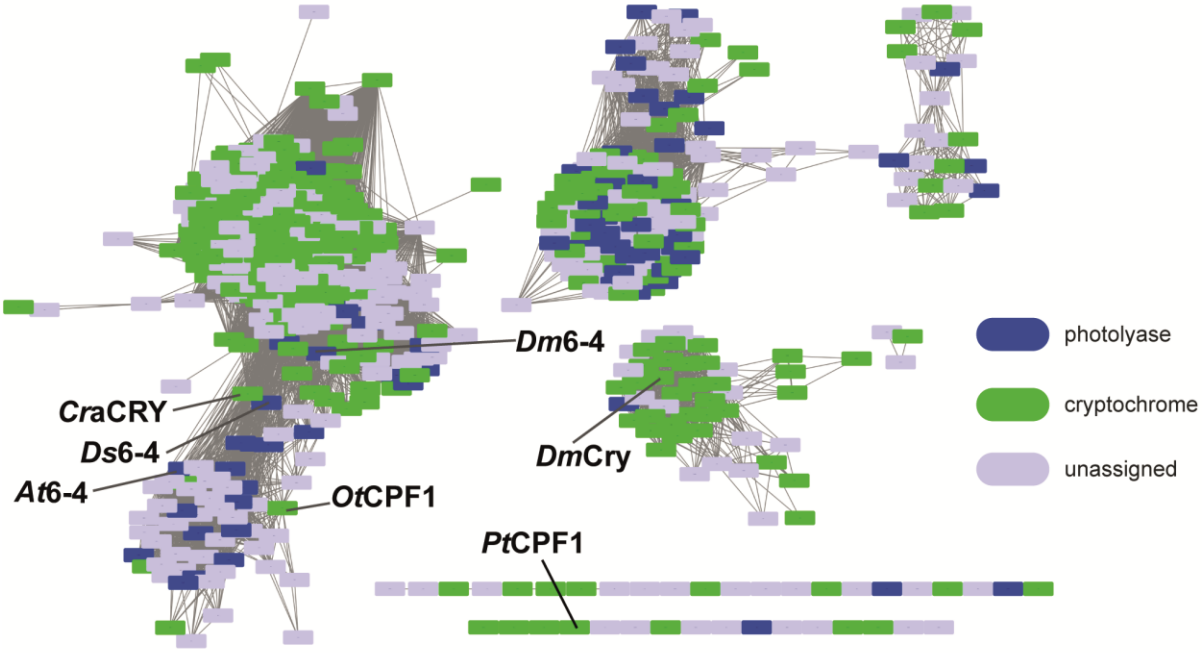

Figure 33 Sequence similarity network of the animal CRY/(6-4)PHL subclass with a BLAST E-value cutoff at 10^{-150}. The colors are based on their assigned functionality. The positions of several algal and most likely bifunctional members (*Cra*CRY, *Ot*CPF1, *Pt*CPF1, *Ds*6-4) and prominent members (*Dm*CRY, *Dm*6-4, *At*6-4) are marked. Figure adapted from (142).

The SSN provides a new approach for classification inside the CPF as new subclasses have been shown. *e.g.* NewCRY, and some classes are more distinct from each other as originally thought. On the contrary, animal CRYs and (6-4)PHLs obviously form a single, major group that also harbors bifunctional members of the animal-like CRY type.

As presented in this thesis, *Cra*CRY and the CPD PHL of *Chlamydomonas* are able to perform photoreactivation, *e.g.* keep the algal cells from dying of UV-induced DNA lesions (142). The specific repair reaction itself is intensely discussed in the “Nucleic Acids Research” publication, presented in section 4.4.

Taking this discussion and also other data into account, new questions arise:

1. How can *Cr*aCRY achieve its bifunctional role?
2. What makes a photolyase? What are the specific building blocks which are necessary for DNA repair?
3. What are the differences between a classical animal CRY and a (6-4)PHL?
4. Why does *Cr*aCRY need this long-lived TyrO° radical?

To answer the question of how *Cr*aCRY can achieve bifunctionality, one has to take a look at the characteristics of animal CRYs as well as (6-4)PHLs and search for differences as well as common features. As described and shown in Figure 32, animal CRYs and (6-4)PHLs cluster in one defined subgroup, when only sequence similarity is taken into account. So the differentiation between CRY and PHL must rely on more structural and biochemical aspects. At the moment (November 2018), only six members of the aCRY/(6-4)PHL group are represented in the RCSB PDB belonging to four different organisms (Table 1).

Table 1: Members of the aCRY/(6-4)PHL group represented in the RCSB protein data bank (PDB) without mutant or co-crystal structures.

Protein	Organism	PDB code	Acronym
(6-4) photolyase	*Arabidopsis thaliana*	3FY4	*At*64
(6-4) photolyase	*Drosophila melanogaster*	2WB2, 3CVU	*Dm*64
CRY type 1	*Drosophila melanogaster*	4JZY, 4GU5	*Dm*CRY
CRY1 type 2	*Mus musculus*	4K0R, 5T5X	*m*CRY1
CRY2 type 2	*Mus musculus*	4I6G	*m*CRY2
aCRY type 1	*Chlamydomonas reinhardtii*	6FN3, 5ZM0	*Cr*aCRY

By comparing the known crystal structures of the aCRY/(6-4)PHL group, no obvious differences can be detected at the first glance (Figure 34). Looking more closely, the connecting linker of the antenna binding domain and the FAD binding domain displays two loop sections, L1 and L2, with a higher structural variability. Another more variable section seems to be around helix 10 and the connecting loop between helix 12 and helix 13

(numbers according to Franz *et al.* (142)). Interestingly, the structural integrity of this region was also shown to be impacted by photoreduction (316). The loop region L3 can be assigned to the so-called phosphate-binding loop, protrusion loop and C-terminal lid in *Dm*CRY (324).

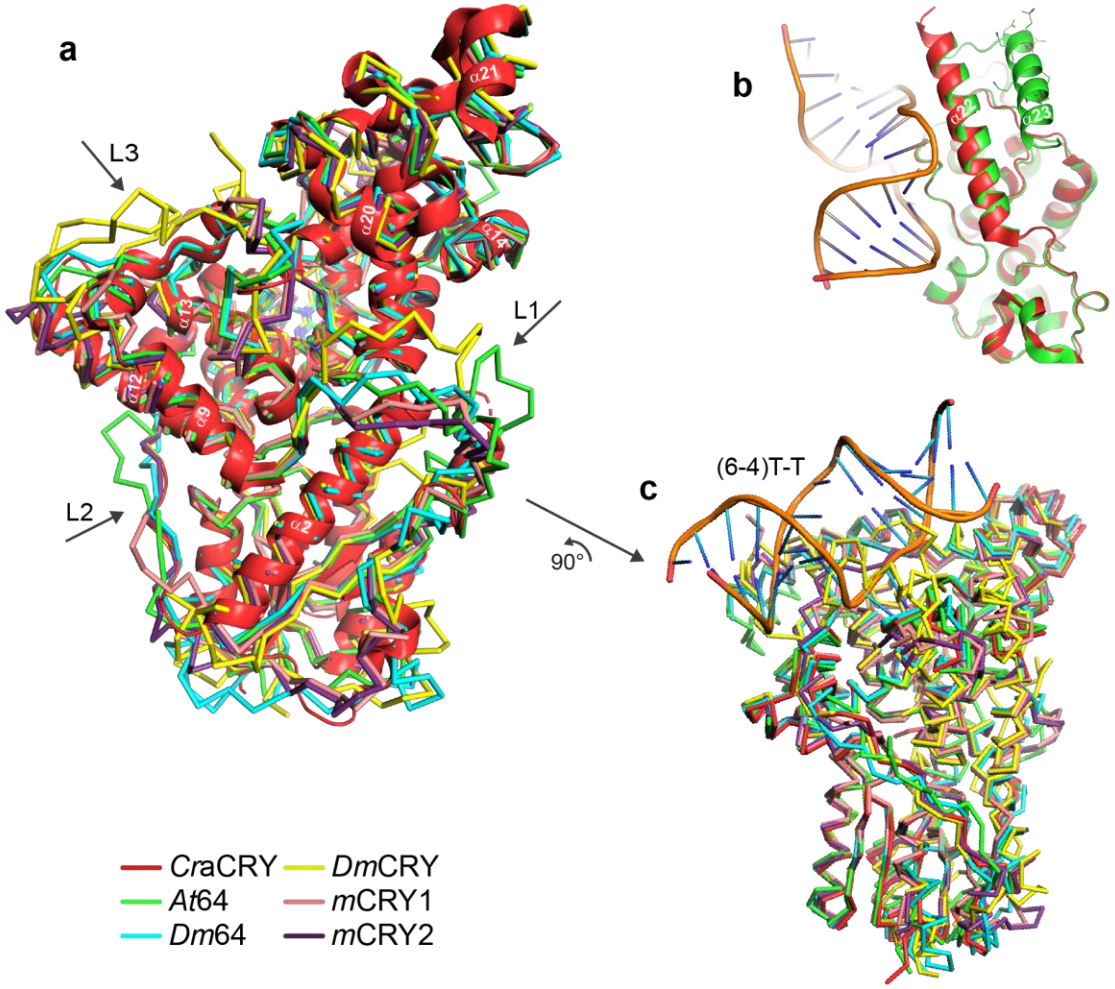

Figure 34 Overall structure of the aCRY/(6-4)PHL subgroup. The (6-4) photolyases of *A. thaliana* (*At*64, green, 3FY4) and *D. melanogaster* (*Dm*64, cyan, 3CVU), the full-length Drosophila CRY (*Dm*CRY, yellow, 4GU5) and PHR domains of murine CRY1 (*m*CRY1, pink, 5T5X) and CRY2 (*m*CRY2, magenta, 4I6G) are presented as ribbon. In (**a**), aCRY from *Chlamydomonas* (*Cr*aCRY, red, 5ZM0) is shown as cartoon and helices are numbered. **b**) A top view of the (6-4) damaged DNA in complex with At64 (green) and CraCRY (red). Both present the flanking helix α22, but in At64 another helix is shown. **c**) Superimposition of all members shown as strings together with the (6-4)PP extracted from *Dm*64-DNA complex (3CVU).

Looking at the C-termini, for *m*CRY1/2 and *Cr*aCRY only the PHR domain is present in the structure without the CTE. The short CTE of *Dm*CRY is bound inside the DNA binding pocket

as described before (section 1.3). It is noticeable, that *At*64 presents an elongated CTE which still misses 12 residues, even though it is a photolyase (Figure 34b). Here, another helix after α22 is present.

Firstly, structures were analyzed in presence of the (6-4) lesion from the *Dm*64 cocrystal structure (3CVU) as well as from the *Cr*aCRY-DNA complex (6FN0) concerning their ability to bind (6-4)PP DNA. Focusing on the overall binding (Figure 34c), *Dm*CRY is not able to bind DNA, as the binding pocket is filled with the CTE which results in an interruption of the charged areas. When the tail is removed from the binding site upon formation of the semiquinone $FAD°^{-}$ an extended charged surface is established (324). For *m*CRY1/2, the binding pocket is in general accessible, but the electron surface potential is rather neutral compared to a highly positive cleft which is presented by *Dm*64, *At*64 and *Cr*aCRY. This positive potential is important not only to bind the lesion, but also to bind the negative phosphate backbone of the DNA and to allow the flip of the (6-4)PP lesion. In case of murine CRYs, the DNA binding site is a docking site for interaction with PER2 or FBXL3 (73, 325) (Figure 35). Noticeable, PER2 also binds to *m*CRY over the antenna binding loop, which is unstructured in the *Cr*aCRY structure in the absence of the antenna cofactor 8-HDF. Comparing this with the structure with incorporated 8-HDF, the antenna binding loop displays a conformation comparable to *m*CRY2.

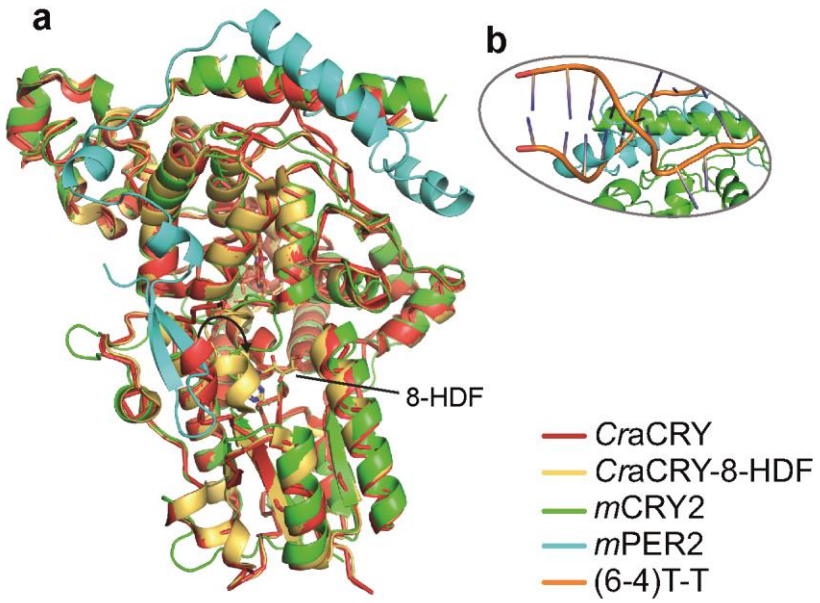

Figure 35 a) Superimposed crystal structures of *Cra*CRY (red, 5ZM0) and *m*CRY2 (green) in complex with *m*PER2 (cyan, 4CT0). The *Cra*CRY structure with incorporated antenna chromophore 8-HDF (6FN2) reveals a flip of a short helix and loop. Therefore, the PER binding of *Cra*CRY could be possible. **b**) (6-4) of *Cra*CRY-complex structure (6FN0) and the C-terminus of *m*PER2 occupy the same binding site.

Secondly, in Figure 36a, the essential residues for DNA binding and repair are displayed with the residues of *Cra*CRY (PDB entry 5ZM0) shown as sticks. Here, all of the six members possess the first histidine residues (His_1), which is essential for the repair reaction (125). One significant difference is shown by the *m*CRY1 structure, in which His_1 is present as another rotamer which faces towards the FAD binding site. This is possible as there is no FAD present in the *m*CRY1 structure. This might be a general feature of type 2 cryptochromes as they do not exhibit a clear photosensory function (35) and demonstrate low affinity to flavin *in vitro* (73). The second histidine is displayed in all members except *Dm*CRY, where an asparagine is presented instead. Also the other residues are mostly the same with exceptions in *m*CRY and *Dm*CRY structure. Therefore, the presence of these residues in the binding site is a good indicator whether one of the members of the aCRY/(6-4)PHL class is capable to bind and repair (6-4)PP.

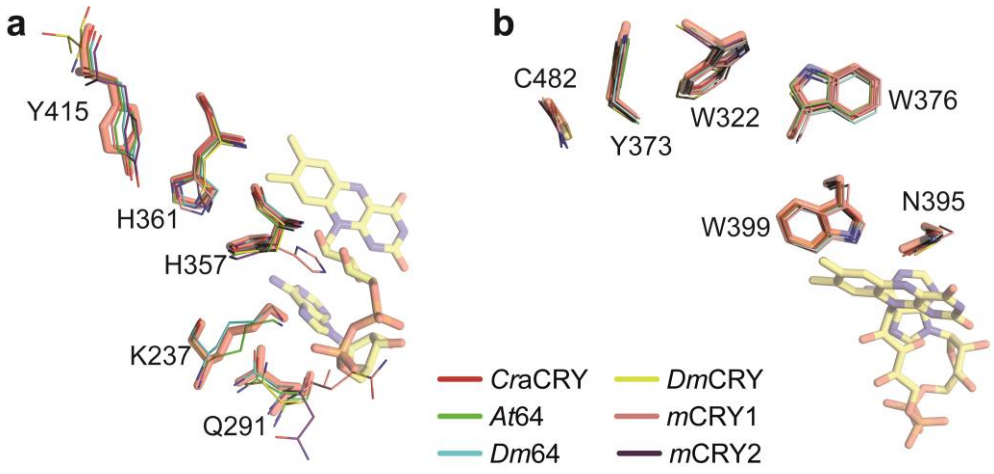

Figure 36 Superimposition of members of the aCRY/(6-4)PHL subclass. Residues of *Cra*CRY (5ZM0) are shown as sticks and the numbers refer to positions in *Cra*CRY. FAD is displayed in yellow. **a**) Comparison of the DNA binding site. The murine CRY1 and CRY2 differ significantly as well as *Dm*CRY. b) Catalytic Trp triad of the CPF. All shown members contain the three Trp. They also show a fourth residue, which is a tyrosine in *Cra*CRY (Y373) but a tryptophan in *Dm*64 (W381), *Dm*CRY (W394), *m*CRY1 (W371) and *m*CRY2 (W389). *At*64 is presenting a phenylalanine (F380) at this position. Additionally to the triad/tetrad, Asn395 is displayed, which is essential for the $FADH^-$ formation as well as C482, which is described in Oldemeyer e*t al.* (294). Except for *Dm*CRY all members harbor an Asn at N395. For C482, *At*64 is the only one with another Cys at this position.

Thirdly, the protein has to be able to form the hydroquinone $FADH^\cdot$ state, which is essential for DNA repair. Therefore, an active photochemistry is needed which is catalyzed by an aromatic triad or tetrad. All members contain the Trp triad (Figure 36b). *Cra*CRY is the only one with a tyrosine as a fourth electron donor whereas *Dm*64, *Dm*CRY, *m*CRY1 and *m*CRY2 all present a tryptophan at this position and *At*64 is the only member with a phenylalanine. As discussed before, *m*CRY1 and *m*CRY2 are photo-insensitive and evolved as components of the molecular clock without any DNA repair function remaining (73). *Dm*CRY can be reduced to its anionic radical by either light excitation or chemical reduction (326). *In vitro*, the hydroquinone of *Dm*CRY can be achieved with chemical reduction, but a physiological role has not been identified yet. In contrast, the formation of the $FAD^{\circ-}$ results in a conformational change of the CTE allowing downstream signaling partners like JET and TIM to bind (186–188). *Cra*CRY can be easily reduced to the hydroquinone $FADH^-$ by illumination, starting from the oxidized or the semireduced state *in vitro*. Another requirement for formation of the $FADH^-$ state is the presence of an asparagine (N395 in *Cra*CRY) in close proximity to the N5 nitrogen of the isoalloxazine ring of the flavin cofactor.

In *Dm*CRY, a Cys is present instead of an Asn, which blocks the protonation of FAD°⁻ and conclusively the formation of FADH° and FADH⁻ (327–329). For comparison, plant CRYs harbor an Asp at this position, which enables them to form the protonated state FADH° (330) and also the hydroquinone (86–88).

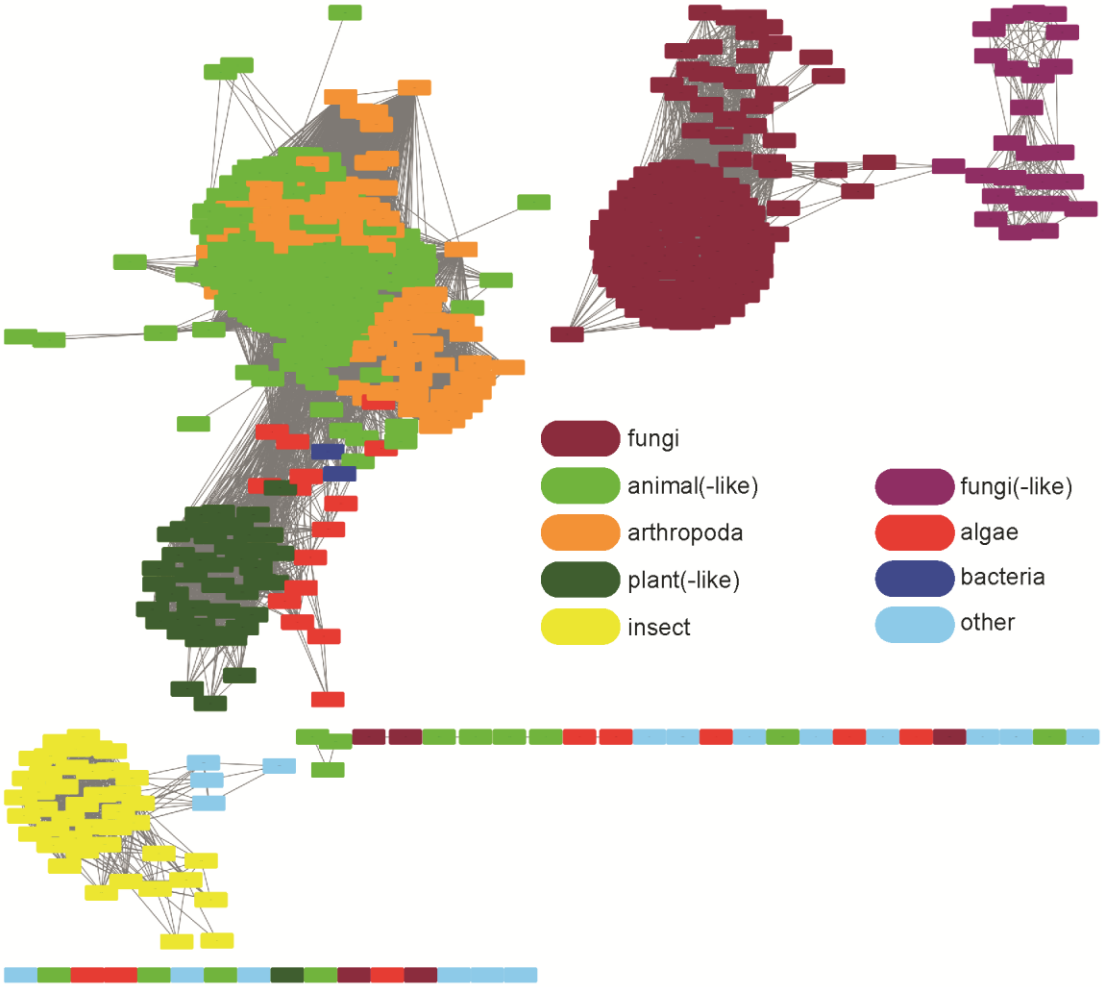

Figure 37 Sequence similarity network of the aCRY/(6-4)PHL family colored by their organism of origin.

These requirements can be mapped onto the SSN of the whole aCRY/(6-4)PHL subclass to see if there is a distribution of cryptochromes, photolyases and bifunctional members in relation to their organismic origin (Figure 37). Also the C482, which is discussed in Oldemeyer *et al.* (294), is taken into account (Figure 38a). This cysteine is in close proximity to the distal Y373 of the electron transfer tetrad. It is discussed to be a potential electron

donor, which could form a disulfide bond with another oxidized species. This Cys is conserved among algal and fungal sequences. The fourth electron donor could be a Tyr or Trp as described in Nohr *et al.* (293). Trp is prominent in animal and insect sequences, whereas Tyr is conserved among algal and fungal species (Figure 38b). In plants, it is either present as a Phe or another residue, so plant (6.4)PHLs contain the “classical” Trp-triad.

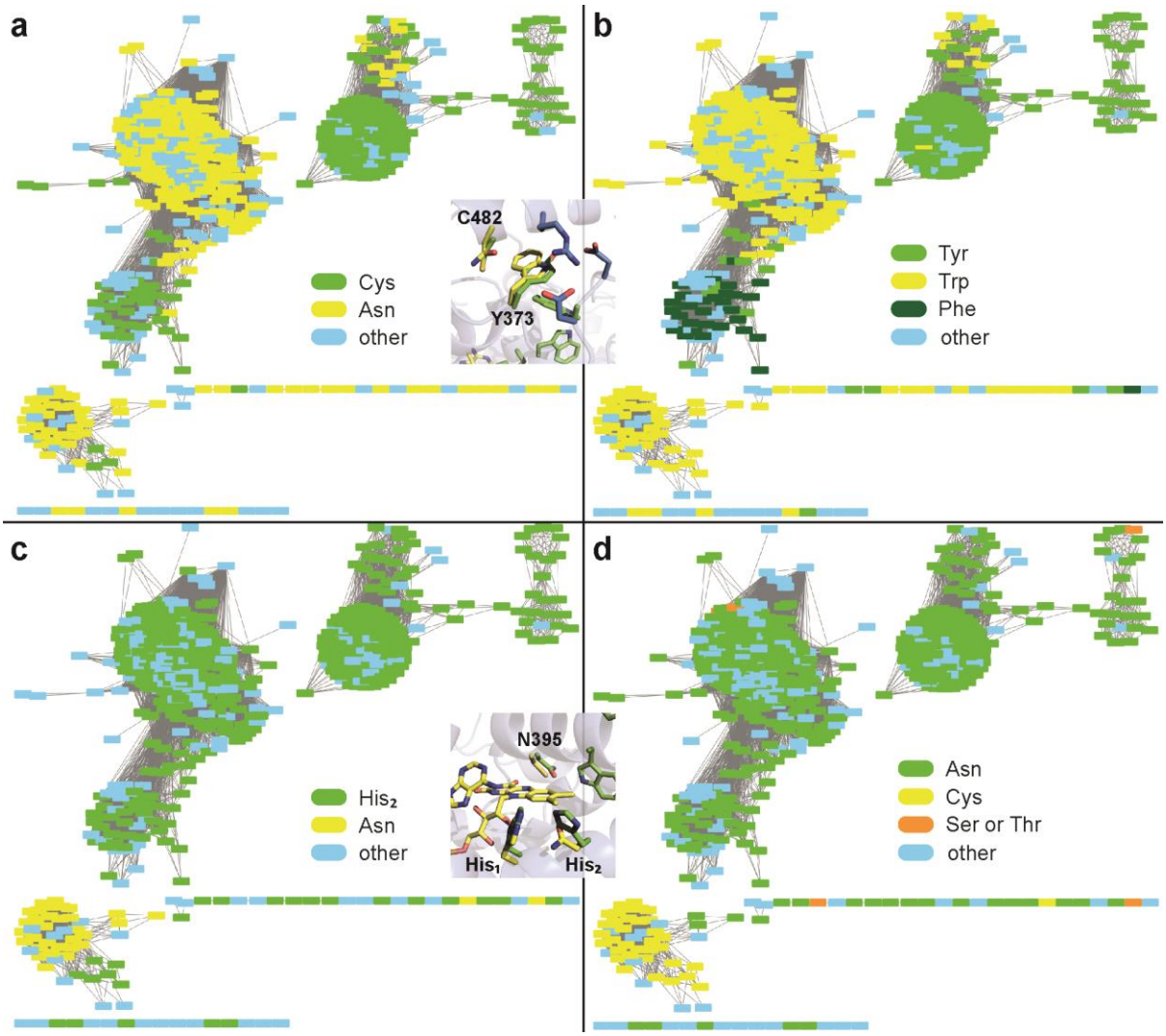

Figure 38 Sequence similarity network of the aCRY/(6-4)PHL family colored by the occurrence of different functional-relevant amino acids. Structures show the superimposition of *Cr*aCRY (green, 5ZM0) and *Dm*CRY (yellow, 4GU5). Numbers refer to the *Cr*aCRY sequence. a) The protein sequences are colored by whether they harbor a Cys (green), Asn (yellow) or a different aa (blue) in close proximity to Trp/Tyr_4 (C483 in *Cr*aCRY). b) The fourth electron donor could be either a Tyr (green) or Trp (yellow). In plant(-like) sequences there is either a Phe (dark green) or another aa (blue) present at this position (Y373 in *Cr*aCRY). c) His_2 (green), which is essential for (6-4)PP repair, is present in *Cr*aCRY (H361), most animals and fungi. Insects harbor Asn (yellow) at this position. d) Most

sequences of this subgroup contain Asn in a short distance to the N5 of the flavin cofactor (N395 in *Cr*aCRY). However, insect sequences harbor a Cys or another residue.

Concerning the catalytic histidine residues His_1 and His_2, all sequences compared in this analysis carry His_1. However, in insect CRYs, His_2 is exchanged to an Asn (Figure 38c). This fact and the missing proton donor near to the flavin (Figure 38c) dismisses this cluster of insect CRYs as potential (6-4)PHLs. Surprisingly, there are a lot of similarities between fungal and algal sequences as almost all fungal proteins contain the residues, which were identified to be responsible for the dual function *Cr*aCRY. They are the only class that also harbors a Tyr as fourth electron donor, so they might also form a stable radical close to the protein surface. A bifunctionality of these fungal CRYs was already suspected for three different members of this group (321–323) and this analysis is giving a new insight in this topic.

To conclude with this part, to function as a photolyase, the enzyme has to have a C-terminal domain with a positively charged cleft for binding of the phosphate backbone of the DNA. Secondly, the residues essential to catalyze and stabilize the electron rearrangement during the (6-4)-bond breakage and rebuilding of intact DNA fragments. And last but not least, the capability to form $FADH^-$ to generate the required $FADH^{-*}$ with a suitable activation energy for electron transfer. If these are the minimal requirements for (6-4) DNA repair, one could think of building an artificial minimal photolyase which fits all these requirements.

To come back to the initial question of how *Cr*aCRY could achieve its bifunctionality, we propose a model (Figure 39) as described in Franz-Badur *et al.* (316). Here, *Cr*aCRY is present in the oxidized state during the night, where it is able to bind a yet unknown binding partner X. This could be the plant CRY in *Chlamydomonas*, which potentially forms a complex with *Cr*aCRY to inhibit mating ability (227). In the day phase, *Cr*aCRY undergoes light-induced reduction of the cofactor. The formation of the long-lived TyrO° triggers the breakage of a hydrogen-bond-network involving helix α22. This leads to a movement of this helix, which results in a rearrangement of the CTE and release of the binding partner X. At the current state, we cannot be sure, if this happens already after reduction from FAD_{OX} to FADH° or if the $FADH^-$ has to be formed, but we would suggest that the first reduction

might already lead to this reaction. Because of the formation of the hydroquinone state, *Cra*CRY is now able to repair (6-4) lesions during the day inside the nucleus.

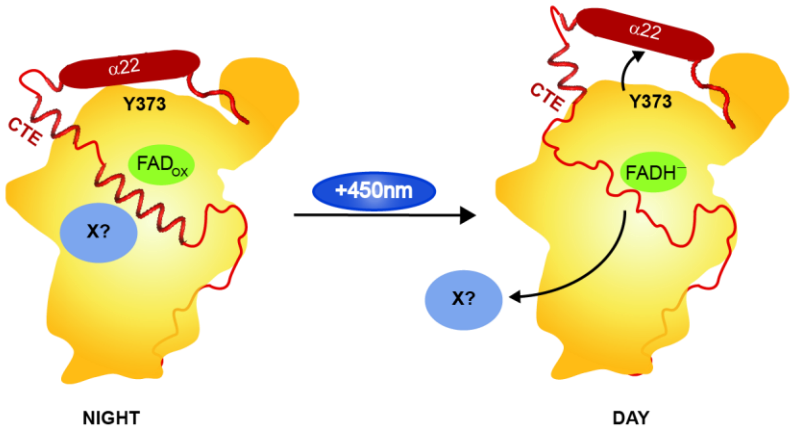

Figure 39 Model of the structural movement in *Cra*CRY from the fully oxidized to the hydroquinone state of the FAD based on the HDX data. In between, the neutral semiquinone state is forming (FADH°), but we have no structural information concerning this. In the shown model, the C-terminal extension (CTE, red) is located over the protein surface and is partly structured. We propose that an unknown signaling partner X (light blue) can bind to *Cra*CRY during the night, when it is located over the whole cell body. During the day, the hydroquinone state is forming ($FADH^-$). Because of the radical pair formation [Y373° and $FADH^{-}$°] during photoreduction, the H-bond network between α22, D323 and D321 is disrupted which leads to a movement of the helix and therefore a change in the CTE. The structured region in the CTE gets unfolded and factor X is getting released.

Magnetoreception

Birds and other animals use the magnetic field of the earth for navigation and orientation. This is known for years, but the primary biological sensor and process has not been fully identified or characterized till today. Already in 1978, Schulten *et al.* (331) proposed a biomagnetic compass based on the spin correlation of a radical pair. It took around two decades to connect this hypothesis with the radical pair produced during cryptochrome photoreduction (332). Today, there are several studies, which link animal CRYs to the process of magnetoreception (see section 1.7). But how does it work and what are the requirements for a protein to act as a magnetoreceptor? Can *Cra*CRY act as a magnetoreceptor?

The basis for a biomagnetic compass, according to the theory of Schulten *et al.* (331), is the generation of a radical pair (RP) with correlated spins and a suitable life time (215). In Figure

40, the photoreduction mechanism of a cryptochrome is shown. Here, FAD gets excited by absorbing energy from blue light. Afterwards ^{S}[FAD°$^{-}$TrpH°$^{+}$] (RP1) forms in a singlet state, which can only be generated by a spin-conserving electron transfer to the photoexcited singlet state of the FAD. By singlet-triplet interconversion, the equilibrium of singlet and triplet states is generated for RP1. Through spin-independent (de)protonation the secondary radical pair (RP2) is formed. In this case, with the life-times obtained from experiments with *At*CRY1 and *Ec*CPD (333, 334), the recombination of RP1 and the conversion of RP1 to RP2 happens on a 1 µs timescale. This is a correct life time to experience magnetic-field effects, as the spin-correlation of RP1 relaxes before RP2 recombines (1-10 ms). Another requirement for magnetoreception is the orientation of the receptors as many radical pairs are needed to achieve a sufficient signal-to-noise ratio. Therefore, the spins have to be at least partially aligned, so the proteins have to be immobilized someway (335–337). This could be realized *via* incorporation of cryptochromes in the cytoskeleton or association to the membrane (215). Whether this requirement is really a limiting factor is questionable. Recent theoretical analysis suggests that even a completely disordered array of CRYs in a cell may be capable to act as directional sensor (338). Additionally, it was demonstrated that the avian compass works best using light in a range of 400-565 nm (339, 340). The FAD_{OX} alone only covers the range up to 500 nm, which leads to the conclusion that also the neutral radical FADH°, which absorbs over 500 nm, may be involved in radical pair formation or decay (341, 342).

The radical pairs of *Cra*CRY were studied with trEPR, transient absorption and TR-UV/Vis spectroscopy (293, 294). In all experiments, the formation of a tyrosyl radical could be observed. There is not much known about the (de)protonation state the tyrosyl adopts after electron transfer, but NOHR (343) suggests, under consideration of data from Tsentalovich *et al.* (344), that the positively charged TyrOH°$^{+}$ is being formed at first and gets deprotonated on a ns scale to TyrO°. Recently, but not yet published, ultra-fast spectroscopic data from P. PLAZA and P. MÜLLER (written correspondence) reveals, that TyrO° is forming in ~712 ps, but the deprotonation of TyrOH°$^{+}$ cannot be observed. They suggest that deprotonation might happen concomitant to electron transfer. In trEPR, the formation of [FADH°TyrO°] (RP2) can

be observed in 6 ms and it takes another 26 ms to decay (293) (Figure 40). Comparing this to the life times of *Dm*CRY with 2.5 µs and 6.8 ms, a striking difference is observable. In the *Cra*CRY-Y373F mutant, life times of 0.62 µs and 8.46 µs are significantly lower and can be compared to the life times of the *Dm*CRY-W394F mutant. Therefore, the stability of RP2 can be explained by the occurrence of the tyrosyl instead of a tryptophanyl radical. As for magnetosensitivity, the optimal time for formation of RP2 to exhibit magnetic field effects should be between ~1 µs and 100 µs (215, 343). For *Dm*CRY, this condition is matched and the fourth tryptophan seems not to shorten the life time of RP1 as much as a tyrosine does. The formation and decay of RP2 with FADH° as substrate was studied by Oldemeyer *et al.* (294). They determined the decay of [$FADH^-$ TyrO°] to 2.6 s, which is unusually long-lived for a tyrosyl radical. Nevertheless, the formation of [$FADH^-$TyrO°] is irrelevant when considering magnetosensitivity, as there is no radical pair with spin-correlation formed.

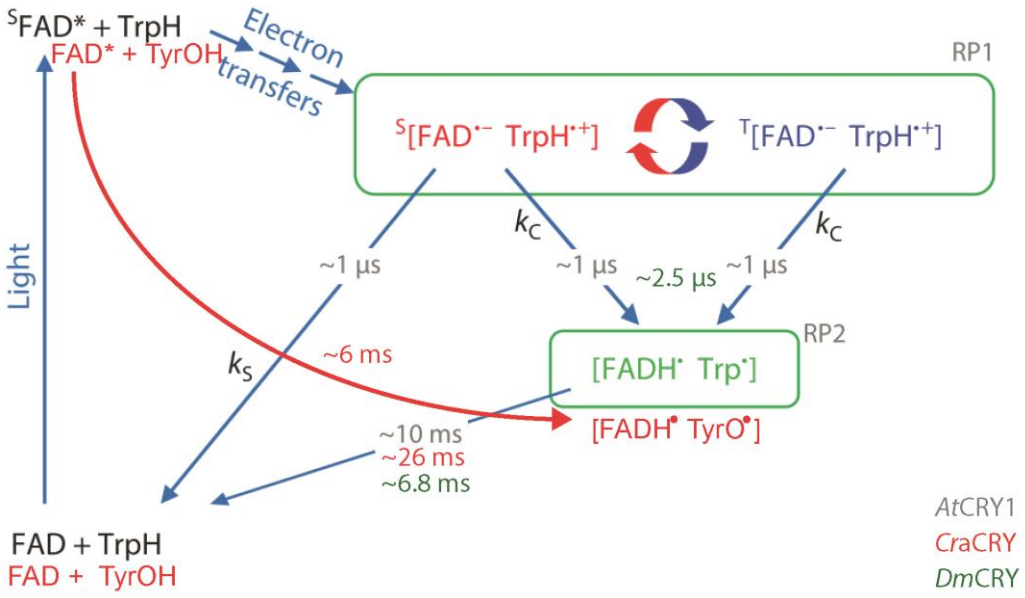

Figure 40 A photochemical reaction scheme of the CPF (adapted from (215)). RP1 is the magnetically sensitive radical pair, which undergoes singlet-triplet interconversion. RP2 gets formed either out of the singlet or triplet state of RP1 with a rate constant k_C. RP2 does not generate magnetic-field effects. Trp is the distal electron donor, in *At*CRY1 it is Trp3, in *Dm*CRY it is Trp4 and in case of *Cra*CRY it should be Tyr (red). The lifetime of RP2 is 10 ms in the garden warbler cryptochrome 1a and 1 ms in *At*CRY1.

In conclusion, we can exclude that *Cra*CRY is capable to function as a potential magnetosensor, because the deprotonation and formation of RP2 happens on a time-scale

unsuitable for magnetosensitivity. Nevertheless, the highly stable tyrosyl radical seems to be an outstanding property of this enzyme and might regulate its bifunctionality. For those CRYs acting as magnetoreceptors, we can state that the elongation of the Trp-triad to a Trp-tetrad appears to be beneficial, at least in the case of insect CRYs (293). The SSN reveals, that animal(-like) CRYs/(6-4)PHLs contain the fourth Trp as well, whereas fungi also harbor a Tyr (Figure 38).

6 Outlook

Our knowledge about CRY-dependent signaling reactions and CRY itself is still a growing field in research. In animals, some CRYs act as blue-light receptors while others seem to have lost their ability to sense light completely. They entrain the circadian rhythm, are transcriptional regulators and control intracellular signaling processes in metabolism and cellular response to DNA damages (section 1.7). They might even play a role in magnetoreception, the process underlying the avian compass. In the last years, oscillating genes of the circadian rhythm could be linked to almost every major disease, which led to the emerging field of chronotherapy (194, 198, 345). Here, not only the entrainment of the clock itself but also the timing of a medication has to be taken into account. A lot of genes that are targeted by drugs belonging to the circadian genes, meaning their expression levels are oscillating over a 24h period. Therefore, these drugs should be given to a patient under consideration of the body time (346–348). The complete understanding of circadian regulators is a necessity for chronotherapy. In terms of drug design to treat circadian diseases, one inhibitor for *m*CRY2 has been already developed through a structure-based approach (205). The compound KL001 binds in the interface of the FAD and DNA-binding site. In *m*CRY2 it prevents the SCF-FBXL3-mediated ubiquitination, but in other CRYs it might inhibit other interactions as well.

Another aspect of the future of cryptochromes is the utilization of these light-activated receptors in the field of optogenetics (349–354). Here, photoreceptors are getting genetically engineered to perform a desired reaction. To specifically manipulate such a system, the structural outputs of the photoreaction as well as the binding partners have to

be known. For CRYs, one optogenetic tool using the *At*CRY2-CIB interaction has already been developed (355), but there is still a lot of potential in this field. *Cr*aCRY could be a potential candidate for the development of an optogenetic sensor, as we already observed some structural changes upon photoreduction (Figure 39). This tool might also be switchable not only by blue, but also by yellow and red light. To utilize *Cr*aCRY for this purpose, the interaction partner should be identified and also the structural changes, *e.g*. in the semiquinone state, should be further investigated. Currently, it is not known in which reduction state *Cr*aCRY is binding an interaction partner and it might be promising to repeat pull-down assays with *Cr*aCRY in its semiquinone and hydroquinone state. The time-resolved SFX project at SACLA is focusing at the moment to resolve the intramolecular structural changes, which happen upon photoreduction of the flavin that might trigger large movements within *Cr*aCRY. Additionally to the photoreduction process, also the repair reactions of a class II CPD photolyase (*Mm*CPDII) and the (6-4)PP repair *via Cr*aCRY are studied now with TR-SFX. We expect that the (6-4) repair mechanism with the current one *vs.* two photon mechanism controversy can be resolved by this method.

Photolyases are already used in sunscreen and anti-aging creams against the formation of skin cancer and this kind of application is becoming increasingly popular in the cosmetics industry (356, 357). For that, the CPDI PHL from *A. nidulans* is getting encapsulated in liposomes and put into a lotion which can be applied to the skin. For this purpose, but also in general, the development of a minimal and highly stable photolyase could be a major advantage. Looking into a future, where data storage becomes a major concern, keeping up the integrity of DNA for long-term storage (358, 359) might be one task photolyases could contribute as well.

6 References

1. Kopp,G. and Lean,J.L. (2011) A new, lower value of total solar irradiance: Evidence and climate significance. *Geophys. Res. Lett.*, **38**, 1–7.
2. Heintzen,C. (2012) Plant and fungal photopigments. *Wiley Interdiscip. Rev. Membr. Transp. Signal.*, **1**, 411–432.
3. Rizzini,L., Favory,J.J., Cloix,C., Faggionato,D., O'Hara,A., Kaiserli,E., Baumeister,R., Schäfer,E., Nagy,F., Jenkins,G.I., *et al.* (2011) Perception of UV-B by the *arabidopsis* UVR8 protein. *Science*, **332**, 103–106.
4. Ernst,O.P., Lodowski,D.T., Elstner,M., Hegemann,P., Brown,L.S. and Kandori,H. (2014) Microbial and animal rhodopsins: Structures, functions, and molecular mechanisms. *Chem. Rev.*, **114**, 126–163.
5. Losi,A. and Gärtner,W. (2012) The Evolution of Flavin-Binding Photoreceptors: An Ancient Chromophore Serving Trendy Blue-Light Sensors. *Annu. Rev. Plant Biol.*, **63**, 49–72.
6. Chaves,I., Pokorny,R., Byrdin,M., Hoang,N., Ritz,T., Brettel,K., Essen,L.-O., van der Horst,G.T.J., Batschauer,A. and Ahmad,M. (2011) The cryptochromes: blue light photoreceptors in plants and animals. *Annu. Rev. Plant Biol.*, **62**, 335–364.
7. Kottke,T., Xie,A., Larsen,D.S. and Hoff,W.D. (2018) Photoreceptors Take Charge: Emerging Principles for Light Sensing. *Annu. Rev. Biophys.*, **47**, annurev-biophys-070317-033047.
8. Van Der Horst,M.A. and Hellingwerf,K.J. (2004) Photoreceptor Proteins, 'Star Actors of Modern Times': A Review of the Functional Dynamics in the Structure of Representative Members of Six Different Photoreceptor Families. *Acc. Chem. Res.*, **37**, 13–20.
9. Möglich,A., Yang,X., Ayers,R.A. and Moffat,K. (2010) Structure and Function of Plant Photoreceptors. *Annu. Rev. Plant Biol.*, **61**, 21–47.
10. Sancar,A. (1994) Structure and function of DNA photolyase. *Biochemistry*, **33**, 2–9.
11. Sancar,A. (2008) Structure and function of photolyase and in vivo enzymology: 50th Anniversary. *J. Biol. Chem.*, **283**, 32153–32157.
12. Kneuttinger,A.C., Kashiwazaki,G., Prill,S., Heil,K. and Carell,T. (2014) Formation and direct repair of UV-induced dimeric DNA pyrimidine lesions. *Photochem. Photobiol.*, **90**, 1–14.
13. Maul,M.J., Barends,T.R.M., Glas,A.F., Cryle,M.J., Domratcheva,T., Schneider,S., Schlichting,I. and Carell,T. (2008) Crystal structure and mechanism of a DNA (6-4) photolyase. *Angew. Chemie - Int. Ed.*, **47**, 10076–10080.
14. Rupert,C.S., Goodgal,S.H. and Herriott,R.M. (1958) Photoreactivation in vitro of ultraviolet-inactivated Hemophilus influenzae transforming factor. *J. Gen. Physiol.*, **41**, 451–471.
15. Kelner,A. (1949) Effect of visible light on the recovery of *Streptomyces griseus conidia* from ultraviolet irradiation injury. *Proc. Natl. Acad. Sci.*, **35**, 73–79.
16. Sancar,A. and Rupert,C.S. (1978) Cloning of the phr gene and amplification of photolyase in *Escherichia coli*. *Gene*, **4**, 295–308.
17. Sancar,A., Smith,F.W. and Sancar,G.B. (1984) Purification of *Escherichia coli* DNA Photolyase. *J. Biol. Chem.*, **259**, 6028–6032.
18. Essen,L.O. and Klar,T. (2006) Light-driven DNA repair by photolyases. *Cell. Mol. Life Sci.*, **63**, 1266–1277.
19. Sancar,A. (2003) Structure and Function of DNA Photolyase and Cryptochrome Blue-Light Photoreceptors. *Chem. Rev.*, **103**, 2203–2238.
20. Deisenhofer,J. (2000) DNA photolyases and cryptochromes. *Mutat. Res. - DNA Repair*, **460**, 143–149.
21. Kim,S.T., Malhotra,K., Smith,C.A., Taylor,J.S. and Sancar,A. (1994) Characterization of (6-4) photoproduct DNA photolyase. *J. Biol. Chem.*, **269**, 8535–8540.

22. Eker,A.P.M., Kooiman,P., Hessels,J.K.C. and Yasui,A. (1990) DNA Photoreactivating Enzyme from the Cyanobacterium *Anacystis nidulans*. *J. Biol. Chem.*, **265**, 8009–8015.
23. Kiener,A., Husain,I., Sancar,A. and Walsh,C. (1989) Purification and properties of Methanobacterium thermoautotrophicum DNA photolyase. *J. Biol. Chem.*, **264**, 13880–13887.
24. Todo,T., Takemori,H., Ryo,H., Ihara,M., Matsunaga,T., Nikaido,O., Sato,K. and Nomura,T. (1993) A new photoreactivating enzyme that specifically repairs ultraviolet light-induced (6-4)photoproducts. *Nature*, **361**, 371–374.
25. Li,Y.F., Kim,S.T. and Sancar,A. (1993) Evidence for lack of DNA photoreactivating enzyme in humans. *Proc. Natl. Acad. Sci.*, **90**, 4389–4393.
26. Hsu,D.S., Zhao,X., Zhao,S., Kazantsev,A., Wang,R.-P., Todo,T., Wei,Y.-F. and Sancar,A. (1996) Putative Human Blue-Light Photoreceptors hCRY1 and hCRY2 Are Flavoproteins. *Biochemistry*, **35**, 13871–13877.
27. Srinivasan,V., Schnitzlein,W.M. and Tripathy,D.N. (2001) Fowlpox Virus Encodes a Novel DNA Repair Enzyme, CPD-Photolyase, That Restores Infectivity of UV Light-Damaged Virus. *J. Virol.*, **75**, 1681–1688.
28. Afonso,C.L., Tulman,E.R., Lu,Z., Oma,E., Kutish,G.F. and Rock,D.L. (1999) The genome of *Melanoplus sanguinipes* entomopoxvirus. *J. Virol.*, **73**, 533–552.
29. Darwin,C. and Darwin,F. (1881) The power of movement in plants. *D. Applet.*
30. Gressel,J. (1979) Blue Light Photoreception. *Photochem. Photobiol.*, **30**, 749–754.
31. Ahmad,M. and Cashmore,A.R. (1993) HY4 gene of A. thaliana encodes a protein with characteristics of a blue-light photoreceptor. *Nature*, **366**, 162–166.
32. Malhotra,K., Kim,S.-T., Batschauer,A., Dawut,L. and Sancar,A. (1995) Putative Blue-Light Photoreceptors from *Arabidopsis thaliana* and *Sinapis alba* with a High Degree of Sequence Homology to DNA Photolyase Contain the Two Photolyase Cofactors but Lack DNA Repair Activity. *Biochemistry*, **34**, 6892–6899.
33. Lin,C. and Todo,T. (2005) The cryptochromes. *Genome Biol.*, **6**, 220.
34. Thresher,R.J., Vitaterna,M.H., Miyamoto,Y., Kazantsev,A., Hsu,D.S., Petit,C., Selby,C.P., Dawut,L., Smithies,O., Takahashi,J.S., *et al.* (1998) Role of mouse cryptochrome blue-light photoreceptor in circadian photoresponses. *Science*, **282**, 1490–4.
35. Ozturk,N. (2017) Phylogenetic and Functional Classification of the Photolyase/Cryptochrome Family. *Photochem. Photobiol.*, **93**, 104–111.
36. Öztürk,N., Song,S.-H., Özgür,S., Selby,C.P., Morrison,L., Partch,C., Zhong,D. and Sancar,A. (2007) Structure and Function of Animal Cryptochromes. *Cold Spring Harb. Symp. Quant. Biol.*, **72**, 119–131.
37. Partch,C.L., Clarkson,M.W., Özgür,S., Lee,A.L. and Sancar,A. (2005) Role of Structural Plasticity in Signal Transduction by the Cryptochrome Blue-Light Photoreceptor. *Biochemistry*, **44**, 3795–3805.
38. Selby,C.P. and Sancar,A. (2006) A cryptochrome/photolyase class of enzymes with single-stranded DNA-specific photolyase activity. *Proc. Natl. Acad. Sci.*, **103**, 17696–17700.
39. Pokorny,R., Klar,T., Hennecke,U., Carell,T., Batschauer,A. and Essen,L.-O. (2008) Recognition and repair of UV lesions in loop structures of duplex DNA by DASH-type cryptochrome. *Proc. Natl. Acad. Sci.*, **105**, 21023–21027.
40. Tagua,V.G., Pausch,M., Eckel,M., Gutiérrez,G., Miralles-Durán,A., Sanz,C., Eslava,A.P., Pokorny,R., Corrochano,L.M. and Batschauer,A. (2015) Fungal cryptochrome with DNA repair activity reveals an early stage in cryptochrome evolution. *Proc. Natl. Acad. Sci.*, **112**, 15130–15135.
41. Zhu,H., Yuan,Q., Briscoe,A.D., Froy,O., Casselman,A. and Reppert,S.M. (2006) The two CRYs of the butterfly. *Curr. Biol.*, **16**, 730.
42. Rubin,E.B., Shemesh,Y., Cohen,M., Elgavish,S., Robertson,H.M. and Bloch,G. (2006) Molecular

and phylogenetic analyses reveal mammalian-like clockwork in the honey bee (*Apis mellifera*) and shed new light on the molecular evolution of the circadian clock. *Genome Res.*, **16**, 1352–1365.

43. Ingram,K.K., Kutowoi,A., Wurm,Y., Shoemaker,D.W., Meier,R. and Bloch,G. (2012) The Molecular Clockwork of the Fire Ant *Solenopsis invicta*. *PLoS One*, **7**, 15–19.
44. Emery,P., So,W. V, Kaneko,M., Hall,J.C. and Rosbash,M. (1998) CRY, a Drosophila clock and light-regulated cryptochrome, is a major contributor to circadian rhythm resetting and photosensitivity. *Cell*, **95**, 669–679.
45. Ozturk,N., Selby,C.P., Song,S.-H., Ye,R., Tan,C., Kao,Y.-T., Zhong,D. and Sancar,A. (2009) Comparative Photochemistry of Animal Type 1 and Type 4 Cryptochromes. *Biochemistry*, **48**, 8585–8593.
46. Rivera,A.S., Ozturk,N., Fahey,B., Plachetzki,D.C., Degnan,B.M., Sancar,A. and Oakley,T.H. (2012) Blue-light-receptive cryptochrome is expressed in a sponge eye lacking neurons and opsin. *J. Exp. Biol.*, **215**, 1278–1286.
47. Müller,W.E.G., Wang,X., Schröder,H.C., Korzhev,M., Grebenjuk,V.A., Markl,J.S., Jochum,K.P., Pisignano,D. and Wiens,M. (2010) A cryptochrome-based photosensory system in the siliceous sponge *Suberites domuncula* (Demospongiae). *FEBS J.*, **277**, 1182–1201.
48. Müller,W.E.G., Wendt,K., Geppert,C., Wiens,M., Reiber,A. and Schröder,H.C. (2006) Novel photoreception system in sponges? Unique transmission properties of the stalk spicules from the hexactinellid *Hyalonema sieboldi*. *Biosens. Bioelectron.*, **21**, 1149–1155.
49. Müller,W.E.G., Schröder,H.C., Markl,J.S., Grebenjuk,V.A., Korzhev,M., Steffen,R. and Wang,X. (2013) Cryptochrome in Sponges: A Key Molecule Linking Photoreception with Phototransduction. *J. Histochem. Cytochem.*, **61**, 814–832.
50. Scheerer,P., Zhang,F., Kalms,J., Von Stetten,D., Krauß,N., Oberpichler,I. and Lamparter,T. (2015) The class III cyclobutane pyrimidine dimer photolyase structure reveals a new antenna chromophore binding site and alternative photoreduction pathways. *J. Biol. Chem.*, **290**, 11504–11514.
51. Oberpichler,I., Pierik,A.J., Wesslowski,J., Pokorny,R., Rosen,R., Vugman,M., Zhang,F., Neubauer,O., Ron,E.Z., Batschauer,A., *et al.* (2011) A Photolyase-Like Protein from Agrobacterium tumefaciens with an Iron-Sulfur Cluster. *PLoS One*, **6**, e26775.
52. Geisselbrecht,Y., Frühwirth,S., Schroeder,C., Pierik,A.J., Klug,G. and Essen,L.-O. (2012) CryB from *Rhodobacter sphaeroides*: a unique class of cryptochromes with new cofactors. *EMBO Rep.*, **13**, 223–229.
53. Zhang,F., Scheerer,P., Oberpichler,I., Lamparter,T., Krauss,N., Krauß,N. and Krauss,N. (2013) Crystal structure of a prokaryotic (6-4) photolyase with an Fe-S cluster and a 6,7-dimethyl-8-ribityllumazine antenna chromophore. *Proc. Natl. Acad. Sci.*, **110**, 7217–7222.
54. Kiontke,S., Geisselbrecht,Y., Pokorny,R., Carell,T., Batschauer,A. and Essen,L.-O. (2011) Crystal structures of an archaeal class II DNA photolyase and its complex with UV-damaged duplex DNA. *EMBO J.*, **30**, 4437–4449.
55. Hitomi,K., Arvai,A.S., Yamamoto,J., Hitomi,C., Teranishi,M., Hirouchi,T., Yamamoto,K., Iwai,S., Tainer,J.A., Hidema,J., *et al.* (2012) Eukaryotic class II cyclobutane pyrimidine dimer photolyase structure reveals basis for improved ultraviolet tolerance in plants. *J. Biol. Chem.*, **287**, 12060–12069.
56. Oliveri,P., Fortunato,A.E., Petrone,L., Ishikawa-Fujiwara,T., Kobayashi,Y., Todo,T., Antonova,O., Arboleda,E., Zantke,J., Tessmar-Raible,K., *et al.* (2014) The Cryptochrome/Photolyase Family in aquatic organisms. *Mar. Genomics*, **14**, 23–37.
57. Coesel,S., Mangogna,M., Ishikawa,T., Heijde,M., Rogato,A., Finazzi,G., Todo,T., Bowler,C. and Falciatore,A. (2009) Diatom PtCPF1 is a new cryptochrome/photolyase family member with

DNA repair and transcription regulation activity. *EMBO Rep.*, **10**, 655–661.
58. Heijde,M., Zabulon,G., Corellou,F., Ishikawa,T., Brazard,J., Usman,A., Sanchez,F., Plaza,P., Martin,M., Falciatore,A., *et al.* (2010) Characterization of two members of the cryptochrome/photolyase family from *Ostreococcus tauri* provides insights into the origin and evolution of cryptochromes. *Plant, Cell Environ.*, **33**, 1614–1626.
59. Park,H.-W.W., Kim,S.-T.T., Sancar,A., Deisenhofer,J., Deissenhofer,J. and Deisenhofer,J. (1995) Crystal structure of DNA photolyase from Escherichia coli. *Science*, **268**, 1866–1872.
60. Hanukoglu,I. (2015) Proteopedia: Rossmann fold: A beta-alpha-beta fold at dinucleotide binding sites. *Biochem. Mol. Biol. Educ.*, **43**, 206–209.
61. Holbrook,J., Liljas,A., Steindel,S. and Rossmann,M. (1975) The Enzymes New York: Academic Press.
62. Zhang,M., Wang,L. and Zhong,D. (2017) Photolyase: Dynamics and Mechanisms of Repair of Sun-Induced DNA Damage. *Photochem. Photobiol.*, **93**, 78–92.
63. Klar,T., Pokorny,R., Moldt,J., Batschauer,A. and Essen,L.O. (2007) Cryptochrome 3 from *Arabidopsis thaliana*: Structural and Functional Analysis of its Complex with a Folate Light Antenna. *J. Mol. Biol.*, **366**, 954–964.
64. Zoltowski,B.D., Vaidya,A.T., Top,D., Widom,J., Young,M.W. and Crane,B.R. (2011) Structure of full-length *Drosophila* cryptochrome. *Nature*, **480**, 396–399.
65. Levy,C., Zoltowski,B.D., Jones,A.R., Vaidya,A.T., Top,D., Widom,J., Young,M.W., Scrutton,N.S., Crane,B.R. and Leys,D. (2013) Updated structure of *Drosophila* cryptochrome. *Nature*, **495**, E3–E4.
66. Rosato,E., Codd,V., Mazzotta,G., Piccin,A., Zordan,M., Costa,R. and Kyriacou,C.P. (2001) Light-dependent interaction between *Drosophila* CRY and the clock protein PER mediated by the carboxy terminus of CRY. *Curr. Biol.*, **11**, 909–917.
67. Ceriani,M.F., Darlington,T.K., Staknis,D., Más,P., Petti,A.A., Weitz,C.J. and Kay,S.A. (1999) Light-Dependent Sequestration of TIMELESS by CRYPTOCHROME. *Science*, **285**, 553–556.
68. Chaves,I., Yagita,K., Barnhoorn,S., Okamura,H., van der Horst,G.T.J. and Tamanini,F. (2006) Functional Evolution of the Photolyase/Cryptochrome Protein Family: Importance of the C Terminus of Mammalian CRY1 for Circadian Core Oscillator Performance. *Mol. Cell. Biol.*, **26**, 1743–1753.
69. van der Schalie,E.A., Conte,F.E., Marz,K.E. and Green,C.B. (2007) Structure/Function Analysis of *Xenopus* Cryptochromes 1 and 2 Reveals Differential Nuclear Localization Mechanisms and Functional Domains Important for Interaction with and Repression of CLOCK-BMAL1. *Mol. Cell. Biol.*, **27**, 2120–2129.
70. Khan,S.K., Xu,H., Ukai-Tadenuma,M., Burton,B., Wang,Y., Ueda,H.R. and Liu,A.C. (2012) Identification of a novel cryptochrome differentiating domain required for feedback repression in circadian clock function. *J. Biol. Chem.*, **287**, 25917–25926.
71. Gao,P., Yoo,S.H., Lee,K.J., Rosensweig,C., Takahashi,J.S., Chen,B.P. and Green,C.B. (2013) Phosphorylation of the cryptochrome 1 C-terminal tail regulates circadian period length. *J. Biol. Chem.*, **288**, 35277–35286.
72. Harada,Y., Sakai,M., Kurabayashi,N., Hirota,T. and Fukada,Y. (2005) Ser-557-phosphorylated mCRY2 is degraded upon synergistic phosphorylation by glycogen synthase kinase-3β. *J. Biol. Chem.*, **280**, 31714–31721.
73. Xing,W., Busino,L., Hinds,T.R., Marionni,S.T., Saifee,N.H., Bush,M.F., Pagano,M. and Zheng,N. (2013) SCF(FBXL3) ubiquitin ligase targets cryptochromes at their cofactor pocket. *Nature*, **496**, 64–68.
74. Rosensweig,C., Reynolds,K.A., Gao,P., Laothamatas,I., Shan,Y., Ranganathan,R., Takahashi,J.S. and Green,C.B. (2018) An evolutionary hotspot defines functional differences between

CRYPTOCHROMES. *Nat. Commun.*, **9**, 1–15.

75. Michael,A.K., Fribourgh,J.L., Chelliah,Y., Sandate,C.R., Hura,G.L., Schneidman-Duhovny,D., Tripathi,S.M., Takahashi,J.S. and Partch,C.L. (2017) Formation of a repressive complex in the mammalian circadian clock is mediated by the secondary pocket of CRY1. *Proc. Natl. Acad. Sci.*, **114**, 1560–1565.
76. Klar,T., Pokorny,R., Moldt,J., Batschauer,A. and Essen,L.-O. (2007) Cryptochrome 3 from Arabidopsis thaliana: structural and functional analysis of its complex with a folate light antenna. *J. Mol. Biol.*, **366**, 954–964.
77. Park,H.W., Kim,S.T., Sancar,A. and Deisenhofer,J. (1995) Crystal structure of DNA photolyase from *Escherichia coli*. *Science*, **268**, 1866–1872.
78. Kiontke,S., Gnau,P., Haselsberger,R., Batschauer,A. and Essen,L.-O.O. (2014) Structural and evolutionary aspects of antenna chromophore usage by class II photolyases. *J. Biol. Chem.*, **289**, 19659–19669.
79. Klar,T., Kaiser,G., Hennecke,U., Carell,T., Batschauer,A. and Essen,L.-O. (2006) Natural and non-natural antenna chromophores in the DNA photolyase from *Thermus thermophilus*. *Chembiochem*, **7**, 1798–1806.
80. Fujihashi,M., Numoto,N., Kobayashi,Y., Mizushima,A., Tsujimura,M., Nakamura,A., Kawarabayasi,Y. and Miki,K. (2007) Crystal structure of archaeal photolyase from *Sulfolobus tokodaii* with two FAD molecules: implication of a novel light-harvesting cofactor. *J. Mol. Biol.*, **365**, 903–910.
81. Harbach,P.H.P., Schneider,M., Faraji,S. and Dreuw,A. (2013) Intermolecular coulombic decay in biology: The initial electron detachment from FADH-in DNA photolyases. *J. Phys. Chem. Lett.*, **4**, 943–949.
82. Kao,Y.T., Tan,C., Song,S.H., Öztürk,N., Li,J., Wang,L., Sancar,A. and Zhong,D. (2008) Ultrafast dynamics and anionic active states of the flavin cofactor in cryptochrome and photolyase. *J. Am. Chem. Soc.*, **130**, 7695–7701.
83. Liu,B., Liu,H., Zhong,D. and Lin,C. (2010) Searching for a photocycle of the cryptochrome photoreceptors. *Curr. Opin. Plant Biol.*, **13**, 578–586.
84. Kim,S.T., Sancar,A., Essenmacher,C. and Babcock,G.T. (1993) Time-resolved EPR studies with DNA photolyase: excited-state FADH0 abstracts an electron from Trp-306 to generate FADH-, the catalytically active form of the cofactor. *Proc. Natl. Acad. Sci.*, **90**, 8023–8027.
85. Kavakli,I.H. and Sancar,A. (2004) Analysis of the role of intraprotein electron transfer in photoreactivation by DNA photolyase in vivo. *Biochemistry*, **43**, 15103–15110.
86. Zeugner,A., Byrdin,M., Bouly,J.-P., Bakrim,N., Giovani,B., Brettel,K. and Ahmad,M. (2005) Light-induced Electron Transfer in *Arabidopsis* Cryptochrome-1 Correlates with in Vivo Function. *J. Biol. Chem.*, **280**, 19437–19440.
87. Banerjee,R., Schleicher,E., Meier,S., Viana,R.M., Pokorny,R., Ahmad,M., Bittl,R. and Batschauer,A. (2007) The Signaling State of *Arabidopsis* Cryptochrome 2 Contains Flavin Semiquinone. *J. Biol. Chem.*, **282**, 14916–14922.
88. Bouly,J.-P., Schleicher,E., Dionisio-Sese,M., Vandenbussche,F., Van Der Straeten,D., Bakrim,N., Meier,S., Batschauer,A., Galland,P., Bittl,R., *et al.* (2007) Cryptochrome blue light photoreceptors are activated through interconversion of flavin redox states. *J. Biol. Chem.*, **282**, 9383–91.
89. Öztürk,N., Song,S.-H., Selby,C.P. and Sancar,A. (2008) Animal type 1 cryptochromes. Analysis of the redox state of the flavin cofactor by site-directed mutagenesis. *J. Biol. Chem.*, **283**, 3256–3263.
90. Dodson,C.A., Hore,P.J. and Wallace,M.I. (2013) A radical sense of direction: Signalling and mechanism in cryptochrome magnetoreception. *Trends Biochem. Sci.*, **38**, 435–446.

91. Song,S.-H., Öztürk,N., Denaro,T.R., Arat,N.Ö., Kao,Y.-T., Zhu,H., Zhong,D., Reppert,S.M. and Sancar,A. (2007) Formation and Function of Flavin Anion Radical in Cryptochrome 1 Blue-Light Photoreceptor of Monarch Butterfly. *J. Biol. Chem.*, **282**, 17608–17612.
92. Aubert,C., Vos,M.H., Mathis,P., Eker,A.P.M. and Brettel,K. (2000) Mechanism of radical transfer during photoactivation of the flavoprotein DNA photolyase. *Nature*, **405**, 586–590.
93. Byrdin,M., Villette,S., Eker,A.P.M. and Brettel,K. (2007) Observation of an intermediate tryptophanyl radical in W306F mutant DNA photolyase from *Escherichia coli* supports electron hopping along the triple tryptophan chain. *Biochemistry*, **46**, 10072–10077.
94. Saxena,C., Sancar,A. and Zhong,D. (2004) Femtosecond dynamics of DNA photolyase: Energy transfer of antenna initiation and electron transfer of cofactor reduction. *J. Phys. Chem. B*, **108**, 18026–18033.
95. Wang,H., Saxena,C., Quan,D., Sancar,A. and Zhong,D. (2005) Femtosecond dynamics of flavin cofactor in DNA photolyase: Radical reduction, local Solvation, and charge recombination. *J. Phys. Chem. B*, **109**, 1329–1333.
96. Brettel,K. and Byrdin,M. (2010) Reaction mechanisms of DNA photolyase. *Curr. Opin. Struct. Biol.*, **20**, 693–701.
97. Li,X., Wang,Q., Yu,X., Liu,H., Yang,H., Zhao,C., Liu,X., Tan,C., Klejnot,J., Zhong,D., *et al.* (2011) *Arabidopsis* cryptochrome 2 (CRY2) functions by the photoactivation mechanism distinct from the tryptophan (trp) triad-dependent photoreduction. *Proc. Natl. Acad. Sci.*, **108**, 20844–9.
98. Gao,J., Wang,X., Zhang,M., Bian,M., Deng,W., Zuo,Z., Yang,Z., Zhong,D. and Lin,C. (2015) Trp triad-dependent rapid photoreduction is not required for the function of *Arabidopsis* CRY1. *Proc. Natl. Acad. Sci.*, **112**, 9135–9140.
99. von Zadow,A., Ignatz,E., Pokorny,R., Essen,L.-O. and Klug,G. (2016) *Rhodobacter sphaeroides* CryB is a bacterial cryptochrome with (6-4) photolyase activity. *FEBS J.*, 10.1111/febs.13924.
100. Narayanan,M., Singh,V.R., Kodali,G., Moravcevic,K. and Stanley,R.J. (2017) An Ethenoadenine FAD Analog Accelerates UV Dimer Repair by DNA Photolyase. *Photochem. Photobiol.*, **93**, 343–354.
101. Liu,Z., Zhang,M., Guo,X., Tan,C., Li,J., Wang,L., Sancar,A. and Zhong,D. (2013) Dynamic determination of the functional state in photolyase and the implication for cryptochrome. *Proc. Natl. Acad. Sci.*, **110**, 12972–12977.
102. Tan,C., Liu,Z., Li,J., Guo,X., Wang,L., Sancar,A. and Zhong,D. (2015) The molecular origin of high DNA-repair efficiency by photolyase. *Nat. Commun.*, **6**, 1–6.
103. Thiagarajan,V., Byrdin,M., Eker,A.P.M., Muller,P. and Brettel,K. (2011) Kinetics of cyclobutane thymine dimer splitting by DNA photolyase directly monitored in the UV. *Proc. Natl. Acad. Sci.*, **108**, 9402–9407.
104. Langenbacher,T., Zhao,X., Bieser,G., Heelis,P.F., Sancar,A. and Michel-Beyerle,M.E. (1997) Substrate and temperature dependence of DNA photolyase repair activity examined with ultrafast spectroscopy. *J. Am. Chem. Soc.*, **119**, 10532–10536.
105. MacFarlane IV,A.W. and Stanley,R.J. (2003) *Cis-Syn* thymidine dimer repair by DNA photolyase in real time. *Biochemistry*, **42**, 8558–8568.
106. Liu,Z., Tan,C., Guo,X., Kao,Y.-T., Li,J., Wang,L., Sancar,A. and Zhong,D. (2011) Dynamics and mechanism of cyclobutane pyrimidine dimer repair by DNA photolyase. *Proc. Natl. Acad. Sci.*, **108**, 14831–14836.
107. Kao,Y.-T., Saxena,C., Wang,L., Sancar,A. and Zhong,D. (2005) Direct observation of thymine dimer repair in DNA by photolyase. *Proc. Natl. Acad. Sci.*, **102**, 16128–16132.
108. Gindt,Y.M., Schelvis,J.P.M., Thoren,K.L. and Huang,T.H. (2005) Substrate binding modulates the reduction potential of DNA photolyase. *J. Am. Chem. Soc.*, **127**, 10472–10473.
109. Wang,J., Du,X., Pan,W., Wang,X. and Wu,W. (2015) Photoactivation of the

cryptochrome/photolyase superfamily. *J. Photochem. Photobiol. C Photochem. Rev.*, **22**, 84–102.
110. Mees,A., Klar,T., Gnau,P., Hennecke,U., Eker,A.P.M., Carell,T. and Essen,L.-O.O. (2004) Crystal structure of a photolyase bound to a CPD-like DNA lesion after *in situ* repair. *Science*, **306**, 1789–1793.
111. Masson,F., Laino,T., Rothlisberger,U. and Hutter,J. (2009) A QM/MM investigation of thymine dimer radical anion splitting catalyzed by DNA photolyase. *ChemPhysChem*, **10**, 400–410.
112. Vande Berg,B.J. and Sancar,G.B. (1998) Evidence for dinucleotide flipping by DNA photolyase. *J. Biol. Chem.*, **273**, 20276–20284.
113. Taylor,J.S. (1994) Unraveling the Molecular Pathway from Sunlight to Skin Cancer. *Acc. Chem. Res.*, **27**, 76–82.
114. Zhao,X., Liu,J., Hsu,D.S., Zhao,S., Taylor,J.S. and Sancar,A. (1997) Reaction mechanism of (6-4) photolyase. *J. Biol. Chem.*, **272**, 32580–32590.
115. Hitomi,K., Kim,S., Iwai,S., Harima,N., Otoshi,E., Ikenaga,M. and Todo,T. (1997) Binding and Catalytic Properties of *Xenopus* (6-4) Photolyase. *J. Biol. Chem.*, **272**, 32591–32598.
116. Yamamoto,J., Tanaka,Y. and Iwai,S. (2009) Spectroscopic analysis of the pyrimidine(6–4)pyrimidone photoproduct: insights into the (6–4) photolyase reaction. *Org. Biomol. Chem.*, **7**, 161–166.
117. Glas,A.F., Schneider,S., Maul,M.J., Hennecke,U. and Carell,T. (2009) Crystal Structure of the T(6-4)C Lesion in Complex with a (6-4) DNA Photolyase and Repair of UV-Induced (6-4) and Dewar Photolesions. *Chem. - A Eur. J.*, **15**, 10387–10396.
118. Borg,O.A., Eriksson,L.A. and Durbeej,B. (2007) Electron-transfer induced repair of 6-4 photoproducts in DNA: A computational study. *J. Phys. Chem. A*, **111**, 2351–2361.
119. Hitomi,K., Nakamura,H., Kim,S.T., Mizukoshi,T., Ishikawa,T., Iwai,S. and Todo,T. (2001) Role of Two Histidines in the (6-4) Photolyase Reaction. *J. Biol. Chem.*, **276**, 10103–10109.
120. Li,J., Liu,Z., Tan,C., Guo,X., Wang,L., Sancar,A. and Zhong,D. (2010) Dynamics and mechanism of repair of ultraviolet-induced (6-4) photoproduct by photolyase. *Nature*, **466**, 887–890.
121. Faraji,S. and Dreuw,A. (2012) Proton-transfer-steered mechanism of photolesion repair by (6-4)-photolyases. *J. Phys. Chem. Lett.*, **3**, 227–230.
122. Domratcheva,T. and Schlichting,I. (2009) Electronic structure of (6-4) DNA photoproduct repair involving a non-oxetane pathway. *J. Am. Chem. Soc.*, **131**, 17793–17799.
123. Sadeghian,K., Bocola,M., Merz,T., Schütz,M. and Schu,M. (2010) Theoretical Study on the Repair Mechanism of the (6−4) Photolesion by the (6−4) Photolyase. *J. Am. Chem. Soc.*, **132**, 16285–16295.
124. Yamamoto,J., Martin,R., Iwai,S., Plaza,P. and Brettel,K. (2013) Repair of the (6-4) photoproduct by DNA photolyase requires two photons. *Angew. Chemie - Int. Ed.*, **52**, 7432–7436.
125. Yamamoto,J., Plaza,P. and Brettel,K. (2017) Repair of (6-4) Lesions in DNA by (6-4) Photolyase: 20 Years of Quest for the Photoreaction Mechanism. *Photochem. Photobiol.*, **93**, 51–66.
126. Cichon,M.K., Arnold,S. and Carell,T. (2002) A (6-4) photolyase model: Repair of DNA (6-4) lesions requires a reduced and deprotonated flavin. *Angew. Chemie - Int. Ed.*, **41**, 767–770.
127. Friedel,M.G., Cichon,M.K. and Carell,T. (2005) Model compounds for (6-4) photolyases: A comparative flavin induced cleavage study of oxetanes and thietanes. *Org. Biomol. Chem.*, **3**, 1937–1941.
128. Stafforst,T. and Diederichsen,U. (2005) (6-4)-Photolyase activity requires a charge shift reaction. *Chem. Commun.*, 10.1039/b503699b.
129. Schleicher,E., Hitomi,K., Kay,C.W.M., Getzoff,E.D., Todo,T. and Weber,S. (2007) Electron nuclear double resonance differentiates complementary roles for active site histidines in (6-4) photolyase. *J. Biol. Chem.*, **282**, 4738–4747.

130. Moughal Shahi,A.R. and Domratcheva,T. (2013) Challenges in computing electron-transfer energies of DNA repair using hybrid QM/MM models. *J. Chem. Theory Comput.*, **9**, 4644–4652.
131. Dreuw,A. and Faraji,S. (2013) A quantum chemical perspective on (6-4) photolesion repair by photolyases. *Phys. Chem. Chem. Phys.*, **15**, 19957–19969.
132. Harbach,P.H.P., Borowka,J., Bohnwagner,M.V. and Dreuw,A. (2010) DNA (6-4) photolesion repair occurs in the electronic ground state of the tt dinucleotide dimer radical anion. *J. Phys. Chem. Lett.*, **1**, 2556–2560.
133. Condic-Jurkic,K., Smith,A.S., Zipse,H. and Smith,D.M. (2012) The protonation states of the active-site histidines in (6-4) potolyase. *J. Chem. Theory Comput.*, **8**, 1078–1091.
134. Faraji,S., Zhong,D. and Dreuw,A. (2016) Characterization of the Intermediate in and Identification of the Repair Mechanism of (6 - 4) Photolesions by Photolyases. *Angew. Chemie Int. Ed.*, **55**, 5175–5178.
135. Toshiaki Matsubara, Nozomi Araida, Daichi Hayashi,H.Y. (2014) Computationa l Study on the Mechanism of the Electron-Transfer- Induced Repair of the (6-4)T-T Photoproduct of DNA by Photolyase : Possibility of a Radical Cation Pathway. *Bull. Chem. Soc. Jpn.*, **87**, 390–399.
136. Domratcheva,T. (2011) Neutral histidine and photoinduced electron transfer in DNA photolyases. *J. Am. Chem. Soc.*, **133**, 18172–18182.
137. Faraji,S., Groenhof,G. and Dreuw,A. (2013) Combined QM/MM investigation on the light-driven electron-induced repair of the (6-4) thymine dimer catalyzed by DNA photolyase. *J. Phys. Chem. B*, **117**, 10071–10079.
138. Faraji,S., Wirz,L. and Dreuw,A. (2013) Quantum chemical study of the enzymatic repair of T(6-4)C/C(6-4)T UV-photolesions by DNA photolyases. *ChemPhysChem*, **14**, 2817–2824.
139. Domratcheva,T., Iwata,T. and Kandori,H. (2016) Single Hydrogen Bond Donation from Flavin N 5 to Proximal Asparagine Ensures FAD Reduction in DNA Photolyase. 10.1021/jacs.5b10533.
140. Faraji,S. and Dreuw,A. (2014) Physicochemical mechanism of light-driven DNA repair by (6-4) photolyases. *Annu. Rev. Phys. Chem.*, **65**, 275–92.
141. Faraji,S. and Dreuw,A. (2017) Insights into Light-driven DNA Repair by Photolyases: Challenges and Opportunities for Electronic Structure Theory. *Photochem. Photobiol.*, 10.1111/php.12679.
142. Franz,S., Ignatz,E., Wenzel,S., Zielosko,H., Putu,E.P.G.N., Maestre-Reyna,M., Tsai,M.-D., Yamamoto,J., Mittag,M. and Essen,L.-O. (2018) Structure of the bifunctional cryptochrome aCRY from Chlamydomonas reinhardtii. *Nucleic Acids Res.*, **46**, 8010–8022.
143. Hoffman,P.D., Batschauer,A. and Hays,J.B. (1996) PHH1 , a novel gene from *Arabidopsis thaliana* that encodes a protein similar to plant blue-light photoreceptors and microbial photolyases. *Mol. Gen. Genet. MGG*, **253**, 259–265.
144. Yang,Z., Liu,B., Su,J., Liao,J., Lin,C. and Oka,Y. (2016) Cryptochromes Orchestrate Transcription Regulation of Diverse Blue Light Responses in Plants. *Photochem. Photobiol.*, **93**, 112–127.
145. Brautigam,C.A., Smith,B.S., Ma,Z., Palnitkar,M., Tomchick,D.R., Machius,M. and Deisenhofer,J. (2004) Structure of the photolyase-like domain of cryptochrome 1 from *Arabidopsis thaliana*. *Proc. Natl. Acad. Sci.*, **101**, 12142–12147.
146. Orth,C., Niemann,N., Hennig,L., Essen,L.O. and Batschauer,A. (2017) Hyperactivity of the *Arabidopsis* cryptochrome (cry1) L407F mutant is caused by a structural alteration close to the cry1 ATP-binding site. *J. Biol. Chem.*, **292**, 12906–12920.
147. Eckel,M., Steinchen,W. and Batschauer,A. (2018) ATP boosts lit state formation and activity of *Arabidopsis* cryptochrome 2. *Plant J.*, 10.1111/tpj.14039.
148. Yu,X., Shalitin,D., Liu,X., Maymon,M., Klejnot,J., Yang,H., Lopez,J., Zhao,X., Bendehakkalu,K.T. and Lin,C. (2007) Derepression of the NC80 motif is critical for the photoactivation of Arabidopsis CRY2. *Proc. Natl. Acad. Sci.*, **104**, 7289–94.
149. Sang,Y., Li,Q.-H., Rubio,V., Zhang,Y.-C., Mao,J., Deng,X. and Yang,H.-Q. (2005) N-Terminal

Domain-Mediated Homodimerization Is Required for Photoreceptor Activity of *Arabidopsis* CRYPTOCHROME 1. *Plant Cell*, **17**, 1569–1584.

150. Rosenfeldt,G., Viana,R.M., Mootz,H.D., von Arnim,A.G. and Batschauer,A. (2008) Chemically Induced and Light-Independent Cryptochrome Photoreceptor Activation. *Mol. Plant*, **1**, 4–14.
151. Partch,C.L. and Sancar,A. (2005) Photochemistry and Photobiology of Cryptochrome Blue-light Photopigments: The Search for a Photocycle. *Photochem. Photobiol.*, **81**, 1291.
152. Shalitin,D., Yang,H., Mockler,T.C., Maymon,M., Guo,H., Whitelam,G.C. and Lin,C. (2002) Regulation of Arabidopsis cryptochrome 2 by blue-light-dependent phosphorylation. *Nature*, **417**, 763–767.
153. Shalitin,D. (2003) Blue Light-Dependent *in Vivo* and *in Vitro* Phosphorylation of *Arabidopsis* Cryptochrome 1. *PLANT CELL ONLINE*, **15**, 2421–2429.
154. Wang,Q., Barshop,W.D., Bian,M., Vashisht,A.A., He,R., Yu,X., Liu,B., Nguyen,P., Liu,X., Zhao,X., *et al.* (2015) The blue light-dependent phosphorylation of the CCE domain determines the photosensitivity of Arabidopsis CRY2. *Mol. Plant*, **8**, 631–643.
155. Liu,Q., Wang,Q., Deng,W., Wang,X., Piao,M., Cai,D., Li,Y., Barshop,W.D., Yu,X., Zhou,T., *et al.* (2017) Molecular basis for blue light-dependent phosphorylation of *Arabidopsis* cryptochrome 2. *Nat. Commun.*, **8**, 15234.
156. Özgür,S. and Sancar,A. (2006) Analysis of Autophosphorylating Kinase Activities of *Arabidopsis* and Human Cryptochromes †. *Biochemistry*, **45**, 13369–13374.
157. Tan,S.-T., Dai,C., Liu,H.-T. and Xue,H.-W. (2013) *Arabidopsis* Casein Kinase1 Proteins CK1.3 and CK1.4 Phosphorylate Cryptochrome2 to Regulate Blue Light Signaling. *Plant Cell*, **25**, 2618–2632.
158. Kondoh,M., Shiraishi,C., Müller,P., Ahmad,M., Hitomi,K., Getzoff,E.D. and Terazima,M. (2011) Light-Induced Conformational Changes in Full-Length *Arabidopsis thaliana* Cryptochrome. *J. Mol. Biol.*, **413**, 128–137.
159. Lau,O.S. and Deng,X.W. (2012) The photomorphogenic repressors COP1 and DET1: 20 years later. *Trends Plant Sci.*, **17**, 584–593.
160. Holm,M., Hardtke,C.S., Gaudet,R. and Xing-Wang,D. (2001) Identification of a structural motif that confers specific interaction with the WD40 repeat domain of *Arabidopsis*COP1. *EMBO J.*, **20**, 118–127.
161. Osterlund,M.T., Hardtke,C.S., Ning,W. and Deng,X.W. (2000) Targeted destabilization of HY5 during light-regulated development of *Arabidopsis*. *Nature*, **405**, 462–466.
162. Liu,B., Zuo,Z., Liu,H., Liu,X. and Lin,C. (2011) *Arabidopsis* cryptochrome 1 interacts with SPA1 to suppress COP1 activity in response to blue light. *Genes Dev.*, **25**, 1029–1034.
163. Zuo,Z., Liu,H., Liu,B., Liu,X. and Lin,C. (2011) Blue light-dependent interaction of CRY2 with SPA1 regulates COP1 activity and floral initiation in arabidopsis. *Curr. Biol.*, **21**, 841–847.
164. Liu,L.-J., Zhang,Y.-C., Li,Q.-H., Sang,Y., Mao,J., Lian,H.-L., Wang,L. and Yang,H.-Q. (2008) COP1-mediated ubiquitination of CONSTANS is implicated in cryptochrome regulation of flowering in *Arabidopsis*. *Plant Cell*, **20**, 292–306.
165. Liu,H., Yu,X., Li,K., Klejnot,J., Yang,H., Lisiero,D. and Lin,C. (2008) Photoexcited CRY2 Interacts with CIB1 to Regulate Transcription and Floral Initiation in *Arabidopsis*. *Science*, **322**, 1535–1539.
166. Ma,D., Li,X., Guo,Y., Chu,J., Fang,S., Yan,C., Noel,J.P. and Liu,H. (2016) Cryptochrome 1 interacts with PIF4 to regulate high temperature-mediated hypocotyl elongation in response to blue light. *Proc. Natl. Acad. Sci.*, **113**, 224–229.
167. Pedmale,U. V., Huang,S.S.C., Zander,M., Cole,B.J., Hetzel,J., Ljung,K., Reis,P.A.B., Sridevi,P., Nito,K., Nery,J.R., *et al.* (2016) Cryptochromes Interact Directly with PIFs to Control Plant Growth in Limiting Blue Light. *Cell*, **164**, 233–245.

168. Cashmore,A.R., Jarillo,J.A., Wu,Y.-J. and Liu,D. (1999) Cryptochromes: Blue Light Receptors for Plants and Animals. *Science*, **284**, 760–765.
169. Wu,G. and Spalding,E.P. (2007) Separate functions for nuclear and cytoplasmic cryptochrome 1 during photomorphogenesis of *Arabidopsis* seedlings. *Proc. Natl. Acad. Sci.*, **104**, 18813–18818.
170. Zuo,Z.-C., Meng,Y.-Y., Yu,X.-H., Zhang,Z.-L., Feng,D.-S., Sun,S.-F., Liu,B. and Lin,C.-T. (2012) A Study of the Blue-Light-Dependent Phosphorylation, Degradation, and Photobody Formation of *Arabidopsis* CRY2. *Mol. Plant*, **5**, 726–733.
171. Más,P., Devlin,P.F., Panda,S. and Kay,S.A. (2000) Functional interaction of phytochrome B and cryptochrome 2. *Nature*, **408**, 207–211.
172. Sellaro,R., Hoecker,U., Yanovsky,M., Chory,J. and Casal,J.J. (2009) Synergism of Red and Blue Light in the Control of *Arabidopsis* Gene Expression and Development. *Curr. Biol.*, **19**, 1216–1220.
173. Ma,L., Li,J., Qu,L., Hager,J., Chen,Z. and Zhao,H. (2001) Light Control of *Arabidopsis* Development Entails Coordinated. *Plant Cell*, **13**, 2589–2607.
174. Liu,H., Liu,B., Zhao,C., Pepper,M. and Lin,C. (2011) The action mechanisms of plant cryptochromes. *Trends Plant Sci.*, **16**, 684–691.
175. Yang,Z., Yang,L., Liu,Q., Liu,W., Han,Y. and Kim,J. (2016) Photoactivation and inactivation of *Arabidopsis* cryptochrome 2. *Science*, **354**, 343–347.
176. Pittendrigh,C.S. (1993) Temporal organization: reflections of a Darwinian clock-watcher. *Annu. Rev. Physiol.*, **55**, 16–54.
177. Michael,A.K., Fribourgh,J.L., Van Gelder,R.N. and Partch,C.L. (2017) Animal Cryptochromes: Divergent Roles in Light Perception, Circadian Timekeeping and Beyond. *Photochem. Photobiol.*, **93**, 128–140.
178. Emerson,K.J., Bradshaw,W.E. and Holzapfel,C.M. (2008) Concordance of the circadian clock with the environment is necessary to maximize fitness in natural populations. *Evolution (N. Y).*, **62**, 979–983.
179. Frank,K.D. and Zimmerman,W.F. (1969) Action Spectra for Phase Shifts of a Circadiain Rhythm in *Drosophila*. *Science*, **163**, 688–689.
180. Klemm,E. and Ninnemann,H. (1976) Detailed action spectrum for the daily shift in pupal emergence of *Drosophila psedoobscura*. *Photochem.Photobiol.*, **24**, 369–371.
181. Konopka,R.J. and Benzer,S. (1971) Clock Mutants of *Drosophila melanogaster*. *Proc. Natl. Acad. Sci.*, **68**, 2112–2116.
182. Bargiello,T.A., Jackson,F.R. and Young,M.W. (1984) Restoration of circadian behavioural rhythms by gene transfer in *Drosophila*. *Nature*, **312**, 752–754.
183. Stanewsky,R., Kaneko,M., Emery,P., Beretta,B., Wager-Smith,K., Kay,S.A., Rosbash,M. and Hall,J.C. (1998) The cry(b) mutation identifies cryptochrome as a circadian photoreceptor in *Drosophila*. *Cell*, **95**, 681–692.
184. Mealey-Ferrara,M.L., Montalvo,A.G. and Hall,J.C. (2003) Effects of combining a cryptochrome mutation with other visual-system variants on entrainment of locomotor and adult-emergence rhythms in *Drosophila*. *J. Neurogenet.*, **17**, 171–221.
185. Busza,A. (2004) Roles of the Two *Drosophila* CRYPTOCHROME Structural Domains in Circadian Photoreception. *Science*, **304**, 1503–1506.
186. Koh,K., Zheng,X. and Sehgal,A. (2006) JETLAG Resets the *Drosophila* Circadian Clock by Promoting Light-Induced Degradation of TIMELESS. *Science*, **312**, 1809–1812.
187. Ozturk,N., Selby,C.P., Annayev,Y., Zhong,D. and Sancar,A. (2011) Reaction mechanism of *Drosophila* cryptochrome. *Proc. Natl. Acad. Sci.*, **108**, 516–521.
188. Peschel,N., Veleri,S. and Stanewsky,R. (2006) Veela defines a molecular link between Cryptochrome and Timeless in the light-input pathway to *Drosophila's* circadian clock. *Proc.*

Natl. Acad. Sci., **103**, 17313–17318.
189. VanVickle-Chavez,S.J. and Van Gelder,R.N. (2007) Action Spectrum of *Drosophila* Cryptochrome. *J. Biol. Chem.*, **282**, 10561–10566.
190. Ozturk,N., VanVickle-Chavez,S.J., Akileswaran,L., Van Gelder,R.N. and Sancar,A. (2013) Ramshackle (Brwd3) promotes light-induced ubiquitylation of *Drosophila* Cryptochrome by DDB1-CUL4-ROC1 E3 ligase complex. *Proc. Natl. Acad. Sci.*, **110**, 4980–4985.
191. Van Der Horst,G.T.J., Muijtjens,M., Kobayashi,K., Takano,R., Kanno,S.I., Takao,M., De Wit,J., Verkerk,A., Eker,A.P.M., Van Leenen,D., *et al.* (1999) Mammalian Cry1 and Cry2 are essential for maintenance of circadian rhythms. *Nature*, **398**, 627–630.
192. Shearman,L.P., Sriram,S., Weaver,D.R., Maywood,E.S., Chaves,I., Zheng,B., Kume,K., Lee,C.C., van der Horst,G.T., Hastings,M.H., *et al.* (2000) Interacting molecular loops in the mammalian circadian clock. *Science*, **288**, 1013–1019.
193. Selby,C.P., Thompson,C., Schmitz,T.M., Van Gelder,R.N. and Sancar,A. (2000) Functional redundancy of cryptochromes and classical photoreceptors for nonvisual ocular photoreception in mice. *Proc. Natl. Acad. Sci.*, **97**, 14697–14702.
194. Zhang,R., Lahens,N.F., Ballance,H.I., Hughes,M.E. and Hogenesch,J.B. (2014) A circadian gene expression atlas in mammals: Implications for biology and medicine. *Proc. Natl. Acad. Sci.*, **111**, 16219–16224.
195. Koike,N., Yoo,S.H., Huang,H.C., Kumar,V., Lee,C., Kim,T.K. and Takahashi,J.S. (2012) Transcriptional architecture and chromatin landscape of the core circadian clock in mammals. *Science*, **338**, 349–354.
196. Stratmann,M., Stadler,F., Tamanini,F., Van Der Horst,G.T.J. and Ripperger,J.A. (2010) Flexible phase adjustment of circadian albumin D site-binding protein (Dbp) gene expression by CRYPTOCHROME1. *Genes Dev.*, **24**, 1317–1328.
197. Ye,R., Selby,C.P., Ozturk,N., Annayev,Y. and Sancar,A. (2011) Biochemical analysis of the canonical model for the mammalian circadian clock. *J. Biol. Chem.*, **286**, 25891–25902.
198. Gustafson,C.L. and Partch,C.L. (2015) Emerging models for the molecular basis of mammalian circadian timing. *Biochemistry*, **54**, 134–149.
199. Glossop,N.R.J., Lyons,L.C. and Hardin,P.E. (1999) Interlocked Feedback Loops Within the Drosophila Circadian Oscillator. *Science*, **286**, 766–768.
200. Busino,L., Bassermann,F., Maiolica,A., Lee,C., Nolan,P.M., Godinho,S.I.H., Draetta,G.F. and Pagano,M. (2007) SCFFbxl3 Controls the Oscillation of the Circadian Clock by Directing the Degradation of Cryptochrome Proteins. *Science*, **316**, 900–904.
201. Godinho,S.I.H., Maywood,E.S., Shaw,L., Tucci,V., Barnard,A.R., Busino,L., Pagano,M., Kendall,R., Quwailid,M.M., Romero,M.R., *et al.* (2007) The After-Hours Mutant Reveals a Role for Fbxl3 in Determining Mammalian Circadian Period. *Science*, **316**, 897–900.
202. Siepka,S.M., Yoo,S.H., Park,J., Song,W., Kumar,V., Hu,Y., Lee,C. and Takahashi,J.S. (2007) Circadian Mutant *Overtime* Reveals F-box Protein FBXL3 Regulation of *Cryptochrome* and *Period* Gene Expression. *Cell*, **129**, 1011–1023.
203. Yoo,S.H., Mohawk,J.A., Siepka,S.M., Shan,Y., Huh,S.K., Hong,H.K., Kornblum,I., Kumar,V., Koike,N., Xu,M., *et al.* (2013) Competing E3 ubiquitin ligases govern circadian periodicity by degradation of CRY in nucleus and cytoplasm. *Cell*, **152**, 1091–1105.
204. Hirota,T., Lee,J.W., St. John,P.C., Sawa,M., Iwaisako,K., Noguchi,T., Pongsawakul,P.Y., Sonntag,T., Welsh,D.K., Brenner,D.A., *et al.* (2012) Identification of Small Molecule Activators of Cryptochrome. *Science*, **337**, 1094–1097.
205. Nangle,S., Xing,W. and Zheng,N. (2013) Crystal structure of mammalian cryptochrome in complex with a small molecule competitor of its ubiquitin ligase. *Cell Res.*, **23**, 1417–1419.
206. Lamia,K.A., Papp,S.J., Yu,R.T., Barish,G.D., Uhlenhaut,N.H., Jonker,J.W., Downes,M. and

Evans,R.M. (2011) Cryptochromes mediate rhythmic repression of the glucocorticoid receptor. *Nature*, **480**, 552–556.
207. Zhang,E.E., Liu,Y., Dentin,R., Pongsawakul,P.Y., Liu,A.C., Hirota,T., Nusinow,D.A., Sun,X., Landais,S., Kodama,Y., *et al.* (2010) Cryptochrome mediates circadian regulation of cAMP signaling and hepatic gluconeogenesis. *Nat. Med.*, **16**, 1152–1156.
208. Davis,S. and Mirick,D.K. (2006) Circadian disruption, shift work and the risk of cancer: A summary of the evidence and studies in Seattle. *Cancer Causes Control*, **17**, 539–545.
209. Papagiannakopoulos,T., Bauer,M.R., Davidson,S.M., Heimann,M., Subbaraj,L., Bhutkar,A., Bartlebaugh,J., Vander Heiden,M.G. and Jacks,T. (2016) Circadian Rhythm Disruption Promotes Lung Tumorigenesis. *Cell Metab.*, **24**, 324–331.
210. Takahashi,J.S., Hong,H.-K., Ko,C.H. and McDearmon,E.L. (2008) The genetics of mammalian circadian order and disorder: implications for physiology and disease. *Nat. Rev. Genet.*, **9**, 764–775.
211. Gauger,M.A. and Sancar,A. (2005) Cryptochrome, Circadian Cycle, Cell Cycle Checkpoints, and Cancer. *Cancer Res.*, **65**, 6828–6834.
212. Ozturk,N., Lee,J.H., Gaddameedhi,S. and Sancar,A. (2009) Loss of cryptochrome reduces cancer risk in *p53* mutant mice. *Proc. Natl. Acad. Sci.*, **106**, 2841–2846.
213. Kang,T.-H., Lindsey-Boltz,L.A., Reardon,J.T. and Sancar,A. (2010) Circadian control of XPA and excision repair of cisplatin-DNA damage by cryptochrome and HERC2 ubiquitin ligase. *Proc. Natl. Acad. Sci.*, **107**, 4890–4895.
214. Kang,T.H. and Sancar,A. (2009) Circadian regulation of DNA excision repair: Implications for chrono-chemotherapy. *Cell Cycle*, **8**, 1665–1667.
215. Hore,P.J. and Mouritsen,H. (2016) The Radical-Pair Mechanism of Magnetoreception. *Annu. Rev. Biophys.*, **45**, 299–344.
216. Zwang,T.J., Tse,E.C.M., Zhong,D. and Barton,J.K. (2018) A Compass at Weak Magnetic Fields Using Thymine Dimer Repair. *ACS Cent. Sci.*, **4**, 405–412.
217. Gegear,R.J., Casselman,A., Waddell,S. and Reppert,S.M. (2008) Cryptochrome mediates light-dependent magnetosensitivity in *Drosophila*. *Nature*, **454**, 1014–1018.
218. Fedele,G., Green,E.W., Rosato,E. and Kyriacou,C.P. (2014) An electromagnetic field disrupts negative geotaxis in *Drosophila* via a CRY-dependent pathway. *Nat. Commun.*, **5**, 4391.
219. Foley,L.E., Gegear,R.J. and Reppert,S.M. (2011) Human cryptochrome exhibits light-dependent magnetosensitivity. *Nat. Commun.*, **2**, 356.
220. Qin,S., Yin,H., Yang,C., Dou,Y., Liu,Z., Zhang,P., Yu,H., Huang,Y., Feng,J., Hao,J., *et al.* (2016) A magnetic protein biocompass. *Nat. Mater.*, **15**, 217–226.
221. Liedvogel,M., Maeda,K., Henbest,K., Schleicher,E., Simon,T., Timmel,C.R., Hore,P.J. and Mouritsen,H. (2007) Chemical magnetoreception: bird cryptochrome 1a is excited by blue light and forms long-lived radical-pairs. *PLoS One*, **2**, e1106.
222. Wiltschko,R., Munro,U., Ford,H., Stapput,K., Thalau,P. and Wiltschko,W. (2014) Orientation of migratory birds under ultraviolet light. *J. Comp. Physiol. A Neuroethol. Sensory, Neural, Behav. Physiol.*, **200**, 399–407.
223. Merchant,S.S., Prochnik,S.E., Vallon,O., Harris,E.H., Karpowicz,S.J., Witman,G.B., Terry,A., Salamov,A., Fritz-Laylin,L.K., Maréchal-Drouard,L., *et al.* (2007) The Chlamydomonas genome reveals the evolution of key animal and plant functions. *Science*, **318**, 245–250.
224. Kottke,T., Oldemeyer,S., Wenzel,S., Zou,Y. and Mittag,M. (2017) Cryptochrome photoreceptors in green algae: Unexpected versatility of mechanisms and functions. *J. Plant Physiol.*, **217**, 4–14.
225. Hegemann,P. (2008) Algal Sensory Photoreceptors. *Annu. Rev. Plant Biol.*, **59**, 167–189.
226. Kianianmomeni,A. and Hallmann,A. (2014) Algal photoreceptors: *In vivo* functions and potential

applications. *Planta*, **239**, 1–26.
227. Zou,Y., Wenzel,S., Müller,N., Prager,K., Jung,E.-M., Kothe,E., Kottke,T. and Mittag,M. (2017) An Animal-Like Cryptochrome Controls the *Chlamydomonas* Sexual Cycle. *Plant Physiol.*, **174**, 1334–1347.
228. Müller,N., Wenzel,S., Zou,Y., Künzel,S., Sasso,S., Weiß,D., Prager,K., Grossman,A., Kottke,T. and Mittag,M. (2017) A Plant Cryptochrome Controls Key Features of the *Chlamydomonas* Circadian Clock and Its Life Cycle. *Plant Physiol.*, **174**, 185–201.
229. Goodenough,U., Lin,H. and Lee,J.H. (2007) Sex determination in *Chlamydomonas*. *Semin. Cell Dev. Biol.*, **18**, 350–361.
230. Mittag,M., Kiaulehn,S. and Johnson,C.H. (2005) The circadian clock in *Chlamydomonas reinhardtii*. What is it for? What is it similar to? *Plant Physiol.*, **137**, 399–409.
231. Beel,B., Prager,K., Spexard,M., Sasso,S., Weiss,D., Müller,N., Heinnickel,M., Dewez,D., Ikoma,D., Grossman,A.R., *et al.* (2012) A flavin binding cryptochrome photoreceptor responds to both blue and red light in *Chlamydomonas reinhardtii*. *Plant Cell*, **24**, 2992–3008.
232. Beel,B., Müller,N., Kottke,T. and Mittag,M. (2013) News about cryptochrome photoreceptors in algae. *Plant Signal. Behav.*, **8**, e22870.
233. Beel,B., Prager,K., Spexard,M., Sasso,S., Weiss,D., Muller,N., Heinnickel,M., Dewez,D., Ikoma,D., Grossman, a. R., *et al.* (2012) A Flavin Binding Cryptochrome Photoreceptor Responds to Both Blue and Red Light in *Chlamydomonas reinhardtii*. *Plant Cell*, **24**, 2992–3008.
234. Berman,H.M., Westbrook,J., Feng,Z., Gilliland,G., Bhat,T.N., Weissig,H., Shindyalov,I.N. and Bourne,P.E. (2000) The Protein Data Bank. *Nucleic Acids Res.*, **28**, 235–42.
235. KENDREW,J.C., BODO,G., DINTZIS,H.M., PARRISH,R.G., WYCKOFF,H. and PHILLIPS,D.C. (1958) A three-dimensional model of the myoglobin molecule obtained by x-ray analysis. *Nature*, **181**, 662–6.
236. NASA (2018) Tour of the Electromagnetic Spectrum. *https://science.nasa.gov/ems/01_intro* (Abrufdatum: 15.01.2018).
237. Chayen,N.E. and Saridakis,E. (2008) Protein crystallization: From purified protein to diffraction-quality crystal. *Nat. Methods*, **5**, 147–153.
238. Jones,N. (2014) Crystallography: Atomic secrets. *https://www.nature.com/news/crystallography-atomic-secrets-1.14608* (Abrufdatum: 7.11.2018).
239. Chayen,N.E. (1998) Comparative studies of protein crystallization by vapour-diffusion and microbatch techniques. *Acta Crystallogr. Sect. D Biol. Crystallogr.*, **54**, 8–15.
240. Chayen,N.E., Shaw Stewart,P.D., Maeder,D.L. and Blow,D.M. (1990) An automated system for micro-batch protein crystallization and screening. *J. Appl. Crystallogr.*, **23**, 297–302.
241. Bragg,W.H. and Bragg,W.L. (1913) The Reflection of X-rays by Crystals. *Proc. R. Soc. A Math. Phys. Eng. Sci.*, **88**, 428–438.
242. Drenth,J. (2010) Principles of Protein X-Ray Crystallography 3rd ed. Springer.
243. Perutz,M.F., Rossmann,M.G., Cullis,A.F., Muirhead,H., Will,G. and North,A.C.T. (1960) Structure of Hæmoglobin: A three-dimensional fourier synthesis at 5.5-. resolution, obtained by X-ray analysis. *Nature*, **185**, 416–422.
244. Kahn,R., Fourme,R., Bosshard,R., Chiadmi,M., Risler,J.L., Dideberg,O. and Wery,J.P. (1985) Crystal structure study of *Opsanus tau parvalbumin* by multiwavelength anomalous diffraction. *FEBS Lett.*, **179**, 133–137.
245. Hendrickson,W.A., Horton,J.R., Murthy,H.M.K., Pahler,A. and Smith,J.L. (1989) Multiwavelength anomalous diffraction as a direct phasing vehicle in macromolecular crystallography. *Synchrotron Radiat. Struct. Biol.*, 10.1007/978-1-4684-8041-2_28.
246. Argos,P. and Rossman,M.G. (1980) Molecular Replacement Method. In *Theory and Practice of Direct Methods in Crystallography*. Springer US, Boston, MA, pp. 361–417.

247. Lebedev,A.A., Vagin,A.A. and Murshudov,G.N. (2007) Model preparation in MOLREP and examples of model improvement using X-ray data. *Acta Crystallogr. Sect. D Biol. Crystallogr.*, **64**, 33–39.
248. Murshudov,G.N., Skubák,P., Lebedev,A.A., Pannu,N.S., Steiner,R.A., Nicholls,R.A., Winn,M.D., Long,F. and Vagin,A.A. (2011) REFMAC5 for the refinement of macromolecular crystal structures. *Acta Crystallogr. Sect. D Biol. Crystallogr.*, **67**, 355–367.
249. Spence,J.C.H. (2017) XFELs for structure and dynamics in biology. *IUCrJ*, **4**, 322–339.
250. Madey,J.M.J. (1971) Stimulated emission of bremsstrahlung in a periodic magnetic field. *J. Appl. Phys.*, **42**, 1906–1913.
251. Pellegrini,C., Marinelli,A. and Reiche,S. (2016) The physics of x-ray free-electron lasers. *Rev. Mod. Phys.*, **88**, 1–55.
252. Narumi,S. (2011) SACLA X-ray Free Electron Laser Facility. *https://www.nippon.com/en/features/c00501/*.
253. Milton, S.V., Gluskin, E., Arnold, N.D., Benson, C., Berg, W., *et al.* (2001) Exponential Gain and Saturation of a Self-Amplified Spontaneous Emission Free-Electron Laser. *Science*, **292**, 2037–2041.
254. Yabashi,M., Tanaka,H. and Ishikawa,T. (2015) Overview of the SACLA facility. *J. Synchrotron Radiat.*, **22**, 477–484.
255. Schmidt,M. (2013) Mix and inject: Reaction initiation by diffusion for time-resolved macromolecular crystallography. *Adv. Condens. Matter Phys.*, **2013**.
256. Boutet,S., Lomb,L., Williams,G.J., Barends,T.R.M., Aquila,A., Doak,R.B., Weierstall,U., DePonte,D.P., Steinbrener,J. and Shoeman,R.L. (2012) High-resolution protein structure determination by serial femtosecond crystallography. *Science*, **337**, 362–364.
257. Barends,T.R.M., Foucar,L., Botha,S., Doak,R.B., Shoeman,R.L., Nass,K., Koglin,J.E., Williams,G.J., Boutet,S., Messerschmidt,M., *et al.* (2014) De novo protein crystal structure determination from X-ray free-electron laser data. *Nature*, **505**, 244–247.
258. Pellegrini,C. (2016) X-ray free-electron lasers: from dreams to reality. *Phys. Scr.*, **T169**, 014004.
259. Levantino,M., Yorke,B.A., Monteiro,D.C.F., Cammarata,M. and Pearson,A.R. (2015) Using synchrotrons and XFELs for time-resolved X-ray crystallography and solution scattering experiments on biomolecules. *Curr. Opin. Struct. Biol.*, **35**, 41–48.
260. Moffat,K. (2014) Time-resolved crystallography and protein design: signalling photoreceptors and optogenetics. *Philos. Trans. R. Soc. B Biol. Sci.*, **369**, 20130568–20130568.
261. Schlichting,I., Almo,S.C., Rapp,G., Wilson,K., Petratos,K., Lentfer,A., Wittinghofer,A., Kabsch,W., Pai,E.F. and Petsko,G.A. (1990) Time-resolved X-ray crystallographic study of the conformational change in Ha-Ras p21 protein on GTP hydrolysis. *Nature*, **345**, 309–315.
262. Kirian,R.A., Wang,X., Weierstall,U., Schmidt,K.E., Spence,J.C.H., Hunter,M., Fromme,P., White,T., Chapman,H.N. and Holton,J. (2010) Femtosecond protein nanocrystallography—data analysis methods. *Opt. Express*, **18**, 5713.
263. Weierstall,U., Spence,J.C.H. and Doak,R.B. (2012) Injector for scattering measurements on fully solvated biospecies. *Rev. Sci. Instrum.*, **83**.
264. Park,J., Joti,Y., Ishikawa,T. and Song,C. (2013) Monte Carlo study for optimal conditions in single-shot imaging with femtosecond x-ray laser pulses. *Appl. Phys. Lett.*, **103**, 264101.
265. Sugahara,M., Mizohata,E., Nango,E., Suzuki,M., Tanaka,T., Masuda,T., Tanaka,R., Shimamura,T., Tanaka,Y., Suno,C., *et al.* (2014) Grease matrix as a versatile carrier of proteins for serial crystallography. *Nat. Methods*, **12**, 61–63.
266. Tono,K., Nango,E., Sugahara,M., Song,C., Park,J., Tanaka,T., Tanaka,R., Joti,Y., Kameshima,T., Ono,S., *et al.* (2015) Diverse application platform for hard X-ray diffraction in SACLA (DAPHNIS): Application to serial protein crystallography using an X-ray free-electron laser. *J. Synchrotron*

Radiat., **22**, 532–537.
267. Nakane,T., Joti,Y., Tono,K., Yabashi,M., Nango,E., Iwata,S., Ishitani,R. and Nureki,O. (2016) Data processing pipeline for serial femtosecond crystallography at SACLA. *J. Appl. Crystallogr.*, **49**, 1035–1041.
268. Barty,A., Kirian,R.A., Maia,F.R.N.C., Hantke,M., Yoon,C.H., White,T.A. and Chapman,H. (2014) *Cheetah* : software for high-throughput reduction and analysis of serial femtosecond X-ray diffraction data. *J. Appl. Crystallogr.*, **47**, 1118–1131.
269. White,T.A., Mariani,V., Brehm,W., Yefanov,O., Barty,A., Beyerlein,K.R., Chervinskii,F., Galli,L., Gati,C., Nakane,T., *et al.* (2016) Recent developments in CrystFEL. *J. Appl. Crystallogr.*, **49**, 680–689.
270. Maier,C.S. and Deinzer,M.L. (2005) Protein conformations, interactions, and H/D exchange. *Methods Enzymol.*, **402**, 312–360.
271. Englander,S.W. and Kallenbach,N.R. (1983) Hydrogen exchange and structural dynamics of proteins and nucleic acids. *Q. Rev. Biophys.*, **16**, 521–655.
272. Hamuro,Y., Coales,S.J., Southern,M.R., Nemeth-Cawley,J.F., Stranz,D.D. and Griffin,P.R. (2003) Rapid analysis of protein structure and dynamics by hydrogen/deuterium exchange mass spectrometry. *J. Biomol. Tech.*, **14**, 171–182.
273. DeLano,W.L. (2002) The PyMOL user's manual. DeLano Scientific, San Carlos, CA.
274. Kaltashov,I.A., Bobst,C.E. and Abzalimov,R.R. (2009) H/D exchange and mass spectrometry in the studies of protein conformation and dynamics: Is there a need for a top-down approach? *Anal. Chem.*, **81**, 7892–7899.
275. DePristo,M.A., De Bakker,P.I.W. and Blundell,T.L. (2004) Heterogeneity and inaccuracy in protein structures solved by X-ray crystallography. *Structure*, **12**, 831–838.
276. Steinchen,W., Linne,U. and Bange,G. (2017) HDX-MS in den Lebenswissenschaften. *BioSpektrum*, **23**, 772–775.
277. Cooke,R.M. (1997) Protein NMR extends into new fields of structural biology. *Curr. Opin. Chem. Biol.*, **1**, 359–364.
278. Liebert,M.A., Garcia,R.A., Pantazatos,D. and Villarreal,F.J. (2004) Investigating Protein-Ligand Interactions. **2**.
279. Schiemann,O. and Prisner,T.F. (2007) Long-range distance determinations in biomacromolecules by EPR spectroscopy. *Q. Rev. Biophys.*, **40**, 1–53.
280. Sale,K., Faulon,J.-L., Gray,G.A., Schoeniger,J.S. and Young,M.M. (2004) Optimal bundling of transmembrane helices using sparse distance constraints. *Protein Sci.*, **13**, 2613–2627.
281. Jeschke,G. (2005) EPR techniques for studying radical enzymes. *Biochim. Biophys. Acta - Bioenerg.*, **1707**, 91–102.
282. Nohr,D., Rodriguez,R., Weber,S. and Schleicher,E. (2015) How can EPR spectroscopy help to unravel molecular mechanisms of flavin-dependent photoreceptors? *Front. Mol. Biosci.*, **2**, 1–16.
283. Frey,P.A., Hegeman,A.D. and Reed,G.H. (2006) Free radical mechanisms in enzymology. *Chem. Rev.*, **106**, 3302–3316.
284. Klare,J.P. and Steinhoff,H.J. (2009) Spin labeling EPR. *Photosynth. Res.*, **102**, 377–390.
285. Bittl,R. and Weber,S. (2005) Transient radical pairs studied by time-resolved EPR. *Biochim. Biophys. Acta - Bioenerg.*, **1707**, 117–126.
286. Spexard,M., Thöing,C., Beel,B., Mittag,M. and Kottke,T. (2014) Response of the sensory animal-like cryptochrome aCRY to blue and red light as revealed by infrared difference spectroscopy. *Biochemistry*, **53**, 1041–1050.
287. Franz,S. (2014) Strukturelle und funktionelle Charakterisierung des animal-like Cryptochromes aCRY aus *Chlamydomonas reinhardtii*. Philipps-University Marburg.

288. Müller,P., Yamamoto,J., Martin,R., Iwai,S. and Brettel,K. (2015) Discovery and functional analysis of a 4th electron-transferring tryptophan conserved exclusively in animal cryptochromes and (6-4) photolyases †. *RSC Chem Comm.*, 10.1039/C5CC06276D.
289. Biskup,T., Schleicher,E., Okafuji,A., Link,G., Hitomi,K., Getzoff,E.D. and Weber,S. (2009) Direkte Detektion eines lichtinduzierten Radikalpaars in einem Cryptochrom-Blaulichtrezeptor. *Angew. Chemie*, **121**, 411–415.
290. Biskup,T., Hitomi,K., Getzoff,E.D., Krapf,S., Koslowski,T., Schleicher,E. and Weber,S. (2011) Unexpected Electron Transfer in Cryptochrome Identified by Time-Resolved EPR Spectroscopy. *Angew. Chemie Int. Ed.*, **50**, 12647–12651.
291. Biskup,T., Paulus,B., Okafuji,A., Hitomi,K., Getzoff,E.D., Weber,S. and Schleicher,E. (2013) Variable electron transfer pathways in an amphibian cryptochrome tryptophan versus tyrosine-based radical pairs. *J. Biol. Chem.*, **288**, 9249–9260.
292. Petersen,J.L. and Ronan,P.J. (2010) Critical Role of 7 , 8-Didemethyl-8-hydroxy-5-deazariboflavin for Photoreactivation in *Chlamydomonas reinhardtii*. *J. Biol. Chem.*, **285**, 32467–32475.
293. Nohr,D., Franz,S., Rodriguez,R., Paulus,B., Essen,L.-O.O., Weber,S. and Schleicher,E. (2016) Extended Electron-Transfer in Animal Cryptochromes Mediated by a Tetrad of Aromatic Amino Acids. *Biophys. J.*, **111**, 301–311.
294. Oldemeyer,S., Franz,S., Wenzel,S., Essen,L.-O., Mittag,M. and Kottke,T. (2016) Essential Role of an Unusually Long-lived Tyrosyl Radical in the Response to Red Light of the Animal-like Cryptochrome aCRY. *J. Biol. Chem.*, **291**, 14062–14071.
295. Immeln,D., Weigel,A., Kottke,T. and Pérez Lustres,J.L. (2012) Primary events in the blue light sensor plant cryptochrome: Intraprotein electron and proton transfer revealed by femtosecond spectroscopy. *J. Am. Chem. Soc.*, **134**, 12536–12546.
296. Reisdorph,N.A. and Small,G.D. (2004) The CPH1 gene of Chlamydomonas reinhardtii encodes two forms of cryptochrome whose levels are controlled by light-induced proteolysis. *Plant Physiol.*, **134**, 1546–54.
297. Engelhard,C., Wang,X., Robles,D., Moldt,J., Essen,L.-O., Batschauer,A., Bittl,R. and Ahmad,M. (2014) Cellular Metabolites Enhance the Light Sensitivity of *Arabidopsis* Cryptochrome through Alternate Electron Transfer Pathways. *Plant Cell Online*, **26**, 4519–4531.
298. Müller,P., Bouly,J.-P., Hitomi,K., Balland,V., Getzoff,E.D., Ritz,T. and Brettel,K. (2014) ATP binding turns plant cryptochrome into an efficient natural photoswitch. *Sci. Rep.*, **4**, 5175.
299. Takahashi,F., Yamagata,D., Ishikawa,M., Fukamatsu,Y., Ogura,Y., Kasahara,M., Kiyosue,T., Kikuyama,M., Wada,M. and Kataoka,H. (2007) AUREOCHROME, a photoreceptor required for photomorphogenesis in stramenopiles. *Proc. Natl. Acad. Sci.*, **104**, 19625–19630.
300. Ishikawa,M., Takahashi,F., Nozaki,H., Nagasato,C., Motomura,T. and Kataoka,H. (2009) Distribution and phylogeny of the blue light receptors aureochromes in eukaryotes. *Planta*, **230**, 543–552.
301. Suetsugu,N. and Wada,M. (2013) Evolution of Three LOV Blue Light Receptor Families in Green Plants and Photosynthetic Stramenopiles: Phototropin, ZTL/FKF1/LKP2 and Aureochrome. *Plant Cell Physiol.*, **54**, 8–23.
302. Takahashi,F. (2016) Blue-light-regulated transcription factor, Aureochrome, in photosynthetic stramenopiles. *J. Plant Res.*, **129**, 189–197.
303. Herrou,J. and Crosson,S. (2011) Function, structure and mechanism of bacterial photosensory LOV proteins. *Nat. Rev. Microbiol.*, **9**, 713–723.
304. Conrad,K.S., Manahan,C.C. and Crane,B.R. (2014) Photochemistry of flavoprotein light sensors. *Nat. Chem. Biol.*, **10**, 801–9.
305. Herman,E., Sachse,M., Kroth,P.G. and Kottke,T. (2013) Blue-Light-Induced Unfolding of the Jα

Helix Allows for the Dimerization of Aureochrome-LOV from the Diatom *Phaeodactylum tricornutum*. *Biochemistry*, **52**, 3094–3101.

306. Herman,E. and Kottke,T. (2015) Allosterically Regulated Unfolding of the A'α Helix Exposes the Dimerization Site of the Blue-Light-Sensing Aureochrome-LOV Domain. *Biochemistry*, **54**, 1484–1492.
307. Toyooka,T., Hisatomi,O., Takahashi,F., Kataoka,H. and Terazima,M. (2011) Photoreactions of aureochrome-1. *Biophys. J.*, **100**, 2801–2809.
308. Banerjee,A., Herman,E., Kottke,T. and Essen,L.O. (2016) Structure of a Native-like Aureochrome 1a LOV Domain Dimer from *Phaeodactylum tricornutum*. *Structure*, **24**, 171–178.
309. Heintz,U. and Schlichting,I. (2016) Blue light-induced LOV domain dimerization enhances the affinity of Aureochrome 1a for its target DNA sequence. *Elife*, **5**, e11860.
310. Mitra,D., Yang,X. and Moffat,K. (2012) Crystal structures of Aureochrome1 LOV suggest new design strategies for optogenetics. *Structure*, **20**, 698–706.
311. Hisatomi,O., Nakatani,Y., Takeuchi,K., Takahashi,F. and Kataoka,H. (2014) Blue Light-induced Dimerization of Monomeric Aureochrome-1 Enhances Its Affinity for the Target Sequence. *J. Biol. Chem.*
312. Hisatomi,O. and Furuya,K. (2015) A light-regulated bZIP module, photozipper, induces the binding of fused proteins to the target DNA sequence in a blue light-dependent manner. *Photochem. Photobiol. Sci.*, **14**, 1998–2006.
313. Akiyama,Y., Nakasone,Y., Nakatani,Y., Hisatomi,O. and Terazima,M. (2016) Time-Resolved Detection of Light-Induced Dimerization of Monomeric Aureochrome-1 and Change in Affinity for DNA. *J. Phys. Chem. B*, **120**, 7360–7370.
314. Banerjee,A., Herman,E., Serif,M., Maestre-Reyna,M., Hepp,S., Pokorny,R., Kroth,P.G., Essen,L.-O. and Kottke,T. (2016) Allosteric communication between DNA-binding and light-responsive domains of diatom class I aureochromes. *Nucleic Acids Res.*, 10.1093/nar/gkw420.
315. Yamashita,K., Hirata,K. and Yamamoto,M. (2018) KAMO : towards automated data processing for microcrystals. *Acta Crystallogr. Sect. D Struct. Biol.*, **74**, 1–9.
316. Franz-Badur,S., Penner,A., Straß,S., Von Horsten,S., Linne,U. and Essen,L.-O. (2018) Structural changes within the bifunctional cryptochrome/photolyase CraCRY upon blue light excitation. *Submitt. Manuscr.*
317. Gerlt,J.A., Bouvier,J.T., Davidson,D.B., Imker,H.J., Sadkhin,B., Slater,D.R. and Whalen,K.L. (2015) Enzyme function initiative-enzyme similarity tool (EFI-EST): A web tool for generating protein sequence similarity networks. *Biochim. Biophys. Acta - Proteins Proteomics*, **1854**, 1019–1037.
318. Essen,L.-O., Franz,S. and Banerjee,A. (2017) Structural and evolutionary aspects of algal blue light receptors of the cryptochrome and aureochrome type. *J. Plant Physiol.*, **217**, 27–37.
319. Finn,R.D., Tate,J., Mistry,J., Coggill,P.C., Sammut,S.J., Hotz,H.-R., Ceric,G., Forslund,K., Eddy,S.R., Sonnhammer,E.L.L., *et al.* (2007) The Pfam protein families database. *Nucleic Acids Res.*, **36**, D281–D288.
320. Biesemann,C., Krappmann,S., Galland,P., Braus,G.H., Bayram,O., Biesemann,C., Krappmann,S., Galland,P., Braus,G.H., Bayram,O., *et al.* (2008) More Than a Repair Enzyme: *Aspergillus nidulans* Photolyase-like CryA Is a Regulator of Sexual Development. *Mol. Biol. Cell*, **19**, 3254–3262.
321. Bluhm,B.H. and Dunkle,L.D. (2008) PHL1 of *Cercospora zeae-maydis* encodes a member of the photolyase/cryptochrome family involved in UV protection and fungal development. *Fungal Genet. Biol.*, **45**, 1364–1372.
322. Guzmán-Moreno,J., Flores-Martínez,A., Brieba,L.G. and Herrera-Estrella,A. (2014) The *Trichoderma reesei* Cry1 protein is a member of the cryptochrome/ photolyase family with 6-4 photoproduct repair activity. *PLoS One*, **9**, 1–13.

323. García-Esquivel,M., Esquivel-Naranjo,E.U., Hernández-Oñate,M.A., Ibarra-Laclette,E. and Herrera-Estrella,A. (2016) The *Trichoderma atroviride* cryptochrome/photolyase genes regulate the expression of blr1-independent genes both in red and blue light. *Fungal Biol.*, **120**, 500–512.
324. Czarna,A., Berndt,A., Singh,H.R., Grudziecki,A., Ladurner,A.G., Timinszky,G., Kramer,A. and Wolf,E. (2013) Structures of Drosophila Cryptochrome and Mouse Cryptochrome1 Provide Insight into Circadian Function. *Cell*, **153**, 1394–1405.
325. Schmalen,I., Reischl,S., Wallach,T., Klemz,R., Grudziecki,A., Prabu,J.R., Benda,C., Kramer,A. and Wolf,E. (2014) Interaction of circadian clock proteins CRY1 and PER2 is modulated by zinc binding and disulfide bond formation. *Cell*, **157**, 1203–1215.
326. Vaidya,A.T., Top,D., Manahan,C.C., Tokuda,J.M., Zhang,S., Pollack,L., Young,M.W. and Crane,B.R. (2013) Flavin reduction activates *Drosophila* cryptochrome. *Proc. Natl. Acad. Sci.*, **110**, 20455–20460.
327. Hense,A., Herman,E., Oldemeyer,S. and Kottke,T. (2015) Proton Transfer to Flavin Stabilizes the Signaling State of the Blue Light Receptor Plant Cryptochrome. *J. Biol. Chem.*, **290**, 1743–1751.
328. Müller,P., Brettel,K., Grama,L., Nyitrai,M. and Lukacs,A. (2016) Photochemistry of Wild-Type and N378D Mutant *E. coli* DNA Photolyase with Oxidized FAD Cofactor Studied by Transient Absorption Spectroscopy. *ChemPhysChem*, **17**, 1329–1340.
329. Balland,V., Byrdin,M., Eker,A.P.M., Ahmad,M. and Brettel,K. (2009) What makes the difference between a cryptochrome and DNA photolyase? A spectroelectrochemical comparison of the flavin redox transitions. *J. Am. Chem. Soc.*, **131**, 426–427.
330. Kottke,T., Batschauer,A., Ahmad,M. and Heberle,J. (2006) Blue-light-induced changes in *arabidopsis* cryptochrome 1 probed by FTIR difference spectroscopy. *Biochemistry*, **45**, 2472–2479.
331. Schulten,K., Swenberg,C.E. and Weller,A. (1978) A Biomagnetic Sensory Mechanism Based on Magnetic Field Modulated Coherent Electron Spin Motion. *Zeitschrift für Phys. Chemie*, **111**, 1–5.
332. Ritz,T., Adem,S. and Schulten,K. (2000) A model for photoreceptor-based magnetoreception in birds. *Biophys. J.*, **78**, 707–718.
333. Maeda,K., Robinson, a. J., Henbest,K.B., Hogben,H.J., Biskup,T., Ahmad,M., Schleicher,E., Weber,S., Timmel,C.R. and Hore,P.J. (2012) Magnetically sensitive light-induced reactions in cryptochrome are consistent with its proposed role as a magnetoreceptor. *Proc. Natl. Acad. Sci.*, **109**, 4774–4779.
334. Ahmad,M., Galland,P., Ritz,T., Wiltschko,R. and Wiltschko,W. (2007) Magnetic intensity affects cryptochrome-dependent responses in *Arabidopsis thaliana*. *Planta*, **225**, 615–624.
335. Hill,E. and Ritz,T. (2010) Can disordered radical pair systems provide a basis for a magnetic compass in animals? *J. R. Soc. Interface*, **7**, S265–S271.
336. Solov'Yov,I.A., Mouritsen,H. and Schulten,K. (2010) Acuity of a cryptochrome and vision-based magnetoreception system in birds. *Biophys. J.*, **99**, 40–49.
337. Lau,J.C.S., Wagner-Rundell,N., Rodgers,C.T., Green,N.J.B. and Hore,P.J. (2010) Effects of disorder and motion in a radical pair magnetoreceptor. *J. R. Soc. Interface*, **7**, S257–S264.
338. Lau,J.C.S., Rodgers,C.T. and Hore,P.J. (2012) Compass magnetoreception in birds arising from photo-induced radical pairs in rotationally disordered cryptochromes. *J. R. Soc. Interface*, **9**, 3329–3337.
339. Wiltschko,W., Munro,U., Ford,H. and Wiltschko,R. (1993) Red light disrupts magnetic orientation of migratory birds. *Nature*, **364**, 525–527.
340. Wiltschko,R., Stapput,K., Thalau,P. and Wiltschko,W. (2010) Directional orientation of birds by the magnetic field under different light conditions. *J. R. Soc. Interface*, **7**, S163–S177.

341. Niessner,C., Denzau,S., Peichl,L., Wiltschko,W. and Wiltschko,R. (2014) Magnetoreception in birds: I. Immunohistochemical studies concerning the cryptochrome cycle. *J. Exp. Biol.*, **217**, 4221–4224.
342. Nießner,C., Denzau,S., Stapput,K., Ahmad,M., Peichl,L., Wiltschko,W. and Wiltschko,R. (2013) Magnetoreception: activated cryptochrome 1a concurs with magnetic orientation in birds. *J. R. Soc. Interface*, **10**, 20130638.
343. Nohr,D. (2018) Von der Triade zur Tetrade: Erweiterter Elektronentransfer in Cryptochromen und dessen Bedeutung für die Magnetorezeption.
344. Tsentalovich,Y.P. and Morozova,O.B. (2000) Laser flash photolysis and time resolved CIDNP study of photoreaction of 2,2'-dipyridyl with N-acetyl tyrosine in aqueous solutions. *J. Photochem. Photobiol. A Chem.*, **131**, 33–40.
345. Mormont,M.C. and Levi,F. (2003) Cancer chronotherapy: Principles, applications, and perspectives. *Cancer*, **97**, 155–169.
346. Anafi,R.C., Francey,L.J., Hogenesch,J.B. and Kim,J. (2017) CYCLOPS reveals human transcriptional rhythms in health and disease. *Proc. Natl. Acad. Sci.*, **114**, 5312–5317.
347. Yamada,R.G. and Ueda,H.R. (2017) Compass in the data ocean: Toward chronotherapy. *Proc. Natl. Acad. Sci.*, **114**, 5069–5071.
348. Ozturk,N., Ozturk,D., Kavakli,I.H. and Okyar,A. (2017) Molecular aspects of circadian pharmacology and relevance for cancer chronotherapy. *Int. J. Mol. Sci.*, **18**.
349. de Mena,L., Rizk,P. and Rincon-Limas,D.E. (2018) Bringing Light to Transcription: The Optogenetics Repertoire. *Front. Genet.*, **9**, 1–12.
350. Renicke,C., Schuster,D., Usherenko,S., Essen,L.-O. and Taxis,C. (2013) A LOV2 domain-based optogenetic tool to control protein degradation and cellular function. *Chem. Biol.*, **20**, 619–626.
351. O'Banion,C.P. and Lawrence,D.S. (2018) Optogenetics: A Primer for Chemists. *ChemBioChem*, **19**, 1201–1216.
352. Losi,A., Gardner,K.H. and Möglich,A. (2018) Blue-Light Receptors for Optogenetics. *Chem. Rev.*, 10.1021/acs.chemrev.8b00163.
353. Che,D.L., Duan,L., Zhang,K. and Cui,B. (2015) The Dual Characteristics of Light-Induced Cryptochrome 2, Homo-oligomerization and Heterodimerization, for Optogenetic Manipulation in Mammalian Cells. *ACS Synth. Biol.*, **4**, 1124–1135.
354. Tischer,D. and Weiner,O.D. (2014) Illuminating cell signalling with optogenetic tools. *Nat. Rev. Mol. Cell Biol.*, **15**, 551–558.
355. Kennedy,M.J., Hughes,R.M., Peteya,L.A., Schwartz,J.W., Ehlers,M.D. and Tucker,C.L. (2010) Rapid blue-light–mediated induction of protein interactions in living cells. *Nat. Methods*, **7**, 973–975.
356. Berardesca,E., Bertona,M., Altabas,K., Altabas,V. and Emanuele,E. (2012) Reduced ultraviolet-induced DNA damage and apoptosis in human skin with topical application of a photolyase-containing DNA repair enzyme cream: Clues to skin cancer prevention. *Mol. Med. Rep.*, **5**, 570–574.
357. Jans,J., Schul,W., Sert,Y.-G., Rijksen,Y., Rebel,H., Eker,A.P.M., Nakajima,S., van Steeg,H., de Gruijl,F.R., Yasui,A., *et al.* (2005) Powerful Skin Cancer Protection by a CPD-Photolyase Transgene. *Curr. Biol.*, **15**, 105–115.
358. Church,G.M., Gao,Y. and Kosuri,S. (2012) Next-Generation Digital Information Storage in DNA. *Science*, **337**, 1628–1628.
359. Cox,J.P.L. (2001) Long-term data storage in DNA. *Trends Biotechnol.*, **19**, 247–250.

7 Appendix

Table 2 List of abbreviations used in this work.

(6-4)PP	Pyrimidine-(6-4)-pyrimidone photoproducts
ΔCTE	Mutant without the C-terminal extension
8-HDF	8-hydroxydeazaflavin
aCRY	Animal-like cryptochrome
Ade	Adenine-moiety
ADP	Adenosine diphosphate
AMP	Adenosine monophosphate
AMP-PNP	5'-adenylyl-β-γ-imidodiphosphate
An	*Anacystis nidulans*
At	*Arabidopsis thaliana*
ATP	Adenosine triphosphate
AUREO	Aureochrome
BCP	Bacterial cryptochromes and photolyases
BET	Back electron transfer
BL	Blue light
BLUF	Blue-light using flavin protein
BRWD3	Bromodomain and WD repeat-containing protein 3
cAMP	Cyclic adenosine monophosphate
CD	Circular dichroism
CPD	Cyclobutane pyrimidine dimer
CPF	Cryptochrome/photolyase family
Cr	*Chlamydomonas reinhardtii*
CRY	Cryptochrome
CryPro	Cryptochromes in proteobacteria
CTE	C-terminal extension
DAPHNIS	Diverse application platform for hard X-ray diffraction in SACLA
DASH	*Drosophila Arabidopsis Synechocystis Human*
DLZ	6,7-dimethyl-8-ribityllumazine
Dm	*Drosophila melanogaster*
DNA	Deoxyribonucleic acid
Ds	*Dunaliella salina*
dsDNA	Double stranded DNA
E. coli or Ec	*Escherichia coli*
e.g.	For example
EM	Electron microscopy
EPR	Electron paramagnetic resonance
FAD	Flavin adenine dinucleotide

FeS	Iron-sulfur cluster
FET	Forward electron transfer
FID	Free interface diffusion
FMN	Flavin mononucleotide
FTIR	FOURIER-transform infrared spectroscopy
GPCR	G protein-coupled receptor
HDX	Hydrogen/deuterium exchange
HPLC	High performance liquid chromatography
Lf	Lumiflavin
linac	Linear electron accelerator
LOV	Light-oxygen-voltage proteins
MAD	Multi-wavelength anomalous diffraction
mCRY	Mouse cryptochrome
MD	Molecular dynamic
MIR	Multiple isomorphous replacement
Mm	*Methanosarcina mazei*
MR	Molecular replacement
MS	Mass spectrometry
MTHF	5,10-methenyltetrahydrofolate
NADP	Nicotinamide adenine dinucleotide phosphate
NER	Nucleic excision repair
Ot	*Ostreococcus tauri*
pCRY	Plant cryptochrome
PDB	Protein data bank
PHL	Photolyase
PHOT	Phototropin
PHR	Photolyase homology region
Pt	*Phaeodactylum tricornutum*
PYP	Photoactive yellow proteins
RL	Red light
SACLA	Spring-8 Angstrom Compact Free Electron Laser
SAR	Shade avoidance response
SAXS	Small angle X-ray scattering
SEC	Size exclusion chromatography
SFX	Serial femtosecond X-ray crystallography
ssDNA	Single stranded DNA
SSN	Sequence-similarity network
TR	Time-resolved
tr	Transient
TTFL	Transcription-translation feedback loop
UV	Ultraviolet
UVR8	UV-light resistant locus

Vc	*Volvox carteri*
Vf	*Vaucheria frigida*
Vis	Visible
WAXS	Wide angle X-ray scattering
WT	Wildtype
XFEL	X-ray free electron laser
Xl	*Xenopus laevis*

Table 3 List of the amino acids and their abbreviations.

Amino acid	**Three-letter symbols**	**One-letter symbols**
Alanine	Ala	A
Arginine	Arg	R
Asparagine	Asn	N
Aspartic acid	Asp	D
Cysteine	Cys	C
Glutamic acid	Glu	E
Glutamine	Gln	Q
Glycine	Gly	G
Histidine	His	H
Isoleucine	Ile	I
Leucine	Leu	L
Lysine	Lys	K
Methionine	Met	M
Phenylalanine	Phe	F
Proline	Pro	P
Serine	Ser	S
Threonine	Thr	T
Tryptophan	Trp	W
Tyrosine	Tyr	Y
Valine	Val	V

8 Acknowledgements – Danksagung

Ich danke Professor Lars-Oliver Essen für die Möglichkeit diese Arbeit in seiner Gruppe anfertigen zu dürfen. Ich bin ihm sehr dankbar für seine Begeisterung, sein Vertrauen und seine Unterstützung in den letzten vier Jahren. Bedanken möchte ich mich weiterhin für die Aufenthalte in Texas, Taiwan, Japan, Grenoble und im KWT. Nichts gibt einem so viel Motivation wie Wissenschaft bei gutem Essen zu besprechen.

Ich danke Professor Alfred Batschauer für die Übernahme des Zweitgutachtens sowie für die Unterstützung in den letzten Jahren. Vielen Dank auch an die Mitglieder der AG Batschauer für die Hilfe beim Umzug in die Biologie und allem was dazu gehört.

Weiterhin danke ich Professor Norbert Hampp für die Teilnahme in meiner Prüfungskomission.

Ich danke alle meinen Vertiefungsstudenten, die ich über die Jahre betreuen durfte: Laura Sinatra, Filipp Bezold, Laura Werel, Carsten Schotte, Vinzent Schulz, Ammar Alhaj Zein und Alexander Penner. Außerdem danke ich meiner Bachelor-Studentin Nicole Mench und meinen Master-Studis Simon Straß, Christine Kupschus, Elias Maiterth und Hans-Joachim Emmerich. Vielen Dank für euren Beitrag zu dem Projekt und eure Motivation.

Ein besonderer Dank gilt meinen tollen Kollegen, die mir immer mit Rat und Tat zur Seite standen. Während meiner Zeit in der AG Essen waren das: Petra Gnau, Barbara Mertins, Timo Kraushaar, Katrin Anders, Michael Kock, Silke von Horsten, Ankan Banerjee, Vitali Kalugin, Elisabeth Ignatz, Thomas Marcellino, Marian Vogt, Viktoria Reithofer, Sebastian Hepp, Christof Taxis, Roberta Spadaccini, Max Biermeier, Johannes Scheffer, Jonathan Trauth, Filipp Bezold, Laura Werel, Martin Saft, Bastian Pook und Hans-Joachim Emmerich. Vielen Dank für die tolle Zeit im und außerhalb des Labors. Danke fur Team Photo, TripleS, Einhörner, Glitzer und „Rat mal wer zum Essen kommt?“.

Besonderer Dank gilt Petra Gnau, Silke von Horsten, Katrin Anders, Thomas Marcellino und Sebastian Hepp. Vielen Dank, dass ihr mir immer den Rücken gestärkt habt auch wenn es gerade nicht so einfach war. Merci beaucoup!

Weiterhin danke ich Ralf Pöschke für das Pipettieren von Kristallisationsscreens und Uwe Linne sowie Wieland Steinchen für die Durchführung von HDX Experimenten.

Ich danke dem Max Planck Institut Marburg und der Marburg Research Academy für die finanzielle Unterstützung sowie Professor Uwe Maier und Dr. Seigo Shima für die Übernahme meines *Thesis Advisory Committee*.

Ein großer Dank geht an meine Kooperationspartner, Daniel Nohr und Erik Schleicher, und an die Mitglieder der DFG Forschergruppe „*Specific Ligth-Driven Reactions in Unicellular Model Algae*“ (FOR 1261). Vielen Dank für die Experimente und die tollen Diskussionen rund um das Projekt.

I also like to thank my colleagues at the *Academia Sinica* Taipei and in Osaka. Special thanks to “the international troublemakers”: Manuel Maestre-Reyna, Wen-Jin Wu, Raheka and Junpei Yamamoto. Gracias, xièxiè, terima kasih and arigato! Thank you for being such wonderful hosts.

I like to thank all the wonderful and successful female scientists I met over the past years. Especially Prof. Dr. Ada Yonath, who inspired me to study in the fascinating field of structural biology.

Ein herzlicher Dank geht an meine Familie und meine Freunde, bei denen ich immer Kraft tanken konnte, vor allem wenn es gerade mal nicht so lief. Besonders danke ich meinen Eltern für die Unterstützung in den letzten Monaten vor Abgabe dieser Arbeit. Weiterhin danke ich Susanne Pulz, Jasmin Quentin und Nathalie Nett für die zahlreichen Mädelsabende und den Zusammenhalt während der ganzen Studienzeit.

Zuletzt möchte ich meinem Mann Thorben danken. Vielen Dank für deine Ruhe, deinen Optimismus, dein Vertrauen in mich und die Kraft, die mir das gegeben hat. Auf ins nächste Abenteuer!